TECHNISCHE UNIVERSITÄT MÜNCHEN

Department of Chemistry and Catalysis Research Center
Chair of Technical Electrochemistry

Oxygen and Water Transport in the Microporous Layer of Polymer Electrolyte Membrane Fuel Cells

Christoph Rudolf Theodor Simon

Vollständiger Abdruck der von der Fakultät für Chemie der Technischen Universität München zur Erlangung des akademischen Grades eines

Doktor-Ingenieurs (Dr.-Ing.)

genehmigten Dissertation.

Vorsitzender:	Prof. Dr.-Ing. Kai-Olaf M. Hinrichsen
Prüfer der Dissertation:	1. Prof. Dr. Hubert A. Gasteiger
	2. Prof. Dr.-Ing. Harald Klein

Diese Dissertation wurde am 20.01.2020 bei der Technischen Universität München eingereicht und durch die Fakultät für Chemie am 29.04.2020 angenommen.

Abstract

Polymer electrolyte membrane fuel cells with renewable hydrogen as fuel can contribute to a sustainable energy economy. A higher power output per electrode area could save expensive materials, increase the efficiency, and increase the power density of the system, which can help the technology to a market success. The target of this thesis is to reduce the voltage loss of PEM fuel cells at high current density operation by gaining a better understanding of the species transport processes in the fuel cell and to improve the transport processes by developing advanced materials.

Inside the electrochemical cell, the gas diffusion layer (GDL) is responsible for the transport of gases, water, and electrons between the catalyst layer and the flow field gas channels. In particular, the hindering of the oxygen transport by liquid water results in severe voltage losses in a PEM fuel cell. The GDL consists of a gas diffusion layer substrate (e.g. carbon fiber paper) and an adjacent microporous layer (MPL) contacting the electrode, typically consisting of carbon particles and a hydrophobic polymer binder.

In this dissertation, various microporous layer materials with different properties (porosity, pore size distribution, hydrophobicity/hydrophilicity) were prepared, characterized by mercury intrusion porosimetry and scanning electron microscopy and tested in a fuel cell. The performance, impedance spectra and the oxygen transport resistance were measured under different dry and humid fuel cell operating conditions.

The investigations lead to the following results: (1) by measuring a GDL under various compressions, we revealed an additional oxygen transport resistance caused by a liquid water film at the interface between microporous layer and electrode; (2) all-hydrophilic microporous layers prepared with a hydrophilic binder resulted in severe electrode flooding in comparison to hydrophobic microporous layers with conventional hydrophobic binder; (3) a high thermal conductivity of the gas diffusion layer substrate exhibits an early mass transport limitation due to flooding and a lower sensitivity towards microporous layer properties; and (4) the oxygen transport at humid conditions and the overall fuel cell performance can be significantly improved by using carbon fibers instead of carbon black as carbon material or by the introduction of perforations in the MPL, both leading to larger pores available for liquid water transport. Applying these approaches, we could improve the fuel cell performance by 49% for our

best-performing material compared to a commercial microporous layer.

Kurzfassung

Mit erneuerbarem Wasserstoff betriebene Polymerelektrolytmembran (PEM)-Brennstoffzellen können einen Beitrag für eine nachhaltigere Energiewirtschaft leisten. Eine höhere Leistungsabgabe bezogen auf die verwendete Elektrodenfläche kann den Einsatz an teuren Materialien reduzieren, die Effizienz verbessern und die Leistungsdichte des Systems erhöhen, was der Technologie zum Marktdurchbruch verhelfen kann. Die Zielsetzung dieser Arbeit ist es, den Spannungsverlust einer PEM-Brennstoffzelle bei hohen Stromdichten durch ein besseres Verständnis der Transportprozesse innerhalb der Brennstoffzelle und den resultierenden Verbesserungen des Stofftransports durch Anwendung von weiterentwickelten Materialien zu verbessern.

Innerhalb der elektrochemischen Zelle ist die Gasdiffusionsschicht (engl. gas diffusion layer, GDL) verantwortlich für den Transport von Gasen, Wasser und Elektronen zwischen der Kathodenschicht und den Gaskanälen des Flussfeldes. Insbesondere die Blockierung des Sauerstofftransports durch Flüssigwasser führt zu signifikanten Spannungsverlusten der Brennstoffzelle. Die Gasdiffusionsschicht besteht aus einem Substrat (z.B. Kohlefaserpapier) und einer daran gebundenen mikroporösen Schicht (engl. microporous layer, MPL), welche in Kontakt zur Elektrode steht und typischerweise aus Kohlenstoffpartikeln und hydrophobem Polymer-Binder zusammengesetzt ist.

Für diese Arbeit wurden verschiedene MPL-Materialien mit unterschiedlichen Eigenschaften (Porosität, Porengrößenverteilung, Hydrophobizität/Hydrophilizität) hergestellt, mittels Quecksilberporosimetrie und Rasterelektronenmikroskopie charakterisiert und in einer Einzelzelle untersucht. Das Leistungsverhalten, Impedanz-Spektren und der Sauerstofftransportwiderstand wurden bei verschiedenen trockenen und feuchten Betriebsbedingungen gemessen.

Die Untersuchungen haben zu den folgenden Ergebnissen geführt: (1) bei der Untersuchung einer GDL unter verschiedenen Kompressionen wurde ein zusätzlicher Sauerstofftransportwiderstand entdeckt, welcher durch einen Flüssigwasserfilm an der Grenzfläche zwischen mikroporöser Schicht und Elektrode hervorgerufen wird; (2) MPLs, welche durch die Verwendung eines alternativen Binders komplett hydrophil sind, führen zu starken Flutungserscheinungen im Vergleich zu MPLs mit konventionellem hydrophobem Binder; (3) eine hohe thermische Leitfähigkeit der Gasdiffusionsschicht führt zu einer frühen Stofftransportlimitierung durch Flüssigwasserflutung, jedoch zu

einer geringeren Sensitivität der GDL gegenüber der Eigenschaften der mikroporösen Schicht; und (4) der Sauerstofftransportwiderstand und die Brennstoffzellenleistung kann durch die Verwendung von Kohlefasern anstatt Rußen und durch Perforationen in der MPL signifikant verbessert werden, wobei beide Maßnahmen größere Poren hervorrufen, welche den Flüssigwassertransport erleichtern. Durch Anwendung dieser Methoden konnten wir die Brennstoffzellenleistung um 49% bei Verwendung des besten Materials im Vergleich zu einer kommerziellen mikroporösen Schicht verbessern.

Contents

List of Acronyms

Abbreviation	Description
BEV	Battery electric vehicle
BPP	Bipolar plate
CCM	Catalyst coated membrane
DI	Deionized
DP	Dew point
E-REV	Range-extended electric vehicle
ECSA	Electrochemically active surface area
EIS	Electrochemical impedance spectroscopy
EW	Equivalent weight
FC	Fuel cell
FCEV	Fuel cell electric vehicle
GDL	Gas diffusion layer
GDL-S	Gas diffusion layer substrate
HER	Hydrogen evolution reaction
HOR	Hydrogen oxidation reaction
MEA	Membrane electrode assembly
MPL	Microporous layer
OCV	Open circuit voltage
OEM	Original equipment manufacturer
ORR	Oxygen reduction reaction
PEM	Polymer electrolyte membrane
PEMFC	Polymer electrolyte membrane fuel cell
PFSA	Perfluorosulfonic acid
PSD	Pore size distribution
PTFE	Polytetrafluoroethylene
RDE	Rotating disk electrode
RE	Reference electrode
RHE	Reversible hydrogen electrode
SEM	Scanning electron microscopy
SG	Sub-gasket
TEM	Transmission electron microscopy
TGA	Thermogravimetrical analysis

List of Symbols

Latin letters

Symbol	Unit	Description
A	m^2	Area
A_{Pt}	cm^2	Platinum surface area
b	V dec$^-$1	Tafel slope
d_p	nm	Particle diameter
D	$cm^2\,s^{-1}$	Diffusion coefficient
E	V	Voltage / Potential
E_a	$kJ\,mol^{-1}$	Activation energy
E^{eq}	V	Equilibrium potential
E^0	V	Standard electrode potential
ECSA	$m^2\,g^{-1}$	Electrochemical surface area
F	$C\,mol^{-1}$	Faraday constant: $96485\,C\,mol^{-1}$
G	$kJ\,mol^{-1}$	Gibb's free energy
H	$kJ\,mol^{-1}$	Enthalpy
i	A cm$^-$2	Current density
i_s	mA cm$^-$2	Specific activity
i_m	$A\,mg^{-1}$	Mass activity
i	mA cm$^-$2	Current density
i_0	mA cm$^-$2	Exchange current density
I	A	Current
l	cm	Length
L_{cat}	wt.%	Catalyst loading
L_{el}	$mg\,cm^{-2}$	Electrode loading
m	mg	Mass
M	$g\,mol^{-1}$	Molar mass
n	–	Number of electrons
p	Pa	Pressure
Q	C	Charge
R	*various*	Resistance
R_Ω	$\Omega\,cm^2$	Areal resistance
R_T	$s\,cm^{-2}$	Transport resistance
R	$J\,K^{-1}\,mol^{-1}$	Ideal gas constant: $8.3145\,J\,K^{-1}\,mol^{-1}$
rf	$cm^2\,cm^{-2}$	Roughness factor
S	$J\,mol^{-1}\,K^{-1}$	Entropy
T	K	Temperature
t	s	Time
u_{Cat}	%	Catalyst utilization factor
V	ml	Volume

Greek letters

Symbol	Unit	Description
α	–	Transfer coefficient
δ	mm	Thickness
Δ	–	Difference
η	V	Overpotential
ρ	$\mathrm{kg\,m^{-3}}$	Density

Indices

Symbol	Description
A	Anode
ads	Adsorbed
C	Cathode
eff	Effective
el	Electrode (geometrical)
eq	Equilibrium
geo	geometrical

1. Introduction

1.1. The Automotive Industry in Transformation

The automotive industry is currently experiencing major changes - mainly four developments are causing a disruption of the sector:[1,2]

- Digitalization
- Autonomous driving
- New mobility concepts
- Electrification

While the first items are mainly driven by technological progress and socio-economic changes, the electrification of the propulsion system is a result of the growing ecological awareness.

Increasing carbon dioxide emissions since the industrial revolution are considered to be the most influential factor causing global warming. Hence, 195 countries signed the Paris climate agreement in 2015, which includes the limitation of the worldwide temperature increase to 2 °C and the reduction of emissions by at least 60% below 2010 levels by 2050.[3] To achieve this target, also the road mobility sector in the European Union, which causes ~21% of its total CO_2 emissions, has to decrease its fleet carbon dioxide emissions to 95 g/km for passenger vehicles from 2020 onwards.[4,5]

To achieve this target, the electrification of the propulsion system seems currently to be the most promising solution. **Figure 1.1** shows the well-to-wheel CO_2 emissions of various drive trains with combustion engines, hybridized engines, and electrified engines with different power sources.[6,7] While gasoline, diesel, and natural gas engines (CNG) show CO_2 emissions between 100 g/km and 200 g/km even with hybridization, only range-extended electric vehicles (E-REV), battery electric vehicles (BEV), and fuel cell electric vehicles (FCEV) using hydrogen gas as fuel have the potential to reduce the CO_2 emissions below 95 g/km. This, however, only is possible, if a high

amount of the primary energy comes from renewable sources, such as wind or solar. Then E-REVs (in 100% EV mode), BEVs, and FCEVs (in case hydrogen is produced by water electrolysis using 100% renewable energy) emit almost 0 g/km of greenhouse gases. While BEV sales are increasing rapidly, FCEV sales are still very low, which is mainly due to the lower cost and better developed infrastructure for BEVs. Nevertheless, FCEVs have many advantages compared to BEVs, e.g., short refuelling times of <5 min, ranges >500 km with one fuel tank, and a more easily storable energy carrier (hydrogen). Hence, in the future a complementary use of BEVs for short range and small vehicles and of FCEVs for long range and trucks would be a possible scenario.

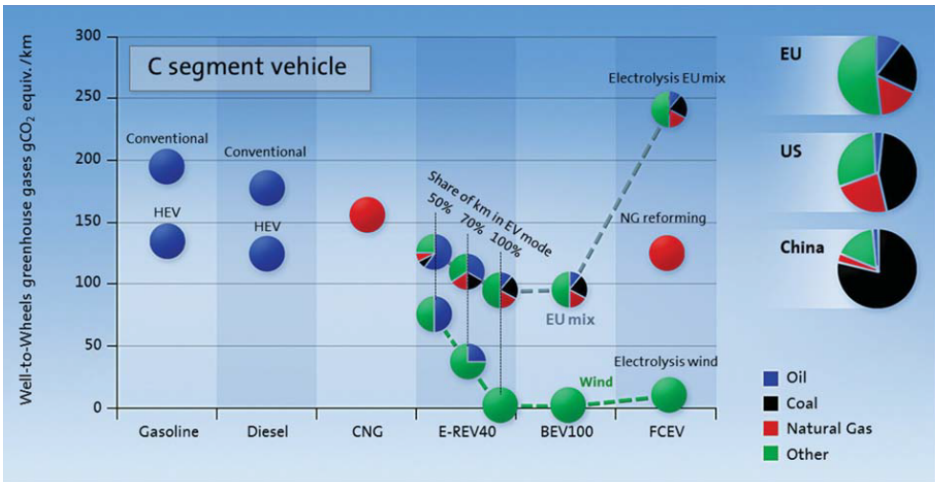

Figure 1.1. Well-to-wheel greenhouse gas emissions of a C segment vehicle with various propulsion systems and energy sources. Reproduced from reference 6 with permission from The Royal Society of Chemistry.

1.2. Challenges for Polymer Electrolyte Membrane Fuel Cells and Motivation for this Thesis

Even though with the Hyundai ix35 FCEV (2013), the Toyota Mirai (2014), the Honda Clarity Fuel Cell (2016), the Hyundai Nexo (2018), and the Mercedes-Benz GLC F-Cell, 4 automakers have meanwhile fuel cell series vehicles on the market, a market breakthrough of the technology is still missing. On the one hand, there is a lack of hydrogen infrastructure, with only 81 refuelling stations in Germany (status January 2020[8]). On the other hand fuel cell vehicles are still expensive for the general market,

with sales prices starting at 69,000 €.

To make fuel cell technology viable for a larger market, mainly cost and efficiency of the fuel cell stack, where the electrochemical reaction takes place, have to be optimized. This is possible by:

- decreasing the cost of expensive and rare materials, such as platinum catalyst and membrane
- increasing the efficiency, i.e., the cell voltage by improving the catalysts for the electrochemical reactions
- improving the utilization of the Pt-based catalyst (and other expensive materials, such as membrane etc.) in terms of the Pt-specific power density (in $\mathrm{kW/g_{Pt}}$) by increasing the current density via reduced transport resistances

The target of the present thesis is to develop a more detailed understanding of the transport processes within and across the various fuel cell component layers in order to design more efficient and more competitive fuel cell systems. In particular, this work is focused on the so called microporous layer (attached to the gas diffusion layer substrate) that is crucial for an efficient transport of oxygen and water. In this thesis, a deeper understanding of this component has been attained and the MPL properties were improved in terms of hydrophobicity/hydrophilicity, porosity, and pore size distribution, ultimately resulting in an improved PEM fuel cell performance by achieving higher current densities at the same or at even higher levels of efficiency.

2. Theoretical Background

This Chapter will provide an overview about the most important aspects of polymer electrolyte membrane fuel cells with a special focus on mass transport phenomena and the gas diffusion layer.

2.1. Working Principle of Polymer Electrolyte Membrane Fuel Cells

2.1.1. Materials and Setup

A polymer electrolyte membrane fuel cell (PEMFC) is an electrochemical cell, which is composed of a combination of two spacially separated electrodes that are in electrical contact over an external circuit and in ionic contact via a polymer electrolyte membrane. While the cathode is in contact with air, the anode is fed with hydrogen resulting in an electrochemical potential difference between the two electrodes.[9] The reactions that are occurring on the anode and cathode of hydrogen driven PEMFC with a proton conducting membrane, are the following:

$$\text{Anode reaction :} \quad \mathrm{H_2} \longrightarrow 2\,\mathrm{H^+} + 2\,\mathrm{e^-} \tag{2.1}$$

$$\underline{\text{Cathode reaction :} \quad {}^1\!/_2\,\mathrm{O_2} + 2\,\mathrm{H^+} + 2\,\mathrm{e^-} \longrightarrow \mathrm{H_2O}} \tag{2.2}$$

$$\text{Cell reaction :} \quad \mathrm{H_2} + {}^1\!/_2\,\mathrm{O_2} \longrightarrow \mathrm{H_2O} \tag{2.3}$$

At the anode (2.1), hydrogen is oxidized to protons and electrons (hydrogen oxidation reaction, HOR), and at the cathode (2.2), oxygen is reduced to water (oxygen reduction reaction, ORR), which in sum results in the reaction of hydrogen and oxygen to water. The reversible cell voltage ($\mathrm{E_{cell}^{rev}}$) is given by the difference of cathode and anode potentials and is 1.23 V at standard conditions.

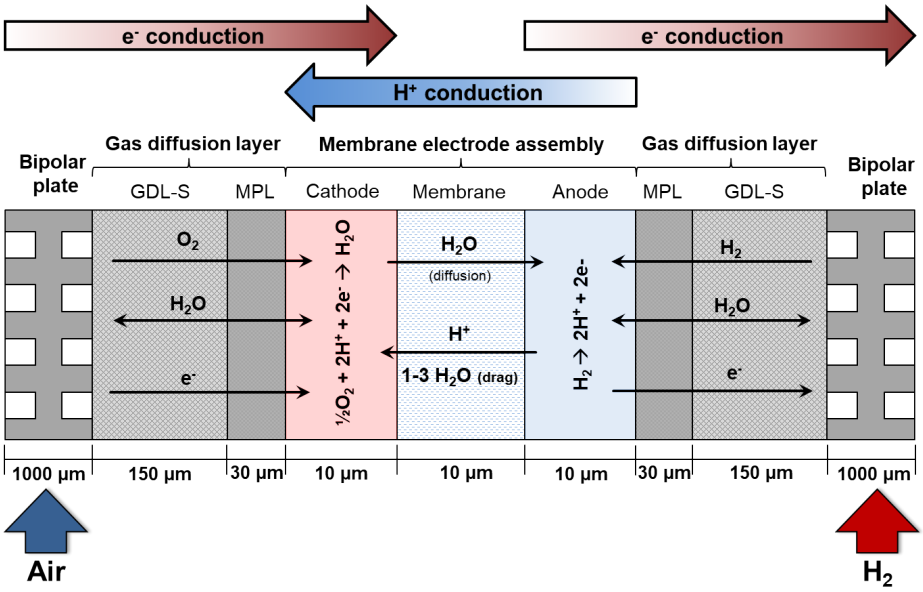

Figure 2.1. Working principle of a single polymer electrolyte membrane fuel cell.

In order to achieve higher power and a more practical voltage, several 100 cells can be stacked to a fuel cell stack. One single cell is set up according to **Figure 2.1**.

The electrochemical cell is sandwiched between two bipolar plates, which contain channels for the supply of air and hydrogen as well as of the coolant. Commercially available plates consist of stainless steel, titanium or graphite.[10–12] In the center between the plates sits the membrane electrode assembly (MEA), which consists of the polymer electrolyte membrane coated with the two electrodes and is surrounded by two gas diffusion layers.

As a material for the polymer electrolyte membrane, perfluorosulfonic acid, a polymeric acid consisting of a fluorinated backbone polymer functionalized with ion conducting sulfonic acid groups is applied.[13,14] On both sides, the membrane is coated with an electrode layer consisting of catalyst to accelerate the hydrogen oxidation and the oxygen reduction reaction, respectively. For this, typically platinum or platinum alloy nanoparticles (cathode: e.g., PtCo, PtNi,; anode: e.g., Pt) supported on a structured carbon material (e.g., Vulcan-XC72, Ketjen Black) is used.[7,10,15,16] The adjacent gas diffusion layer is made of a carbon fiber substrate combined with a microporous layer. Details on these components are presented in section 2.2.

2.1.2. Voltage Loss Contributions in PEM Fuel Cells

The cell voltage of an operating fuel cell (E_{cell}) is determined by the thermodynamics and the kinetics of the half-cell reactions as well as by the transport losses of the reactants/products (O_2, H_2, H_2O, H^+) and the electrical contact resistances. This voltage is depending on the applied current density (i) and can be described by the following equation:

$$E_{\text{cell}} = E^{\text{rev}} + \eta_{\text{ORR}} - \eta_{\text{HOR}} - i \cdot (R_{\text{membrane}} + R_{\text{contact}}) - i \cdot (R_{\text{H}^+,\text{ca}} + R_{\text{H}^+,\text{an}}) - \eta_{\text{tx}} \quad (2.4)$$

Here, η_{ORR} and η_{HOR} are the kinetic overpotentials of the cathodic and anodic reaction, R_{membrane} and R_{contact} are the ohmic resistances of the membrane and electrical contact resistances between the layers (the electrical bulk resistances are generally negligible[17], $R_{\text{H}^+,\text{ca}}$ and $R_{\text{H}^+,\text{an}}$ are the proton transport resistances within the cathode and anode electrode, and η_{tx} is the overpotential induced by the oxygen transport (when operating in pure H_2, its transport resistance is negligible). **Figure 2.2** illustrates the cell voltage contributions for an exemplary PEM fuel cell operated at a cell temperature (T_{cell}) of 80 °C, an absolute pressure (p_{abs}) of 300 kPa and, a relative humidity (RH) of 100%.

Reversible cell voltage

The reversible cell voltage ($E^{\text{rev}}_{\text{cell}}$) is the thermodynamically defined voltage and is the difference between the reversible half-cell potentials of cathode and anode.

$$E^{\text{rev}}_{\text{cell}} = E^{\text{rev}}_{\text{cathode}} - E^{\text{rev}}_{\text{anode}} \quad (2.5)$$

With the Nernst equation, the reversible cell voltages as a function of the reactant concentrations can be calculated. For the fuel cell reaction equation 2.6 can be used:

$$E^{\text{rev}}_{(T,p)} = E^{0}_{(T,p)} + \frac{\text{R}\,T}{2\text{F}} \ln\left(p_{\text{H}_2} \cdot p^{1/2}_{\text{O}_2}\right) \quad (2.6)$$

Here, $E^{0}_{(T,p)}$ is the standard electrode potential at temperature T, R is the universal gas constant (8.3145 J mol^{-1} K^{-1}), F is the Faraday constant (96485 C mol^{-1}), p_{H_2} is the partial pressure of hydrogen, and p_{O_2} is the partial pressure of oxygen. $E^{0}_{(T,p)}$ can be calculated based on the Gibb's free energy (ΔG) and the number of transferred

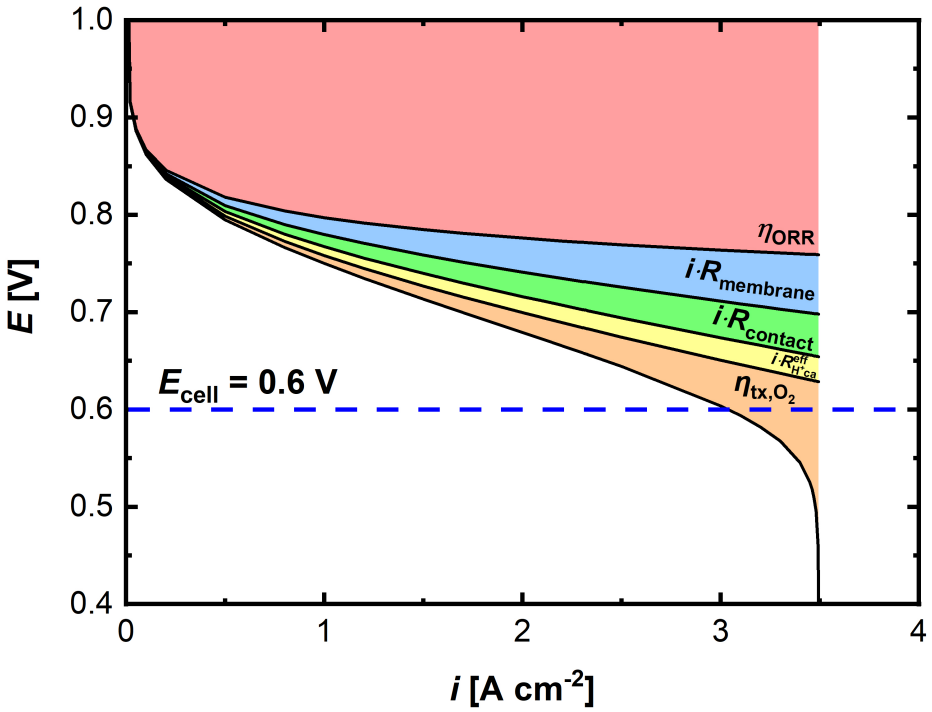

Figure 2.2. Calculated voltage loss contributions for a PEMFC operated at $T_{\text{cell}} = 80\,°\text{C}$, $p_{\text{abs}} = 300\,\text{kPa}$, and $RH = 100\%$. $\eta_{|\text{ORR}}$ represents the kinetic losses due to the oxygen reduction reaction, $i \cdot R_{\text{membrane}}$ the ohmic losses due to proton transport in the membrane, $i \cdot R_{\text{contact}}$ the ohmic losses due to contact resistances, $i \cdot R_{\text{H}^+,\text{ca}}$ the proton transport losses in the cathode ($R_{\text{H}^+,\text{an}}$ is generally negligible), and $\eta_{|\text{tx},\text{O}_2}$ the losses due to oxygen transport. The blue dashed line marks the lower acceptable voltage for PEMFC operation in an FCEV.

electrons ($\text{n} = 2$), which results in 1.23 V at standard conditions ($T = 25\,°\text{C}$, $p_{\text{H}_2} = p_{\text{O}_2} = 100\,\text{kPa}$).

$$E^0 = -\frac{\Delta G}{2 \cdot \text{F}} \tag{2.7}$$

At $T_{\text{cell}} = 80\,°\text{C}$, $p_{\text{abs}} = 300\,\text{kPa}$ and $RH = 100\%$ (equals to $p_{\text{H}_2\text{O}} = 47\,\text{kPa}$ as shown in **Figure 2.2**) the resulting $E^{\text{rev}}_{\text{cell}}$ is 1.19 V.

Kinetic overpotentials

When a current is drawn in a galvanic cell, the electrode potentials deviate from their equilibrium value. The deviation from these equilibrium values are called kinetic overpotentials for the anode ($\eta_{|\text{HOR}}$) and the cathode ($\eta_{|\text{ORR}}$). The current density (i) as a function of the overpotential ($\eta_|$) is described by the Butler-Volmer equation.

$$i = i_0 \cdot rf \left[\exp\left[\frac{\alpha_a \cdot \mathrm{F}}{\mathrm{R} \cdot T} \eta \right] - \exp\left[-\frac{\alpha_c \cdot \mathrm{F}}{\mathrm{R} \cdot T} \eta \right] \right] \tag{2.8}$$

Here, i_0 is the exchange current density (in $\mathrm{A\,cm^{-2}_{Pt}}$) which is a kinetic rate coefficient representing the equilibrium oxidation and reduction current of a half-cell reaction, α_a and α_c are the transfer coefficients for the anodic and cathodic reaction which describe the intrinsic reaction mechanism including the number of transferred electrons in the rate-determining step, and rf is the roughness factor of the electrode, describing the available platinum surface area per geometric electrode area (in $\mathrm{cm^2_{Pt}\,cm^{-2}_{geo}}$).

For high overpotentials, i.e. $\lim_{\eta \to \infty}$ or $\lim_{\eta \to -\infty}$, either the first or the second term of the equation converges to 0. Under these conditions the Butler-Volmer equation simplifies to the so-called Tafel equation. Equation 2.9 represents the Tafel equation for a cathodic reaction, such as the ORR (note that cathodic ORR currents and overpotentials are negative).

$$i = -i_0 \cdot rf \cdot \exp\left[-\frac{\alpha_c \cdot \mathrm{F}}{\mathrm{R} \cdot T} \eta \right] \tag{2.9}$$

When logarithmizing equation 2.9, it results in the following linear correlation 2.10

$$\eta = -\frac{\mathrm{R} \cdot T}{\alpha_c \cdot \mathrm{F}} \ln\left[\frac{i}{i_0 \cdot rf} \right] = -\frac{2.303 \cdot \mathrm{R} \cdot T}{\alpha_c \cdot \mathrm{F}} \log\left[\frac{i}{i_0 \cdot rf} \right] = -b_c \cdot \log\left[\frac{i}{i_0 \cdot rf} \right] \tag{2.10}$$

with

$$b_c = \frac{2.303 \cdot \mathrm{R} \cdot T}{\alpha_c \cdot \mathrm{F}} \tag{2.11}$$

being the Tafel slope.

As the kinetics of the HOR are very fast, the resulting overpotentials even at high current densities are negligible ($< 10\,\mathrm{mV}$) for current MEAs with anode loadings of $0.1\,\mathrm{mg_{Pt}\,cm^{-2}}$.[18–21] The oxygen reduction reaction is the largest contribution to the voltage loss in a PEM fuel cell as shown by the red area in **Figure 2.2**, and can be calculated by using $\alpha_c = 1$, a reaction order towards oxygen of $\gamma = 0.54$, and an activation energy of $E_{act} = 67\,\mathrm{kJ\,mol^{-1}}$; i_0 can be determined individually in fuel cell measurements and is on the order of $10^{-8}\,\mathrm{A\,cm^{-2}_{Pt}}$, depending on the catalyst.[22]

Ohmic potential losses

For ohmic resistances which hinder the charge transport within and across the layers of an electrochemical cell, Ohm's law describes the resulting voltage loss.

$$\Delta U = R_{\Omega} \cdot i \tag{2.12}$$

Ohmic resistances in the fuel cell are specifically the proton transport within the membrane (R_{membrane}) and the electronic contact resistances between the bipolar plates, the gas diffusion layers, and the electrode layers (R_{contact}), which are shown in **Figure 2.2** as blue and green areas.

The resistances within the electrodes depend on the current distribution along the electrode layer thickness that in turn depends on the drawn current and Tafel slope. As the anode reaction kinetics are very fast so that most of the HOR is occurring at the electrode/membrane interface, the proton transport resistance ($R_{\text{H}^+,\text{an}}$) can be neglected. However for the sluggish ORR, the reaction is distributed over the cathode catalyst layer thickness and ($R_{\text{H}^+,\text{ca}}$) can be determined from the proton sheet resistance that can be measured by impedance spectroscopy under blocking electrode conditions (i.e., H_2 and N_2 as feed gases) and a correction factor (ξ).[23]

$$R_{\text{H}^+,\text{ca}} = \frac{R_{\text{sheet}}}{3 + \xi} \tag{2.13}$$

with

$$\xi = \text{f}\left(\frac{i \cdot R_{\text{sheet}}}{b_{\text{c}}}\right) \tag{2.14}$$

The proton transport losses $i \cdot R_{\text{H}^+,\text{ca}}$ are shown in yellow in **Figure 2.2**.

Oxygen transport overpotentials

Concentration overpotentials are caused by a reduction of the species concentrations at the catalyst surface due to transport induced concentration gradients. This results in a shift of the Nernst potential of the electrodes as well as in a deceleration of the reaction kinetics. As a descriptor for the species transport through the porous layers of a fuel cell, a total transport resistance ($R_{\text{T,x}}$ for species x) can be defined, which summarizes all convective and diffusive processes. As hydrogen (1) has a higher

diffusion coefficient than oxygen (~4x faster diffusion in N_2 at 25 °C), (2) is higher concentrated (100% H_2 compared to 21% O_2 in air in our experiments), and (3) can be oxidized at negligible overpotentials, the concentration overpotentials at the anode can generally be neglected.

At the cathode, however, the transport of oxygen can cause severe overpotentials. The total oxygen transport resistance (R_{T,O_2}) can be described as the additive sequence of the oxygen transport resistance from the bulk flow in the flow field to the GDL interface (R_{FF,O_2}), the transport resistance in the GDL-substrate ($R_{GDL–S,O_2}$) and in the MPL (R_{MPL,O_2}), the transport resistance from the cathode catalyst layer surface to the active sites of the platinum catalyst particles ($R_{cathode,O_2}$), and the transport resistances caused by other effects (e.g. interface effects between MPL and catalyst layer).[15,24–34] The terms are illustrated in equation 2.15 and in **Figure 2.3**.

$$R_{T,O_2} = R_{FF,O_2} + R_{GDL–S,O_2} + R_{MPL,O_2} + R_{cathode,O_2} + R_{other,O_2} \tag{2.15}$$

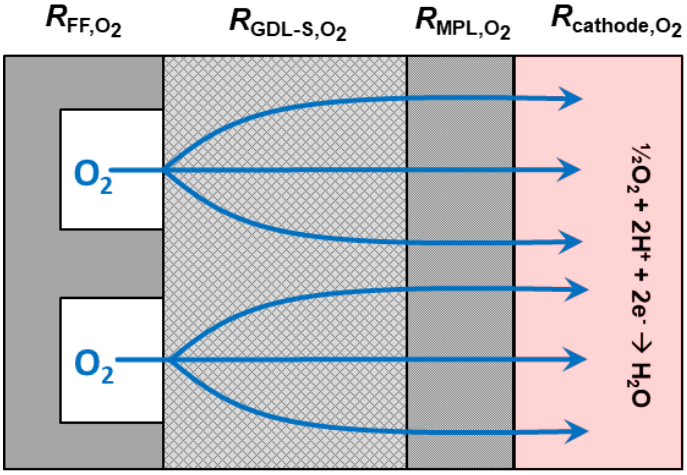

Figure 2.3. Illustration of oxygen transport resistances across the layers of a PEMFC cathode. R_{FF,O_2} is the oxygen transport resistance in the flow fields, $R_{GDL–S,O_2}$ in the GDL substrate, R_{MPL,O_2} in the MPL, and $R_{cathode,O_2}$ in the cathode catalyst layer.

A descriptor for the diffusion mechanism is the ratio of pore mean free path length of the molecules and available pore diameter which is called the Knudsen number (Kn). The total oxygen transport resistance can be divided into molecular diffusion for a

mean free path length of molecules significantly smaller than the pore size ($\lambda << d_p$, i.e., Kn << 1) and Knudsen diffusion for a mean free path length of molecules significantly larger than the pore size ($\lambda >> d_p$, i.e., Kn >> 1). While the molecular diffusion coefficient of O_2 depends on the absolute gas pressure, Knudsen diffusion is independent of the pressure. Assuming that one type of diffusion type is dominant in a specific layer, the pressure-dependent (R_{PD,O_2}) and pressure-independent (R_{PI,O_2}) transport resistances can be summed up:

$$R_{T,O_2} = R_{PD,O_2} + R_{PI,O_2} \tag{2.16}$$

While the diffusion in the GDL-substrate is dominated by molecular diffusion, the diffusion in the electrode is dominated by pressure-independent diffusion (in the pores of the electrode layer and via film diffusion through the ionomer layer to the Pt particle surface).[15,25,29] In the MPL, both types of oxygen diffusion can be present, but depending on the pore size distribution of the layer, one of those is dominating.[25]

R_{T,O_2} is defined as the fraction of the concentration gradient Δc_{O_2} and the molar flux of oxygen $\dot{N}_{O_2}$, which can be converted by Faraday's law into a current density according to 2.17.

$$R_{T,O_2} = \frac{\Delta c_{O_2}}{\dot{N}_{O_2}} = 4F\frac{\Delta c_{O_2}}{i} \tag{2.17}$$

The concentration of oxygen in the flow field channel can be defined with the ideal gas law, the absolute pressure (p_{abs}), the partial pressure of water (p_{H_2O}), and the dry oxygen content of the gas ($x_{O_2}^{dry}$) as follows.

$$c_{O_2} = \frac{p_{abs} - p_{H_2O}}{R \cdot T} \cdot x_{O_2}^{dry} \tag{2.18}$$

For the case that at limiting current density in a differentially operated fuel cell (no gradients of pressure, temperature, concentration), the concentration of oxygen at the catalyst surface area approaches to 0, R_{T,O_2} can be determined by equation 2.19.

$$R_{T,O_2} = 4F\frac{x_{O_2}^{dry}}{i_{lim}} \cdot \frac{p_{abs} - p_{H_2O}}{R \cdot T} \tag{2.19}$$

The overpotential due to the oxygen partial pressure gradient is caused by a deceleration of the reaction kinetics ($\Delta\eta_{ORR}$) and by a shift of the Nernst potential

($\Delta\eta_{\text{Nernst}}$).[35]

$$\eta_{\text{tx,O}_2} = \Delta\eta_{\text{ORR}} + \Delta\eta_{\text{Nernst}} \tag{2.20}$$

$\Delta\eta_{\text{ORR}}$ can be derived from the Tafel equation (equation 2.10) by using the reaction order γ.

$$\Delta\eta_{\text{ORR}} = \frac{\text{R} \cdot T}{\alpha \cdot \text{F}} \cdot \gamma \cdot \ln\frac{p_{\text{FF,O}_2}}{p_{\text{cathode,O}_2}} \tag{2.21}$$

where $p_{\text{FF,O}_2}$ is the bulk oxygen partial pressure in the flow field, and $p_{\text{cathode,O}_2}$ is the oxygen partial rpessure at the cathode electrode. $\Delta\eta_{\text{Nernst}}$ can be derived from the Nernst equation (equation 2.6).

$$\Delta\eta_{\text{Nernst}} = \frac{\text{R} \cdot T}{4 \cdot \text{F}} \cdot \ln\frac{p_{\text{FF,O}_2}}{p_{\text{cathode,O}_2}} \tag{2.22}$$

From equation 2.17 and the ideal gas law, one can determine the partial pressure of oxygen at the cathode electrode ($p_{\text{cathode,O}_2}$).

$$p_{\text{cathode,O}_2} = p_{\text{FF,O}_2} - \frac{\text{R} \cdot T}{4 \cdot \text{F}} \cdot R_{\text{T,O}_2} \cdot i \tag{2.23}$$

Finally, when including equations 2.21, 2.22 and 2.23 into equation 2.20, the oxygen transport induced overpotential can be determined.

$$\eta_{\text{tx,O}_2} = \frac{\text{R} \cdot T}{\text{F}} \cdot \left(\frac{1}{4} + \frac{\gamma}{\alpha}\right) \cdot \ln\left(\frac{p_{\text{FF,O}_2} - \frac{\text{R} \cdot T}{4 \cdot \text{F}} \cdot R_{\text{T,O}_2} \cdot i}{p_{\text{FF,O}_2}}\right) \tag{2.24}$$

When applying different oxygen transport resistances of $1\,\text{s}\,\text{cm}^{-2}$, $2\,\text{s}\,\text{cm}^{-2}$, and $3\,\text{s}\,\text{cm}^{-2}$ in the example from **Figure 2.2**, the sensitivity of the fuel cell at high current densities towards $R_{\text{T,O}_2}$ becomes obvious and is illustrated in **Figure 2.4**.

Thus, when reducing $R_{\text{T,O}_2}$ from $3\,\text{s}\,\text{cm}^{-1}$ to $1\,\text{s}\,\text{cm}^{-1}$, the limiting current density can be significantly increased and the oxygen transport overpotential can be significantly reduced. Consequently, at a typical full load operating voltage of 0.6 V, the power density can be considerably increased from $P_{\text{el}} = 1.3\,\text{W}\,\text{cm}^{-2}$ to $P_{\text{el}} = 2.2\,\text{W}\,\text{cm}^{-2}$.

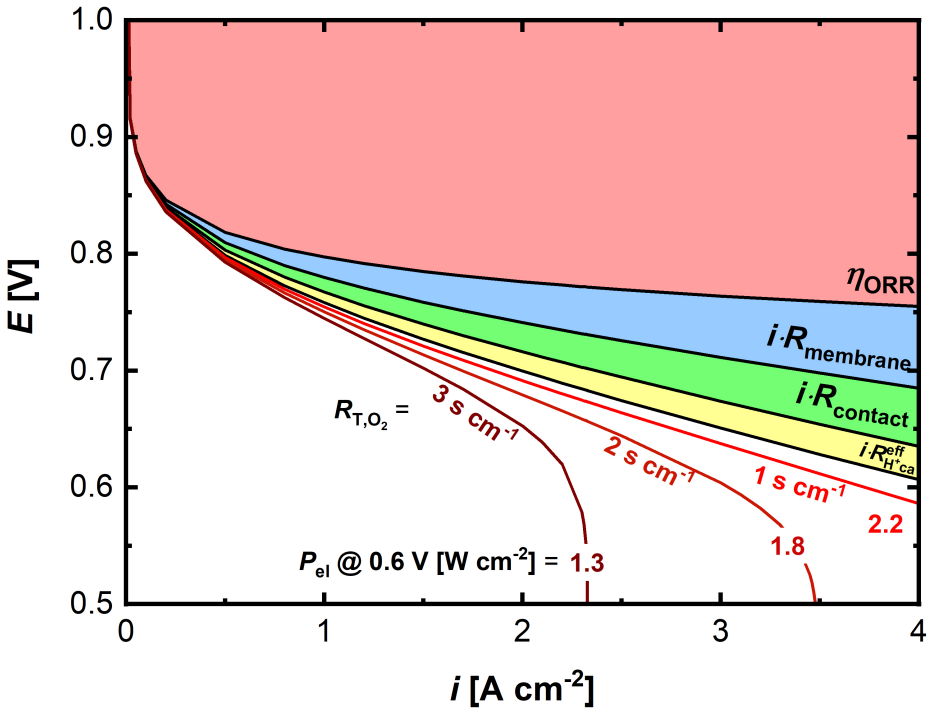

Figure 2.4. Calculated voltage loss contributions for a PEMFC operated at $T_{\text{cell}} = 80\,^{\circ}\text{C}$, $p_{\text{abs}} = 300\,\text{kPa}$, and $RH = 100\%$ with three different oxygen transport resistances ($R_{\text{T,O}_2}$) of $1\,\text{s}\,\text{cm}^{-1}$, $2\,\text{s}\,\text{cm}^{-1}$, and $3\,\text{s}\,\text{cm}^{-1}$.

2.2. Gas Diffusion Layers

2.2.1. Functionality

The gas diffusion layer in a PEM fuel cell has to fulfil the following functions:[17,36–38]

- **Pressure distribution** (GDL-S): The GDL-S has to distribute the pressure over the whole MEA area, which requires a certain amount of bending stiffness to provide an appropriate compression pressure in the unsupported channel center.[39–41]
- **Electron transport** (GDL-S, MPL): The components of the GDL must have a sufficient electronic conductivity in order to reduce ohmic losses; furthermore they must have appropriate surface properties to reduce contact resistances between the GDL-S and the flow fields as well as between the MPL and the electrodes.[17,39,42]
- **Reactant and water transport** (GDL-S, MPL): The GDL has to provide good transport properties for reactant species in order to reduce oxygen transport

overpotentials. In particular at high current densities, where liquid water is formed, the GDL-S and MPL have to provide well-balanced pore properties to efficiently remove the water from the electrode to the flow field channels, but to still guarantee an effective oxygen transport to the cathode. [26,36,43–45]

- **Heat removal** (GDL-S, MPL): To effectively remove the heat of reaction from the electrode, the GDL has to have an appropriate thermal conductivity. [43,46–50]
- **Smooth and close contact to the electrode** (MPL): The MPL has to provide a smooth contact to the electrode layer in order to reduce electric and thermal contact resistances, as well as to prevent flooding of the electrode/GDL interface with liquid water. [36,51–59]

Figure 2.5 illustrates the here described functionalities.

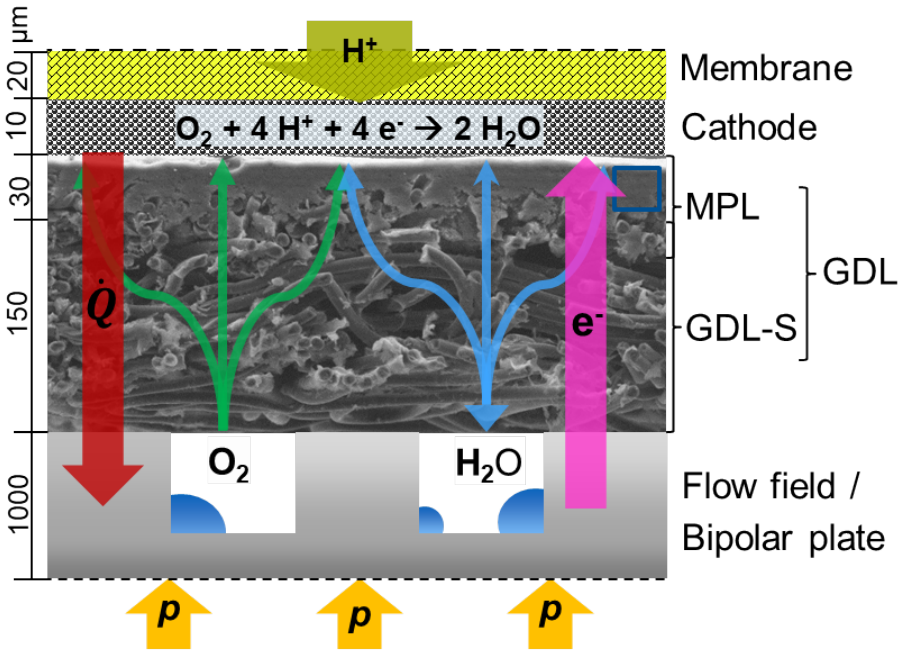

Figure 2.5. Illustration of the functionalities of the gas diffusion layers.

2.2.2. Materials for Gas Diffusion Layer Substrates

In order to fulfil the functionalities listed in section 2.2.1, mainly two classes of materials based on carbon fibers are used as gas diffusion layer substrates: carbon fiber paper (or wet-laid carbon fiber paper; e.g., fabricated by Toray, SGL Carbon, AvCarb)

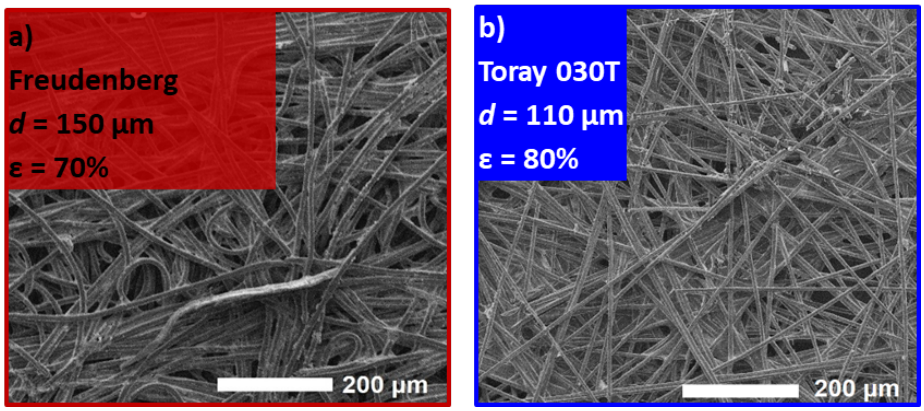

Figure 2.6. Top-view SEM images of the two different GDL-substrates: Freudenberg H1410 I4 (a) and Toray 030T (b).

and non-woven carbon fiber materials (or dry-laid carbon fiber material; e.g. fabricated by Freudenberg). **Figure 2.6** shows a Toray 030T and a Freudenberg H1410 I4 hydrophobically treated carbon fiber substrate. As raw material for both processes polyacrynitrile (PAN) fibers are used. In a carbon paper process, PAN fibers are carbonized at 1200 °C to 1350 °C in nitrogen and afterwards undergo a continuous wet-laid papermaking process. Afterwards, the layers are impregnated with a resin, which is molded to stabilize the paper and then carbonized or graphitized at temperatures $> 2000\,°C$. In case of the non-woven materials, the PAN fibers are dry-laid to form fleece mats and are stabilized mechanically by a hydroentangling process to align the fibers. The product is carbonized at temperatures up to 1500 °C, optionally impregnated and carbonized/graphitized up to 2000 °C.[17] Besides these two material types, there exist carbon cloth substrates (woven materials), carbon foams, and metallic meshes, which however are rather niche products.[38]

The different manufacturing techniques result in varied material properties, such as porosity, pore size distribution, mechanical properties (elastic modulus, shear modulus, characteristic stress-strain curve), as well as electrical and thermal conductivity. For a Freudenberg H1410 I4 and a Toray 030T GDL substrate, the thermal resistivity and estimated thermal gradient under high current density operation at $3.2\,A\,cm^{-2}$ and 0.6 V are shown in **Figure 2.7**. As carbon papers (as Toray 030T) are typically graphitized at temperatures $> 2000\,°C$, while non-wovens (as Freudenberg H1410 I4) are typically partially graphitized at temperatures $< 2000\,°C$, the thermal conductivity for the Freudenberg GDL is lower by a factor of 2.5. This clearly will cause a higher thermal gradient across the GDL-substrate resulting in a higher temperature

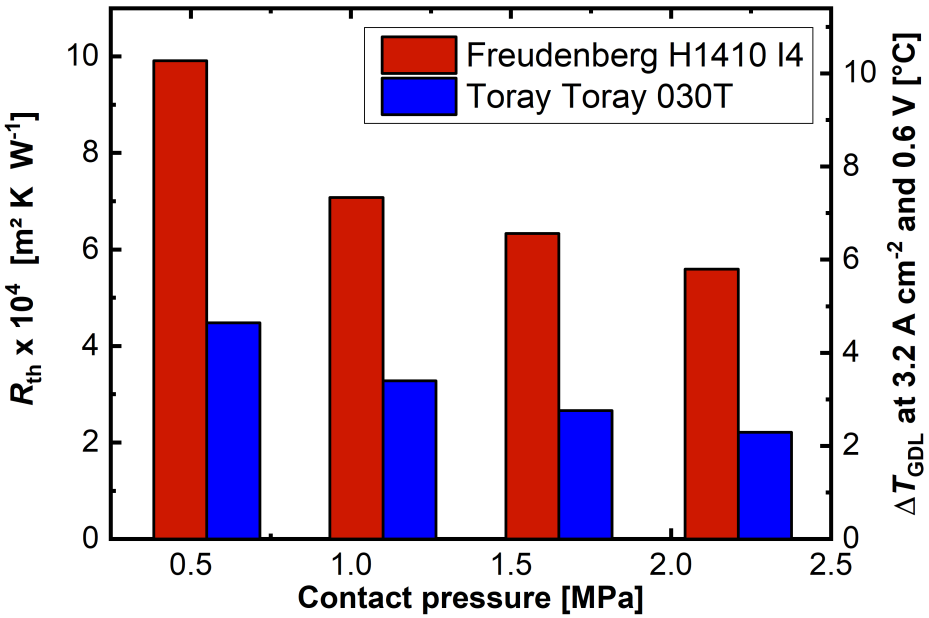

Figure 2.7. Thermal conductivity (left axis) and calculated thermal gradient (right axis) across the GDL-S at 3.2 A cm^{-2} and 0.6 V for two materials: Freudenberg H1410 I4 (red) and Toray 030T (blue). Thermal conductivity measurements were conducted by General Motors.

at the electrodes.

Usually the raw substrate materials are hydrophobically treated with PTFE (or other stable polymers) in order to prevent the material from flooding with liquid water. For that the GDL is impregnated by a PTFE dispersion and thermally treated to temperatures $> 350\,^{\circ}$C to sinter the PTFE particles. The final PTFE content in the GDL-substrate is typically between 5% and 30%, depending on the application.[17]

2.2.3. Microporous Layers

Additionally, GDL-substrates are coated with a microporous layer (MPL) on the MEA facing side to (1) improve the water transport properties, (2) to reduce the contact resistances at the electrode/GDL interface, and (3) to protect the MEA from pinhole formation by vertically oriented carbon fibers extending from the GDL-substrate.[17,36,43,60–64] The micropoporous layer conventionally consists of a carbon material (carbon black, graphite, carbon fibers, etc.) or a mixture thereof and a hydrophobic binder, which is typically polytetrafluoroethylene (PTFE). The choice of carbon material and the amount of binder determine the porosity, pore size distribution, and pore shapes as well as the surface properties of the MPL. In general, the pore

size maximum in the MPL is less than 500 nm compared to that of the GDL-substrate which is typically larger than 10 µm.[17] By adding typically between 10 wt.% and 40 wt.% of PTFE as binder, the MPL is stabilized and hydrophobized to not retain liquid water in its structure.[17,36,65–67] The MPL coating on the GDL-substrate is conventionally between 20 and 50 µm, and an example for an MPL (30 µm in average thickness) on a GDL-substrate is shown in **Figure 2.8**. The MPL contains a smooth surface (top) to contact the electrode layer, and strongly adheres to the GDL-substrate, which is apparent by the enclosed fibers.

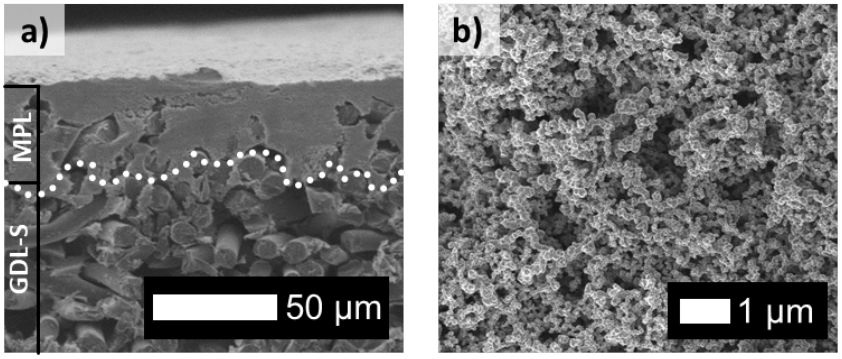

Figure 2.8. Cross-sectional view (a) and top-view (b) SEM images of an MPL coated on a Freudenberg GDL-substrate.

2.2.4. Approaches to Improve Transport Properties

As with recent developments in catalyst technology and system components, the PEMFC is able to achieve high current densities of $1.5\,\mathrm{A\,cm^{-2}}$ and higher, overpotentials due to species transport become important. The reduction of transport overpotentials in the GDL can be achieved with various methods and has to be well balanced with other properties of the GDL.

Figure 2.9 shows the total oxygen transport resistance of a GDL-substrate without (black line) and with an MPL (blue line) versus the limiting current density obtained by measurements with varying O_2 content of the cathode feed gas (0.5% - 28% O_2 in N_2). The operating conditions ($T_{\mathrm{cell}} = 50\,^{\circ}\mathrm{C}$, $p_{\mathrm{abs}} = 400\,\mathrm{kPa}$, and $RH = 77\%$) were chosen so that at small current densities the GDL remains free of liquid water and that with increasing current density the cathode GDL is successively flooded with liquid water from the electrode reaction, resulting in a state of maximum saturation

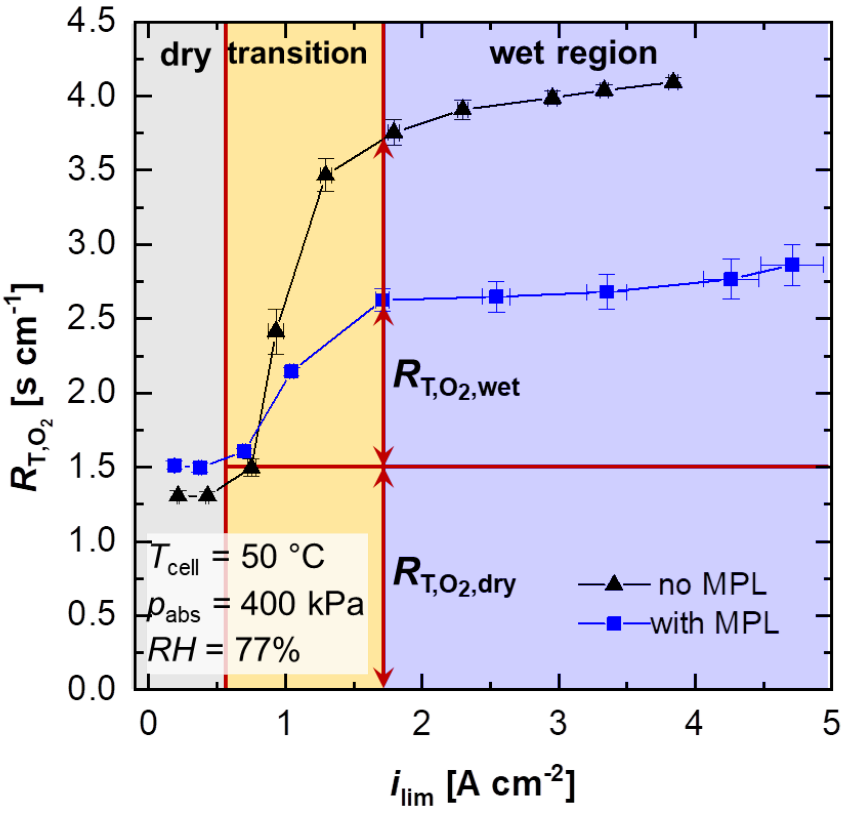

Figure 2.9. Total oxygen transport resistance R_{T,O_2} versus the limiting current density i_{lim} for a substrate without (black symbols) and with MPL (blue symbols). Operating conditions are T_{cell} = 50 °C, p_{abs} = 400 kPa, and RH = 77% using an MEA (from Gore) with an 18µm thick PFSA membrane and with anode/cathode Pt loadings of 0.1/0.4 mg cm^{-2}.

at maximum current density. This behaviour of GDLs has been evaluated in detail by Caulk and Baker.[26] At small current densities of $i < 0.5\,\mathrm{A\,cm^{-2}}$ (i.e., when the GDL is dry), R_{T,O_2} is small and constant, whereby the GDL with an MPL has a slightly higher R_{T,O_2} due to the additional diffusion barrier posed by the MPL. At $0.5\,\mathrm{A\,cm^{-2}} < i < 1.7\,\mathrm{A\,cm^{-2}}$, the transport resistance is gradually increasing due to the formation of liquid water and the partial saturation of the porous structure. At $i > 1.7\,\mathrm{A\,cm^{-2}}$, the GDLs are saturated to a maximum amount with liquid water and R_{T,O_2} is leveling out on a high plateau. Here, the GDL with an MPL has a significantly smaller oxygen transport resistance, as the MPL prevents flooding of the GDL/electrode interface and, hence, provides an efficient transport of oxygen while removing liquid water from the electrodes.

To improve the fuel cell performance at high current densities, the transport prop-

erties of the GDL-substrate, the MPL, and the combination of both can be optimized by different methods. Here, the aim is to reduce the oxygen transport resistance by improving the parallel transport of oxygen and water. In the literature, different approaches can be found, of which many target to optimize the capillary pressure barrier (p_c) of the GDL-S and the MPL, which has to be overcome for water to pass through a pore.

$$p_c = p_l - p_v = 4 \cdot \frac{\gamma_{H_2O} \cdot \cos\Theta}{d_{pore}} \tag{2.25}$$

Here, p_l and p_v are the pressures of the liquid and vapor phase, γ_{H_2O} is the surface tension, Θ is the contact angle of water on the pore surface, and d_{pore} is the pore diameter. The capillary pressure can be reduced by tuning the hydrophilicity/hydrophobicity (i.e., Θ), or the pore size distribution (i.e., d_{pore}).

In general, approaches to optimize the transport properties of the GDL-substrate are:

- Perforations of the GDL-substrate [68–73]
- Variation of the GDL-substrate effective diffusivity (i.e. porosity/pore size distribution) [36,74,75]
- Variation of hydrophobicity/hydrophilicity by varying the amount and the type of binder [74,76,77]
- Optimization of the GDL-substrate thickness [74,76]
- Creation of hydrophilic water pathways [78–80]
- **Variation of physical properties (e.g. thermal conductivity)** [26,43,47]

Approaches to optimize the MPL are:

- **Perforations/cracks in the MPL** [71,72,81,81–88]
- **Variation of the hydrophobicity/hydrophilicity by amount and the type of binder** [67,89–102]
- **Variation of the pore properties by variation of the carbon materials** [54,90,91,103–111]
- Optimization of MPL thickness [107,112–114]
- Creation of pore size or hydrophobicity gradients [36,109,115–118]

The approaches highlighed in bold have been examined in the present thesis to understand and improve the oxygen transport in the GDL. Furthermore, the physical/geometrical properties in the fuel cell setup can be tuned, e.g., by variation of the flow field geometries[30] and by increasing the compression force, which is also investigated in the present work.[25,34,75,119–121]

3. Experimental Methods

In this chapter, experimental methods applied in the present work are explained. As most of the equipment is explained in chapter 4, the following pages will focus on summarizing the approaches and giving additional insights.

3.1. Preparation of Microporous Layers

MPLs were prepared according to the preparation procedures described in the experimental sections of references 54 (for hydrophobic carbon black and perforated MPLs) and 90 (for carbon fiber and hydrophilic MPLs). In **Table 3.1**, all investigated MPLs and their composition are summarized.

3.2. Material Characterization

Raw materials for the preparation of MPLs as well as finished GDL-substrates and MPLs were characterized by scanning electron microscopy, nitrogen sorption measurements, mercury porosimetry and various fuel cell testing methods.

3.2.1. Scanning Electron Microscopy

Two types of scanning electron microscopes were used in the measurements for this thesis: a JCM-6000 benchtop SEM (Jeol) and a FESEM 7500F field emission SEM (Jeol). While the first one was utilized mostly for overview measurements of GDLs and MPLs and for thickness measurements with magnifications up to x5,000, the latter one was used for detailed MPL analysis with magnifications between x10,000 and x250,000 and for the analysis of the carbon materials used for MPL preparation.

The measurements with the JCM-6000 benchtop SEM (Jeol) were taken at 5 kV acceleration voltage and a magnification of x500 by the secondary electron detector,

Table 3.1. Summary of all microporous layers shown in this thesis. Preparation procedures, recipes and results can be found in sections 4.2 and 4.3 or references 34 and 54. Li100 and Li400 are acetylene blacks (from Denka) with BET areas of $68\,m^2\,g^{-1}$ and $39\,m^2\,g^{-1}$, respectively; VGCF-H are carbon fibers (from Showa Denko) with a BET area of $13\,m^2\,g^{-1}$.

Name [-]	Category [-]	Li100 [wt%]	Li400 [wt%]	VGCF-H [wt%]	Macropores[1] [vol%]	PTFE [wt%]	PFSA [wt%]	Current at 0.6 V[2] [$A\,cm^{-2}$]
Li100	hydrophobic	80	-	-	-	20	-	2.03
Li400 (0% VGCF)	hydrophobic	-	80	-	-	20	-	2.28
Li100 perforated	hydrophobic	80	-	-	20	20	-	2.31
Li400 perforated	hydrophobic	-	80	-	20	20	-	2.44
50% VGCF	hydrophobic	-	40	40	-	20	-	2.32
80% VGCF	hydrophobic	-	16	64	-	20	-	2.42
100% VGCF	hydrophobic	-	-	80	-	20	-	2.51
Li400 (0% VGCF)	hydrophilic	-	80	-	-	-	20	2.15
80% VGCF	hydrophilic	-	16	64	-	-	20	2.26

[1] Volume content of polymethacrylate (PMMA) beads with diameter of 30 µm used as pore former.
[2] Current density measured at 0.6 V for the operating conditions $T = 50\,°C$, $p_{abs} = 300kPa$, $RH = 120\%$, using an MEA based on an 18 µm PFSA membrane with anode and cathode loadings of $0.1\,mg\,cm^{-2}$ and $0.4\,mg\,cm^{-2}$ (from Gore).

while for the FESEM 7500F field emission SEM acceleration voltages between 0.5 kV and 1.0 kV were applied.

Top-view images of the MPL were recorded with MPLs coated onto the GDL-substrate, which were fixed by carbon tape on a sample holder. For cross-sectional images, the samples were cut with a razor blade in order to exhibit a clean cutting-edge and fixed onto a cross-section sampled holder. In the experimental sections of the results chapters, details on the specific SEM measurements can be found.[34,54,90]

3.2.2. Mercury Porosimetry

To study the pore size distribution and the porosity of the prepared GDLs and MPLs, mercury porosimetry was used. Both GDL-S/MPL samples and free-standing MPL samples with a sample weight of $m_{\mathrm{sample}} \approx 100$ – 200 mg were characterized in two porosimeters (Pascal 140 and Pascal 440; CE Elantech, Inc. USA). The porosity distributions are illustrated as mass-normalized cumulative pore volume and differential pore volume ($\mathrm{d}\,V/\mathrm{dlog}\,d$) as function of the pore diameter. For free-standing MPLs the porosity ($\varepsilon_{\mathrm{MPL}}$) is calculated based on the pore volume of the MPL from the mercury porosity measurements (v_{pore}), and the total MPL volume (v_{MPL}) is calcuated with the respective mass fractions (w) of the MPL components carbon black (CB), VGCF, and PTFE as binder together with the respective densities (ρ).

$$\varepsilon_{\mathrm{MPL}} = \frac{v_{\mathrm{pore}}}{v_{\mathrm{MPL}}} = \frac{v_{\mathrm{pore}}}{v_{\mathrm{pore}} + \frac{w_{\mathrm{CB}}}{\rho_{\mathrm{CB}}} + \frac{w_{\mathrm{VGCF}}}{\rho_{\mathrm{VGCF}}} + \frac{w_{\mathrm{PTFE}}}{\rho_{\mathrm{PTFE}}}} \tag{3.1}$$

3.2.3. Other Measurement Methods

Further measurement methods were applied where required. The particle size distribution of PMMA particles was determined with a laser scattering particle size analyzer (Retsch Technology, HORIBA LA-960).[54]. Thermogravimetric analyis was used to determine the decomposition temperatures of the MPL materials to develop an optimal heat treatment procedure for the MPL. For this purpose, dried PTFE dispersion, methyl cellulose, TritonX-100, and PMMA particles were characterized with a TGA/DSC (TGA/DSC 1, Mettler Toledo) in synthetic air.[54] Furthermore, pore size analysis and BET surface area measurements were conducted for the carbon blacks Li100 and Li400 (Denka, Japan) in a gas sorption analyszer (Autosorb-iQ,

Quantachrome, USA) with nitrogen as adsorbant.[54] In order to determine the pressure distribution in the fuel cell at various compression levels, FUJIFILM Prescale film was used in ranges from 0.2 MPa to 2.5 MPa by placing the films between flow field and GDL on the cathode side of the fuel cell setup. By this method, the overall pressure, as well as the pressure on the land and channel regions of the flow field can be measured.[34]

3.3. Fuel Cell Testing

3.3.1. Fuel Cell Test Setup

All fuel cell tests were conducted in a custom-designed Greenlight Innovation G60 fuel cell test station equipped with an Agilent N3306A load for recording polarization curves and a Gamry Reference 3000 potentiostat for impedance measurements. Gas flow rates are adjusted by Alicat mass flow controllers, of which for each major gas (hydrogen, air/oxygen, and nitrogen) three MFCs are used to achieve a high accuracy over a wide flow range. The desired relative humidity is achieved by dew point control of humidifiers, and the humidified gases are conducted to the test cell in heated tubes in order to prevent condensation before entering the cell.

The single cell (5 cm^2 active area; Fuel cell Technologies) setup was equipped with custom-designed flow fields (Poco Graphite, for details see section 3.3.3) consisting of 7 channels (channel/land width of 0.5 mm and channel depth of 0.8 mm) in a serpentine arrangement. The fuel cell setup is shown in **Figure 3.1**.

As MEA, a catalyst coated membrane (Primea Mesga A510.1/M715.18/C580.4; W. L. Gore & Associates) with an 18 µm PFSA membrane and platinum loadings of 0.4 mg cm^{-2} on the cathode and 0.1 mg cm^{-2} on the anode was used. The comparably high loadings were necessary in order to prevent significant oxygen transport losses arising from the electrodes, which would disturb our measurements focusing on the gas diffusion layer as limiting factor.[15] The CCM with the GDLs is sandwiched between the bipolar plates, which in turn are sandwiched between gold coated copper current collectors insulated against the aluminum end plates. To achieve the desired GDL compression, gaskets made of PTFE coated fiber glass (Fiberflon) in various thicknesses of d_{anode} and d_{cathode} are used and the cell is compressed with 8 bolts tightened with a torque of 12 Nm. It should be noted that the cell compression is

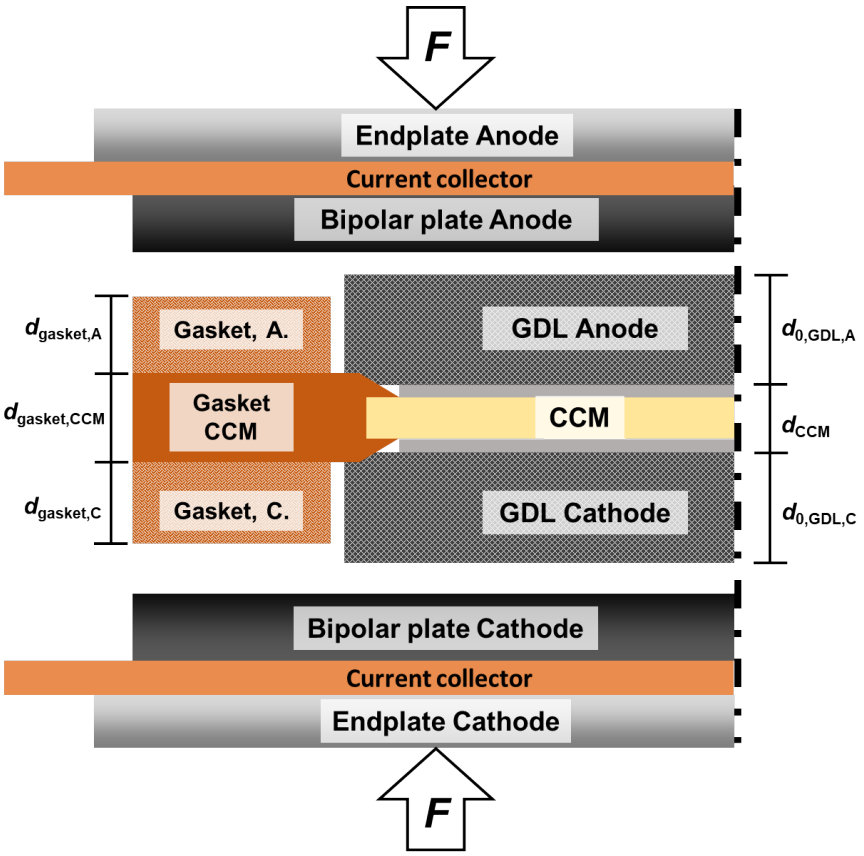

Figure 3.1. Single cell setup showing the cell components such as GDLs, CCM, and gaskets sandwiched between the bipolar plates, current collectors, and the endplates. To achieve the desired cell compression, a force (F) is applied by 8 bolts tightened with a torque of 12 Nm.

based on a hard-stop gasket concept that achieves a defined compressive force on the GDL by controlling its strain. Details can be found in section 4.1 or reference 34.

3.3.2. Measurement Conditions

Details on the procedure of the fuel cell measurements can be found in sections 4.1 and 4.2 as well as in references 34 and 54. This section summarizes the measurement conditions of all publications for polarization curves and limiting current measurements, and is giving a background why these specific conditions were chosen.

All operating conditions used in this study are summarized in **Table 3.2** for polarization curves and in **Table 3.3** for limiting current density measurements.

In order to evaluate materials three cases were considered:

- Dry operating conditions: no or very little water is present in the cell

Table 3.2. Summary of all polarization curve measurement conditions conducted under differential flows of H_2 and air.

Condition [-]	Reference [-]	T_{cell} [° C]	p_{abs} [kPa]	RH [%]
dry 1	4.2[54],4.3[90]	80	170	70
dry 2	4.4	95	300	70
standard	4.2[54]	80	170	100
high pressure/normal	4.2[54],4.4[90]	80	300	100
humid 1	4.2[54],4.3[90]	50	300	120
humid 2	4.4	50	300	100

- Humid operating conditions: water condenses in the cell and significant amounts are present in the GDL and in the flow field channels
- Normal/standard operating conditions: simulating the typical automotive operation of a PEM fuel cell operated either at moderate or elevated pressure.

Major impact factors determining the water balance in the cell are (1) cell temperature, (2) gas pressure, and (3) the relative humidity. As all the measurements in the cell were operated differentially, the conditions at the cell inlet and outlet are considered to be the same (no gradients of pressure, temperature, concentration), which is achieved by high hydrogen and air flow rates of 2000 nccm and 5000 nccm, corresponding to stoichiometries of hydrogen and oxygen of $\geq$ 10 at all times. Note that the stoichiometry defines the ratio of actually consumed reactant over the reactant supplied to the cell. Hence, T_{cell}, p_{abs}, and RH are the only variables except the point of operation in terms of the current density or voltage applied.

According to the equation by Chapman & Enskog (equation 3.2), the binary diffusion coefficient (e.g. of oxygen or water in nitrogen) is inversely proportional to the absolute pressure and proportional to $T^{\frac{3}{2}}$.[122]

$$D_{12} = \frac{1.86 \cdot 10^{-3} \cdot T^{\frac{3}{2}} \cdot \sqrt{1/M_1 + 1/M_2}}{p \cdot \sigma_{12}^2 \cdot \Omega} \tag{3.2}$$

In this equation, D_{12} is the binary diffusion coefficient of species 1 and 2 (in $\text{cm}^2\,\text{s}^{-1}$), T is the absolute temperature (in K), p is the absolute pressure (in atm), M_1 and M_2 are the molar masses of species 1 and 2, σ_{12}^2 is the average collision diameter (in Å),

Table 3.3. Summary of all limiting current density measurement conditions, conducted under differential flows of H_2 and O_2, whereby the O_2 concentration in the cathode feed gas was varied between 0.5% and 28%.

Condition [-]	Reference [-]	T_{cell} [° C]	p_{abs} [kPa]	RH [%]
Compression testing	4.1 [34]	50	200	77
dry 1	4.2 [54],4.3 [90]	80	170	70
dry 2	4.4	95	300	70
standard	4.2 [54]	80	170	100
high pressure/normal	4.2 [54],4.4 [90]	80	300	100
humid 1	4.2 [54],4.3 [90]	50	300	120
humid 2	4.4	50	300	100
transition	4.2 [54],4.3 [90]	50	400	77

and Ω is the collision integral (tabulated e.g., in reference 123).

This means in approximation that with doubling the pressure, the pressure dependent oxygen transport resistance is also doubling, and with increasing temperature, the oxygen transport resistance is decreasing. However, the latter dependency has a low impact, because the of the small considered range of fuel cell operation in absolute temperature between 223 K (50 °C) and 268 K (95 °C). Hence, increasing the pressure (1) leads to an increase of oxygen transport resistance, and (2) facilitates condensation of liquid water as the diffusion coefficient of water in the mixture is also hindered, which leads to a slower removal of water vapor from the electrodes, where it is produced by the ORR. Furthermore, at the same flow rate, an increase in pressure results in a proportional reduction of the volumetric gas flow rate. This means that the water vapor absorption capacity is decreased accordingly, leading to an earlier condensation of liquid water.

Furthermore, the saturation vapor pressure of water (p_s) as a function of temperature has to be considered, which is shown in **Figure 3.2**. The higher the temperature, the higher becomes the water vapor pressure, which describes the maximum capability of the gas phase to absorb water vapor. In case the gas phase is fully saturated, water is condensing. Considering a relative humidity of 70% (= p_{H_2O}/p_s) at 50 ° C, 80 ° C, and 95 ° C, the resulting differences between the water pressure (p_{H_2O}) and the saturation vapor pressure (p_s), are 4 kPa, 14 kPa, and 25 kPa. This means, that

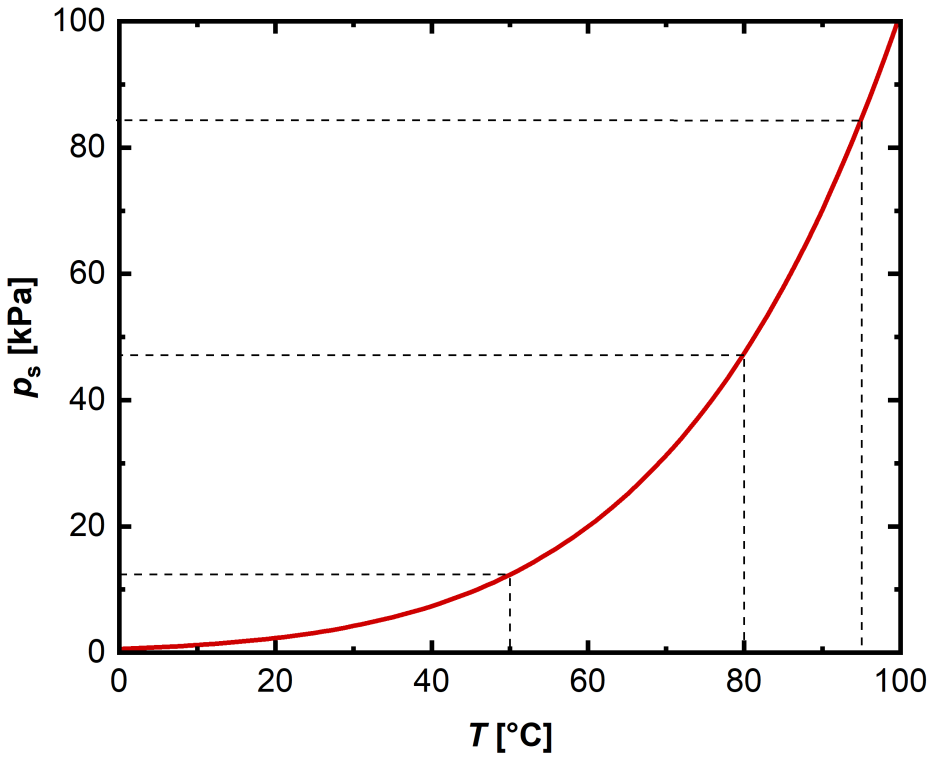

Figure 3.2. Water vapor pressure (p_s) as function of the temperature (T), calculated with the Wagner equation.

at 80 °C the free water capacity is more than 3 times and that at 95 °C more than 6 times higher than that at 50 °C. Hence, the lower the temperature, the earlier (in terms of current density) water condensation will occurr.

The third parameter affecting water condensation is the relative humidity. Of course, the higher the relative humidity, the closer the gas phase is to water saturation, and the earlier condensation occurs. At relative humidities of 100% and higher (meaning liquid water is entering the cell), water condensation within the cell components can occur from the beginning or at very low current densities, and in the GDL/electrodes this can only be prevented by the temperature gradient caused by the reaction heat.

This means that at low temperature, high pressure, and high relative humidity, water tends to condense and that at high temperature, low pressure, and low relative humidity, water transport predominantly occurs in the vapor phase. A normal operating condition was found to be at $T_{\text{cell}} = 80\,^{\circ}\text{C}$, $RH = 100\%$ and $p_{\text{abs}} = 170 - 300\,\text{kPa}$ depending if considering a low or high pressure system. Humid conditions, where the

PEM fuel cell performance is strongly affected by the presence of an excess of liquid water, are considered at $T_{\text{cell}} = 50\,^{\circ}\text{C}$, $RH = 100 - 120\%$, and $p_{\text{abs}} = 300\,\text{kPa}$. Dry operating conditions are considered those where no liquid water is present in the cell and where the performance is most strongly affected by the poor proton conductivity of the ionomer at $T_{\text{cell}} = 80 - 95\,^{\circ}\text{C}$, $RH = 70\%$, and $p_{\text{abs}} = 170 - 300\,\text{kPa}$. The practically relevant ranges for these three types of operating conditions are based on the experimental experience gained while conducting this dissertation research.

3.3.3. Choice of Flow Field

For conducting fuel cell measurements in a differential flow cell, various flow field designs can be found in the literature, e.g., porous metal flow fields,[33] straight channel flow fields,[30,31,83] covered serpentine flow fields with active area cutout,[25,26,32] and serpentine flow fields (only used in our group).[28,34,54,90,124–126] To conduct the measurements for the present thesis, a flow field was developed to fulfill the following properties:

- Low pressure drop (< 10% of abs. pressure at O_2/H_2 stoichiometries >10)
- Measurement of temperature close to the active area
- Able to perform with large amounts of liquid water (oversaturated feed gases)
- Facile assembly and dissassembly of the cell
- Robust design

To fulfill these criteria, the flow field shown in **Figure 3.3a** was constructed and manufactured using graphite (Poco Graphite, Inc.). Drawings of the flow field can be found in appendix A.1. We also compared our experimental data obtained with our flow fields with the findings from Baker, Caulk and co-workers,[25,26,127] who used a different flow field, which is shown in **Figure 3.3b** and with which we also conducted comparative studies. The respective drawings, which have been adapted from reference 25, can be found in appendix A.2. We refer to this flow field as "flow field GM". Both of the flow fields have the same channel/land geometries, with a land width of 0.5 mm, a channel width of 0.5 mm, and a channel depth of 0.8 mm, as given by Baker et al. and as is shown in the sectional view in **Figure 3.4**.[25] By having the same channel geometries, we are able to reproduce the analysis by Baker et al. and by that to examine any possible differences in the data obtained with their versus with

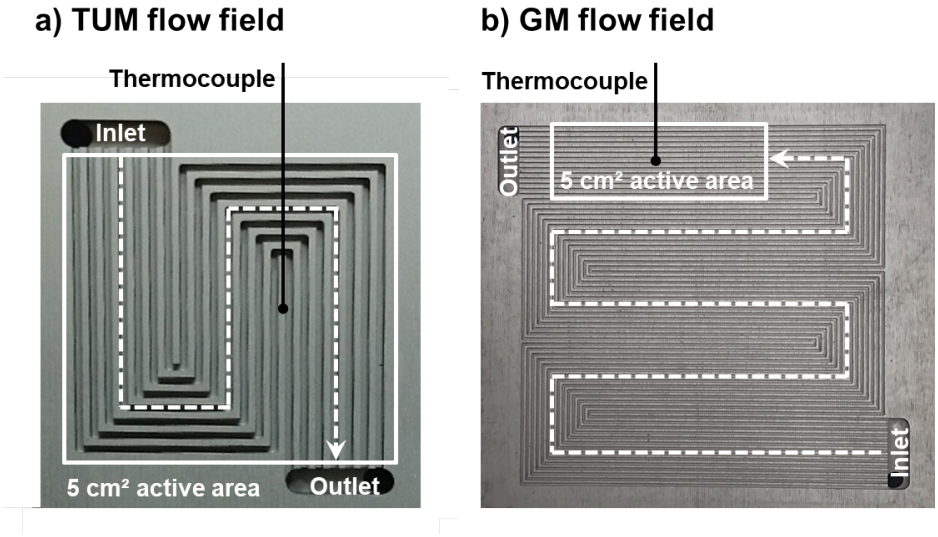

Figure 3.3. Images with details of (a) the TUM flow field and (b) the GM flow field. Detailed drawings can be found in appendix A.1 and A.2

our flow fields.

To compare the two flow fields, we conducted an analysis analogously to Baker et al.[25] We performed our measurements at $T_{\text{cell}} = 80\,^{\circ}\text{C}$, $RH = 70\%$ and pressures of $p_{\text{abs}} = 200/300/400\,\text{kPa}$. The GDLs were compressed to ~20% of their initial thickness. Please note that for the Baker flow field, the pressure drop over the inactive area before entering the cell cannot be neglected. Hence, the pressure is outlet controlled and the inlet RH is controlled online to result in the targeted outlet RH in the active area.

By plotting the limiting current density against the dry oxygen content of the cathode feed gas, based on equation 2.19, the total oxygen transport resistance can be derived from the slope of the linear curve.

$$i_{\text{lim}} = \frac{4\text{F}}{R_{\text{T,O}_2}} \cdot \frac{p_{\text{abs}} - p_{\text{H}_2\text{O}}}{\text{R} \cdot T} \cdot x_{\text{O}_2}^{\text{dry}} \tag{3.3}$$

This relationship is illustrated in **Figure 3.5** for the TUM and for the GM flow field with a Toray 060T GDL-substrate without MPL (see also figure 12 in reference 25). When we compare both flow fields, we can observe linear relationships between i_{lim} and $x_{\text{O}_2}^{\text{dry}}$, with the expected extrapolated intercept in the origin. However, for the TUM flow field the slopes at the respective pressures are higher than for the GM flow fields, indicating a lower oxygen transport resistance. To determine the pressure dependent

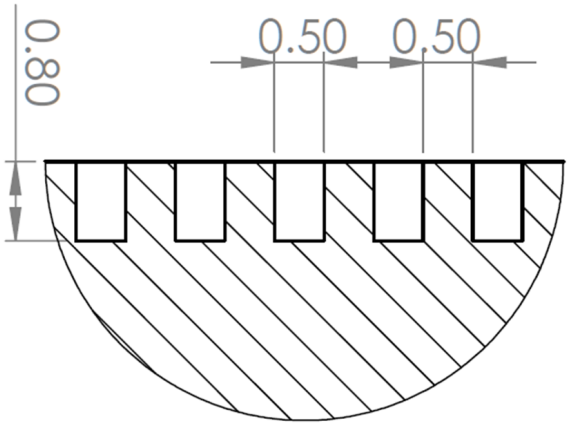

Figure 3.4. Sectional view of the channels of both the TUM and the GM flow field. Details can be found in appendix A.1 and A.2

fraction of the total transport resistance, $R_{\mathrm{T,O_2}}$ is plotted against the absolute pressure in **Figure 3.6**. The intercept is related to the pressure independent fraction ($R_{\mathrm{PI,O_2}}$), while the slope represents the pressure dependent fraction ($R_{\mathrm{PD,O_2}}$) (see equation 40 and figure 13 in reference 25). We can see that the absolute level of $R_{\mathrm{T,O_2}}$ is higher for the GM flow field, resulting in different fitting curves and that the slope of the fitting curve (i.e., $R_{\mathrm{PD,O_2}}$) is ~25% higher than for the TUM flow field (0.0047 $\mathrm{s\,cm^{-1}\,kPa^{-1}}$ vs. 0.0036 $\mathrm{s\,cm^{-1}\,kPa^{-1}}$).

Based on the operational and geometrical parameters, the parameters $R_{\mathrm{FF,O_2}}$, $R_{\mathrm{GDL\text{–}S,O_2}}$, and $R_{\mathrm{cathode,O_2}}$ can be calculated ($R_{\mathrm{MPL,O_2}} = 0$ as only a GDL-substrate without MPL is used, and $R_{\mathrm{other,O_2}}$ is neglected). For the determination of $R_{\mathrm{FF,O_2}}$, the channel model in Baker et al. was used (see equation 22 in reference 25), $R_{\mathrm{GDL\text{–}S,O_2}}$ was calculated from the pressure-dependent fraction of the transport resistance (see equations 22 and 29 in reference 25), and $R_{\mathrm{cathode,O_2}}$ from the pressure-independent fraction of the transport resistance (see equation 40 in reference 25, assuming $R_{\mathrm{PI,O_2}} = R_{\mathrm{cathode,O_2}}$). The results are reported in **Table 3.4**. While $R_{\mathrm{cathode,O_2}}$ for the GM flow field of 0.14 $\mathrm{s\,cm^{-2}}$ is very close to the average value of 0.128 $\mathrm{s\,cm^{-2}}$ determined by Baker et al. who also used an MEA by Gore with a cathode Pt loading of 0.4 $\mathrm{mg_{Pt}\,cm^{-2}}$ similar to our MEA (also from Gore with cathode platinum loading of 0.4 $\mathrm{mg_{Pt}\,cm^{-2}}$), $R_{\mathrm{cathode,O_2}}$ for the TUM flow field is slightly higher with 0.19 $\mathrm{s\,cm^{-2}}$. However, also the extensive study by Baker et al. showed a wide range of these values from $\sim$ 0.07 $\mathrm{s\,cm^{-2}}$ to $\sim$ 0.19 $\mathrm{s\,cm^{-2}}$, so that the $R_{\mathrm{cathode,O_2}}$ values obtained for both flow fields are actually within the expected range. The value $R_{\mathrm{FF,O_2}}$ for the flow field is based on a

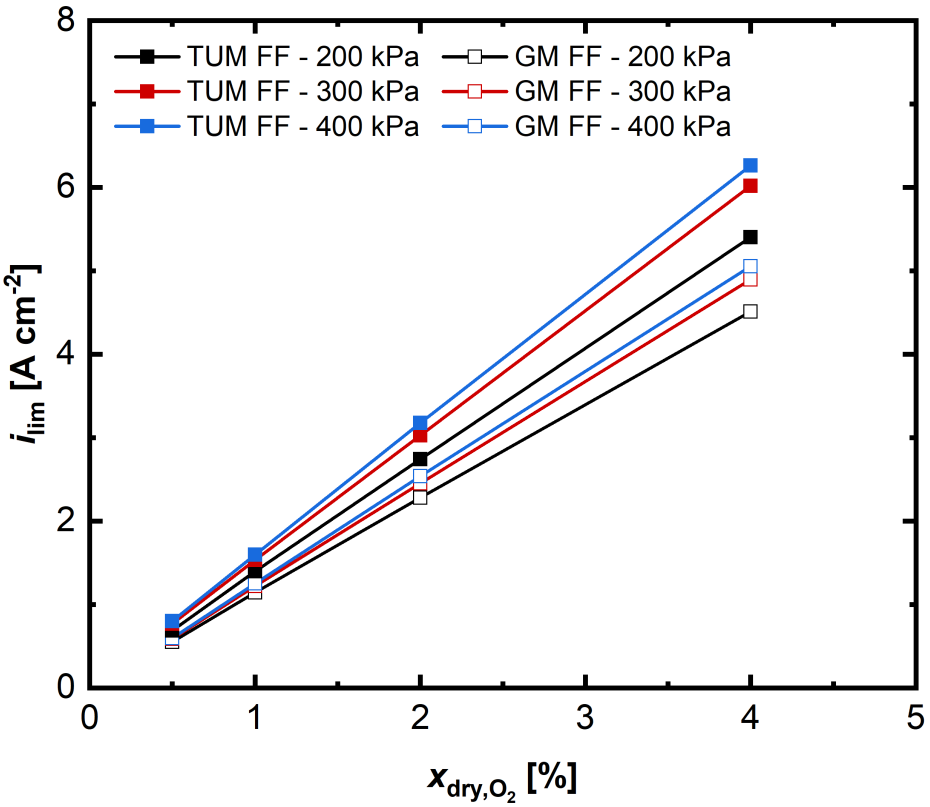

Figure 3.5. i_{lim} plotted against $x_{\mathrm{dry,O_2}}$ for the TUM flow field (full symbols) and the GM flow field (open symbols) at $T_{\mathrm{cell}} = 80\,^{\circ}\mathrm{C}$, $RH = 70\%$ and at three different pressures ($p_{\mathrm{abs}} = 200\,\mathrm{kPa}/300\,\mathrm{kPa}/400\,\mathrm{kPa}$). As GDL, Toray060T without MPL was used on anode and cathode.

channel model calculation considering the concentration gradient along the channel and the continuous depletion of oxygen at the channel/GDL interface (see equation 22 in reference 25). The calculation for the GM flow field and for the TUM flow field lead to the same result of $0.29\,\mathrm{s\,cm^{-1}}$. Finally, $R_{\mathrm{GDL–S,O_2}}$ is calculated from the pressure-dependent fraction of the oxygen transport resistance ($R_{\mathrm{PD,O_2}}$) minus the channel resistance ($R_{\mathrm{FF,O_2}}$) (see equations 22 and 29 in reference 25). The resulting values are $0.68\,\mathrm{s\,cm^{-1}}$ for the TUM flow field and $1.00\,\mathrm{s\,cm^{-1}}$ for the GM flow field. Based on these values, the ratio of binary diffusion coefficient in the humidified air gas mix ($D_{\mathrm{O_2,mix}}$) and the effective through-plane (i.e., in y-direction) diffusion coefficient in the porous GDL-substrate ($D^{\mathrm{y}}_{\mathrm{O_2,GDL–S}}$) can be determined (see equations 23 and 30 in reference 25 with binary diffusion coefficients calculated by equation 17.2-1 in reference 128). Here, a significantly lower value of 2.89 was calculated for the TUM flow field compared to our measurements with the GM flow field with values of 4.22,

Table 3.4. Analysis of the oxygen transport resistance based on the approach by Baker et al.[25] The results values of the transport resistances are calculated at $T_{\text{cell}} = 80\,°\text{C}$, $p_{\text{abs}} = 300\,\text{kPa}$, and $RH = 70\%$.

Flow field [-]	$R_{\text{cathode,O}_2}$[1] [s cm^{-1}]	$R_{\text{FF,O}_2}$[2] [s cm^{-1}]	$R_{\text{GDL–S,O}_2}$[3] [s cm^{-1}]	$\frac{D_{\text{O}_2,\text{mix}}}{D^{\text{y}}_{\text{O}_2,\text{GDL–S}}}$[4] [-]
TUM	0.19	0.29	0.68	2.89
GM	0.14	0.29	1.00	4.22

[1] Equation 40 in reference 25 assuming only $R_{\text{cathode,O}_2} = R_{\text{PI,O}_2}$
[2] Equation 22 in reference 25 based on simulation.
[3] Equation 22 and 29 in reference 25.
[4] Calculation by equation 23 and equation 30 in reference 25 with binary diffusion coefficients calculated by equation 17.2-1 in reference 128.

which in turn is in reasonably good agreement with the value of 3.85 ± 0.28 reported by Baker et al.[25] for their measurements with the GM flow field. In general, $D^{\text{y}}_{\text{O}_2,\text{GDL–S}}$ corresponds to the product of $D_{\text{O}_2,\text{mix}}$ with the ratio of porosity (ε) and tortuosity (τ) defining the effective diffusion coefficient.[129]

$$D^{\text{y}}_{\text{O}_2,\text{GDL–S}} = D_{\text{O}_2,\text{mix}} \cdot \frac{\varepsilon}{\tau} \tag{3.4}$$

Hence, considering the uncertainties in measurement setup, test execution, and material differences, our measured results with the GM flow field align well with the literature, which is expected as the same flow field was used.[25] On the other hand, the TUM flow field differs in both the pressure independent as well as the pressure dependent fraction of the oxygen transport resistance, suggesting that the method from Baker et al. is not applicable completely for this type of flow field. Possible reasons for the deviations are discussed in a later paragraph of this section.

To further analyze these differences, one can examine the derivative of the total oxygen transport resistance with respect to the absolute pressure ($\text{d}R_{\text{T,O}_2}/\text{d}p_{\text{abs}}$) vs. the gas diffusion layer thickness ($d_{\text{GDL–S}}$) times a dimensionless shape factor *f*. The dimensionless shape factor f is dependent on the anisotropy of the GDL-substrate's effective diffusion coefficient in-plane (x-direction) vs. through-plane (y-direction) (for Toray paper, a value of $D^{\text{x}}_{\text{GDL–S}}/D^{\text{y}}_{\text{GDL–S}} = 1.8$ was determined by impedance spectroscopy[130]) and the ratio of channel width (b_{channel}) and GDL thickness $d_{\text{GDL–S}}$.

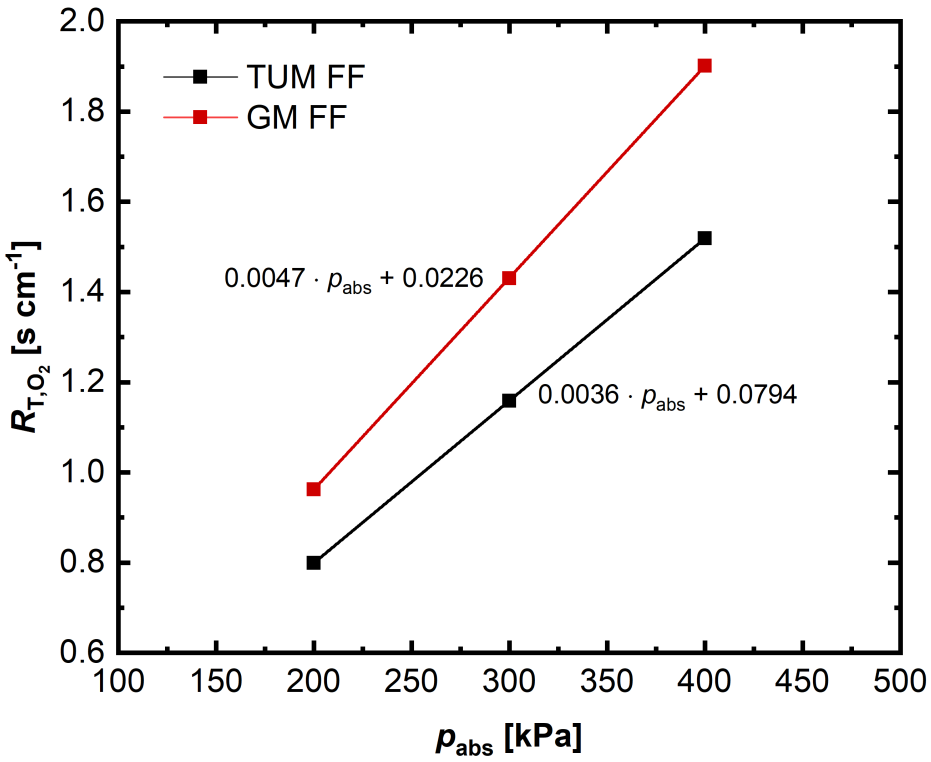

Figure 3.6. R_{T,O_2} plotted against p_{abs} for the TUM flow field (black) and the GM flow field (red) at $T_{cell} = 80\,°C$, $RH = 70\%$. As GDL, Toray060T without MPL was used on anode and cathode.The equations for both data fits are given in the graph.

$$\lambda = \sqrt{\frac{D^{x}_{GDL-S}}{D^{y}_{GDL-S}}} \cdot \frac{d_{GDL-S}}{b_{channel}} \tag{3.5}$$

For $b_{channel} = b_{land}$, as is the case for both of the considered flow fields, the following numerical correlation can be derived.[25]

$$f(\lambda) = 1 + 0.803 \cdot \exp(-1.17\lambda) + 0.197 \cdot \exp(-0.164\lambda) \tag{3.6}$$

Thus, we conducted limiting current measurements with nominally identical GDL-substrates which only differ in thickness. For this, we used hydrophobized Toray GDL-substrates (Toray030T, 060T, 120T), correlating the pressure-dependent transport resistance with the GDL-substrate thickness. The plot of $dR_{T,O_2}/dp_{abs}$ vs. the gas diffusion layer thickness d_{GDL-S} is shown in **Figure 3.7** with the blue line illustrating the data fit by Baker et al.[25] While the data for the GM flow field (black dots in **Figure 3.7**) is very close to the data from the literature (blue line), which

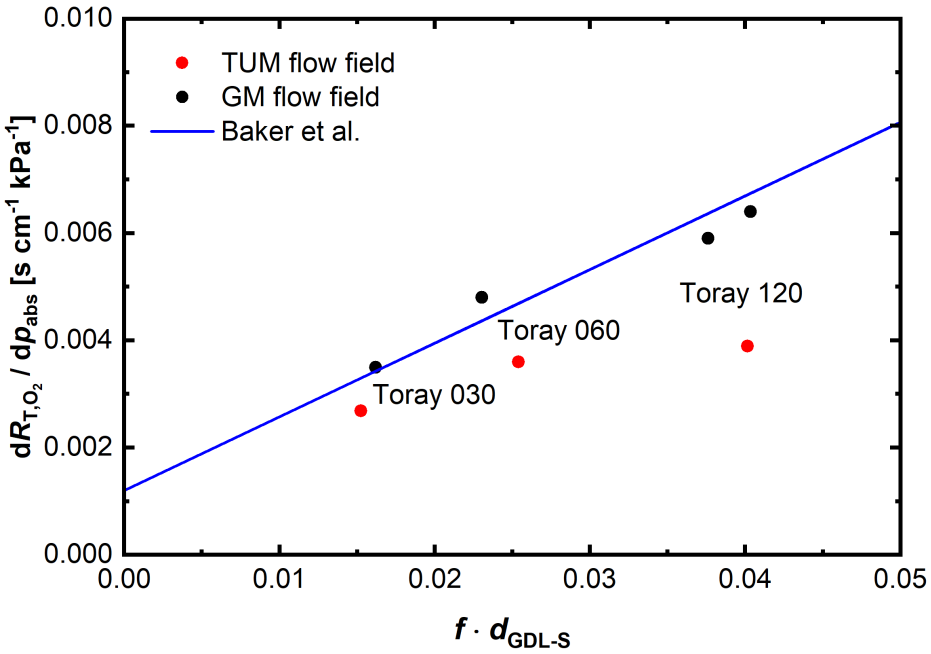

Figure 3.7. Derivative of the total oxygen transport resistance with respect to the absolute pressure ($\mathrm{d}R_{\mathrm{T,O_2}}/\mathrm{d}p_{\mathrm{abs}}$) vs. the gas diffusion layer thickness ($d_{\mathrm{GDL-S}}$) times the dimensionless shape factor f for hydrophobized Toray diffusion layers (Toray 030T, 060T, 120T) measured in the GM flow field (black circles, see appendix A.2) and in the TUM flow field (red circles, see appendix A.1). For benchmarking, the results from Baker et al.[25] are shown as data fit (blue line).

confirms the method of measurement and the data treatment, the values for Toray 030T and 060T in the TUM flow field (red dots) are slightly below the expected curve. However, in case of the thick (320 µm) Toray 120T, the value is significantly below its expected value and is in a similar range as the significantly thinner Toray 060T (160 µm) measured in the same TUM flow field; it is also unexpected that the TUM flow field does not show a linear trend with $f \cdot d_{\mathrm{GDL}}$. In summary, as the absolute values of $R_{\mathrm{T,O_2}}$ with the TUM flow field are lower than with the GM flow field and as the TUM flow field exhibits a lower dependency on pressure, the overall measured transport resistances with the TUM flow field are always smaller than with the GM flow field. Hence, the TUM flow field apparantly and surprisingly has better transport properties.

As the channel and land geometries are identical, the effective transport by diffusion in the GDL must be identical for the two flow fields. Differences in $D_{\mathrm{O_2,mix}}/D^{\mathrm{y}}_{\mathrm{O_2,GDL-S}}$ as shown in **Table 3.4** clearly must be an artifact. Reasons could be that (1) the channel resistance is lower than in the GM flow field, as the channel resistance is

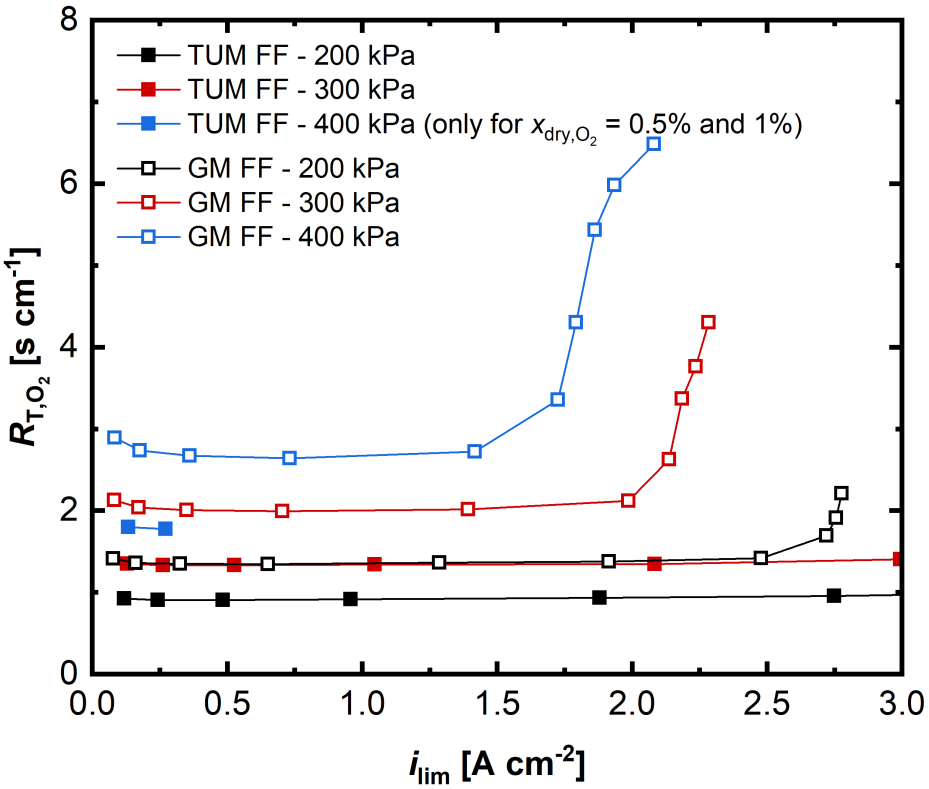

Figure 3.8. R_{T,O_2} plotted against i_{lim} for the TUM flow field (black) and the GM flow field (red) at $T_{cell} = 80\,°C$, $RH = 70\%$, and at three different pressures ($p_{abs} = 200\,kPa/300\,kPa/400\,kPa$). As GDL, Toray 120T with a 30 µm thick Li400 MPL (see reference 54) was used on anode and cathode. The MEA was a 18 µm membrane with anode/cathode loadings of $0.1/0.4\,mg_{Pt}\,cm^{-2}$ from Gore.

based on a laminar flow profile, which could be disturbed by turbulences due to the bends of the serpentine geometry of the TUM flow field and/or (2) that convective flow crossing from neighboring channels via the porous GDL-substrate could reduce the transport resistance. Such flow through porous media can be described by the Darcy equation and depending on the coefficient of permeability, small pressure gradients of a few kPa could result in significant flow rates. This could explain, why the pressure dependency is comparably low for thick Toray 120T (see **Figure 3.7**) as the available cross-sectional area for the Darcy flow is increased. On the other hand this would involve also a non-linearity of R_{T,O_2} vs. p_{abs} in **Figure 3.6** because the pressure drop and hence, the pressure difference between neighboring channels (i.e., the driving force for the Darcy flow) would be reduced by the increasing pressure. Summarized, the transport processes in the TUM flow field seem difficult to be described by simple methods and would require continuative investigations. Nevertheless, we decided to

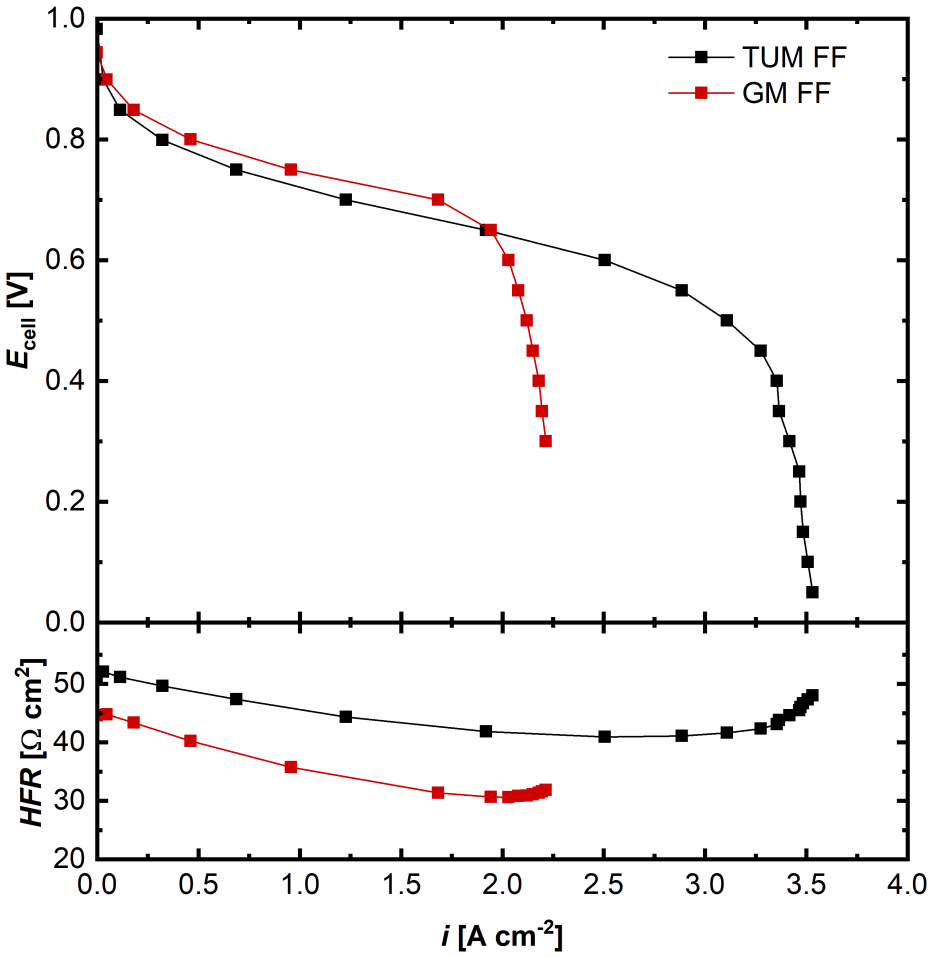

Figure 3.9. E_{cell} (top graph) and *HFR* (bottom graph) plotted against i for the TUM flow field (black) and the GM flow field (red) at $T_{cell} = 80\,°C$, $p_{abs} = 300\,kPa$, and $RH = 70\%$ under differential H_2/air flow conditions. As GDL, Toray 120T with a 30 µm thick Li400 MPL (see reference 54) was used on anode and cathode.

use the TUM flow field for the quantification of our experiments, because of the robust design (able to handle liquid water, simple assembly and disassembly of the cell) and the observation that the transport resistances are in a similar range as in the literature for thinner diffusion media (as shown for Toray 030T and Toray 060T in **Figure 3.7** and for SGL GDL25BC in reference 34). Furthermore, current flow field designs are based on a mesh structure, which actively forces convection in the GDL to enhance oxygen transport and to remove liquid water.[10,131] Hence both, diffusive and convective effects should be considered in GDL development, which seems to be possible in the TUM flow field. This is an indication underlining our previous hypothesis that convective flow could remove water vapor from the GDL-substrate

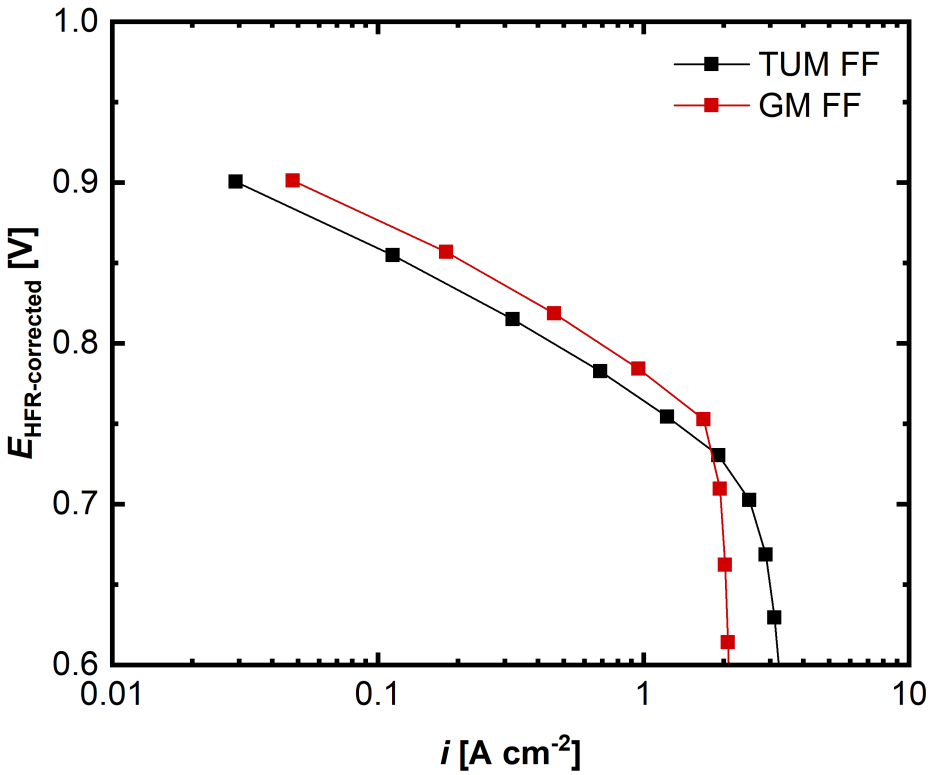

Figure 3.10. Cell voltage corrected for the high-frequency resistance ($E_{\mathrm{HFR-corrected}}$) plotted against i (logarithmic scale) for the TUM flow field (black) and the GM flow field (red) at $T_{\mathrm{cell}} = 80\,^{\circ}\mathrm{C}$, $p_{\mathrm{abs}} = 300\,\mathrm{kPa}$ and $RH = 70\%$ (same data as in **Figure 3.9**). As GDL, Toray120T with a 30 µm thick Li400 MPL (see reference 54) was used on anode and cathode.

and thus prevent condensation.

This enhanced transport behavior of the TUM flow field is also revealed when plotting $R_{\mathrm{T,O_2}}$ as function of i_{lim} with the TUM and the GM flow field for various pressures using a Toray 120T substrate with a 30 µm thick MPL at $T_{\mathrm{cell}} = 80\,^{\circ}\mathrm{C}$, $RH = 70\%$, and three different pressures ($p_{\mathrm{abs}} = 200\,\mathrm{kPa}/300\,\mathrm{kPa}/400\,\mathrm{kPa}$) (see **Figure 3.8**). At dry conditions (i.e., $i_{\mathrm{lim}} < 1.5\,\mathrm{A\,cm^{-2}}$), lower $R_{\mathrm{T,O_2}}$ are observed for the TUM flow field compared to the GM flow field at all pressure levels. Furthermore, while in the GM flow field an increase of $R_{\mathrm{T,O_2}}$ is observed at higher current densities (for $p_{\mathrm{abs}} = 200\,\mathrm{kPa}$ at $i_{\mathrm{lim}} > 2.5\,\mathrm{A\,cm^{-2}}$, for $p_{\mathrm{abs}} = 300\,\mathrm{kPa}$ at $i_{\mathrm{lim}} > 2.0\,\mathrm{A\,cm^{-2}}$, and for $p_{\mathrm{abs}} = 400\,\mathrm{kPa}$ at $i_{\mathrm{lim}} > 1.5\,\mathrm{A\,cm^{-2}}$, i.e., depending on the water uptake capacity of the gas phase at as the respective pressure), for the TUM flow field at neither pressure an increase of $R_{\mathrm{T,O_2}}$ due to liquid water was observed (unfortunately, no complete data set is available at 400 kPa). This indicates that water is significantly more efficiently removed from the MEA and the GDL in case of the TUM flow field.

The smaller transport resistance of the TUM flow field is also reflected in the polarization curves recorded at $T_{\text{cell}} = 80\,^{\circ}\text{C}$, $p_{\text{abs}} = 300\,\text{kPa}$, and $RH = 70\%$ (see **Figure 3.9**). At 0.6 V, the current density of the TUM flow field is 25% higher ($2.5\,\text{A}\,\text{cm}^{-2}$) than that of the GM flow field ($2.0\,\text{A}\,\text{cm}^{-2}$). This is caused by an early mass transport limitation of the GM flow field at ~$2.2\,\text{A}\,\text{cm}^{-2}$ compared to the TUM flow field at ~$3.5\,\text{A}\,\text{cm}^{-2}$. The improved oxygen transport resistance, however, counteracts the high frequency resistance, which is approximately 15% higher for the TUM flow field, probably due to a more efficient water removal and thus a lower membrane *RH*.

Another interesting observation is the higher voltage in the kinetic region at low current densities, which is better illustrated in the Tafel representation in **Figure 3.10**. While both plots reveal a similar Tafel slope of $77\,\text{mV}\,\text{dec}^{-1}$ (consistent with theoretical Tafel slope of $70\,\text{mV}\,\text{dec}^{-1}$ at 80 °C, considering non-ideal experimental conditions (air instead of O_2, 70% *RH* instead of 100% *RH*, no H_2 cross-over correction)), the voltage of the GM flow field is higher up to current densities of $1.6\,\text{A}\,\text{cm}^{-2}$, indicating better kinetics in the GM flow field. As both experiments, however, use the same MEA with the same Pt catalyst based electrodes, a difference in kinetics cannot be possible. One explanation could be edge effects in case of the GM flow field, as the inactive area of the CCM is covered with a gasket, so that due to the porosity of the electrodes or insufficient compression, a small area around the CCM could still contribute to the reaction. However, the intrinsic reason for the difference in kinetics could not be resolved so far.

4. Results

This chapter contains the results of the thesis, which are clustered into three peer-reviewed journal article (sections 4.1, 4.2, and 4.3) and one section with results, which are not contained in a journal publication (section 4.4). The first article in section 4.1 is an investigation of the water and oxygen transport in a fuel cell with a commercial diffusion medium under various compression levels. While in previous works, oxygen transport limitations have only been observed qualitatively at high compressions, the limiting current density method enables for the first time the separation of the oxygen transport resistances from other effects at various GDL compression levels.

Sections 4.2 and 4.3 are consecutive studies of MPL modifications, which could reduce the oxygen transport resistance and increase the fuel cell performance significantly. In section 4.2, two carbon blacks were investigated as materials for the microporous layer, exhibiting different pore size distributions and porosities. By perforating the MPL by applying a pore former polymer, the oxygen transport at humid conditions could be enhanced significantly, and the transport mechanism could be revealed. Section 4.3 modifies one of the previous carbon black based MPLs by replacing the carbon black material with carbon fibers, which could enhance the performance of a fuel cell by 49% compared to a commercial reference MPL. Furthermore, we replaced the hydrophobic polytetrafluoroethylene binder with hydrophilic perfluorosulfonic acid, and by that could illuminate the impact of all-hydrophilic MPLs.

In the fourth part of the results section (section 4.4), we coated two of our microporous layers on two different substrate materials with different properties, and we could reveal the effect of the substrate thermal conductivity. We found that the effect of the microporous layers is different for the two substrates, leading to the conclusion that substrate effects could superimpose onto the transport properties of the microporous layer.

4.1. Influence of the Gas Diffusion Layer Compression on the Oxygen Transport Resistance at High Water Saturation Levels

The article entitled "Influence of the Gas Diffusion Layer Compression on the Oxygen Transport Resistance at High Water Saturation Levels" was submitted in January 2017 and accepted for publication in the peer-reviewed Journal of the Electrochemical Society in March 2017 as an open access article, distributed under the terms of the Creative Commons Attribution 4.0 License (CC BY). The paper was presented by Christoph Simon at the 228th Meeting of The Electrochemical Society (October 2015) in Phoenix, AZ, USA (abstract number: I05-1549). The permanent web link to the article is http://dx.doi.org/10.1149/2.0691706jes.

In this paper, the effect of the compressive strain of the gas diffusion layer on the oxygen transport resistance is analyzed with a focus on the impact of liquid water. In the fuel cell literature, the effect of GDL compression has been studied extensively. It is widely known that there exists a trade-off between reduced electrical and thermal bulk and contact resistances at high compression (i.e. high compaction pressure) and reduced diffusion resistance due to a higher porosity at low compressions. However, the diffusion resistance of oxygen has never before been measured and quantified as a function of compression force and water saturation level.

To investigate the oxygen transport resistance, we use a cell, which we specifically developed for differential flow measurements, characterized by a reduced pressure drop at high flow rates and by a robust design against liquid water formation in the flow field channels. Our analysis is based on the work by Baker and co-workers, who investigated the transport resistance of GDLs for the first time.

We prepared various cells with GDL compressive strains between 8% and 53%, using a commercial GDL-substrate with MPL. For our fuel cell measurements we applied differential flow conditions (stoichiometries on anode and cathode > 7), a cell temperature of 50 °C, and gas pressures of 200 kPa. By varying the oxygen concentration (between 0.5% and 24%) and measuring the current density at cell voltages between 0.05 and 0.3 V (diffusion-limited region), we could calculate the total oxygen transport resistance for various current densities by Fick's law combined with Faraday's law and the ideal gas law.

We found that at low currents (i.e., at low water saturation level) the oxygen transport resistance is increasing with increasing compression due to a reduction in porosity, which is expected. However, at high current densities (i.e., at high water saturation level) we observed an increase of the oxygen transport resistance. By comparison to the behavior of the same GDL-substrate without MPL and by measurements of the compression pressure, we developed the hypothesis that a liquid water film might be formed between MPL and cathode electrode layer that is acting as a diffusion barrier.

In conclusion, we found that the GDL has an optimum compression (i.e., minimum in oxygen transport resistance), at which the MPL has a good contact to the electrode layers and at the same time sufficient porosity for gas diffusion.

Author contributions

C.S. and H.G. developed the flow fields used for the differential flow measurements and the test plan. C.S. conducted the experimental work and analyzed the data (fuel cell measurements, pressure distribution measurements, SEM analysis) and drafted the manuscript. All authors discussed the data, commented on the results, and reviewed the manuscript.

Influence of the Gas Diffusion Layer Compression on the Oxygen Transport in PEM Fuel Cells at High Water Saturation Levels

Christoph Simon,*,z Frédéric Hasché,* and Hubert A. Gasteiger**

Chair of Technical Electrochemistry, Department of Chemistry and Catalysis Research Center, Technical University of Munich, D-85748 Garching, Germany

The impact of the gas diffusion layer (GDL) compression on the oxygen transport is investigated in single cell assemblies at 50°C, $RH = 77\%$, 200 kPa_{abs} and under differential flow conditions. For this, the oxygen transport resistance at low and high current densities is determined by limiting current density measurements at various oxygen concentrations for GDLs with and without microporous layer (MPL). At small current densities ($\leq$0.4 A cm^{-2}), where no liquid water in the GDL/MPL is present, a linear increase of oxygen transport resistance with GDL compression is observed, with the GDL without MPL exhibiting a significantly lower transport resistance. For low compressions of ≈8%, we find that the oxygen transport resistance for the GDL with MPL is increasing disproportionately high in the high current density region (>1.5 A cm^{-2}), where water condensation in the porous media takes place. A similar trend is observed for a GDL without MPL at a typical compression of 22%. Based on these results, we hypothesize that a developing liquid water film is hindering the oxygen diffusion at the interface between MPL and cathode, analogous to what is known to be formed on the cathode surface for GDLs without MPL.

Manuscript submitted January 19, 2017; revised manuscript received March 14, 2017. Published March 28, 2017. This was Paper 1549 presented at the Phoenix, Arizona, Meeting of the Society, October 11–15, 2015.

The gas diffusion layer (GDL) is a key component of polymer electrolyte membrane fuel cells (PEMFCs). It is sandwiched between flow field and electrode and its function is to supply reactant gases to the electrodes, to remove product water as well as to provide good electrical and thermal contact.[1,2] Typically, the GDL consists of a hydrophobically treated carbon fiber paper including a microporous layer (MPL) facing the electrodes. At high current densities, the formation of liquid water inside the GDL can substantially reduce oxygen transport to the cathode and cause a significant voltage drop due to mass transport limitations.[3–5] Thus, the overall fuel cell performance decreases significantly.[5,6] To mitigate this behavior and to allow an operation at high current densities, a microporous layer coated on the GDL and facing the electrode surface is commonly used. The MPL substantially reduces the impact of water condensation by providing a uniform contact between the layers (GDL/MPL/electrode). Hence, liquid water accumulation does not occur in the vicinity of the electrode surface but rather inside the carbon fibers after passing the MPL.[5,7,8] Several high-resolution X-ray tomography studies have shown that liquid water transport through the MPL occurs preferably via open pathways provided by cracks in the MPL.[9–11] This mechanism enables the parallel transport of liquid water and oxygen, thereby minimizing the voltage drop caused by mass transport resistances. The areal crack density of a commercially available SGL MPL was found to vary between 3% and 9%,[12] but is very much dependent on the specific MPL properties. Furthermore, the interfacial region between MPL and catalyst layer can have a significant impact on the transport properties. X-ray imaging shows the presence of gaps between the two layers depending on the surface roughness of MPL and catalyst layer and the compression force applied.[13] Modeling studies demonstrate that a poor contact due to interfacial gaps can cause an increased ohmic contact resistances,[14–16] but the gaps can also serve as liquid water reservoir hindering the transport of oxygen.[14,17]

Typically, diffusion media are compressed between the flow field land areas by ≈20% to 25% based on their initial thickness, which corresponds to a contact pressure in the region of 1 to 2 MPa, depending on the individual mechanical properties of the GDL. On the one hand, high contact pressure reduces the electrical and thermal bulk as well as contact resistances between flow field land, GDL, and electrode interfaces.[1,18–21] On the other hand the resulting high compression reduces the GDL and MPL porosity. This in turn results in a lower effective diffusivity and a higher oxygen transport resistance at dry conditions.[22–26] Thus, there exists an optimum compression, taking into account the electrical and mass transport losses.[27,28] Additionally, in a fuel cell assembly the influence of the land and channel geometry has to be taken into account, which creates a heterogeneity of material properties. The GDL compression and contact pressure in the area of the channels were shown to be significantly lower compared to the land region, which causes a higher contact resistance between MPL and electrode as well as a higher porosity in the vicinity of the channels.[29–31]

An experimental method to quantify the mass transport resistance of oxygen is the measurement of limiting current densities for various oxygen concentrations. Based on these measurements, Baker et al. developed a technique to separate the impact of flow field channels, GDL, MPL as well as other sources and presented a model to extract effective diffusion coefficients at the so-called dry conditions at low current densities.[23] There exist several studies that utilized this approach to quantify the influence of different GDL materials, MPLs, catalyst loadings, and operating conditions on the oxygen transport resistance on the cathode side.[3,4,32–37] It was shown that material properties like substrate type (paper, non-woven, etc.) and particularly thermal conductivity of the GDL have a significant influence on the effective diffusion and the formation of liquid water, which appears as an increase in oxygen transport resistance from a low plateau at dry conditions (i.e., absence of liquid water in GDL/MPL) to a higher plateau at wet conditions (i.e., at high water saturation levels in GDL/MPL).[3] This view of a transition from absence of water to high water saturation in the GDL/MPL with increasing current density was proven by Owejan et al. by comparing the local water saturation in the GDL extracted from neutron imaging in an operating fuel cell with limiting current density measurements. For this they determined the exponent of a modified Bruggeman equation for two different GDL materials.[33] In addition, it was shown that the flow field land-to-channel ratio has a significant impact on the diffusion limitation of a fuel cell. Shorter diffusion pathways and a more homogeneous current density distribution seem to enhance the oxygen transport for smaller lands.[34] Furthermore, the transport resistance in the electrode with various platinum loadings was investigated.[32,34,36,37]

In this paper we will use the differential cell approach to analyze the influence of the gas diffusion layer compression on the oxygen transport. Single cells with different applied GDL compressions ranging

*Electrochemical Society Student Member.
**Electrochemical Society Fellow.
zE-mail: christoph.simon@tum.de

from 8% to 53% based on their initial thickness, using a commercial GDL with MPL (SGL Sigracet GDL 25BC) are evaluated by limiting current measurements. Transport resistances are extracted for low current densities, i.e., in the dry region in the absence of water in the GDL/MPL as well as under the influence of high water saturation levels at elevated current densities. To explain the behavior at small compressions, the results are compared to measurements with a GDL without MPL (SGL Sigracet GDL 25BA). To underline our findings, we will furthermore present scanning electron microscope cross-sections of the two GDLs and pressure distribution measurements in the single cell at different compressions. For the first time, mass transport resistances as function of the GDL compression at conditions of high liquid water saturation are reported and discussed.

Experimental

Materials.—In this study, a commercial GDL with MPL (SGL Sigracet GDL 25BC, ≈235 ±20 μm thick, hydrophobically treated) and without MPL (SGL Sigracet GDL 25BA, ≈190 μm thick, hydrophobically treated) is used for the cathode side, while for all tests a GDL with MPL (GDL 25BC) is used on the anode. It is important to note that GDL 25BC is based on the GDL 25BA substrate, which is additionally coated with an MPL. Fuel cell tests are performed by using a Primea Mesga catalyst coated membrane (CCM, W. L. Gore & Associates A510.1/M715.18/C580.4 equipped with a gasket) with electrode loadings of 0.4 mg_{Pt} cm^{-2} on the cathode and 0.1 mg_{Pt} cm^{-2} on the anode. The cell is sealed by PTFE coated glass fabrics (FIBERFLON GmbH & Co. KG) with various thicknesses. The active electrode area is 5.0 cm^2, while the GDL area is 5.8 cm^2 in order to prevent misalignment of GDL and CCM during cell assembly.

Scanning electron microscopy.—Cross-sectional images of both GDLs with and without MPL were recorded in a scanning electron microscope (SEM) model JCM-6000 (Jeol). Samples are prepared by cutting the materials with a razor blade in order to create a clean cutting edge; subsequently the materials are fixed in a cross-section sample holder. Images were taken at 5 kV acceleration voltage at 300x magnification by a secondary electron detector. In order to determine the sample thickness, material diameters for 3 representative images at 10 positions each are measured and averaged.

Fuel cell measurement setup.—Fuel cell polarization curves are measured in a 5 cm^2 single cell setup (Fuel Cell Technologies, Inc.) with individually designed graphite flow fields (Poco Graphite, Inc.), which comprise mirror-symmetrical flow patterns for the anode and the cathode. The flow field consists of 7 parallel channels with a channel and land width of 0.5 mm and a channel depth of 0.8 mm, which are arranged in one serpentine. More details are shown in Reference 38. The cell temperature is measured by a thermocouple directly at the center of the cathode flow field block. This corresponds to a distance of 6 mm from the flow field/GDL interface, which minimizes temperature gradients between GDL and temperature measurement location.

Different values for the GDL compression are obtained by variation of the thicknesses of the gaskets on anode and cathode side, which sandwich the gasket attached to the CCM around the active area. The compression of the GDL (C_{GDL}) is defined as the following:

$$C_{GDL} = \left(1 - \frac{d_{GDL,\,A} + d_{GDL,C}}{d_{0,GDL,\,A} + d_{0,GDL,C}}\right) \quad [1]$$

with $d_{0,GDL,A}$ and $d_{0,GDL,C}$ being the initial thicknesses and $d_{GDL,A}$ and $d_{GDL,C}$ the compressed thicknesses of the respective anode and cathode GDLs. The compression is calculated by

$$C_{GDL} = 1 - \frac{(d_{gasket,A} + d_{gasket,C} + d_{gasket,\,CCM}) \cdot (1 - C_{gaskets}) - d_{CCM}}{d_{0,GDL,\,A} + d_{0,GDL,C}} \quad [2]$$

taking into account the sum of anode and cathode gaskets $d_{gaskets,A}$ and $d_{gaskets,C}$, the gasket attached to the CCM $d_{gasket,CCM}$, an experimentally determined compression of the gaskets of $C_{gaskets} = 7\%$ in the tightened cell and the thickness of the active area of the CCM d_{CCM}. Here, C_{GDL} is referring to the compression at the land area of the cell. The cell setup including all components is illustrated in Figure 1. The initial thicknesses are measured by a Mitutoyo dial gauge series 543 (±3 μm accuracy) at five positions for the GDLs and eight positions for the gaskets for each measurement and the average is taken for the above calculation (for details see Ref. 38). The thicknesses of CCM and CCM gasket are measured by a SEM cross-section.

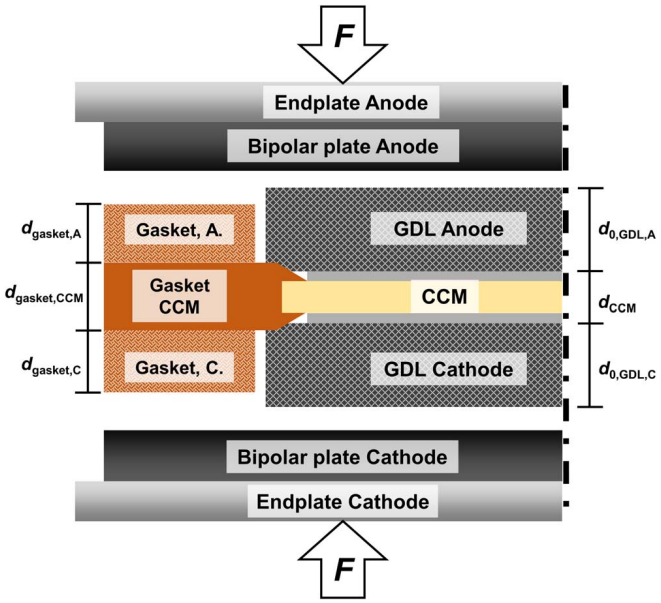

Figure 1. Illustration of the cell setup to clarify the calculation of the GDL compression (Eq. 2). Cell components such as GDLs, CCM, and gaskets are sandwiched between the bipolar plates and the endplates. The force (F) in order to achieve the desired GDL compression (C_{GDL}) is provided by 8 bolts which are tightened with a torque of 12 Nm.

The CCM is sandwiched between the two GDL sheets and the flow fields. The cell endplates are tightened by eight bolts with a torque of 12 Nm in order to achieve the desired compression. The cell was connected to a custom-designed Greenlight Innovation G60 fuel cell test station equipped with an Agilent N3306A load for recording polarization curves and a Gamry Reference 3000 potentiostat for electrochemical impedance spectroscopy.

Pressure distribution measurements.—In order to determine the pressure distribution inside the fuel cell active area at various GDL compressions, FUJIFILM Prescale film was used in the ranges from 0.2 MPa to 0.6 MPa (ultra super low pressure range, LLLW) or from 0.5 MPa to 2.5 MPa (super low pressure range, LLW). For that, the two-sheet film was placed between flow field and GDL on the cathode side of a complete fuel cell setup (incl. CCM, gaskets, GDLs). The cell was tightened and held for 2 min; then the pressure was released. After 30 min of color developing, the films were scanned (Epson Perfection V33) and evaluated using the provided software (Fujifilm FPD-8010E).

Experimental procedure.—For each GDL compression, which is listed in Table I, several individual cells were assembled and measured with C_{GDL} ranging from 8% to 53% for GDLs with MPL (GDL 25BC) and at a single compression of $C_{GDL} = 22\%$ for GDLs without MPL (GDL 25BA) on the cathode side. Prior to fuel cell testing, each cell was conditioned by stepping the voltage under hydrogen and air at 60°C, 150 kPa_{abs}, and full humidification in the following sequence: 0.6 V for 45 min, 0.95 V for 10 min, and 0.85 V for 5 min, which was repeated for eight times. For the measurement of the limiting current density, high flow rates of 1000 nccm H_2 on the anode and 5000 nccm (normal cubic centimers per minute; volumetric flow rate

Table I. Average GDL compressions (C_{GDL}) and number of individually measured cells with SGL SIGRACET GDL 25BC (with MPL) or GDL 25BA (without MPL) on the cathode side. Anode GDL: SGL SIGRACET GDL 25BC. The indicated ±variations represent the standard deviations between the individually measured cells.

Cathode GDL type	MPL	C_{GDL} [%]	Number of tested cells [-]
25BC	yes	8 ± 1	4
25BC	yes	13 ± 2	4
25BC	yes	19 ± 1	3
25BC	yes	23 ± 2	3
25BC	yes	35 ± 2	3
25BC	yes	53 ± 1	3
25BA	no	22 ± 1	2

normalized to 273 K and 1 atm) diluted oxygen in 12 different dry mole fraction ($x_{O_2,dry}$) between 0.5% and 24% on the cathode side are applied. This corresponds to high stoichiometries of >7 for both reactants at all measurement conditions. The cell is adjusted to the following conditions: cell temperature of 50°C, inlet pressure (p_{abs}) of 200 kPa, and relative humidity (*RH*) of 77% (dew point of 44.8°C) on anode and cathode side. High stoichiometries and a low pressure drop of <15 kPa minimize concentration and *RH* gradients between inlet and outlet of the flow field, enabling differential-flow conditions. For each cathode gas mixture, a polarization curve in the mass transport limited region at voltages of 0.30 V, 0.20 V, 0.15 V, 0.10 V and 0.05 V is recorded. Each voltage is held for 2 min at steady-state prior to recording the data point (average of 15 sec).

Results

Pressure distribution.—In order to evaluate the pressure distribution over the active area, Figure 2b shows three examples of FUJIFILM Prescale images and Figure 2a shows the analyzed pressure applied in the channel center, land center, and on average over the active area for the various compressions. As expected, the increase of the applied pressure with compression is in agreement with the material data provided by SGL Carbon,[39] which is also reproduced in the appendix. It is experimentally and theoretically evident that the contact pressure in the channel center is significantly lower than in the land area, because of an absent mechanical support in the channel area.[18,26,31] Furthermore, imaging studies show that under compression, the diffusion medium intrudes into the flow channel, creating a variation of local GDL thickness and porosity.[29,30] The present measurement confirms this trend: at C_{GDL} of 20%, an average pressure of 1.1 MPa was measured, while the pressure at the land center is 1.3 MPa and 0.4 MPa at the channel center. It has been reported that the ratio between land, channel, and average pressure is a strong function of the flow field dimensions, especially of the channel width and stiffness of the GDL material.[18,26,31] Unfortunately, for a low compression of 8%, no differentiation between channel and land pressure is possible from the pressure distribution image: due to the stiffness of the Prescale film itself, the image shows a very homogeneous distribution of the pressure. However in a real cell setup without a mechanically stabilizing layer, the trend of a significantly lower channel pressure compared to the average pressure shown in Figure 2a is also expected at C_{GDL} of 8%.

Scanning electron microscopy.—Figure 3 shows representative SEM images of a GDL without MPL (a) and a GDL with MPL (b). The thicknesses of the GDL without MPL of ≈156 ±8 µm (GDL 25BA) and of the GDL with MPL ≈205 ±22 µm (GDL 25BC) measured by SEM equate to an approximate MPL thickness of ≈49 ±23 µm. These values are reasonably similar to those measured using a dial gauge, viz., ≈153 ±14 µm for the GDLs without MPL and ≈220 ±10 µm for GDLs with MPL. Here it has to be stated that the shown SEM images illustrate only a small fraction of the utilized GDL

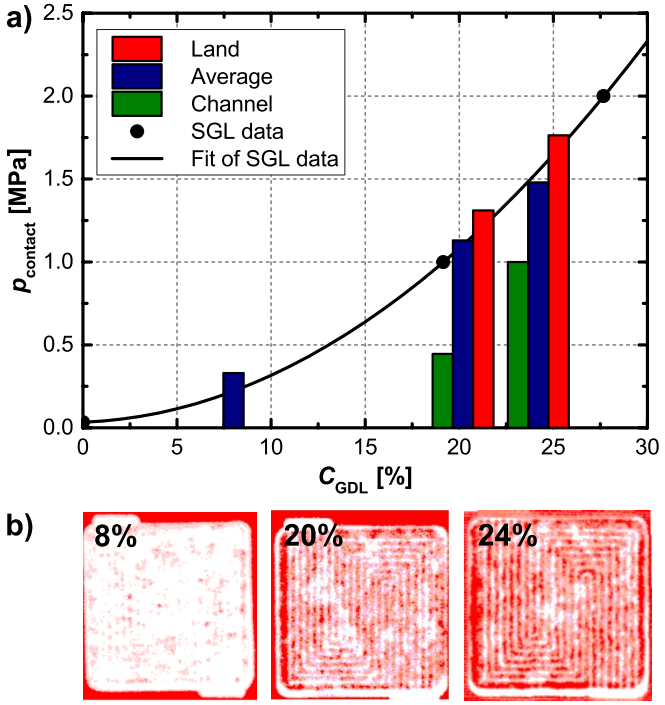

Figure 2. a) Measured contact pressure $p_{contact}$ as a function of applied compression C_{GDL} for GDLs with MPL (GDL 25BC), measured with FUJIFILM Prescale. Black circles: stress-strain information from manufacturer's material data sheet[39] (unfortunately not available online anymore, but reproduced in the appendix). Bar diagram: average pressure in the channel center (green), the land center (red), and averaged over the entire active area (blue). FUJIFILM Prescale super low pressure range (LLW, pressure range 0.5–2.5 MPa) is used for C_{GDL} = 20% and 24%, ultra super low pressure range (LLLW, pressure range 0.2–0.6 MPa) used for C_{GDL} = 8%. For C_{GDL} = 8%, the pressure on land and channel could not be separated (see text). b) Images of FUJIFILM Prescale pressure paper super low pressure range (LLW) at respective C_{GDL}.

and that even within one sample, significant variations of thickness on the order of ±10% were observed. The above determined thicknesses for the GDL with and without MPL are in reasonable agreement with the manufacturer's information of 235 ±20 µm (a similarly large standard deviation as in our SEM measurement), while above obtained thickness of the GDL without MPL is quite a bit lower than the 190 µm specified by the manufacturer (the origin of this discrepancy is not understood).

Limiting current measurements and data processing.—Figure 4a shows exemplary polarization curves for two individually measured cells with different GDL compressions of 9% and 21% at three

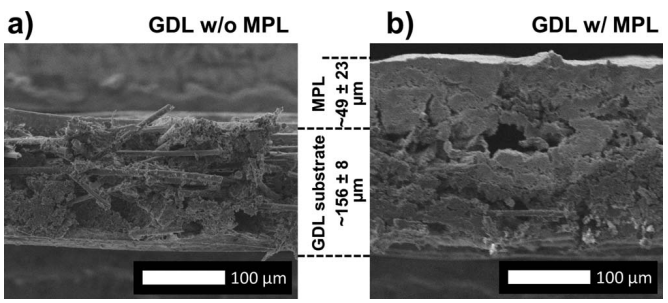

Figure 3. Scanning electron microscopy images of (a) GDL without MPL (GDL 25BA) and (b) with MPL (GDL 25BC). The GDL substrate thickness of ≈156 ±8 µm and the thickness of the GDL with MPL of ≈205 ±22 µm were extracted from SEM images (the MPL thickness indicated in the figure is estimated from the difference between (a) and (b)).

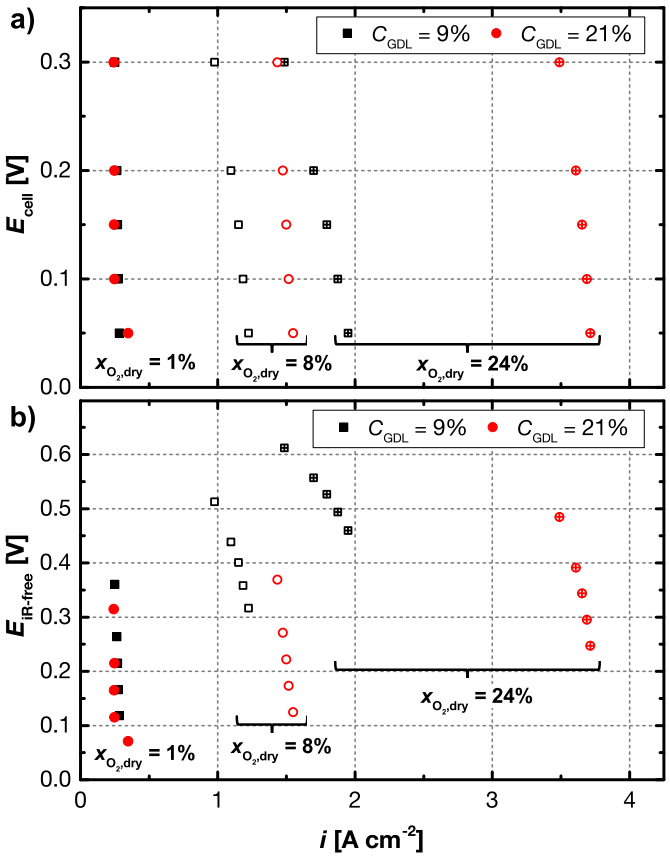

Figure 4. Polarization curves for three oxygen dry gas contents of $x_{O_2,dry}$ = 1% (full symbols), 8% (open symbols), and 24% (open, crossed symbols) for two cells with cathode GDLs with MPL (GDL 25BC) at compressions of C_{GDL} = 9% (black squares) and 21% (red circles): a) Cell voltage (E_{cell}); b) HFR-corrected voltage ($E_{iR\text{-}free}$).

different dry mole fractions of oxygen of $x_{O_2,dry}$ = 1%, 8%, and 24%. The measured geometric area normalized current densities (i) are increasing with increasing $x_{O_2,dry}$ due to an enhanced oxygen flux to the cathode catalyst layer. At a small dry mole fraction of 1%, the current densities at the two compressions are almost superimposed. However, at a high dry mole fraction of 24%, i.e., when large amounts of water are formed, the compression of 21% shows a significantly higher current density compared to the less compressed material. Another difference between the two compressions is the slope of the curve at $x_{O_2,dry}$ of 8% and 24%. The polarization curve at high compressions (red symbols in Figure 4a) is almost vertical. This shape clearly indicates a mass transport limitation and excludes major influences from kinetics, proton conduction in the membrane and electrodes as well as electronic conduction resistances. In contrast, at low compressions (black symbols in Figure 4a) the curve is slightly bended. From an experimental point of view, this could be caused by high ohmic or thermal resistances as both are affected by a decrease in contact pressure.[1,18,19] The former is indicated by the much increased high frequency resistances (*HFR*) of 150–240 mΩ cm^2 (measured at 0.3 V) at C_{GDL} of 9%, compared to 45–65 mΩ cm^2 for compressions of 21%. This could be either caused by an increase in contact resistance or by a higher proton resistance due to a heating of the membrane (caused by an increase in thermal resistance). In order to evaluate the *HFR* impact, Figure 4b shows the *iR*-corrected voltages of the polarization curves. Due to the higher *HFR* at C_{GDL} = 9%, the *iR*-free voltages at this low compression are considerably higher than for C_{GDL} = 21%, particularly at the higher current densities obtained for $x_{O_2,dry}$ = 24%. This might lead to the effect that a diffusion limiting current density could not be entirely reached at low compression, in which case the oxygen transport resistance would be overestimated.

The other possible explanation could be the hindered heat flux by a high thermal through-plane resistance at low compressions.[19–21] When the cell voltage is decreased, the fuel cell efficiency is also decreasing and more heat is released. This could result in a heating-up of the CCM, which would enhance mass transport, but could also lead to a membrane dry-out (already considered in the *HFR*). The temperature increase would result in a higher diffusion coefficient and lower liquid water saturation, which would cause a shift in diffusion limitation toward higher current densities, when the cell voltage is decreased. This effect would be more pronounced at low compressions as observed in the present measurement and would in contrary to above discussed ohmic resistive effects result in an underestimation of the oxygen transport resistance.

Nevertheless, the clear difference in the current density of ≈1.5 A cm^{-2} at $x_{O_2,dry}$ = 24% in Figure 4b at the same $E_{iR\text{-}free}$ potential between C_{GDL} of 9% and 21% is indicating that the measurement is indeed dominated by oxygen transport limitations. While the ohmic resistances affect the limiting current density contrary to the thermal contact resistances at low GDL compressions and hence, might cancel each other out, we will extract the values at the same voltage for all compressions to estimate the transport resistance. This may lead to errors on the order of ≈10% as estimated from Figure 4b.

In summary, to extract the limiting current density (i_{lim}), the value of i at 0.15 V was taken for $x_{O_2,dry}$ between 0.5% and 2%, at 0.10 V between 3% and 8% and at 0.05 V between 12% and 24%. It should be noted that at low voltages and low oxygen gas content, hydrogen evolution currents become significant; hence the limiting current was extracted at 0.15 V. On the other hand, at higher oxygen concentrations and higher current densities, above mentioned effects from the electrical resistance become more significant; hence the limiting current at the lowest recorded voltage was taken into account.

The total oxygen transport resistance (R_T) from the channels to the catalyst surface is calculated by the following equation:

$$R_T = \frac{4 \cdot F}{i_{lim}} \cdot c_{O_2} = \frac{4 \cdot F}{i_{lim}} \cdot \frac{p_{abs} - p_{H_2O}}{R \cdot T} \cdot x_{O_2,dry} \quad [3]$$

Here, F is the Faraday constant (96485 C mol^{-1}), R is the universal gas constant (8.3145 J mol^{-1} K^{-1}), c_{O_2} is the oxygen concentration in the channel, T is the cell temperature, p_{abs} is the absolute gas pressure and p_{H_2O} is the partial pressure of water. R_T consists of the following resistances in series:[3,32,36]

$$R_T = R_{ch} + R_{GDL} + R_{MPL} + R_{electrode} + R_{other} \quad [4]$$

Analogous to serial electrical resistances, all single oxygen transport resistances can be summed up to a total oxygen transport resistance (R_T). R_{ch} relates to the oxygen transport resistance originating from the transport of O_2 from the bulk flow field channel to the carbon fiber material surface. R_{GDL} and R_{MPL} are referring to the resistances due to the mass transport through GDL and MPL. $R_{electrode}$ describes the transport inside the electrode layer and the film diffusion to the catalytic active sites. R_{other} is a term for resistances from other sources and includes also interfacial resistances.

Figure 5 shows the total oxygen transport resistance R_T plotted versus the limiting current density i_{lim} for various GDL compressions. Here, the data from independent repeat experiments (s. Table I) were used to construct R_T vs. i_{lim} curves, from which then the R_T values at any given selected i_{lim} value were determined by interpolation, so that finally an average R_T value and its standard deviation over all repeat experiments could be plotted vs. i_{lim}. Significant differences in the trend of the curves are observed. Researchers at General Motors already presented data for various GDL materials with microporous layer at similar conditions for a typical compression of ≈20%, which is comparable to the curve for 19% and 23% in Figure 5 (green/red solid lines).[3,4] In general, three regions in oxygen transport (dry, transition and wet) can be discerned for GDLs with MPL, which depend on the current density. These different regions of total oxygen transport resistance are directly linked to different states of water transport through the GDL. In the dry region, at small limiting current densities (≲0.7 A cm^{-2}), the total oxygen transport resistance is constant at

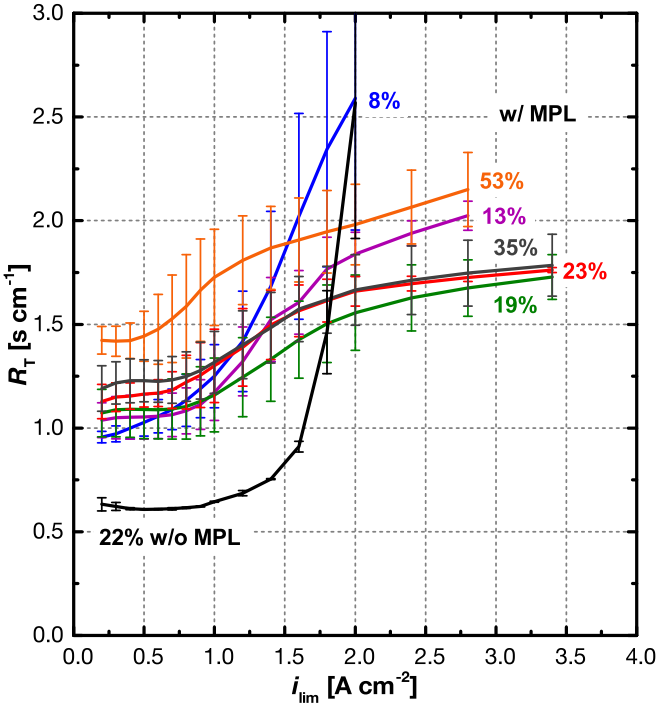

Figure 5. Average total oxygen transport resistance R_T calculated by Eq. 3 as a function of the limiting current density i_{lim} for cathode GDLs with MPL (GDL 25BC) and without MPL (GDL 25BA) at various compressions (C_{GDL}) between 8% and 53%. Error bars represent the standard deviation from independent repeat experiments (the respective number of repeats are listed in Table I), which are averaged over the same current densities. Measurement conditions are T_{cell} = 50°C, p_{abs} = 200 kPa, RH = 77%; the anode GDL is always SGL 25BC.

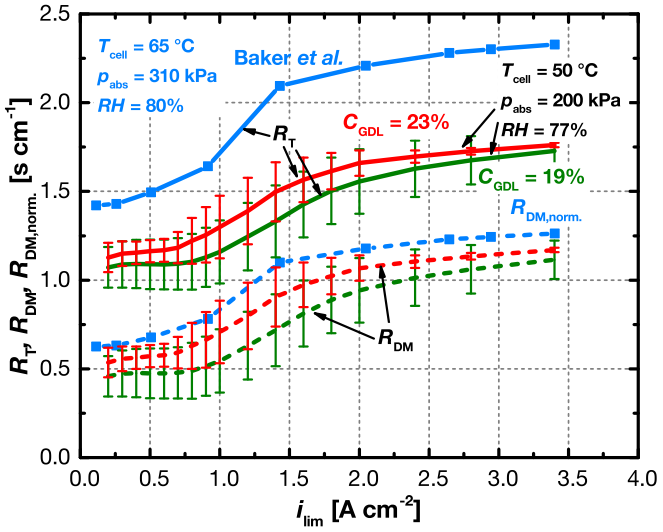

Figure 6. Total oxygen transport resistances (R_T, solid lines) and (normalized) diffusion medium transport resistances (R_{DM}/$R_{DM,norm.}$, dotted lines) for: GDL with MPL (GDL 25BC) at GDL compressions of 19% (green lines) and 23% (red lines) measured in our study as well as for the same GDL by Baker et al.[4] Data for 19% and 23% compression are taken from Figure 5 and were measured at T_{cell} = 50°C, p_{abs} = 200 kPa, RH = 77%; data from Baker et al.[4] were measured at T_{cell} = 65°C, p_{abs} = 310 kPa, RH = 80%. In order to determine the comparable (normalized) diffusion medium resistance (R_{DM}/$R_{DM,norm.}$, dotted lines), Eq. 6 and Eq. 7 are applied.

a relatively small level (≈1.1 s cm^{-1}). Here, the GDL remains dry and the transport of water is purely driven by vapor diffusion. With increasing current density, R_T is entering a transition region, where water condensation is starting to hinder diffusion pathways of oxygen, until it reaches a reasonably constant plateau (≳2 A cm^{-2}) characterized by an R_T at an elevated level (≈1.7 s cm^{-1}). In this so-called wet region, the GDL is saturated to a maximum level with water, which causes an approximately constant total oxygen transport resistance with increasing current density. The values for R_T in the dry and wet region are in good agreement with data presented by Caulk and Baker for their unspecified material C, for which ≈1.0 s cm^{-1} and ≈1.8 s cm^{-1} were measured at the same conditions as in this study (see Figure 8 in Reference 3).

In a different article, Baker et al. showed for SGL 25BC (the same material as used in this paper) the existence of the dry, the transition, and the wet region, however measured at different operating conditions (T_{cell} = 65°C, p_{abs} = 310 kPa and RH = 80% compared to T_{cell} = 50°C, p_{abs} = 200 kPa and RH = 77%[4]). Hence, the data are not directly comparable. Unfortunately, the applied compression in their study was not specified, but we assume that they used a value of ≈20%, as this is most typically used as standard compression by the GM group.[23,36] In order to compare our data with what has been measured in the literature, Figure 6 shows the comparison for two data sets from this study (C_{GDL} = 19% and 23%, green/red solid lines) and the data for GDL 25BC (light blue solid line) from Baker et al.[4] Due to the different measurement conditions, the data differ significantly from each other. For a comparison, we analyze the pressure dependent part of R_T (O_2 transport by molecular diffusion) in the dry region (≤0.4 A cm^{-2}), which is attributed to the diffusion medium (GDL and MPL, R_{DM}).

$$R_{DM} = R_{GDL} + R_{MPL} \quad [5]$$

Combined with Eq. 4, this results in Eq. 6. Under the assumption, that $R_{other} \approx 0$, because no interfacial effects are hindering oxygen transport for this compression range (explanation see later discussion), we can simplify the equation to yield:

$$R_{DM} = R_T - R_{ch} - R_{electrode} - R_{other} \approx R_T - R_{ch} - R_{electrode} \quad [6]$$

By measurements at different pressures (150 kPa, 200 kPa and 300 kPa), one can separate the pressure dependent (R_{DM} + R_{ch}) from the pressure independent part ($R_{electrode}$) of the total transport resistance.[23] By applying this approach, we calculate values for $R_{electrode}$ between 0.36 s cm^{-1} and 0.40 s cm^{-1} for our data shown in Figure 5. This value is higher than what has been reported in the literature, where values of, e.g., 0.02–0.08 s cm^{-1} at 80°C and 62% RH,[4] ≈0.15 s cm^{-1} at 80°C and 62%/90% RH,[23,40,41] 0.2 s cm^{-1} at 80°C and 64–80% RH,[36] 0.24 s cm^{-1} at 80°C and 75% RH[35] and 0.31 s cm^{-1} at 55°C and 75% RH[35] can be found for comparable cathode catalyst loadings of 0.3–0.4 mg_{Pt} cm^{-2}. The most probable reasons for the variations of $R_{electrode}$ at the same operating temperature are different data treatment approaches, varying cell designs and individual electrode compositions and structures. Therefore, for the correction of the data by Baker et al.,[4] we assume the value of 0.15 s cm^{-1}, that has been reported for 80°C and 62% RH in their subsequent publication[23] using an advanced data treatment model. However it has been shown that from 80°C to 65°C, $R_{electrode}$ is increasing by ≈25% due to the temperature dependencies of Knudsen diffusion (minor) and ionomer film diffusion.[35] This effect is considered in the correction.

R_{ch} is calculated based on a channel analysis, assuming the given flow field geometry for this study (0.23 s cm^{-1}) and the flow field used in Reference 23 for the literature data (0.33 s cm^{-1}) at the respective operating conditions. To compare the values for R_{DM} from this study and Baker et al., we normalized the literature data (condition 2: T_{cell} = 65°C, p_{abs} = 310 kPa, RH = 80%) to the conditions of this study (condition 1: T_{cell} = 50°C, p_{abs} = 200 kPa, RH = 77%) by the following relation.

$$R_{DM(normalized)} = R_{DM,2} \cdot \frac{D_{OM,2}}{D_{OM,1}} \quad [7]$$

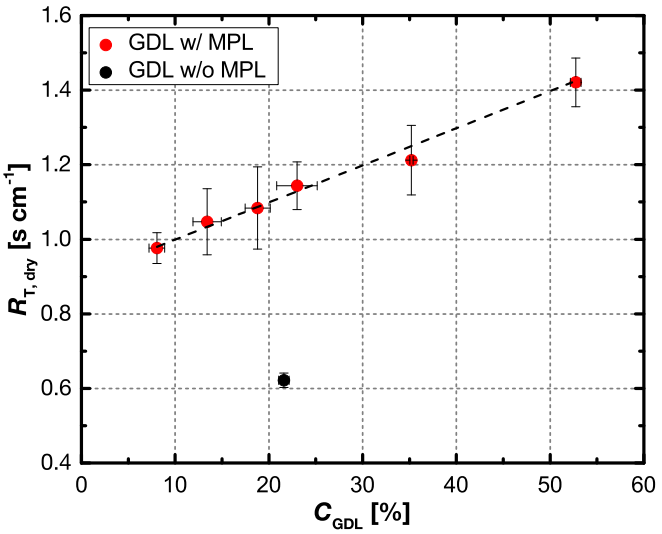

Figure 7. Total dry oxygen transport resistance $R_{T,dry}$, calculated from the average transport resistance between 0.2–0.4 A cm^{-2} as a function of the GDL compression C_{GDL} for cathode GDL 25BC with MPL (red circle) and GDL 25BA without MPL (black circle). Values are extracted from Figure 5.

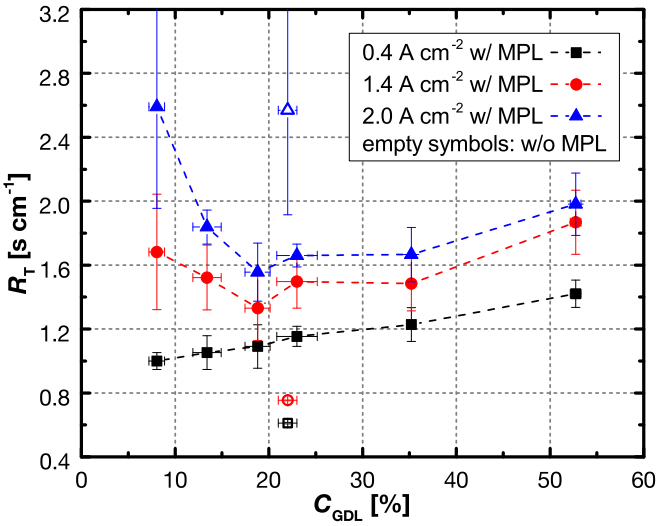

Figure 8. Total oxygen transport resistance R_T as function of the GDL compression (C_{GDL}) for GDLs with MPL (GDL 25BC; filled symbols) and GDL without MPL (GDL 25BA; empty symbols), plotted for three different current densities of 0.4 A cm^{-2} (black squares), 1.4 A cm^{-2} (red circles), and 2.0 A cm^{-2} (blue triangles). Values are extracted from Figure 5 at the respective current densities.

Here D_{OM} is the diffusion coefficient of oxygen in the respective gas mixture and is calculated from the binary diffusion coefficients of oxygen in nitrogen and water[42] and a mixture law.[23] Eq. 7 is valid because the same geometry factor, which is based on the channel and land widths (note that the channel and land widths in the study by Baker et al.[4] was also 0.5 mm), the diffusion media thickness and the ratio of in-plane to through-plane diffusion coefficient does apply.

The calculated diffusion media resistance (R_{DM}) for compressions of 19% and 23% as well as the normalized diffusion media resistance ($R_{DM,normalized}$) for the literature data is plotted in Figure 6 (dotted lines). The shapes of the curves are very similar, and the curve with 23% compression is the closest to the data by Baker et al.[4] In the dry region, the data from our study are 12%–25% smaller than the values from Baker et al. This can have several reasons, e.g., a higher GDL compression for their cell or an unconsidered influence of the different flow field geometries. However, due to the various assumptions made for the correction, the different cell setups, and the different measurement equipment, the agreement between the different data sets is actually quite reasonable.

Dry region – absence of water.—In the region of low current densities ($\lesssim$ 0.7 A cm^{-2}), no liquid water is expected to be formed inside the cell at an *RH* of 77%. Hence, in this region only porosity and tortuosity of the carbon fiber material and the microporous layer determine the local diffusion of oxygen. When taking the average value of R_T between 0.2 A cm^{-2} and 0.4 A cm^{-2} for each adjusted compression, a total dry oxygen transport resistance ($R_{T,dry}$) is determined and shown in Figure 7. This resistance $R_{T,dry}$ should only be affected by the GDL material properties itself, its compression, and thickness besides the fixed properties of the flow field, the electrodes and the operating condition. For 19% to 23% compression, an $R_{T,dry}$ of $\approx$1.1 s cm^{-1} is measured for GDLs with MPL (GDL 25BC). This value is in good agreement with what would be expected from Baker et al. (estimated from the normalized value from Figure 6: $R_{T,dry} \approx R_{DM,dry} + R_{electrode} + R_{ch} \approx (0.65 + 0.15 \cdot 1.25 + 0.33)$ s cm$^{-1} \approx$ 1.2 s cm^{-1}). For the GDL without MPL (GDL 25BA), a $\approx$45% lower $R_{T,dry}$ of $\approx$0.65 s cm^{-1} is observed, as shown in Figure 7 (black circle). This can be explained by the fact that the material without MPL is $\approx$30% thinner than the material with MPL ($\approx$153 $\pm$ 14 µm vs. $\approx$220 $\pm$ 10 µm based on our dial gauge measurements) and that the overall oxygen transport is less hindered by the material without an MPL, which acts as a series diffusion resistance with typically less porosity and smaller pore sizes. This is indicated by air permeability measurements, which show an approximately 200 times smaller value for GDL 25BC compared to GDL 25BA.[43] The vapor diffusivity (which theoretically scales linearly with the oxygen diffusivity) is $\approx$38% smaller for GDL 25BC (with MPL) than for GDL 25BA (without MPL).[43] Normalized to the thickness (measured by dial gauge), this is resulting in a $\approx$57% smaller transport resistance for the material without MPL (GDL 25BA), which is in reasonable agreement with our findings.

For GDLs with MPL (GDL 25BC), a linear relationship between the total dry oxygen transport resistance $R_{T,dry}$ and C_{GDL} was found, with a slope of 0.01 s cm^{-1} per % of C_{GDL} (s. Figure 7). A similar linear relationship was found for the ratio of bulk and effective diffusion coefficient for a non-hydrophobically treated Toray 060 by limiting current density measurements.[23] This trend was explained by a decrease in porosity with increasing compression and was confirmed by ex-situ measurements which yielded comparable results in diffusivity and permeability.[4,22,24–26] The data from Baker et al.[23] would result in a slope for the respective recalculated values of $R_{T,dry} \approx 0.005$ s cm^{-1} per % of C_{GDL} (fitted between C_{GDL} of 5% and 30%, at higher compression stagnation of $R_{T,dry}$), which is half of the value observed in this study and which may be related to the different microstructure of the Toray paper used by Baker et al.[23] compared to the GDL 25BC material used in our study (e.g., the use of untreated Toray paper vs. the hydrophobically treated GDL 25BC, differences in porosity) and the absence of an MPL for the Toray paper.

Wet region – high water saturation levels.—At compressions of 19%, 23%, and 35%, Figure 5 shows a reasonably flat upper plateau of R_T at $i_{lim} > 2$ A cm^{-2} for GDLs with MPL (GDL 25BC), as would be expected from the literature.[3,4,33] This, however, is not the case at lower compressions (8% and 13%), where continuously increasing R_T values with increasing limiting current density are observed. This means that for very low C_{GDL} values of 8%, the total oxygen transport resistance in the wet region is significantly higher and the limiting current densities are smaller than those obtained for conventional compressions of C_{GDL} values of $\approx$20%, even if the initial dry total oxygen transport resistance is smaller for low compressions (8% and 13%). To illustrate the R_T for different current densities as a function of compression, data from Figure 5 were replotted in Figure 8.

For the small limiting current density of 0.4 A cm^{-2}, where water transport is purely gas phase driven, an almost linear behavior between R_T and C_{GDL} is observed (see section Dry region and Figure 7). At higher limiting current densities of 1.4 A cm^{-2} and 2.0 A cm^{-2}, where the GDL is partially saturated with liquid water, the total oxygen transport resistance R_T at low compressions is increasing disproportionately compared to its behavior at higher compressions. Hence, a minimum of R_T is observed at C_{GDL} of ≈19%, which clearly originates purely from different oxygen transport rates. It is well known that the GDL compression has an optimum, where a maximum in fuel cell performance is achieved. So far, it has been expected that this originates mainly from a trade-off between a better mass transport at lower compressions (see section Dry region and Figure 7) and a lower electrical resistance at higher compressions, which has also been shown by fuel cell measurements with a minimum compression of 15%.[27] However, R_T data clearly show that this is not the only reason, because for high current densities of 1.4 A cm^{-2} and 2.0 A cm^{-2}, the smallest value for R_T is not observed at the smallest compression, but at an intermediate compression of 19%. We believe that the reason why this has not been observed previously is due to the fact that compressions far below 15% have not been examined. It is also noteworthy that for small compressions, the standard deviation for the measuring points in the wet region (expressed by the error bars in Figure 5) increase significantly due to the steep slopes of the curves. This indicates that water transport phenomena in this region are very sensitive toward compression.

The trend seen at low compressions is very similar to what is observed for GDLs without MPL (GDL 25BA), which is showing also a steep increase of R_T when water condensation is taking place (see black line in Figure 5, and open symbols in Figure 8). This is indicating that similar effects of oxygen transport hindrance by liquid water are taking place for both a GDL/MPL at low compression (<15%) and for a GDL without MPL at conventionally applied compression (≈20%).

Discussion

Various in-situ X-ray or neutron tomography and radiography studies show a preferred water condensation in the vicinity of the flow field lands.[8,33,44–46] This is explained by better thermal contact in the land areas contacting the bipolar plate compared to the channel areas exposed to the gas convection in the flow field channels. Consequently, a cold spot between the lands and the electrode layer is formed, where water preferentially starts to condense. A transport model was proposed by Manke et al., who suggest that condensed water is eruptively transported from the land area into the flow field channels, which is confirmed by imaging the time-resolved formation, growth, and disappearance of water droplets in the vicinity of the land/channel interface.[46] On the other hand, Zenyuk et al. found in their X-ray computed tomography (X-ray CT) studies that water condensation occurs in the channel regions as the GDL compression is being increased from low values (15%) to very high values (35% and 47%). They explain their observation with a non-uniform porosity distribution at high compressions, which would preferably allow liquid water to be transported through the larger pores in the channel region.[47] Contrary to the other tomography studies, this latter work was conducted with a GDL without MPL (SGL GDL 10 BA), which could be the reason for this discrepancy; however, it should be noted that in the X-ray CT study by Deevanhxay et al.,[8] water formation at the cathode interface was predominantly in the land region both with and without MPL. Therefore, it is indeed likely that in the study by Zenyuk et al.,[47] the very high land compression resulted in an overall very poor permeability in the land regions and such a locally very low current density and water production rate.

Regarding the function of an MPL and the origin of its beneficial effect on fuel cell performance, several different hypotheses have been advanced (for a detailed summary, see Owejan et al.[5]). One is that the MPL might limit the number of liquid water entry points into the GDL, both in the channel and land region, thereby decreasing the local water saturation in the GDL at the point of water breakthrough.[48,49] An alternative explanation supported by experiments with various MPL configurations is that the primary role of the cathode MPL might be to prevent the formation and/or the accumulation of liquid water at the cathode interface, suggesting that liquid water accumulation in a GDL/MPL configuration is only taking place in the larger pores of the GDL substrate, while the MPL itself would remain free of liquid water, thereby preventing the contact of liquid water formed in the large GDL pores with the catalyst layer.[5] We believe that it is this latter effect which causes the different behavior of the transport resistance in the presence of liquid water, when comparing GDL with and without MPL at comparable compressions of ≈20%, as shown in Figure 5 (s. green and red lines vs. black line). While for GDLs with MPL (GDL 25BC), R_T increases to a wet plateau which is only ≈1.5-fold higher than the dry plateau and which is caused by reaching a partial saturation of the GDL substrate at high current densities, the GDL without MPL (GDL 25BA) is showing a steep ≈4-fold increase of R_T without ever reaching a plateau (at least within the range of oxygen concentrations used in our study). This is consistent with the very poor low-temperature fuel cell performance without MPL shown by Owejan et al.[5] and with the reduced water saturation at the cathode interface in the presence of an MPL, as shown in the X-ray CT measurements by Deevanhxay et al.[8] as well as by Tabe et al.[7] by cryo-microscopy.

These findings lead us to a reasonable explanation for the increase of R_T for GDLs with MPL (GDL 25BC) at very small compressions (<15%). While the contact between MPL and cathode electrode layer at high compression is expected to remain very tight even in the channel region, the cathode/MPL interface in the channel regions is likely to partially separate at very low GDL compressions. This would happen preferentially in the flow field channel areas, because there the GDL is unsupported and can enter the flow field channels. Hence, the contact pressure between MPL and cathode electrode layer is only a small fraction of that under the land area as shown in Figure 2.[18,26,31] The pressure distribution across land and channel region is also illustrated in Figure 9. If the MPL loses its contact to the cathode electrode layer, water can accumulate on the more hydrophilic surface of the catalyst layer, which would lead to a similar effect as

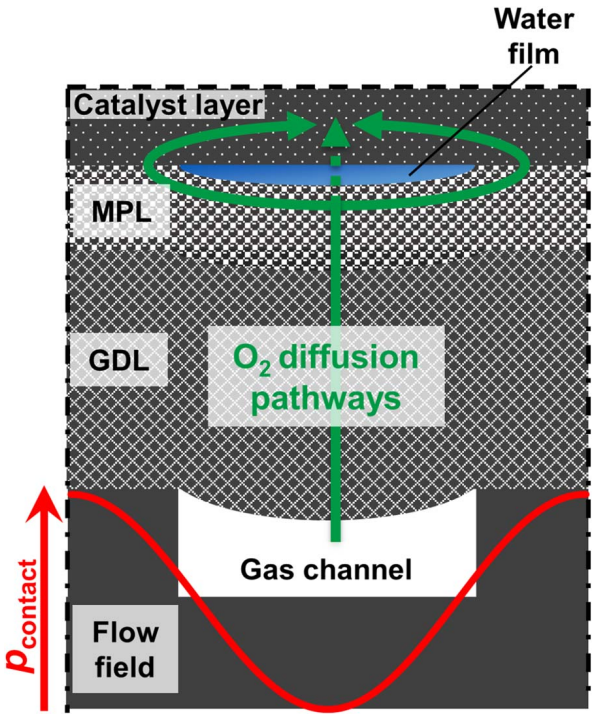

Figure 9. Illustration of the hypothesized water film formation at the interface of the cathode electrode layer and the MPL at low GDL compressions. Here, $p_{contact}$ represents the contact pressure between the cathode GDL and the MEA.

that which was suggested to happen in the absence of an MPL by Owejan et al.[5]

Our findings show that the effect of water accumulation can be measured by varying the GDL compression. While for our flow field geometries the contact pressure in the channel center is at a reasonably high level at $C_{GDL} = 20\%$, this value would drop to much less than 0.3 MPa for 8% compression (i.e., much below the average compression shown in Figure 2) and below. As sketched in Figure 9, a liquid water film could be formed for these small contact pressures in the channel region, which would represent a strong diffusion barrier for the transport of oxygen to the cathode catalyst layer. Transport of gas can either occur via diffusion through this hypothesized water film or via a longer diffusion pathway through the MPL. This would cause an increase in mass transport resistance, resulting in a lower i_{lim} and a larger R_T, as is shown in Figure 6 for 8% compression; conceptually, this corresponds to an increase in the interfacial resistance contribution of R_{other} in Eq. 3. This behavior is obviously quite comparable to that of a GDL without MPL, which is showing a similar trend: i) they both have the lowest dry total oxygen transport resistances (that of the GDL without MPL is significantly smaller due to the absence of an additional diffusion barrier); ii) both show the highest values in the wet region without exhibiting a wet plateau as well as a similarly large increase of R_T between 0 and 2 A cm^{-2}, viz., ≈2.5-fold for the GDL with MPL at 8% compression (s. blue line in Figure 5) and ≈4-fold for the GDL without MPL (s. black line in Figure 5). It should be noted that a water film of only 0.02 µm thickness (t_{H_2O}) between the MPL and the cathode catalyst layer would result in a local oxygen transport resistance of $R_{other} \approx 2$ s cm^{-1} for the operating temperature used in Figure 5 (50°C) based on the known O_2 solubility (Henry constant $H_{O_2|H_2O} = 1.1 \cdot 10^{-8}$ Pa (mol l^{-1})$^{-1}$) and diffusivity in water (diffusion coefficient $D_{O_2|H_2O} = 4.1 \cdot 10^{-9}$ m^2 s^{-1}).[50,51] Here, R_{other} is estimated by the following equation based on the oxygen flux by Fick's diffusion (J_{O_2}) for an applied oxygen gas concentration gradient (Δc_{O_2}).

$$R_{other} = \frac{\Delta c_{O_2}}{J_{O_2}} = \frac{\frac{\Delta p_{O_2}}{R \cdot T}}{\frac{D_{O_2|H_2O}}{t_{H_2O}} \cdot \frac{\Delta p_{O_2}}{H_{O_2|H_2O}}} = \frac{t_{H_2O} \cdot H_{O_2|H_2O}}{D_{O_2|H_2O} \cdot R \cdot T} \quad [8]$$

Assuming that the water film would only be occurring in the channel region, the area averaged R_T value would be approximately half of this value for the here used channel/land ratio of 1/1 (≈1 s cm^{-1}). The estimated value is consistent with the difference between the maximum R_T value measured for a compression of 8% (≈2.6 s cm^{-1}) and the value at the comparable limiting current density for a compression of 19% (≈1.6 s cm^{-1}). This illustrates that an only 0.02 µm thin water film in the channel region could explain our R_T measurements.

A reason why such a water film in the channel region has not yet been detected by in-situ imaging techniques with GDLs with MPL, could be that even with sophisticated measurement setups with the highest possible spatial resolutions of ca. 12 µm for neutron imaging[33] and ca. 1.33–3 µm for X-ray radiography,[46,47] the detection of such thin water films of on the order of 0.02 µm would not be possible. Furthermore, when using platinum based catalysts, the very high X-ray absorption coefficient of Pt renders the detection of liquid water at the MPL/cathode layer interface very challenging.[52] However, in recent studies using cryo-microscopy, significant amounts of liquid water were found at the cathode MPL interface in the vicinity of the flow field channels under high-humidity conditions. Aoyama et al. investigated the effect of the preparation procedure of the MEA on liquid water formation by cryo-scanning electron microscopy.[53] They found significant amounts of ice at the cathode/MPL interface in the channel region after operating the fuel cell with a CCM manufactured by the decal transfer method, indicating that liquid water is accumulating in this region. In contrast to the decal transfer method, no ice was found in MEAs with gas diffusion electrodes (GDE), in which the catalyst layer is directly applied to the MPL and for which a better adhesion between electrode and MPL is expected. Based on these findings, the authors concluded that the water accumulation in case of the catalyst coated membrane is caused by a poor contact between catalyst layer and MPL in the channel region, leading to the formation of a water film. One light microscope study focused on the effect of the microporous layer on water transport.[7] While for GDLs without an MPL, ice was found equally distributed among flow field channel and land areas, for GDLs equipped with an MPL, ice was preferentially found in the flow field channel regions. This suggests that the MPL can prevent water accumulation in the flow field land area, where high contact pressure is observed; at the same time, however, at the decreased contact pressure in the channel regions, liquid water can accumulate in gaps between the MPL and the cathode electrode layer.[7,14,15,53] Finally, this is also supported by the calculation of the water storage capacities at the cathode/MPL interface based on surface roughness measurements: Swamy et al. predict a three times higher maximum water content inside interfacial gaps without applied compression in the flow field channels compared to 1.5 MPa, which corresponds to a typical flow field land compression pressure.[14]

The here presented effect of high oxygen mass transport resistances at very low compressions is not only relevant in case of inhomogeneous compression of the diffusion medium, e.g., if the cells of a stack are locally under compressed. But it might also be relevant when considering to increase the flow field channel-to-land ratio in automotive fuel cells, which can result in very low contact pressures at the channel center.[26,34] This would be expected to facilitate the proposed water film formation even if the dry transport resistance for a high channel-to-land ratio is smaller than for narrow channels.[34] Likewise, a trend toward thinner GDLs could result in similar effects as observed in this study: while their advantage is an improved mass transport, their disadvantage is the concomitant decrease of the shear and bending stiffness, which results in a smaller contact pressure in the channel center. Therefore, interfacial effects between MPL and electrode layer have to be taken into account when optimizing flow field, GDL, MPL, and CCM for high performance.

Conclusions

In conclusion, we show experimental data at T_{cell} of 50°C, *RH* of 77% and p_{abs} of 200 kPa which allow the determination of the total oxygen transport resistance R_T between the gas flow field channels and the cathode electrode as a function of the applied gas diffusion layer compression (C_{GDL}) of a GDL with MPL (SGL GDL 25BC). We observe that oxygen transport in dry GDLs with MPL at small limiting current densities <0.7 A cm^{-2}, where transport of water is purely driven by vapor diffusion and no liquid water is expected, is hindered by an increase in compression due to a loss in GDL porosity. Hence, we measure a linear increase of R_T with increasing C_{GDL}.

For current densities >1.5 A cm^{-2}, where liquid water is formed, the total oxygen transport resistance R_T is increasing disproportionately for less compressed diffusion layers, i.e., for $C_{GDL} \leq 13\%$. We find a minimum value of R_T at GDL compressions of 19%, which solely originates from an optimum of the oxygen transport rate. Comparative measurements with a GDL without MPL (GDL 25BA) show a similar trend, viz., a significantly increasing R_T at higher current densities, which can be explained by the flooding of the GDL close to the cathode surface. For GDLs with MPL, the formation of a liquid water film as illustrated in Figure 9 at the cathode/MPL interface in the flow field channel region can rationalize this phenomenon.

Acknowledgments

This research was carried out within the framework of the joint project "Optigaa2". Financial support by the German Federal Ministry of Economic Affairs and Energy (grant number 03ET6015E), Freudenberg Performance Materials SE & Co. KG and Daimler AG is gratefully acknowledged. We are also thankful for valuable discussions with Daniel Baker (General Motors) and David Müller (TUM).

Table AI. Material properties of SGL GDL 25 BC reproduced from a table given in the manufacturer's information,[39] which is unfortunately not anymore available online.

Properties	Units	GDL 25BC
Ash content[1]	%	<0.25
Areal weight[2]	g m^{-2}	90 ± 10
Thickness (@ 5psi load)[3]	µm	235 ± 20
Thickness (@ 1 MPa load)[3]	µm	190 ± 20
Thickness (@ 2 MPa load)[3]	µm	170 ± 20
Compressibility (@ 1 MPa)[4]	%	ca. 19
TP El. Resistance (@ 1MPa)[5]	mΩ cm^2	<12
IP Pressure Drop (@ 1 MPa)	bar	0.8

[1]DIN 51903;
[2]SGL internal, based on DIN EN ISO 536;
[3]SGL internal, based on DIN EN ISO 9073;
[4]SGL internal, based on DIN 53885;
[5]SGL internal, based on DIN 51911.

Appendix

See Table AI.

References

1. M. F. Mathias, J. Roth, J. Fleming, and W. Lehnert, in *Handbook of Fuel Cells*, W. Vielstich, H. A. Gasteiger, and A. Lamm Editors, John Wiley & Sons, Ltd (2010).
2. J. M. Morgan and R. Datta, *J. Power Sources*, **251**, 269 (2014).
3. D. A. Caulk and D. R. Baker, *J. Electrochem. Soc.*, **157**, B1237 (2010).
4. D. R. Baker, C. Wieser, K. C. Neyerlin, and M. W. Murphy, *ECS Transactions*, **3**, 989 (2006).
5. J. P. Owejan, J. E. Owejan, W. B. Gu, T. A. Trabold, T. W. Tighe, and M. F. Mathias, *J. Electrochem. Soc.*, **157**, B1456 (2010).
6. H. Li, Y. H. Tang, Z. W. Wang, Z. Shi, S. H. Wu, D. T. Song, J. L. Zhang, K. Fatih, J. J. Zhang, H. J. Wang, Z. S. Liu, R. Abouatallah, and A. Mazza, *J. Power Sources*, **178**, 103 (2008).
7. Y. Tabe, Y. Aoyama, K. Kadowaki, K. Suzuki, and T. Chikahisa, *J. Power Sources*, **287**, 422 (2015).
8. P. Deevanhxay, T. Sasabe, S. Tsushima, and S. Hirai, *Electrochem. Commun.*, **34**, 239 (2013).
9. H. Markotter, J. Haussmann, R. Alink, C. Totzke, T. Arlt, M. Klages, H. Riesemeier, J. Scholta, D. Gerteisen, J. Banhart, and I. Manke, *Electrochem. Commun.*, **34**, 22 (2013).
10. H. Markötter, I. Manke, P. Krüger, T. Arlt, J. Haussmann, M. Klages, H. Riesemeier, C. Hartnig, J. Scholta, and J. Banhart, *Electrochem. Commun.*, **13**, 1001 (2011).
11. P. Deevanhxay, T. Sasabe, S. Tsushima, and S. Hirai, *J. Power Sources*, **230**, 38 (2013).
12. F. E. Hizir, S. O. Ural, E. C. Kumbur, and M. M. Mench, *J. Power Sources*, **195**, 3463 (2010).
13. S. Prass, S. Hasanpour, P. K. Sow, A. B. Phillion, and W. Mérida, *J. Power Sources*, **319**, 82 (2016).
14. T. Swamy, E. C. Kumbur, and M. M. Mench, *J. Electrochem. Soc.*, **157**, B77 (2010).
15. I. V. Zenyuk, E. C. Kumbur, and S. Litster, *J. Power Sources*, **241**, 379 (2013).
16. S. Kim, M. Khandelwal, C. Chacko, and M. M. Mench, *J. Electrochem. Soc.*, **156**, B99 (2009).
17. A. R. Kalidindi, R. Taspinar, S. Litster, and E. C. Kumbur, *Int. J. Hydrogen Energy*, **38**, 9297 (2013).
18. J. Kleemann, F. Finsterwalder, and W. Tillmetz, *J. Power Sources*, **190**, 92 (2009).
19. I. Nitta, O. Himanen, and M. Mikkola, *Fuel Cells*, **8**, 111 (2008).
20. E. Sadeghi, N. Djilali, and M. Bahrami, *J. Power Sources*, **196**, 246 (2011).
21. G. Karimi, X. Li, and P. Teertstra, *Electrochim. Acta*, **55**, 1619 (2010).
22. P. K. Das, X. G. Li, and Z. S. Liu, *Applied Energy*, **87**, 2785 (2010).
23. D. R. Baker, D. A. Caulk, K. C. Neyerlin, and M. W. Murphy, *J. Electrochem. Soc.*, **156**, B991 (2009).
24. N. Zamel, X. G. Li, and J. Shen, *Energ Fuel*, **23**, 6070 (2009).
25. N. Zamel, N. G. C. Astrath, X. G. Li, J. Shen, J. Q. Zhou, F. B. G. Astrath, H. J. Wang, and Z. S. Liu, *Chem. Eng. Sci.*, **65**, 931 (2010).
26. I. Nitta, T. Hottinen, O. Himanen, and M. Mikkola, *J. Power Sources*, **171**, 26 (2007).
27. J. Ge, A. Higier, and H. Liu, *J. Power Sources*, **159**, 922 (2006).
28. M. B. Sassin, Y. Garsany, B. D. Gould, and K. Swider-Lyons, *J. Electrochem. Soc.*, **163**, F808 (2016).
29. C. Totzke, G. Gaiselmann, M. Osenberg, J. Bohner, T. Arlt, H. Markotter, A. Hilger, F. Wieder, A. Kupsch, B. R. Muller, M. P. Hentschel, J. Banhart, V. Schmidt, W. Lehnert, and I. Manke, *J. Power Sources*, **253**, 123 (2014).
30. N. Khajeh-Hosseini-Dalasm, T. Sasabe, T. Tokumasu, and U. Pasaogullari, *J. Power Sources*, **266**, 213 (2014).
31. H. Butsch, C. Roth, D. Ritzinger, G. Hoogers, and A. Bock, *J. Electrochem. Soc.*, **159**, B709 (2012).
32. T. A. Greszler, D. Caulk, and P. Sinha, *J. Electrochem. Soc.*, **159**, F831 (2012).
33. J. P. Owejan, T. A. Trabold, and M. M. Mench, *Int. J. Heat Mass Transfer*, **71**, 585 (2014).
34. Y. Fukuyama, T. Shiomi, T. Kotaka, and Y. Tabuchi, *Electrochim. Acta*, **117**, 367 (2014).
35. Z. Lu, J. Waldecker, M. Tam, and M. Cimenti, *ECS Transactions*, **69**, 1341 (2015).
36. J. P. Owejan, J. E. Owejan, and W. B. Gu, *J. Electrochem. Soc.*, **160**, F824 (2013).
37. A. Kongkanand and M. F. Mathias, *The Journal of Physical Chemistry Letters*, **7**, 1127 (2016).
38. C. Simon, F. Hasché, D. Müller, and H. A. Gasteiger, *ECS Transactions*, **69**, 1293 (2015).
39. *SIGRACET GDL - Gas Diffusion Layer non-woven fabric (booklet)*, SGL CARBON GmbH (2014), downloaded in 01/2015.
40. Y. Ono, T. Mashio, S. Takaichi, A. Ohma, H. Kanesaka, and K. Shinohara, *Ecs Transactions*, **28**, 69 (2010).
41. K. Sakai, K. Sato, T. Mashio, A. Ohma, K. Yamaguchi, and K. Shinohara, *Ecs Transactions*, **25**, 1193 (2009).
42. R. Bird, W. Stewart, and E. Lightfoot, *Transport Phenomena (revised second ed.)*, John Wiley & Sons (2007).
43. J. M. LaManna and S. G. Kandlikar, *Int. J. Hydrogen Energy*, **36**, 5021 (2011).
44. I. Manke, C. Hartnig, M. Grünerbel, W. Lehnert, N. Kardjilov, A. Haibel, A. Hilger, J. Banhart, and H. Riesemeier, *Appl. Phys. Lett.*, **90**, 174105 (2007).
45. T. Sasabe, S. Tsushima, S. Hirai, K. Minami, and K. Yada, *ECS Transactions*, **25**, 513 (2009).
46. I. Manke, C. Hartnig, N. Kardjilov, H. Riesemeier, J. Goebbels, R. Kuhn, P. Krüger, and J. Banhart, *Fuel Cells*, **10**, 26 (2010).
47. I. V. Zenyuk, D. Y. Parkinson, G. Hwang, and A. Z. Weber, *Electrochem. Commun.*, **53**, 24 (2015).
48. J. T. Gostick, M. A. Ioannidis, M. W. Fowler, and M. D. Pritzker, *Electrochem. Commun.*, **11**, 576 (2009).
49. Z. Lu, M. M. Daino, C. Rath, and S. G. Kandlikar, *Int. J. Hydrogen Energy*, **35**, 4222 (2010).
50. T. R. Rettich, R. Battino, and E. Wilhelm, *J. Chem. Thermodyn.*, **32**, 1145 (2000).
51. R. T. Ferrell and D. M. Himmelblau, *J. Chem. Eng. Data*, **12**, 111 (1967).
52. C. Hartnig, I. Manke, R. Kuhn, S. Kleinau, J. Goebbels, and J. Banhart, *J. Power Sources*, **188**, 468 (2009).
53. Y. Aoyama, K. Suzuki, Y. Tabe, T. Chikahisa, and T. Tanuma, *J. Electrochem. Soc.*, **163**, F359 (2016).

4.2. Impact of Microporous Layer Pore Properties on Liquid Water Transport in PEM Fuel Cells: Carbon Black Type and Perforation

The article entitled "Impact of Microporous Layer Pore Properties on Liquid Water Transport in PEM Fuel Cells: Carbon Black Type and Perforation" was submitted in September 2017 and accepted for publication in the peer-reviewed Journal of the Electrochemical Society in December 2017 as an open access article, distributed under the terms of the Creative Commons Attribution 4.0 License (CC BY-NC-ND). The paper was presented by Christoph Simon at the Gordon Research Seminar and Conference (August 2016) in Easton, MA, USA. The permanent web link to the article is http://dx.doi.org/10.1149/2.1321714jes.

In this publication, we investigate how MPL pore properties impact the oxygen transport resistance and the overall fuel cell performance. In the experimental section, we present our procedure to prepare MPLs with different types of carbon black. Furthermore, we manufacture MPLs with perforations by introducing thermally decomposable polymer beads with a diameter of $\sim 30\,\mu\,\mathrm{m}$.

In the first part of the study, we characterize and test MPLs with two carbon blacks and benchmark them against a commercial MPL (all based on the same GDL-substrate) and the substrate without MPL. Mercury porosimetry data shows that the pore size distribution can be significantly influenced by the choice of carbon material. Fuel cell tests show that the different pore size distribution in particular impacts the performance at humid operating conditions, with the MPL with larger pores exhibiting lower oxygen transport resistances and higher cell voltages at the same high frequency resistance. We argue that larger hydrophobic pores have a lower capillary pressure and hence, that liquid water is removed more easily without blocking the oxygen transport pathways.

In the second part, MPLs with perforations were analyzed based on the same two different carbon blacks as before. SEM analysis shows that the MPLs consist of large cracks and pores in the range of several µm. At dry operating conditions, these materials do not show any benefits, but significant performance enhancements are observed at humid operating conditions. Based on the oxygen transport resistances at dry and humid conditions, we propose a water and oxygen transport mechanism with

the liquid water beeing removed via the large cracks and perforations, while oxygen is diffusing through the pores of the carbon black base structure.

Finally, we test our best-performing materials with and without perforation against a commercial MPL at operating conditions potentially relevant for high-pressure automotive fuel cell systems (cell temperature of 80 °C, gas pressures of 300 kPa, and 100% RH) with two different oxygen concentrations, simulating the inlet and outlet of the fuel cell stack. Here, our so called "Li400 perforated MPL" exhibits a 45% current density increase compared to the commercial MPL.

Author contributions

C.S., D.K., and D.M. conducted the experimental work and analyzed the data (preparation of microporous layers, fuel cell measurements, nitrogen sorption measurements, particle size distribution and SEM analysis). F.W. contributed the pore size analysis. C.S. wrote and H.G. revised the manuscript. All authors discussed the data, commented on the results and reviewed the manuscript.

Impact of Microporous Layer Pore Properties on Liquid Water Transport in PEM Fuel Cells: Carbon Black Type and Perforation

Christoph Simon,[a,*,z] Dena Kartouzian,[a,b] David Müller,[a] Florian Wilhelm,[b] and Hubert A. Gasteiger[a,]**

[a]*Chair of Technical Electrochemistry, Department of Chemistry and Catalysis Research Center, Technical University of Munich, D-85748 Garching, Germany*
[b]*Centre for Solar Energy and Hydrogen Research Baden-Wuerttemberg, Division 3, Electrochemical Energy Storage and Conversion, D-89081 Ulm, Germany*

The oxygen and water transport through various microporous layers (MPLs) is investigated by fuel cell tests in a 5 cm^2 active area cell under differential-flow conditions, analyzing polarization curves, the associated high-frequency resistance, and the oxygen transport resistance extracted from limiting current density measurements. In this study, MPLs with two different carbon blacks are prepared and compared to a commercial material, all coated on the same GDL-substrate (Freudenberg); furthermore, perforated MPLs with large pores produced by a thermally decomposable polymeric pore former with a particle diameter of ≈30 μm are examined. The materials are characterized by mercury porosimetry, nitrogen adsorption and scanning electron microscopy. While at dry conditions (T_{cell} = 80°C, RH = 70%, p_{abs} = 170 kPa) the performance of all materials is similar, at conditions of high water saturation (T_{cell} = 50°C, RH = 120%, p_{abs} = 300 kPa), MPLs with larger pores or perforations exhibit a performance improvement due to a ≈30% reduction in oxygen transport resistance. The results indicate that liquid water is transported exclusively through these large pores, while the oxygen transport occurs in the small pores defined by the carbon black structure.
 [DOI: 10.1149/2.1321714jes]

Manuscript submitted September 21, 2017; revised manuscript received December 6, 2017. Published December 23, 2017.

The gas diffusion layer (GDL) is a crucial component in polymer electrolyte fuel cells (PEMFC), which has to fulfil the following functions: diffusion of reactant gases from the flow fields to the catalyst layers, transport of product water in the opposite direction, conduction of electrons and reaction heat, and mechanical support of the MEA across the heterogeneous contact area between the flow field channels and lands (particularly critical under differential gas pressures between anode and cathode).[1] The GDL conventionally consists of a gas diffusion layer substrate (furtheron referred to as GDL-substrate or GDL-S) coated with a microporous layer (MPL). The GDL-substrate may be a carbon fiber paper, a non-woven carbon fiber material, or a woven carbon fiber material, usually hydrophobized by 5 wt% to 30 wt% PTFE.[1] The microporous layer is known to improve the water management at humid conditions, but also provides protection for the membrane from substrate fibers.[1–3] It consists of carbon or graphite particles and between 10 wt% and 40 wt% hydrophobic binder, characterized by pore sizes of less than 500 nm compared to the substrate pores of more than 10 μm.[1,3–5] Measurements have shown that the GDL-substrate is flooded immediately at conditions of high humidity in the absence of an MPL, initiated by water accumulation in the large pores between the fibers at the interface between the cathode electrode and the GDL-substrate, which in turn effectively blocks the diffusion of oxygen to the cathode electrode.[2,6,7] A microporous layer with its small hydrophobic pores prevents water accumulation at this critical interface between the GDL-substrate and the electrode, and also reduces the water saturation level in the GDL-substrate.[8,9]

The small pores in MPLs with a hydrophobic PTFE binder result in a high capillary pressure, which is the reason why liquid water is transported preferably via an eruptive release through cracks and larger pores.[6,10] These are either random defects in the microporous layer[11,12] or purposely designed defects.[13–18] There exist several X-ray imaging studies, which describe the liquid water transport through perforations and cracks.[14,19–21] Fuel cell tests of these types of materials have shown that specifically engineered large pores in the MPL/GDL-S can enhance the overall fuel cell performance, increase the limiting current density and accordingly reduce the oxygen transport resistance.[16,18,22]

This can be understood by considering the capillary pressure (p_c) for a hydrophobic pore as defined by the Washburn equation:[23]

$$p_c = p_L - p_V = \frac{4 \cdot \gamma_{H_2O} \cdot \cos\theta}{d_{pore}} \quad [1]$$

where γ_{H_2O} is the surface tension of water, θ is the inner contact angle of water with the pore surface, d_{pore} is the pore diameter, and p_c is the capillary pressure describing the difference between the liquid pressure (p_L) and the corresponding vapor phase pressure (p_V). The capillary pressure has to be overcome in order to fill the pore with liquid water. Since larger hydrophobic pores have a lower capillary pressure than smaller hydrophobic pores, liquid water transport should proceed predominantly through the largest pores of the MPL (under the assumption that θ is constant and >90° for all pores), thereby defining the break-through pressure through the MPL.

One method to characterize the oxygen transport in the GDL-substrate and the MPL is the measurement of the limiting current density (i_{lim}) in a differentially operated fuel cell.[24–28] By variation of the oxygen concentration in the cathode feed gas, it is possible to measure the total oxygen transport resistance (R_{T,O_2}) at small and large current densities. This approach allows to characterize the oxygen transport at different operating conditions in the presence and absence of liquid water as well as the gradual saturation of the GDL.[25,26,28] Here, R_{T,O_2} is described by the sum of sequential oxygen transport resistances in the flow channels (R_{FF,O_2}), in the GDL-substrate ($R_{GDL\text{-}S,O_2}$), in the MPL (R_{MPL,O_2}), in the cathode electrode ($R_{cathode,O_2}$), as well as by transport resistances from other sources (R_{other,O_2}):[24]

$$R_{T,O_2} = R_{FF,O_2} + R_{GDL-S,O_2} + R_{MPL,O_2} + R_{cathode,O_2} + R_{other,O_2} \quad [2]$$

The total oxygen transport resistance R_{T,O_2} under differential-flow conditions (i.e., constant temperature, cell pressure, partial pressure, and relative humidity from cell inlet to outlet) is calculated at each dry oxygen content in the O_2/inert gas mixture ($x_{O_2,dry}$) by Eq. 3 based on Fick's law and Faraday's law:[26]

$$R_{T,O_2} = \frac{4 \cdot F \cdot x_{O_2,dry}}{i_{lim}} \cdot \frac{p_{abs} - p_{H_2O}}{R \cdot T_{cell}} \quad [3]$$

where T_{cell} is the cell temperature, p_{abs} is the total inlet pressure, p_{H_2O} is the vapor pressure of water at the cell temperature, F is the Faraday constant, and R is the universal gas constant. By varying the cell

*Electrochemical Society Student Member.
**Electrochemical Society Fellow.
zE-mail: christoph.simon@tum.de

Table I. MPL ink compositions and properties.

	Ink composition							MPL properties	
MPL	Carbon [g]	Triton X-100[1] [g]	Methyl cellulose [g]	DI Water [g]	PTFE[2] [ml]	PMMA [g]	Ink solids content[3] [wt%]	PTFE content[4] [wt%]	PMMA volume fraction[5] [vol%]
Li100	6.40	0.176	0.77	34.00	1.83	0	18	20	0
Li100 perforated	6.40	0.176	0.77	34.00	1.83	6.34	16	20	20
Li400	6.40	0.176	0.77	34.00	1.83	0	18	20	0
Li400 perforated	6.40	0.176	0.77	34.00	1.83	4.53	16	20	20

[1]For accurate admixing, an aqueous solution with 0.2 $ml_{Triton\ X\text{-}100}/g$ was used.
[2]Added volume of a 58 wt% TF 5035GZ dispersion from 3 M Dyneon.
[3]Content of carbon and PTFE in the ink, defined as $m_{carbon\ +\ PTFE}/m_{ink}$.
[4]PTFE content in the MPL, assuming that only carbon and PTFE remain in the MPL after heat-treatment, and defined as $m_{PTFE}/m_{carbon\ +\ PTFE}$.
[5]Estimated PMMA volume fraction in the final MPL calculated with Equation 5 and data from Table I and Table II).

pressure, the inert gas type (N_2/He), and the MPL and GDL-substrate thicknesses, these resistances can be separated and furthermore divided into the relative contributions from Knudsen and molecular diffusion processes.[24,27] Limiting current density measurement, for example, have demonstrated that a GDL-substrate with a laser perforated MPL can indeed decrease the oxygen transport resistance at humid conditions.[18] The molecular diffusion contribution for each of the above transport resistances is generally described by the effective diffusion coefficient (D_{eff}) through a porous layer, which is defined by the tortuosity factor (τ) and the porosity (ε):

$$D_{eff} = D \cdot \frac{\tau}{\epsilon} \qquad [4]$$

where D is the molecular bulk diffusion coefficient. A commonly used estimate for τ is provided by the Bruggeman model for the diffusion around randomly distributed spheres, yielding a value of $\tau = \varepsilon^{-0.5}$.[29,30] However, it has to be considered that diffusive transport in real electrochemical systems can deviate substantially from the Bruggeman prediction.[31]

The target of this study is to give novel insights into oxygen and water transport mechanisms through the MPL and to show how perforations of the MPL affect its transport properties, particularly at humid conditions. For that, we prepare MPLs with two different types of carbon black coated on a commercial GDL-substrate, further modifying the MPLs with pore-forming polymer micro-beads to produce well defined perforated MPLs. With this novel approach, we are able to engineer more defined pores compared to studies, in which salt or sucrose are used as pore-forming agent creating less defined structures.[22,32] As carbon materials, acetylene blacks are utilized, which have shown superior performance over alternative carbon materials (e.g. graphite, Vulcan XC-72).[33–37] Besides a material with typical specific surface area of 68 $m^2\ g^{-1}$, we additionally investigate an acetylene black with a low specific surface area of 39 $m^2\ g^{-1}$, which to our knowledge has not been investigated for MPL application so far. All materials are characterized by scanning electron microscopy (SEM), nitrogen adsorption (BET), mercury porosimetry, and thermogravimetric analysis. The prepared MPL/GDL-S materials are tested in a 5 cm^2 single-cell fuel cell at various conditions (temperature, relative humidity (*RH*), and pressure) with over-stoichiometric gas flow rates (i.e., under differential-flow conditions). This method allows the extraction of differential-flow polarization curves, the associated high frequency resistances (measured by AC impedance spectroscopy), and the total oxygen transport resistances, which are reported altogether for the first time for a variety of MPL materials. Our results show how the perforation of MPLs affects the oxygen transport at dry and humid conditions, and also prove that perforations in the MPL create exclusive liquid water transport pathways. Finally, we demonstrate the superior performance of our novel MPLs under fuel cell operation conditions which are considered for future fuel cell system architectures.

Experimental

MPL/GDL-substrate materials.—Two acetylene blacks Denka black Li100 (Denka; specification: spec. surface area = 68 $m^2\ g^{-1}$, average particle size = 35 nm) and Li400 (Denka; specification: spec. surface area = 39 $m^2\ g^{-1}$, average particle size = 48 nm) are used as framework components for the MPLs (furtheron referred to as "Li100" and "Li400" MPLs). As hydrophobic agent and binder, 58 wt% PTFE dispersion (TF 5035GZ from 3 M Dyneon) with an average particle size of 200 nm is added in order to achieve 20 wt% of PTFE in the final MPL. As solvent, deionized water (Milli-Q, 18 MΩ cm) is used. To tune the dispersibility and rheological properties of the ink, Triton X-100 (Sigma Aldrich) and methyl cellulose (Sigma-Aldrich) are admixed. For the perforated MPLs (furtheron referred to as "Li100 perforated" and "Li400 perforated" MPLs), monodisperse poly(methyl methacrylate) (PMMA) particles with a denoted average diameter of 30 μm (Soken MX-3000) are utilized as pore former polymer. All resulting inks have a volume of ≈40 ml. The composition for each MPL ink is listed in Table I including the resulting ink and MPL compositions/specifications. Here, the amount of PMMA is adjusted such that a volume fraction of PMMA (ϕ_{PMMA}) and hence, an estimated volume fraction of large pores in the final MPL of 20 vol.% for both perforated MPL types (based on Li100 and Li400) is achieved. ϕ_{PMMA} is defined according to Equation 5, where the volumes of PMMA, carbon and PTFE, calculated from the masses of the components in Table I and their material densities (ρ_{PTFE} = 2.16 g cm^{-3}, ρ_{carbon} = 1.9 g cm^{-3}, and ρ_{PMMA} = 1.19 g cm^{-3}), as well as the porosity of the carbon/PTFE fraction ε_{MPL} are considered. Based on the assumption that the porosities of the carbon black MPLs are the same as the porosities of the carbon/PTFE structure within the perforated MPLs, we use ε_{MPL} of the non-perforated Li100 and Li400 MPLs (determined from MPL weight and thickness measurements, see Equation 7 and Table II).

$$\phi_{PMMA} = \frac{V_{PMMA}}{V_{PMMA} + \frac{V_{carbon}+V_{PTFE}}{1-\epsilon_{MPL}}} = \frac{m_{PMMA}/\rho_{PMMA}}{m_{PMMA}/\rho_{PMMA} + \frac{m_{carbon}/\rho_{carbon}+V_{PTFE}/\rho_{PTFE}}{1-\epsilon_{MPL}}} \qquad [5]$$

As a reference MPL/GDL-substrate material, commercially available GDL with MPL (Freudenberg) is used, which consists of a carbon black based MPL applied to a GDL-substrate, the same substrate which is used for MPL coatings in this study. Hence, when comparing different cathode GDLs, the only difference should be the MPL.

MPL preparation.—Carbon black (Li100 or Li400 type carbons), DI water, Triton X-100 and methyl cellulose are added at the specified amount (see Table I) into a 100 ml polypropylene cup. The cup is fixed into a cooling holder maintained at ≈0°C (Thinky 250AD-COOL) and mixing is conducted in an ARV-310 planetary mixer (Thinky) for 2 min at 2000 rpm and ambient pressure. Subsequently,

Table II. Carbon black powder and freestanding MPL properties. The maximum pore size is based on the d*V*/dlog*d* plot in Figure 4. The MPL porosity ε_{MPL} is derived from two different methods.

MPL	BET area (powder) [$m^2\ g^{-1}$]	BET area (MPL) [$m^2\ g^{-1}$]	MPL porosity[1] (weight/thickness) [%]	MPL porosity (Hg intrusion)[2] [%]	Maximum pore size (Hg intrusion) [nm]
Li100	64.0	35.5	80	79 ± 1	67
Li400	37.4	19.6	73	68 ± 1	328

[1]Calculated with Eq. 7.
[2]Calculated with Eq. 9 from data in Figure 4.

the specified amount of PTFE dispersion (see Table I) is added and the ink is mixed for another 18 min at the same conditions. For inks for the perforated MPLs (Li100 perforated, Li400 perforated), PMMA particles are added at this point and intermixed for 2 min at 2000 rpm. Last, the ink is degassed under vacuum (30 kPa_{abs}) for 2 min at 2000 rpm in order to remove air bubbles.

The ink is coated onto GDL-substrate (Freudenberg; hydrophobically treated, ≈154 ± 10 μm thick) using a doctor blade and a stainless steel stencil with a 3.5 cm × 3.5 cm square opening and a thickness of 100 μm (for Li100 and Li400) or 75 μm (for Li100 perforated and Li400 perforated), which corresponds to a targeted MPL thickness of ≈30 μm. For freestanding MPLs used for BET analysis and mercury porosimetry, MPL inks are coated onto a smooth glass plate instead of a GDL-substrate. The coatings on the GDL-substrate or on the glass plate are immediately dried at 80°C for 30 min. Afterwards the freestanding MPLs are non-destructively removed from the glass plate by a razor blade.

In a final step the MPL/GDL-S and the freestanding MPLs are heat treated in an atmospheric oven under air in order to decompose all additive components (Triton X-100, methyl cellulose, PMMA) and to sinter the PTFE particles. The temperature is increased according to the following procedure (also see Figure 1): 10°C min^{-1} from room temperature to 200°C, 2.5°C min^{-1} from 200°C to 250°C, hold for 10 min at 250°C, 10°C min^{-1} from 250°C to 330°C, 2.5°C min^{-1} from 330°C to 380°C, hold for 30 min at 380°C, and finally cooled down to room temperature over the course of ≈2 hours.

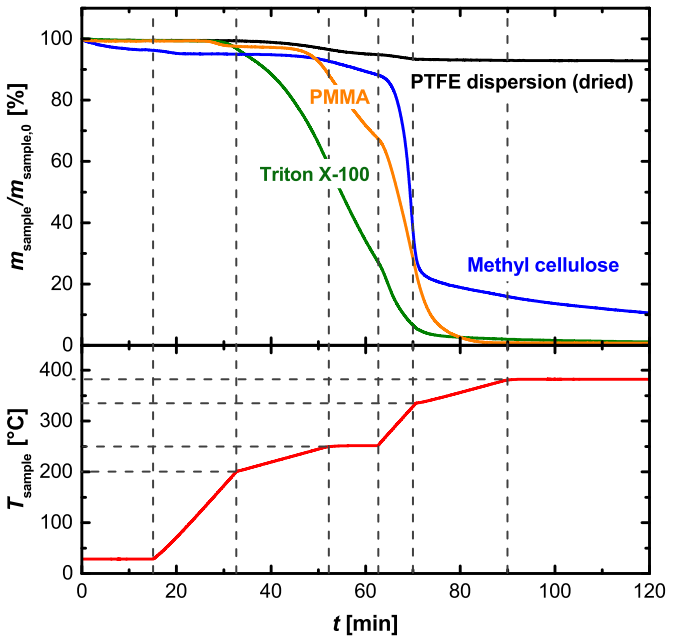

Figure 1. Thermogravimetric analysis under synthetic air (20% O_2 in N_2) of dried PTFE dispersion (black line), Triton X-100 (green line), methyl cellulose (blue line), and 30 μm PMMA particles (orange line). Normalized sample weight $m_{sample}/m_{sample,0}$ and sample temperature T_{sample} (red line) are plotted as function of time *t*, whereby the temperature/time profile is identical to the heat-treatment procedure used for the preparation of GDLs and of freestanding MPLs (see Experimental).

The final thickness of the MPL is determined with a dial gauge (Mitutoyo series 543; ±3 μm accuracy) by taking the thickness of the GDLs (i.e., MPL/GDL-substrate) at five positions and subtracting the thickness of the GDL-substrate, which is measured at 8 positions around the coated area. MPLs considered for fuel cell testing have a thickness of $d_{MPL} = 30 \pm 5$ μm.

$$d_{MPL} = d_{MPL/GDL-S} - d_{GDL-S} \quad [6]$$

Thermogravimetric analysis.—In order to evaluate the stability of all components during the applied MPL heat-treatment procedure, thermogravimetric analysis is performed with a TGA/DSC 1 (Mettler Toledo) on dried PTFE dispersion, methyl cellulose, Triton X-100, and PMMA particles. The applied temperature ramp is the same as for the above described MPL heat-treatment procedure (see also Figure 1). In order to simulate atmospheric conditions, the experiment is performed in 20% O_2 in N_2.

MPL porosity determination by thickness and weight.—For porosity measurements of the Li100 and Li400 MPLs, freestanding MPL samples are utilized. The MPL samples are weighed (m_{MPL}) and their thickness (d_{MPL}) is measured by a dial gauge (Mitutoyo series 543; ±3 μm accuracy) at five positions. The MPL porosity (ε_{MPL}) is determined under consideration of the material densities of PTFE ($\rho_{PTFE} = 2.16$ g cm^{-3}) and carbon black ($\rho_{carbon} = 1.9$ g cm^{-3}; manufacturer's information) and calculated MPL composition:

$$\epsilon_{MPL} = 1 - \frac{V_{solids}}{V_{MPL}} = 1 - \frac{m_{MPL} \cdot \left(\frac{w_{carbon}}{\rho_{carbon}} + \frac{w_{PTFE}}{\rho_{PTFE}}\right)}{d_{MPL} \cdot A} \quad [7]$$

where V_{solids} is the true volume of all solids in the MPL (carbon black and PTFE), V_{MPL} is bulk volume of the MPL, m_{MPL} is the mass of the MPL, d_{MPL} is the MPL thickness, *A* is the coating area of 3.5 cm × 3.5 cm, and w_{carbon} and w_{PTFE} are the mass fractions in the MPL for carbon (= 0.8) and PTFE (= 0.2). The results are shown in Table II.

Mercury intrusion porosimetry.—Mercury intrusion porosimetry measurements are carried out employing two porosimeters (Pascal 140 and Pascal 440; CE Elantech, Inc. USA). GDL samples (2 samples from one batch; m_{sample} = 210 mg–270 mg) and freestanding MPL samples (4 samples from two different batches; m_{sample} = 100 mg–220 mg) are inserted in a dilatometer (sample holder). The Pascal 140 instrument is used to measure the macropore distribution by mercury intrusion at pressures ranging from vacuum to 400 kPa. On the other hand, the Pascal 440 instrument is used to measure the micropore distribution, whereby the pressure is increased in 6–19 MPa steps up to the maximum of 375 MPa while the volume increase of the mercury in the dilatometer is measured. Afterwards the pressure is decreased to vacuum in 8–35 MPa steps and the volume decrease of the mercury in the dilatometer is measured. The pore diameter (d_{pore}) is calculated using Washburn's equation

$$d_{pore} = -\frac{4 \cdot \gamma_{Hg} \cos(\theta)}{p} \quad [8]$$

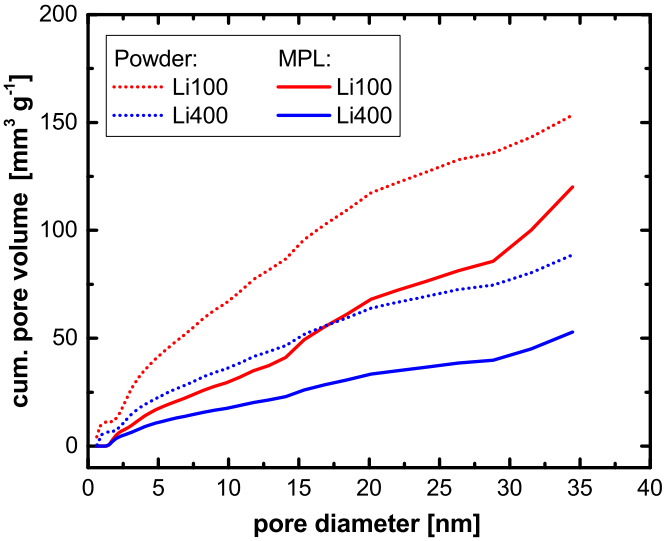

Figure 2. Cumulative pore volume as function of pore diameter measured by nitrogen sorption for Li100 and Li400 carbon powders (red/blue solid lines) and for the correspondent freestanding MPLs (red/blue dotted lines), evaluated using the QSDFT slit pore model. For better comparison of powder (carbon) and MPL (carbon and PTFE), all cum. pore volumes are normalized to the carbon weight.

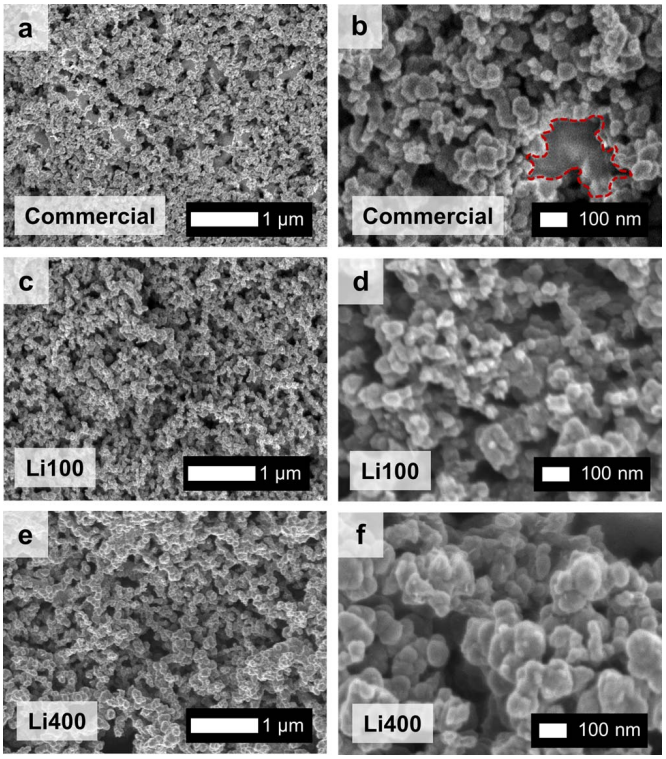

Figure 3. Scanning electron microscopy top-view images of the commercial MPL (Freudenberg) (a,b) and MPLs based on Li100 (c,d) and Li400 (e,f) carbons. Magnifications are x25,000 (a,c,e) and x100,000 (b,d,f). The red dotted marking (b) shows what we believe to be a region in which PTFE is accumulated.

where γ_{Hg} is the surface tension of mercury (0.48 N m^{-1}), θ is the inner contact angle of mercury with the pore surface (140°), and p is the mercury penetration pressure.

To exclude measurement artefacts from additional interfacial pore volume between the single sample sheets, all cumulative pore volumes are zeroed for pore diameters >10 µm for freestanding MPLs. The porosity of the MPL (ε_{MPL}) is then calculated from the data at maximum mercury saturation (i.e. at the maximum capillary pressure of 375 MPa) under consideration of the corrected total cumulative pore volume normalized to the sample mass v_{pore} (in units of mm^3_{pore}/g_{sample}) and the bulk MPL volume v_{MPL} (in units of mm^3_{MPL}/g_{sample}).

$$\epsilon_{MPL} = \frac{v_{pore}}{v_{MPL}} = \frac{v_{pore}}{v_{pore} + \frac{w_{carbon}}{\rho_{carbon}} + \frac{w_{PTFE}}{\rho_{PTFE}}} \quad [9]$$

Gas sorption analysis.—Pore size analysis and surface area measurements are performed on a gas sorption analyzer (Autosorb-iQ, Quantachrome, USA) using nitrogen as adsorbent at 77 K. Samples of the pure carbon powders Li100 and Li400 as well as of the standalone MPLs are outgassed at 250°C for 6 h under vacuum. The sample weights were chosen in order to achieve minimum absolute surface areas of >10 m^2 inside the sample vessel to attain sufficient accuracy. Adsorption and desorption isotherms with 79 points are recorded in the relative pressure range of $0.005 \leq (p/p_0) \leq 0.995$ and used to calculate surface areas with the BET method. In order to achieve comparability between powder and MPL samples, BET areas are normalized to the carbon weight (i.e., excluding PTFE weight in the case of MPLs) and are shown in Table II. Furthermore, mesoporous pore size distributions were determined using a quenched solid density functional theory (QSDFT) slit pore model (see Figure 2).[38,39]

PMMA particle size analysis.—One tip of a spatula of PMMA particles with a denoted average diameter of 30 µm (Soken MX-3000) is dispersed in water by sonication and filled together with a magnetic stirrer into the fraction cell of a laser scattering particle size analyzer (Retsch Technology, HORIBA LA-960). The measurement was evaluated with a real part refractive index of 1.49 for PMMA in water (provided in HORBIBA Control and Data Treatment Software). The resulting particle size distribution is illustrated in Figure 6.

Scanning electron microscopy.—Top-view and cross-sectional images of GDLs with and without MPL are recorded with two different scanning electron microscopes (SEM). Top view images of MPLs w/o perforation (Li100, Li400, and the commercial MPL (Freudenberg)) are recorded in a FESEM 7500F field emission SEM (JEOL) at magnifications of x25,000 and x100,000. Secondary electron imaging is applied at an acceleration voltage between 0.8 and 1.0 kV. The images are shown in Figure 3.

All investigated GDLs are also examined in top and cross-sectional view with a JCM-6000 benchtop SEM (JCM-6000Plus, JEOL) at a magnification of x500. Cross-sectional samples are prepared by cutting the materials with a razor blade in order to create a clean cutting edge; subsequently, the materials are fixed in a cross-section sample holder together with the top-view sample. Images are taken at 5 kV acceleration voltage by a secondary electron detector and are shown in Figure 7.

Fuel cell test setup.—Fuel cell tests are realized in a 5 cm^2 active area single cell hardware (Fuel Cell Technologies) with individually designed graphite flow fields (Poco Graphite), which comprise mirror-symmetrical flow patterns for anode and cathode. The flow fields consist of 7 parallel channels with a channel and land width of 0.5 mm and a channel depth of 0.8 mm, which are arranged in one serpentine. Details are shown in Reference 40. In all experiments, a commercial anode GDL is used (Freudenberg, GDL-substrate with MPL), while the cathode GDL consists of a GDL-substrate (Freudenberg) either without or with an MPL (either a commercial MPL (Freudenberg) or MPLs developed in this study and referred to as Li100, Li400, Li100 perforated, and Li400 perforated). A Primea Mesga catalyst coated membrane (CCM, W. L. Gore & Associates A510.1/M715.18/C580.4 equipped with a sub-gasket) with catalyst loadings of 0.4 mg_{Pt} cm^{-2} on the cathode and 0.1 mg_{Pt} cm^{-2} on the anode is utilized as membrane electrode assembly (MEA). The square active electrode area is 5.0 cm^2, while the GDL cuttings are 5.8 cm^2 (i.e., when perfectly aligned, the GDL will extend 0.9 mm beyond the active area) in order

to assure that the GDL will always cover the active area within the errors of alignment.

A strain-controlled GDL compression of ∼20% of its initial thickness is targeted in the single cell setup for a sufficient contact pressure between the layers. To realize this, PTFE coated glass fabrics (FIBERFLON GmbH & Co. KG) in the properly selected thickness are placed on the anode and cathode side as gaskets to achieve the desired compression. The initial thicknesses of the GDLs are measured at five positions and of the gaskets at eight positions by a Mitutoyo dial gauge series 543 (±3 μm accuracy, flat cylindrical tip) and the average is taken, respectively. The thicknesses of CCM and CCM gasket are measured by a SEM cross section. A detailed description of the compression calculation can be found in Reference 41.

Last, the CCM is sandwiched between the two GDLs and the flow fields. The cell endplates are tightened by eight bolts with a torque of 12 Nm in order to seal the cell. The cell is connected to a custom-designed Greenlight Innovation G60 fuel cell test station equipped with a 120 A load module (Agilent N3306A) and a potentiostat (Gamry Reference 3000).

Fuel cell test procedure.—Prior to fuel cell testing, each cell is conditioned by stepping the voltage under hydrogen (constant flows of 1390 nccm) and air (constant flow of 3320 nccm) at $T_{cell} = 80°C$, $p_{abs} = 150$ kPa, and full humidification in the following sequence: 0.6 V for 45 min, 0.95 V for 10 min, and 0.85 V for 5 min, which is repeated for ten times. Within an extensive test protocol, the following measurements are accomplished and presented in this paper. All mentioned pressures (p_{abs}) are referring to the inlet pressure in the cell, while the pressure drop is <30 kPa during all measurements (depending on operating conditions).

Potentiostatically controlled polarization curves are recorded by stepping the voltage from 0.9 V to 0.3 V (or in some cases 0.05 V) in steps of 50 mV before measuring the open circuit voltage (OCV). Each voltage is held for 10 min in controlled steady state and a 30 s average data point is recorded. After each recorded data point, an impedance spectrum is recorded from 100 kHz to 10 Hz with a perturbation voltage of 10 mV in the low noise setup of the hybrid impedance mode; the high frequency resistance (*HFR*) is determined from the high-frequency intercept of the real axis in the Nyquist representation (imaginary part vs. real part of impedance). The current-voltage curves are recorded with high constant flow rates of 2000 nccm of hydrogen and 5000 nccm of air for achieving differential flow (corresponding to H_2 and oxygen stoichiometries of s_{H_2} and s_{O_2} ≥10 at all conditions) at the following operating conditions: (i) $T_{cell} = 80°C$, $p_{abs} = 170$ kPa, $RH = 70\%$ (referred to as "dry" conditions); (ii) $T_{cell} = 80°C$, $p_{abs} = 170$ kPa, $RH = 100\%$ (referred to as "standard" conditions); (iii) $T_{cell} = 50°C$, $p_{abs} = 300$ kPa, $RH = 120\%$ ("humid" conditions); and, (iv) $T_{cell} = 80°C$, $p_{abs} = 300$ kPa, $RH = 100\%$ (referred to as "high pressure" conditions). For condition (iv), also a polarization curve in 10% O_2/N_2 is recorded in order to simulate the oxygen concentration at the stack-outlet when operating at an oxygen stoichiometry of ≈1.75 at 100% inlet *RH* (for these measurements, s_{O_2} ≥8 at all conditions).

For the measurement of the limiting current density, flow rates of 2000 nccm H_2 on the anode and 5000 nccm diluted oxygen in nitrogen in 10 different dry mole fraction ($x_{O_2,dry}$) between 0.5% and 28% on the cathode side are set. At each $x_{O_2,dry}$ the current densities corresponding to 0.30 V, 0.15 V, 0.10 V and 0.05 V are recorded by holding for 2 min in steady-state at each voltage and averaging the measured current for 15 s. The measurement conditions were the same as for the polarization curves (i), (ii), (iii), (iv) with an additional measurement at (v) $T_{cell} = 50°C$, $p_{abs} = 400$ kPa, $RH = 77\%$. The total oxygen transport resistance (R_{T,O_2}) is calculated according to Eq. 3. For all limiting current measurements recorded for this study, s_{H_2} and s_{O_2} are always ≥10 and ≥8.

Of each investigated MPL/GDL-S material two samples of the same batch are measured two times in individual cell setups. The average values and standard deviations are calculated and shown in Figure 8 (polarization curves, high frequency resistance, and oxygen transport resistance at conditions (i), (ii), (iii)), Figure 10 (summary of oxygen transport resistance), Figure 9 (oxygen transport resistance at $T_{cell} = 50°C$, $p_{abs} = 400$ kPa, $RH = 77\%$) and Figure 12 (polarization curves, high frequency resistance and oxygen transport resistance at condition (iv)).

Results

Characterization of carbon black MPLs.—In order to evaluate the thermal stability of the various MPL components during the MPL heat-treatment procedure in air, thermogravimetric analysis under air is performed following the same temperature-time profile (see lower panel of Figure 1) with all components of the MPL ink (except the carbon, which is stable under air up to ≈500°C[42]), viz., the PTFE dispersion, the Triton X-100 surfactant, the methyl cellulose thickener, and the PMMA particles used for preparing the perforated MEAs. Figure 1 shows the TGA data and the applied temperature ramp mimicking the heat-treatment procedure during the preparation of GDLs and freestanding MPLs, which is necessary to decompose undesired components in the MPL, such as emulsifiers and thickeners, and to sinter PTFE particles, which improves the overall performance.[33,34]

The dried PTFE dispersion consists of PTFE and emulsifier and is showing a weight loss of 7 wt% over the whole heat-treatment procedure, initiating at a temperature of ≈210°C and completed once the final temperature of 380°C is reached (black line in Figure 1). The observed weight loss can be explained by the loss of the surfactant, which according to the manufacturer amounts to ≈5 wt% in the dried PTFE dispersion. Thus, it can be concluded that the PTFE does not decompose to any significant fraction during the MPL heat-treatment procedure. The Triton X-100 surfactant (green line) starts to decompose after 30 min of the heat-treatment (at ≈160°C) and is completely decomposed without leaving any residue after 90 min, once a temperature of 380°C is reached; thus, the Triton X-100 surfactant added to our MPL ink will be completely removed from the MPL after its heat-treatment. This is different for the methyl cellulose thickener component added to the MPL ink (blue line). After an intial weight loss of 5 wt% after 20 min (at ≈70°C) which can be accounted to the water content in the hygroscopic substance, its rather rapid decomposition starts after 60 min (at ≈255°C), but after the end of the heat-treatment procedure (at 120 min), still 11 wt% of residue is left. Considering the composition of the MPL ink (see Table I) and that carbon and PTFE are essentially unaffected by the heat-treatment, the 11 wt% methyl cellulose residue would contribute only ≈1 wt% to the final weight of the heat treated MPL, a negligible amount which will thus not be considered in our further discussion. Finally, for the preparation of perforated MPLs, assuring the complete thermal decomposition of the PMMA pore former during temperature treatment is essential. This is indeed the case, as can be seen by the complete oxidative removal of the PMMA particles (orange line) once the temperature of 380°C is reached.

To investigate the impact of the two different carbon blacks (Li100 and Li400) on the morphology of the prepared MPLs, nitrogen sorption measurements, porosimetry results and SEM images are compared. The cumulative pore volume from nitrogen sorption measurements as function of the pore diameter for the two carbon blacks as well as for the respective MPLs is shown in Figure 2. Li100 carbon has a higher cumulative pore volume of 153 $mm^3\ g^{-1}$ between 0 nm and 35 nm compared to Li400 carbon with 88 $mm^3\ g^{-1}$. When preparing an MPL from these carbon blacks, the values decrease to 120 $mm^3\ g^{-1}$ and 52 $mm^3\ g^{-1}$, respectively, which corresponds to a pore volume reduction of 22% and 41% in the micro- and mesoporous region. This can be explained by the blocking of micro- and mesopores by the PTFE binder, which is also reflected by a decrease in BET surface area from 64.0 $m^2\ g^{-1}$ to 35.5 $m^2\ g^{-1}$ for Li100 and from 37.4 $m^2\ g^{-1}$ to 19.6 $m^2\ g^{-1}$ for Li400. As will be shown, the here observed lower cumulative pore volume of the Li400 MPL is also reflected in the pore size range between 4 nm and 50 μm by its lower cumulative pore volume in mercury porosimetry measurements (see Figure 5) and in its lower overall porosity (see Table II).

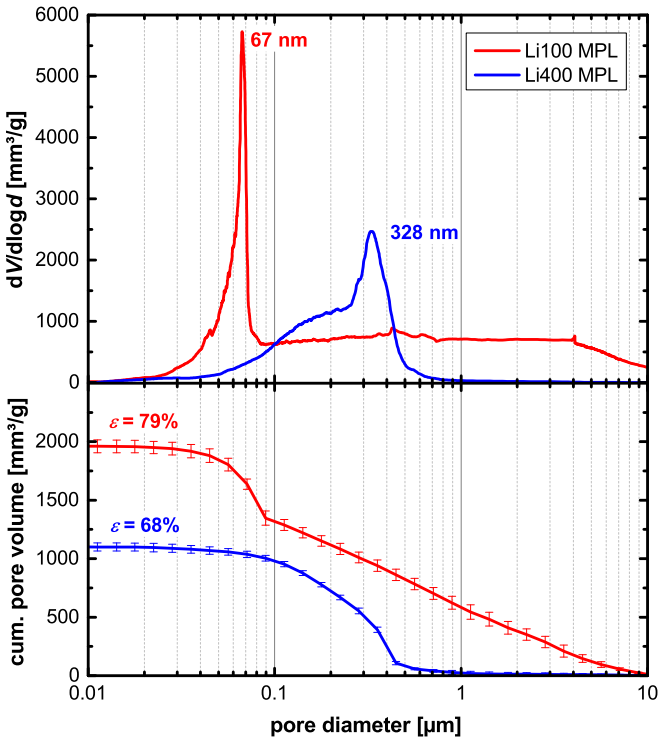

Figure 4. Cumulative pore volume (lower panel) and differential pore volume d*V*/dlog*d* (upper panel) as function of pore diameter for freestanding MPLs based on Li100 (red lines) and Li400 (blue lines) carbon measured by mercury intrusion porosimetry. The lines represent the average and the error bars the standard deviation of 4 measurements for each material.

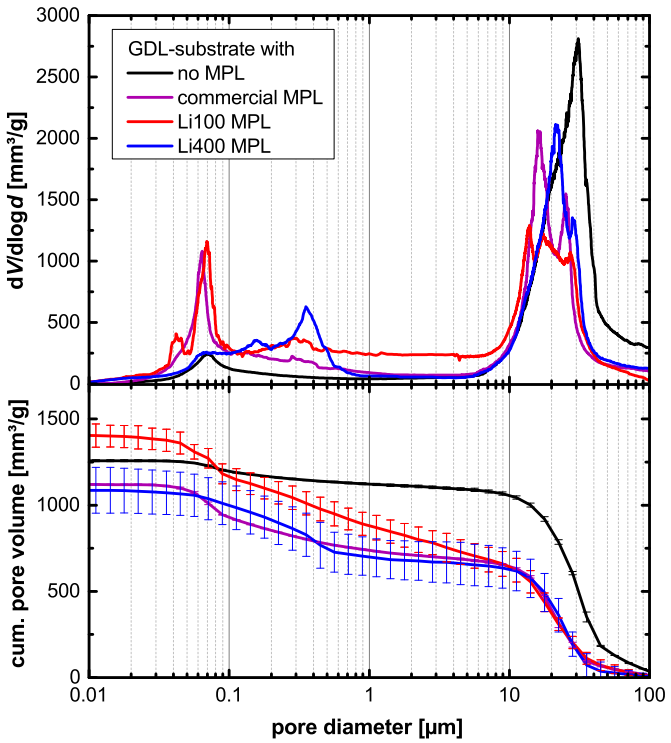

Figure 5. Cumulative pore volume (bottom) and differential pore volume d*V*/dlog*d* (top) as function of pore diameter measured by mercury intrusion porosimetry for Freudenberg GDL-substrate w/o MPL (black lines) and for GDLs based on the same substrate coated with the following MPLs: commercial MPL (Freudenberg; purple lines), Li100 based MPL (red lines) and Li400 based MPL (blue lines). The lines represent the average and the error bars the standard deviation of 2 measurements for each material.

Next, we examine the morphology of the commercial MPL (MPL/GDL-S from Freudenberg) and compare it to our experimental MPLs (Li100 and Li400 MPLs) using SEM. Figure 3 shows SEM top-view images of these MPLs with magnifications of 25,000 and 100,000, where the porous structure of the MPL, the carbon black primary particles, and the agglomerate structure can be discerned. Here it should be noted that the non-conductive PTFE component in the MPL can hardly be distinguished in the images. However, in the case of the commercial MPL (Figures 3a and 3b) we can see agglomerates on the order of ≈100–300 nm in diameter (see red dotted marking in Figure 3b) which are characterized by a uniform surface significantly different from carbon black particles. Hence, they can be attributed to contaminations, residues from additives, or to accumulated, non-dispersed PTFE, which is either available as homogeneous particle or is covering a carbon black agglomerate. In the case of the Li100 and Li400 based MPLs, such spots are not observed. Since the PTFE particles in the dispersion used in this study have a mean particle size of 200 nm, this observation is an indication that the PTFE in our MPLs is dispersed as a thin film or as substantially smaller particles. This would create more homogeneously hydrophobic surfaces throughout and across the whole MPL.

With respect to the primary particle size of the different carbons, the SEM images of the commercial and the Li100 MPL (Figures 3b and 3d) reveal similar primary particle sizes, whereas clearly larger primary particle sizes are observed for the Li400 carbon in the Li400 MPL (Figure 3f). The larger primary particle size of the Li400 carbon compared to the Li100 carbon as observed in these SEM images is consistent with the manufacturer's specifications (48 nm for Li400 and 35 nm for Li100) and also with the ≈1.5-fold lower BET area of the Li400 carbon. A comparison of Figures 3b and 3d with Figure 3f also indicates qualitatively that the average macropore size in the commercial and the Li100 MPL is substantially smaller than that of the Li400 MPL.

A more quantitative description of the macropore size distribution of the Li100 and Li400 based MPLs can be obtained by mercury porosimetry of the freestanding Li100 and Li400 MPLs, which is illustrated in Figure 4. The pore sizes of the Li100 MPL show a very broad distribution between ≈30 nm and ≈10 µm, with a maximum in the d*V*/dlog*d* plot at 67 nm (upper panel, red line). As already indicated in the above SEM analysis, this is much smaller than the pore size distribution maximum of 328 nm observed for the Li400 MPL (blue line). The reason for the substantial pore volume in the >1 µm range of the freestanding Li100 MPL (ca. 29%, see lower panel of Figure 4) is not yet clear, but it is also observed for the Li100 MPL coated on the GDL-substrate (Figure 5) and may be due to some cracks in the layer (see later discussion on SEM cross-sections). The total cumulative pore volumes of the freestanding MPLs (lower panel) significantly differ from each other, with the Li100 MPL exhibiting 1101 ± 36 $mm^3\ g^{-1}$ and the Li400 MPL 1969 ± 56 $mm^3\ g^{-1}$; based on Equation 9, this corresponds to overall MPL porosities (ε_{MPL}) of 79% (Li100 MPL) and of 68% (Li400 MPL), suggesting a higher packing density for the Li400 carbon within the MPL.

The results of the porosity analysis are listed in Table II. The porosities determined by the two different methods (weight and thickness measurements or Hg intrusion on freestanding MPLs) are in quite excellent agreement and clearly show that the packing density of the Li400 carbon in the MPL is higher than that of the Li100 carbon. In summary, the Li400 MPL composed of the carbon with the larger primary particles has a maximum in the pore size distribution which is at a substantially larger diameter (consistent with the visual observations in Figure 3), but exhibits smaller porosity compared to the Li100 MPL.

In order to investigate the interaction between MPL and GDL-substrate and to compare MPL/GDL-substrate samples with the commercial GDL-substrate and the commercial MPL/GDL-substrate, Figure 5 shows the Hg intrusion porosimetry results for the substrate and the respective MPLs including the commercial MPL coated on the same substrate. The GDL-substrate itself (black curve in Figure 5)

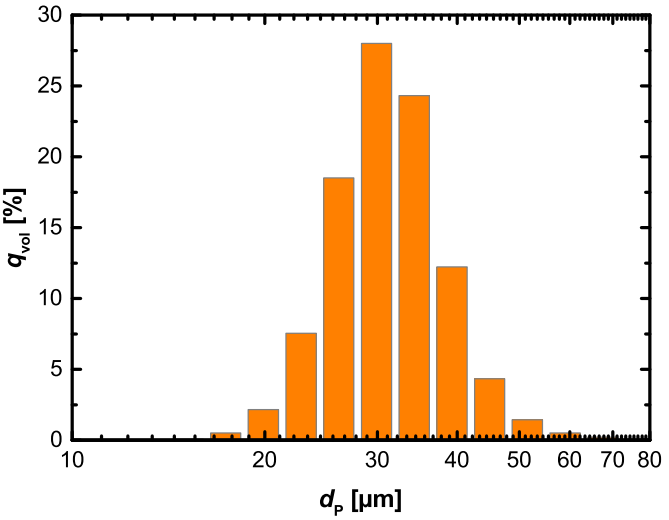

Figure 6. Volumetric particle size distribution of Soken PMMA 30 µm particles measured by laser scattering in aqueous dispersion (note that the particle diameter is plotted on a logarithmic scale).

has a peak maximum at 30.5 µm (upper panel) and ≈89% of the pore volume in the >1 µm range (lower panel). A small peak in the pore size distribution is visible at a pore diameter of ≈70 nm; this, we believe, originates from carbon particles which are a constituent of the GDL-substrate and which are also visible in the SEM images in Figures 7a and 7b. The GDL-substrate pore size distributions (>10 µm) of the GDL-substrate coated with MPLs (magenta, red, and blue lines) all show a slight shift toward smaller pore sizes compared to the virgin substrate, suggesting that large pores close to the substrate surface are partially filled with the MPL ink during coating, therby leading to a reduction of pore volume in the large pore range. The Hg porosimetry data of the GDL-substrate with the different MPLs also allows a comparison of the Li100 and Li400 based MPLs with the commercial reference MPL, showing that the pore size maximum of the commercial MPL (≈64 nm) is essentially identical to that of the Li100 MPL on the GDL-substrate (≈69 nm) and that of the freestanding Li100 MPL (≈67 nm; see Figure 4), with both being substantially smaller than the pore size maximum of the Li400 MPL on the GDL-substrate (≈353 nm) and of the freestanding Li400 MPL (≈328 nm; see Figure 4). In the ≈0.6-6 µm region where there is no contribution from the GDL-substrate, the pore volume of the GDL-substrate supported Li100 MPL is quite substantial, while it is insignificant for the GDL-substrate supported Li400 MPL, essentially identical with the data for the freestanding MPLs (Figure 4). In this same pore size region, the commercial MPL resembles the behavior of the Li400 MPLs, also not exhibiting any significant pore volume. One possible reason for the presence/absence of pore volume in the ≈0.6-6 µm region can be gleaned from the inspection of SEM cross-sectional images and will be discussed later.

Characterization of perforated MPLs.—Perforations in the Li100 and Li400 MPLs are obtained by mixing the MPL ink with PMMA particles serving as pore former, which will be completely decomposed during the MPL heat-treatment (after 90 min at 380°C, see Figure 1). Hence, the final MPL would be expected to contain holes in the size of the PMMA particles. The volumetric particle size distribution of the PMMA powder is shown in Figure 6. In the logarithmic plot an approximate normal distribution is observed with a maximum at 30 µm, which is also the mean particle diameter and in agreement with the product specifications. The chosen particle diameter of 30 µm is identical with the targeted MPL thickness, with the expectation that after the thermal decomposition of the PMMA particles large pores through the entire thickness of the MPL be formed, which would provide pathways for liquid water transport through the whole MPL.

To investigate the MPL/GDL-substrate structures in the µm-range (i.e., in the range of the targeted MPL perforations), Figure 7 is illustrating SEM images at 500x magnification in top-view (MPL side) and cross-sectional view of all prepared and tested GDLs. All considered MPLs are coated on substrate, which is shown in Figures 7a and 7b. The non-woven fabric is 154 ± 4 µm thick and consists of ≈10 µm thick carbon fibers (estimated from SEM images), which are disorderly arranged. At the boundary points between the fibers, an aggregation of material is observed which must originate from the production process of the substrate (remainings of a pyrolized resin binder) and/or from a subsequent hydrophobic treatment including a carbon component in order to prevent water adhesion in the substrate (the latter would explain the observed pore size distribution maximum at ≈70 nm of the GDL-substrate in Figure 5). Figures 7c–7l illustrate the coated MPLs on GDL-substrate in top-view and cross-sectional view (MPL on top, GDL-substrate on the bottom).

The commercial MPL (Figures 7c and 7d) reveals small holes of a few µm in diameter on the surface, which could originate from air bubbles. Other than that, the surface is crack-free, which is also observed in the cross-sectional view. The interface between the MPL and the GDL-substrate is rather sharp, suggesting that minimal penetration of the MPL ink into the GDL-substrate during the coating process. The Li100 (Figures 7e and 7f) and Li400 (Figures 7i and 7j) MPLs also exhibit almost faultless MPL top surfaces, while the cross-sections reveal the presence of cracks which partially penetrate through the MPL (mostly originating at the MPL/GDL-substrate interface). This is particularly pronounced for the Li100 MPL, which might be the origin of its substantial pore volume in the ≈0.6-6 µm range observed by mercury porosimetry (see Figure 5). Contrary to the commercial MPL/GDL-substrate, a distinct intrusion of the MPL ink into the substrate is observed for the Li100 and Li400 samples, clearly discernable by the MPL-surrounded fibers.

The perforated MPLs based on Li100 (Figures 7g and 7h) and Li400 (Figures 7k and 7l) feature several µm wide cracks and holes on the surface and across the thickness of the MPL. Some of the pores invade deeply into the material and penetrate through the entire MPL; however, even though PMMA particles with a mean diameter of 30 µm are utilized, we were not able to see ≈30 µm pores in the SEM images. Nevertheless, as intended by our MPL design strategy, µm large pathways across the MPL have indeed been accomplished, and it remains to be seen whether they will positively affect the transport of liquid water. However, compared to non-perforated MPLs, the pore former clearly creates a very uneven surface (Figures 7g and 7k). Although the PMMA content is supposed to form 20 vol.% of additional perforation pore volume which would result in a porosity of 86% for the perforated Li100 MPL (based on ε_{MPL} = 79% for the Li100 MPL from Table II) and of 77% for the perforated Li400 MPL (based on ε_{MPL} = 68% for the Li400 MPL from Table II), it might be the case that the pore volume is larger than expected due to the formation of additional cracks caused by tension around the PMMA particle during the drying procedure. Unfortunately, based on the available methods it is experimentally not possible to determine the porosity of the perforated MPL, because the perforated MPLs are too brittle and uneven to measure their accurate thickness or to perform mercury porosimetry. As well, the MPLs coated on the GDL-substrate have similar pore sizes as the substrate itself which would make a deconvolution between substrate pores and large MPL pores challenging.

Fuel cell tests.—Results from the fuel cell tests with the different cathode MPLs are shown in Figure 8. Differential-flow polarization curves (top) at dry (a), standard (b) and humid (c) conditions together with the associated *HFR* values (middle) as well as the total oxygen transport resistances R_{T,O_2} (bottom) are shown. The dry conditions (a) at T_{cell} = 80°C, RH = 70% and p_{abs} = 170 kPa represent an operating condition, in which no liquid water is expected to be present, neither in the MPL/GDL-substrate due to the low relative humidity and the high operating temperature, nor in the flow field channels due to high flow rates. On the contrary, the humid conditions (c) at low operating

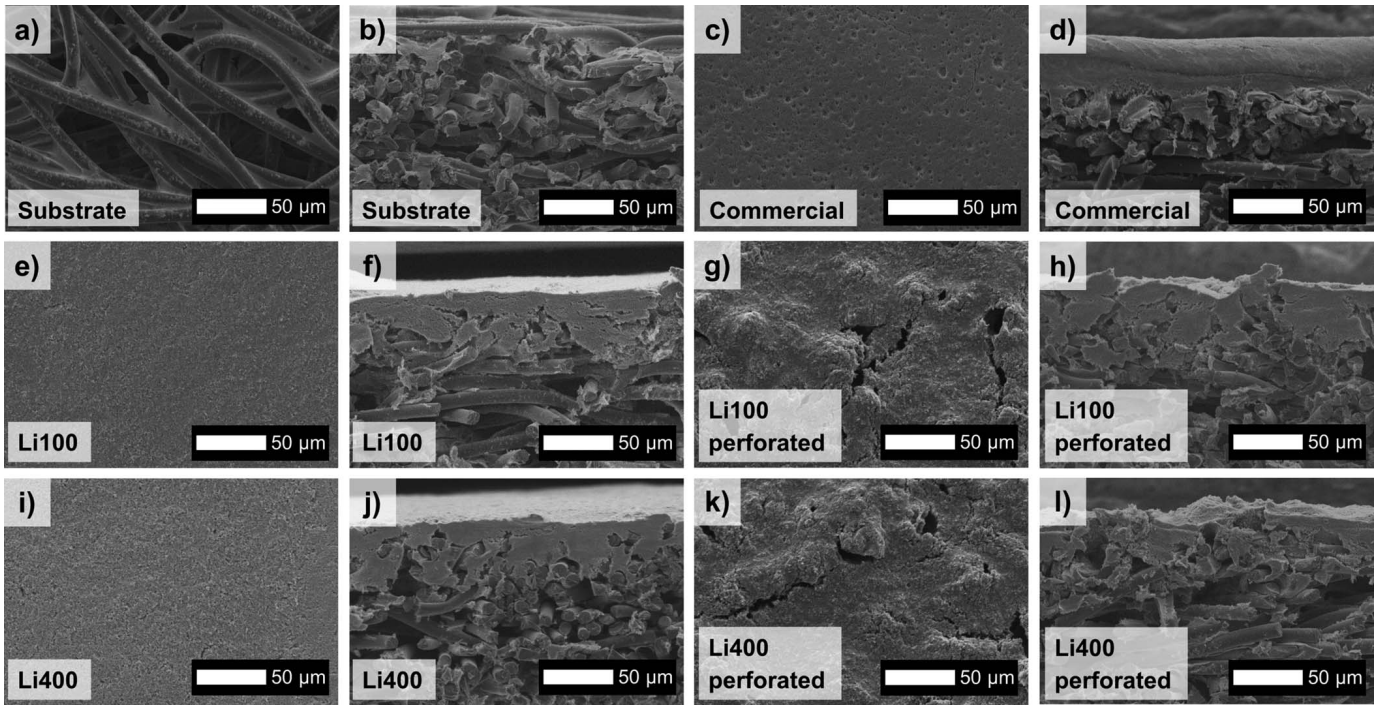

Figure 7. Scanning electron microscopy images for MPLs in top-view (a,c,e,g,i,k) and cross-sectional view (c,d,f,h,j,l) for Freudenberg GDL-substrate w/o MPL (a,b) and the following MPLs coated on the same substrate: commercial MPL (Freudenberg) (c,d), Li100 based MPL (e,f), perforated Li100 based MPL (g,h), Li400 based MPL (i,j), perforated Li400 based MPL (k,l). Magnification for all images is x500.

temperature of $T_{cell} = 50°C$ (small saturation vapor pressure), oversaturated gas fluxes with $RH = 120\%$ (fully saturated gas phase) and a high pressure of $p_{abs} = 300$ kPa (decreased diffusivity of water vapor in the gas phase) facilitate the condensation of liquid water inside the MPL/GDL-substrate. Finally, the standard conditions (b) represent a typical operating state of a PEM fuel cell at $T_{cell} = 80°C$, $RH = 100\%$, $p_{abs} = 170$ kPa. Although fully saturated gas streams are fed into the fuel cell at these operating conditions, we will show that our data suggest that liquid water does not play a major role here in terms of oxygen transport.

The differential-flow polarization curves at dry and standard conditions show a very similar trend. The region from 0 A cm^{-2} to ≈2.5 A cm^{-2} is dominated by kinetic and ohmic resistances, whereas from ≈2.5 A cm^{-2} on mass transport losses become significant, which is indicated by the change from a nearly linear voltage loss with current density between ≈1.0 A cm^{-2} and 2.5 A cm^{-2} to a more rapid decrease of cell voltage. At a cell voltage of 0.6 V, the performance curves for all materials except the Li100 MPL with perforation reach ≈1.7 A cm^{-2} at dry and ≈2.2 A cm^{-2} at standard conditions. The smaller current density at dry conditions can be explained with the high frequency resistance, which is 50% higher at dry conditions (≈45 mΩ cm^2) than at standard conditions (≈30 mΩ cm^2), showing that the lower *RH* of 70% leads to an increased membrane resistance and a concomitantly higher proton conduction resistance in the electrodes. The significant increase of the *HFR* at current densities exceeding ≈3 A cm^{-2} under both dry and standard conditions indicates a reduced local *RH* (at the electrode and the membrane) due to a growing temperature gradient between the flow field and the MEA. The polarization curve of the Li100 MPL with perforation, however performs worse than the other GDLs for both conditions at 80°C. For this GDL material, the *HFR* is ≈10 mΩ cm^2 higher than for the others, which would predict a voltage difference of 20 mV at 2.0 A cm^{-2}. This value is in reasonable agreement with the difference of the polarization curves. The most likely reason for this difference in *HFR* is a higher contact resistance caused by an uneven contact area by the perforation (see Figure 7g), particularly since the differences are the same for both 70% and 100% *RH* conditions. Why this is not observed for the Li400 MPL despite its similar surface morphology (see Figure 7k) is unclear at this point.

In contrast to the dry and standard conditions, significant differences in the polarization curves are measured at humid conditions. At 0.6 V, the performance varies between 1.8 A cm^{-2} and 2.4 A cm^{-2} in the following ascending order: commercial MPL, no MPL, Li100 MPL, Li400 MPL, Li100 MPL with perforation and Li400 MPL with perforation. This trend becomes even more pronounced at lower voltages, where mass transport limitations become relevant. Under these conditions, the *HFR* for the perforated Li100 MPL is now only slightly higher than that for the other GDLs (by ≈3-5 mΩ cm^2), which might be due to a higher compressive force induced by membrane swelling under over-humidified conditions, which in turn would reduce the effect from contact resistance differences between the MPL surface and the electrode. Clearly, however, the performance differences cannot be due to ohmic resistances and must be caused by differences in the oxygen transport resistance R_{T,O_2}.

At current densities below ≈1.5 A cm^{-2}, the total oxygen transport resistance is almost identical for dry and standard conditions (lower panels in Figures 8a and 8b) and also varies very little with the type of GDL: the substrate without MPL has the smallest R_{T,O_2} (as expected in the absence of liquid water[41]), followed in increasing order by the GDLs with perforated MPLs, with the Li100/Li400 MPLs, and with the commercial MPL. On the other hand, large differences in R_{T,O_2} are observed under humid conditions (lower panel in Figure 8c), with the highest value observed for the substrate without MPL. This can be attributed to water condensation at interface between the GDL-substrate and the cathode catalyst layer, which hinders oxygen diffusion.[2] Clearly, while an MPL is not necessary and actually adds oxygen transport resistance under dry conditions, it prevents the accumulation of water at the electrode/GDL interface under humid conditions and thereby reduces the oxygen transport resistance. Hence, all MPLs significantly reduce R_{T,O_2} in the following order beginning with the highest R_{T,O_2}: commercial MPL, Li100 MPL, Li400 MPL, Li100 perforated MPL and Li400 perforated MPL, while the latter two exhibit almost the same resistance. In general, it has to be

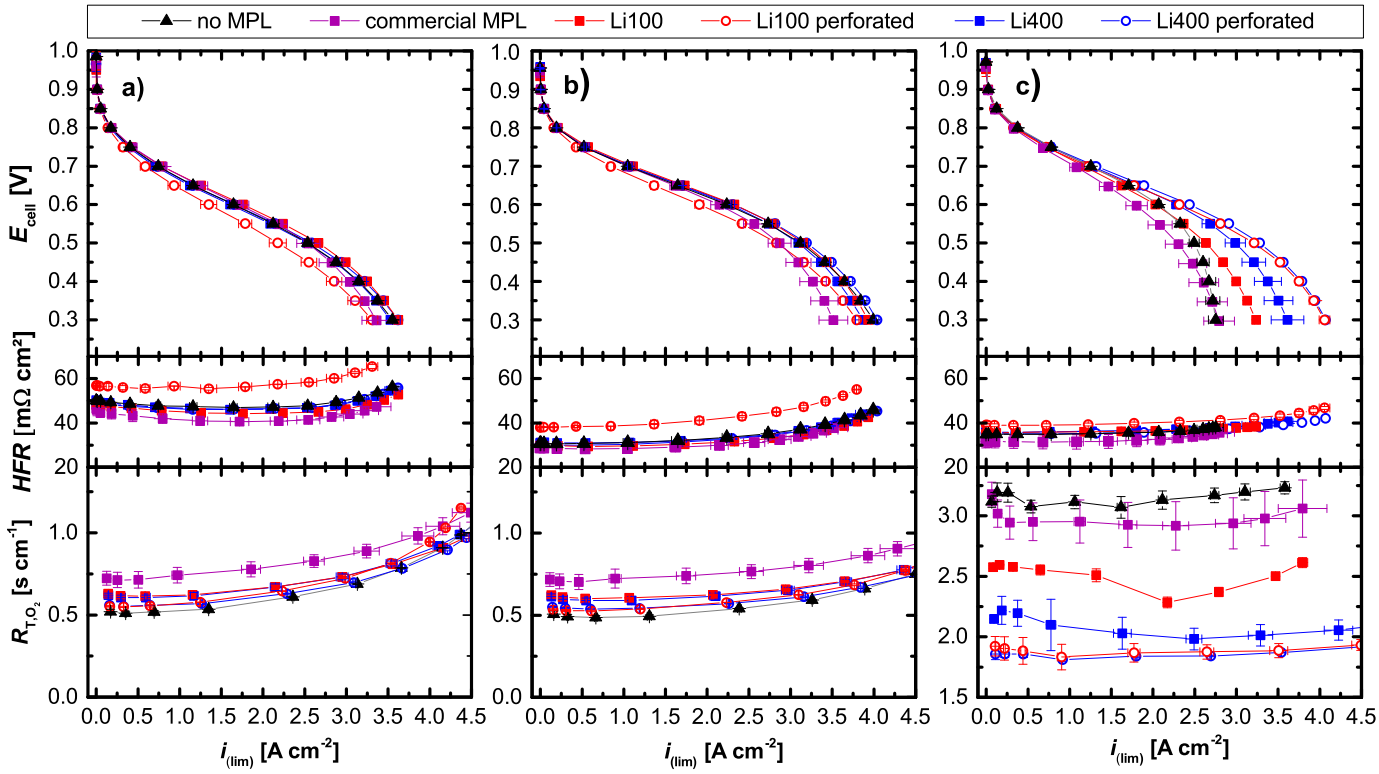

Figure 8. Differential-flow polarization curves showing cell voltage (E_{cell}, top) and high frequency resistance (*HFR*, middle) versus current density (i) as well as total oxygen transport resistance (R_{T,O_2}, bottom) versus the limiting current density (i_{lim}) for GDL-substrate with no MPL and the following MPLs coated on the same substrate: commercial MPL (Freudenberg), Li100 MPL, Li100 perforated MPL, Li400 MPL, Li400 perforated MPL. Operating conditions are (a) dry: $T_{cell} = 80°C$, $RH = 70\%$, $p_{abs} = 170$ kPa; (b) standard: $T_{cell} = 80°C$, $RH = 100\%$, $p_{abs} = 170$ kPa; and, (c) humid: $T_{cell} = 50°C$, $RH = 120\%$, $p_{abs} = 300$ kPa. The limiting current density is measured for various dry oxygen contents ($x_{O_2,dry}$) between 0.5% and 28%. The error bars represent the standard deviation of two independent measurements.

noted that the cell performance at the here chosen humid conditions is similar to that under standard and dry conditions, despite the impact of liquid water formation. This is mainly attributed to the higher pressure of 300 kPa compared to 170 kPa, which enhances the oxygen reduction kinetics (the decrease in the oxygen diffusion coefficient with increasing pressure is compensated by the higher oxygen partial pressure).

An interesting feature of the oxygen transport resistances shown in Figures 8a and 8b is that they increase at different degrees depending on the relative humidity as the limiting current density exceeds ≈1.5 A cm^{-2}, which in principle could be caused by the formation of liquid water within the MPL and/or the GDL-substrate.[26] However, if it were indeed caused by water condensation, the increase of R_{T,O_2} would be more pronounced at $RH = 100\%$ than at 70% *RH*. As our data show the opposite trend (from 1.5 to 4.5 A cm^{-2}, R_{T,O_2} increases by a factor of ≈1.6-2 at 70% *RH* and of ≈1.2-1.5 at 100% *RH*), the increase of R_{T,O_2} with current density is rather caused by an unfortunate shortcoming of the determination of R_{T,O_2} by the limiting current density method: as i_{lim} is measured at 0.05 V for $x_{O_2,dry} \geq 12\%$, significant amounts of heat are released at elevated limiting current density, which can result in a significant increase of the MEA temperature (compared to the nominal flow field temperature) and a concomitant decrease of the local relative humidity at the MEA. This, in turn would lead to an increase of the ionic conduction resistance in the membrane, as is indeed apparent in the *HFR* data (see middle panels of Figures 8a and 8b) and therefore also in the electrodes. Under these circumstances, the current density distribution in the cathode electrode will be skewed toward the cathode/membrane interface,[43] leading to a higher local current density and thus to an increase in the non-Fickian transport resistance ($R_{O_2,cathode}$ and $R_{O_2,other}$ in Equation 2), ultimately reducing i_{lim} and thus increasing the calculated R_{T,O_2}.[44] The observation that this increase of R_{T,O_2} with increasing current density is lower at 100% *RH* than at 70% *RH* clearly supports that it originates from membrane and electrode dry-out. On the other hand, for the over-humidified condition at low-temperature and high-pressure (Figure 8c), the R_{T,O_2} remains constant with current density, since the GDL is water-saturated at already low current densities and since the local temperature rise of the MEA (also indicated by the *HFR* increase) is not sufficient to remove liquid water and to dry-out the MEA.

At small limiting current densities, i.e., where R_{T,O_2} is constant, the above described dry-out effect is not relevant and this condition is best suited to evaluate the more subtle differences between the GDLs. Figure 9 shows R_{T,O_2} measured at comparable oxygen concentration gradients (i.e., at equal and low $x_{O_2,dry}$). As expected, under dry and standard conditions, the GDL-substrate without MPL (black bars) has the lowest R_{T,O_2}, as any MPL adds an additional transport barrier; the Li100 and Li400 MPLs (red and blue bars) show a small and similar increase in R_{T,O_2}, while the perforated MPLs (hatched bars) offer some direct diffusion pathways which leads to a reduced R_{T,O_2} compared to the non-perforated materials. The highest R_{T,O_2} is determined for the GDL with commercial MPL, which is due to the fact that it is ≈60% thicker. Under humid conditions, R_{T,O_2} increases by a large factor due to the higher operating pressure (300 kPa vs. 170 kPa) and due to water-saturation of the GDL. Here, the GDL-substrate without MPL now has the highest transport resistance, while the other GDLs follow the same trend as under dry and standard conditions.

To investigate the impact of the MPL on the dry-to-wet transition, Figure 10 shows R_{T,O_2} at $T_{cell} = 50°C$, $RH = 77\%$ and $p_{abs} = 400$ kPa, which is representing an under-humidified condition. The constant R_{T,O_2} level at $\lesssim$0.75 A cm^{-2} is showing the dry operation, where no water condensation is expected. With increasing i_{lim}, more water is produced until it starts to condense and to partially saturate the MPL/GDL-substrate and the electrode/MPL interface.

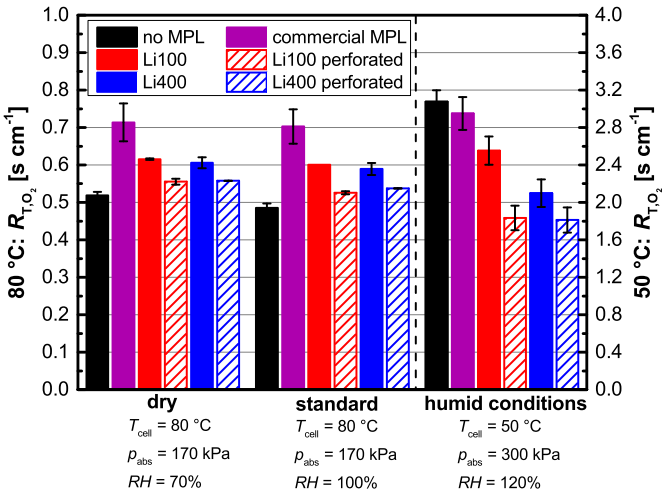

Figure 9. Total oxygen transport resistance (R_{T,O_2}) for GDL-substrate without MPL and the following MPLs coated on the same substrate at the three different operating conditions examined in Figure 8: commercial MPL (Freudenberg), Li100 MPL, Li100 perforated MPL, Li400 MPL, Li400 perforated MPL. R_{T,O_2} values are extracted from Figure 8 at $x_{O_2,dry} = 2\%$ for 80°C and $x_{O_2,dry} = 4\%$ for 50°C, which corresponds to the dry plateau region (for dry and standard conditions) and to the wet plateau region (for humid condition). Note that R_{T,O_2} at humid conditions is plotted on the right y-axis. The error bars represent the standard deviation of two independent measurements.

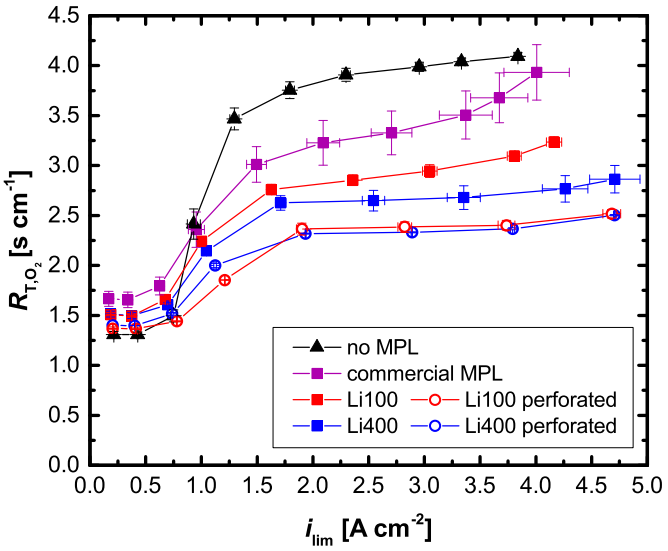

Figure 10. R_{T,O_2} as function of limiting current density for substrate with no MPL and the following MPLs coated on the same substrate: commercial MPL (Freudenberg), Li100 MPL, Li100 perforated MPL, Li400 MPL, Li400 perforated MPL. Operating conditions are $T_{cell} = 50°C$, $RH = 77\%$, $p_{abs} = 400$ kPa; i_{lim} was measured for various dry oxygen contents ($x_{O_2,dry}$) between 0.5% and 28%. The error bars represent the standard deviation of two independent measurements.

This leads to an increase in R_{T,O_2} until a maximum level of saturation is reached. From this point on, a roughly constant R_{T,O_2} at a high level is measured.[26,28] In the dry region, the same trends appear as for dry and standard conditions in Figures 8a and 8b and in Figure 9. The transition to a water-saturated diffusion medium is starting at a similar i_{lim} for all materials. In the wet region, i.e., at $\gtrsim$1.5 A cm^{-2}, differences between the materials are clearly visible and follow the trend as under humid conditions in Figure 8c and in Figure 9.

Discussion

Oxygen transport in the dry region.—The presented results of the Li100 and Li400 MPLs reveal only a minor impact of the utilized carbon black and the resulting porous structure on the total oxygen transport through the respective dry GDLs in the absence of liquid water (i.e., in the so-called dry region). At $p_{abs} = 170$ kPa, their transport resistance is almost identical at dry (80°C/70% *RH*) and standard conditions (80°C/100% *RH*), with $R_{T,O_2} \approx 0.6$ s cm^{-1} (see left and middle panels in Figure 9). When subtracting the transport resistance of the uncoated GDL-substrate ($R_{T,O_2} \approx 0.5$ s cm^{-1}), the resulting transport resistance through the Li100 and Li400 MPLs is $R_{MPL,O_2} \approx 0.12 \pm 0.01$ s cm^{-1} (Li100 MPL) and $R_{MPL,O_2} \approx 0.10 \pm 0.03$ s cm^{-1} (Li400 MPL). As all tested Li100 and Li400 MPLs have the same thickness, the effective diffusion coefficient (inversely proportional to the pressure-dependent contribution of R_{O_2}) for both MPLs and thus the ratio of τ/ε (see Eq. 4) is essentially identical. However, the here used assumption that the MPL transport resistance can be considered a property which is entirely independent of the GDL-substrate is only a zero-order estimate for the Li100 and Li400 MPLs, as there clearly is a significant intrusion of these MPLs into the GDL-substrate (see Figures 7f and 7j). This is different for the commercial MPL (see Figure 7e), with its ≈2-fold higher oxygen transport resistance through the MPL of $R_{MPL,O_2} \approx 0.22 \pm 0.06$ s cm^{-1} under these conditions (based on $R_{T,O_2} \approx 0.71$ s cm^{-1}) which in consequence means that the different MPL/GDL-substrate interfaces (less intrusion for commercial MPL) and the only ≈1.6-fold higher thickness cannot entirely explain the 2-fold increase of R_{MPL,O_2}. The exclusively smaller pore sizes of the commercial MPL (see Figure 5) however can rationalize its higher diffusion resistance. The same trends can be observed at the higher pressure of $p_{abs} = 400$ kPa (Figure 10): subtracting the GDL-substrate transport resistance ($R_{T,O_2} \approx 1.31$ s cm^{-1}), oxygen transport resistance contribution from the commercial MPL ($R_{MPL,O_2} \approx 0.35 \pm 0.10$ s cm^{-1}) is ≈1.8-fold larger than that for the Li100 and Li400 MPLs ($R_{MPL,O_2} \approx 0.19 \pm 0.03$ s cm^{-1} and $R_{MPL,O_2} \approx 0.19 \pm 0.06$ s cm^{-1}).

In conclusion, while the total transport resistance of the various GDLs in the dry plateau region only varies by less than ≈30% (i.e., between the commercial MPL/GDL-substrate and the MPL-free GDL-substrate), reflected by the essentially identical differential-flow performance curves (see Figures 8a and 8b), the nominal contribution from the MPL (R_{MPL,O_2}) differs by a factor of ≈2. Further improvements in the MPL transport resistance in the dry plateau region, are observed with the perforation of the Li100 and Li400 MPLs: at $T_{cell} = 80°C$ and $p_{abs} = 170$ kPa, R_{MPL,O_2} amounts to $\approx 0.04 \pm 0.02$ s cm^{-1} (Li100 perforated MPL) and $\approx 0.05 \pm 0.01$ s cm^{-1} (Li400 perforated MPL; see left and middle panel of Figure 9) and at $T_{cell} = 50°C$ and $p_{abs} = 400$ kPa, R_{MPL,O_2} is $\approx 0.06 \pm 0.04$ s cm^{-1} (Li100 perforated MPL) and $\approx 0.09 \pm 0.03$ s cm^{-1} (Li400 MPL), showing that in both cases the large pores in the perforated MPLs (see Figures 7g and 7k) substantially enhance the oxygen transport. Since the MPL thickness remained the same and since the impact of the overall MPL void volume fraction is expected to be only minor (Li100 MPL: increase of ε from 79% to 86% would result in an 8% reduction of R_{MPL,O_2}; Li400 MPL: increase of ε from 68% to 77% results in a 12% reduction of R_{MPL,O_2}) this implies a much lower tortuosity τ for perforated MPLs (see Eq. 4), providing strong support to the presence of large pores/cracks extending across the MPL. However, these differences have almost no impact on the polarization curves under dry and standard conditions at a commonly used benchmark cell voltage of 0.6 V (see Figure 8), as the differences in total mass transport resistance are small.

Impact of carbon black type in non-perforated MPLs in the presence of liquid water.—In contrast to the above described performance in the dry region, the total oxygen transport resistance of the GDL at humid conditions, i.e, in the so called wet region where the GDL is partially water-filled, is significantly impacted by the MPL. This is also illustrated by the large differences in the fuel cell polarization curves (see Figure 8c), indicating different oxygen transport mechanisms in the presence of liquid water. It has been shown that

the MPL prevents the accumulation of liquid water in the porous structure of the substrate close to the cathode and that it also creates preferred water transport pathways, which reduces the water saturation level inside the substrate.[2,6,7] This effect is also observed in our data, where the substrate without MPL reveals the highest oxygen transport resistance due to severe water blockage in the GDL pores close to the electrode, while all MPLs show an improvement in terms of oxygen transport (lower panel of Figure 8c). Amongst the non-perforated carbon black based MPLs, the Li400 MPL exhibits the smallest R_{T,O_2} of ≈2.1 s cm^{-1}, followed by the Li100 MPL with ≈2.6 s cm^{-1}, and lastly by the commercial MPL with a much higher value of ≈3.9 s cm^{-1}.

First considering the here prepared non-perforated Li400 and Li100 MPLs, their different oxygen transport properties in the wet region could be explained by their different morphology, with the better performing Li400 MPL showing a larger maximum in its pore size distribution compared to the Li100 MPL (≈328 nm vs. ≈67 nm; see Figure 4, Figure 5, and Table II). Under the assumption that in the wet region liquid water will have to penetrate the MPL by an eruptive release mechanism of water from the cathode through the MPL (which means a continuous filling and emptying of pores with water), the Washburn equation (Eq. 1) would predict that larger pores in the MPL would facilitate liquid water transport and are thus preferred at these operating conditions. The smaller these hydrophobic pores on the other hand, the larger would be the extent of water retention and its accumulation at the cathode/MPL interface, thereby reduce the effective diffusion of oxygen. This would explain the lower oxygen transport resistance and the better performance of the Li400 vs. the Li100 MPL (see Figure 8c). At first glance inconsistent with this hypothesis is the fact that the Li100 MPL coated on the GDL-substrate also exhibits many larger pores with diameters between ≈0.1 −10 μm (see Figure 5) which should more easily facilitate liquid water transport. However, as none of these large pores in the micrometer range are observed in the top-view SEM images (see Figure 7e), we assume that these are internal pores, which can be recognized as small cracks in cross-sectional images (see Figure 7f). This means that liquid water still has to percolate through the small pores located at the surface of the MPL. This leaves the question why the commercial MPL with a similar maximum in the pore size distribution (≈64 nm; Figure 5) as the Li100 MPL displays a much higher R_{T,O_2} value and much worse fuel cell performance (Figure 8c). While part of it may be ascribed to its 60% larger thickness, it may also be related to differences in the MPL/GDL-substrate interface, which is very sharp for the commercial MPL and more intertwined for the Li100 MPL (compare Figures 7d and 7f), whereby the latter may be conductive to water transfer into the GDL-substrate.

Impact of MPL perforation in the presence of liquid water.—The perforation of MPLs creates a heterogeneous pore structure with a microporous framework defined by the carbon black (see Hg porosimetry in Figure 4) and by large micrometer-sized pores going all across the MPL which are produced by the pore former (see SEM images in Figure 7). Extending on the above discussion, such an MPL structure should facilitate the transport of liquid water through the large pores at very low capillary pressure, at which the small pores defined by the carbon black would remain water-free and thus serve as oxygen transport pathway. This proposed mechanism is illustrated in Figure 11, where the expected liquid water transport pathway through the MPL is shown by an SEM image of a perforated Li400 based MPL, visualizing our hypothesis that the large pores penetrating across the MPL are preferentially filled with liquid water, while the small pores defined by the carbon black structure remain water-free, enabling efficient oxygen transport without an additional transport barrier.

As one would expect based on this hypothesis, the experimental data clearly show that the oxygen transport resistance in the wet plateau region is indeed substantially lower for the perforated MPLs compared to the non-perforated MPLs (see Figure 10). Under conditions where liquid water is present in the GDL, the perforation reduces R_{T,O_2} by ≈25% for the Li100 MPL and by ≈14% for the

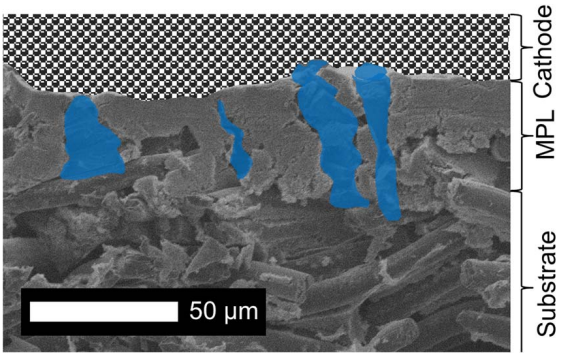

Figure 11. Illustration of the proposed liquid water transport mechanism through perforated MPLs from the cathode electrode (upper hatched region) toward the GDL-substrate, using an SEM image for a perforated Li400 MPL. Large pores caused by the pore former are hypothesized to allow the effective transport of liquid water (blue colored region) while most regions of the MPL are free of liquid water and thus available for efficient oxygen gas transport.

Li400 MPL at both $T_{cell} = 50°C$, $RH = 120\%$ and $p_{abs} = 300$ kPa and $T_{cell} = 50°C$, $RH = 77\%$ and $p_{abs} = 400$ kPa (see right panel of Figure 9 and Figure 10). This impacts also the polarization curves, where in Figure 8c the perforated MPLs show the highest performance with 2.3 A cm^{-2} (Li100 perforated) and 2.4 A cm^{-2} (Li400 perforated) at 0.6 V as well as the highest limiting current densities. A particularly interesting feature of the perforated MPLs under these humid conditions is that their oxygen transport resistance (lower panel of Figure 8c) is essentially identical ($R_{T,O_2} \approx 1.8$ s cm^{-1}), even though both MPLs without perforation show very different R_{T,O_2} (≈2.6 s cm^{-1} for the Li100 MPL vs. 2.1 s cm^{-1} for the Li400 MPL). The same behavior is even more clearly illustrated in Figure 10, where due to the higher pressure and the lower relative humidity the dry-to-wet plateau transition can be followed. At small current densities (i.e., in the dry plateau region), the non-perforated Li100/Li400 MPLs show the same R_{T,O_2} (≈1.5 s cm^{-1}) and their perforated versions the same slightly smaller R_{T,O_2} (≈1.4 s cm^{-1}). The start of water condensation is observed at ≈0.75 A cm^{-2} for all GDLs, which is indicated by a rapid increase of R_{T,O_2}. A state of high water saturation is reached for all materials at ≈1.5 A cm^{-2}. From this point on, a further more gradual increase of R_{T,O_2} for the Li100 and the commercial MPL suggests a continuous accumulation of water at an already high saturation level, while R_{T,O_2} for the Li400 and the perforated MPLs remain at an essentially constant level. Analogous to the humid condition at 300 kPa and $RH = 120\%$ (lower panel, Figure 8c) where the wet plateau region is established already at the lowest current density, different R_{T,O_2} values are observed for the non-perforated Li100/Li400 MPLs, while both perforated MPLs end up at the same R_{T,O_2} value. This actually confirms our above hypothesis that there exist two transport pathways in the perforated MPLs, namely transport of liquid water in the large pores at low capillary pressure while oxygen is transported in the small micropores within the non-cracked MPL segments which remain water-free at low capillary pressure (see Figure 11): in this case, the identical dry plateau oxygen transport resistance for the non-perforated Li100 and Li400 MPLs would predict the observed identical R_{T,O_2} in the wet plateau for the perforated MPLs. Similarly, in case of the non-perforated Li100 and Li400 MPLs, where oxygen and liquid water have to share pores of similar size as transport pathways, the MPL with the larger pore size distribution maximum (≈328 nm for Li400 vs. ≈67 nm for Li100) should have a lower R_{T,O_2} in the wet plateau region, exactly as observed in Figure 8c and Figure 10. These observations, we believe, provide rather strong evidence for the transport mechanisms in perforated (or cracked) MPLs which are illustrated in Figure 11.

These results are also in agreement with studies from Lu et al.,[18] Gerteisen et al.,[16] Kong et al.[22] and Selvarani et al.[32] For laser

perforated MPLs[18] or GDLs,[16] significant improvements in limiting current density were measured at humid conditions (i.e., at low cell temperatures of $T_{cell} = 55°C$[16] and $T_{cell} = 40°C$[16]). Also for MPLs, which are perforated by using pore-forming agents, significant performance enhancements are observed in oxygen or air at 60°C[32] and 75°C[22] and fully humidified gases with a maximum performance for an optimum pore former content. But we do not agree with the explanation of Kong et al. for this observation, who argue with the effect of capillary condensation in sub-nanometer size pores, which, however, are not relevant for gas transport through the layer, and their assumption that oxygen transport is realized in large dry pores. Thus, they completely neglect the more likely capillary effect, which is also suggested by other studies and would result in oxygen transport in smaller pores, while liquid transport is occurring in the larger pores.[10,14,19] On the contrary, Owejan et al. found no impact of intentionally introduced cracks in the MPL on the fuel cell performance at both dry ($T_{cell} = 80°C$, $p_{abs} = 150$ kPa and $RH = 66\%$) and humid conditions ($T_{cell} = 60°C$, $p_{abs} = 270$ kPa and $RH = 100\%$).[2] The authors conclude that even at humid conditions water vapor transport is sufficient to remove product water from the electrode through the MPL. From the SEM cross-sectional images one can estimate that the average distance between the cracks is ca. 200 μm compared to ca. 50 μm in the present study (compare Figure 2 in Ref. 2 to Figures 7h and 7l in this study). It is unclear whether the crack density in the study by Owejan et al. was sufficient to allow for the here proposed bi-functional transport pathways (see Figure 11). Based on geometric arguments, effective dual transport pathways would require distances between cracks which are on the order of the electrode thickness (≈10 μm), and average crack distances of >100 μm are probably not effective, which might be the origin of the discrepancy between their and our findings.

An alternative explanation for the observed phenomena in the present study could be a change of the temperature distribution inside the MEA with different MPL materials. Previous studies have shown that the MPL type, thickness, and its intrusion into the substrate affect its thermal conductivity and thus influence the temperature gradient between the electrode and the GDL-substrate.[45–48] The lower the thermal conductivity of the MPL, the higher is this temperature gradient, which enables a larger fraction of liquid water to be transported by vapor phase diffusion, presumably reducing the liquid water fraction inside the porous layers and reducing oxygen transport resistances. For the same MPL composition, the thermal conductivity should obviously decrease with increasing porosity, so that a larger thermal gradient and thus improved oxygen transport would be predicted for perforated MPLs on this basis, which is indicated by the reduced R_{T,O_2} in our measurements.

However, based on this thesis, a larger thermal gradient would also cause a smaller membrane hydration at high current densities due to a decreased local *RH*,[45,49] which should manifest itself in a larger increase of the *HFR* for the perforated MPLs at elevated current densities, in particular at dry conditions. This is not the case as can be seen in Figure 8a. Furthermore, assuming a similar bulk thermal conductivity of the two utilized acetylene black based MPLs (same PTFE content) would also suggest, that the Li100 MPL (ε = 79%) should show a smaller R_{T,O_2} compared to the Li400 MPL (ε = 68%) due to its higher porosity, which again is not supported by our measured oxygen transport resistances (see Figure 8c, Figure 9, and Figure 10). Finally, small MPL thermal conductivity differences would also likely be minimized by the presence of high water contents, which significantly increase the overall thermal conductivity of porous media.[50] From these observations, we conclude that the oxygen transport resistance differences between our different MPLs are not related to MPL thermal conductivity differences, but are mostly caused by an efficient liquid water transport as stated before.

Thus, based on our data and analysis, a bi-functional pore network is able to facilitate liquid water transport through the MPL and to reduce the oxygen transport resistance at humid conditions (i.e., in the wet plateau region). As water in these structures is transported primarily through the large pores, the total oxygen mass transport resistance

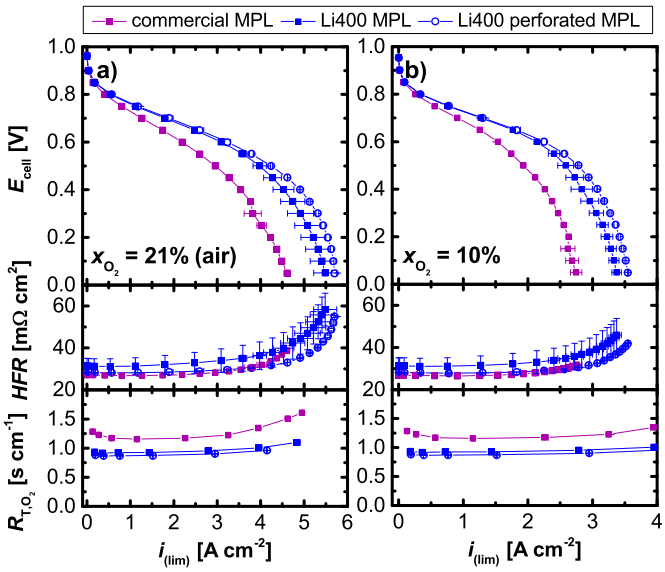

Figure 12. Cell voltage (E_{cell}, top) and high frequency resistance (*HFR*, middle) vs. current density (i) and total oxygen transport resistance (R_{T,O_2}, bottom) vs. the limiting current density for GDL-substrate coated with the following MPLs: commercial MPL (Freudenberg), Li400 MPL, and Li400 perforated MPL. Operating conditions are: (a) $T_{cell} = 80°C$, $RH = 100\%$, $p_{abs} = 300$ kPa, with cathode feed air ($x_{O_2,dry} = 21\%$); (b) $T_{cell} = 80°C$, $RH = 100\%$, $p_{abs} = 300$ kPa, with cathode feed $x_{O_2,dry} = 10\%$ in N_2. Limiting current densities (i_{lim}) are measured for various dry oxygen contents ($x_{O_2,dry}$) between 0.5% and 24%. The error bars represent the standard deviation of two independent measurements.

becomes largely independent from the pore size distribution within the solid part of the MPL (defined by the carbon black structure), as long as the oxygen transport resistance through the MPL in the dry plateau region is comparable. This provides a new design strategy for MPLs: while the "ideal" MPL would exhibit independent arrays of hydrophilic and hydrophobic pores/regions (as, e.g., demonstrated for GDL-substrates by Forner-Cuenca et al.[51]), an alternative approach shown here is to create a bi-modal pore size distribution of small and large pores, both with hydrophobic properties. In general, the here presented approach of applying a pore former polymer to produce such a bi-functional porous network is in principal cost-efficient and applicable to a large-scale production. Despite these advantages, this strategy also raises some critical questions toward the practicality in a fuel cell. The MPL perforation leads to an inhomogeneous surface, which could cause localized resistance variations (as indicated by the increased *HFR* of the perforated Li100 MPL), but could also affect the heat transfer and result in local hot-spots. Furthermore, the CCM is mechanically less stabilized if the perforations are too large. These thermal and mechanical stresses might lead to local degradation phenomena over extended operating times, which certainly needs to be evaluated before an actual application of perforated MPLs.

Impact of pressure and oxygen concentration on the MPL Performance.—Although the here prepared GDLs show advantages under humid conditions ($T_{cell} = 50°C$, $RH = 120\%$, $p_{abs} = 300$ kPa), it is somewhat disappointing that no benefits are observed under standard operating conditions ($T_{cell} = 80°C$, $RH = 100\%$, $p_{abs} = 170$ kPa) at which the GDL water saturation level is low (compare Figures 8a and 8b with 8c). However, in the recent years, in order to reach a high efficiency (cell voltage of >0.6 V) of the fuel cell system at high current densities (>2 A cm^{-2}), higher operating pressures are being considered for automotive fuel cell systems.[44] Here, a trade-off between the higher air compressor power requirement and the fuel cell power improvement has to be considered. To evaluate the performance gains at high pressure, differential-flow polarization curves at $T_{cell} = 80°C$, $RH = 100\%$ and $p_{abs} = 300$ kPa are recorded for the

commercial MPL, the Li400 MPL and the Li400 perforated MPL. Two different oxygen contents of 21% of O_2 in N_2 and 10% of O_2 in N_2 simulate the concentrations at the cell air inlet and its outlet at an assumed cathode stoichiometry of ≈1.75. The results are shown in Figure 12.

Due to a doubling of oxygen partial pressure at p_{abs} = 300 kPa (Figure 12a), the oxygen reduction kinetics are significantly enhanced compared to p_{abs} = 170 kPa (Figure 8b). This effect causes higher voltages in the kinetically dominated region, indicated by the cell voltages obtained at 1 A cm^{-2} of 0.77 V (Li400 and perforated Li400 MPLs) or 0.73 V (commercial MPL) at 300 kPa compared to 0.71 V at 170 kPa for these three GDLs. While at 170 kPa (Figure 8b) the differences between the three GDLs are marginal at 0.6 V, significant improvements by the advanced MPL materials are observed at 300 kPa. At 21% O_2 (Figure 12a), the commercial MPL exhibits 2.2 A cm^{-2}, the Li400 MPL 3.1 A cm^{-2}, and the Li400 perforated MPL 3.2 A cm^{-2}; at 10% O_2 (Figure 12b), analogously high improvements are observed (1.5 A cm^{-2} for the commercial MPL vs. 2.1 A cm^{-2} for the Li400 MPL and 2.2 A cm^{-2} for the perforated Li400 MPL). This corresponds to a total performance improvement of ≈45% for both air and 10% O_2, and thus to a reduction of the platinum specific power density at 0.6 V of ≈30% from ≈0.38 g_{Pt}/kW for the commercial MPL/GDL-substrate to ≈0.26 g_{Pt}/kW for the perforated Li400 MPL. While ≈0.26 g_{Pt}/kW are still quite a bit off from the DoE target of ≤0.1 g_{Pt}/kW, preliminary data have already shown that combination of advanced MEAs (thinner membranes and lower Pt loadings) with sophisticated MPL materials very closely approach the DoE target under these high-pressure conditions.

As a last step, we want to examine the origin of the observed large fuel cell performance improvement of the Li400 MPL and the perforated Li400 MPL with fully-humidified reactants at 300 kPa (Figure 12) compared to the minor differences at 170 kPa (Figure 8b), namely whether this is due to improved liquid water transport (as clearly is the case at the humid conditions shown in Figure 8c) or whether it is due to the enhanced oxygen transport in the absence of water saturation. This is not a priori obvious, since the binary diffusion coefficient of water vapor in the oxygen/nitrogen/vapor gas mixture (M) decreases with $D_{H_2O|M} \sim {p_{abs}}^{-1}$, and the resulting slower water vapor transport was shown lead to water condensation, i.e., to a shift of the dry-to-wet-plateau transition to lower current densities.[26]

In general, the effect of pressure on the total oxygen transport resistance is different for the different terms in Equation 2. The pressure independent contribution to the total oxygen transport, R_{PI,O_2}, is caused by Knudsen diffusion resistances in small pores (mainly in the catalyst layer) and a resistance attributed to the Pt surface or the ionomer film, which is dependent on the electrode roughness factor.[24,44] Raising the operating pressure, this term stays constant as the oxygen partial pressure gradient from flow field to the catalyst surface during operation is increased[24,26] and for a similar cathode electrode, it was determined as $R_{PI,O_2} \approx 0.15$ s cm^{-1} (at 80°C for 0.4 mg_{Pt} cm^{-2}).[24] On the other hand, the pressure dependent part (R_{PD,O_2}) is proportional to the total pressure: $R_{PD,O_2} \sim {D_{O_2|M}}^{-1} \sim p_{abs}$,[26] where $D_{O_2|M}$ represents the binary diffusion coefficient of oxygen in the oxygen/nitrogen/vapor gas mixture (M). Hence the performance effect of the oxygen pressure gradient increase is almost cancelled out by the increase of transport resistance. Based on the R_{T,O_2} from Figure 8b at 170 kPa, we can estimate the R_{T,O_2} at 300 kPa with Equation 10.

$$R_{T,O_2(p_2)} = \left(R_{T,O_2(p_1)} - R_{PI,O_2}\right) \cdot \frac{p_2}{p_1} + R_{PI,O_2} \quad [10]$$

With $R_{PI,O_2} \approx 0.15$ s cm^{-1} (see above), R_{T,O_2} is expected to increase from 0.59 s cm^{-1} at 170 kPa (from Figure 8b) to 0.93 s cm^{-1} at 300 kPa for the Li400 MPL, from 0.54 s cm^{-1} at 170 kPa (from Figure 8b) to 0.87 s cm^{-1} at 300 kPa for the perforated Li400 MPL, and from 0.70 s cm^{-1} at 170 kPa (from Figure 8b) to 1.12 s cm^{-1} at 300 kPa for the commercial MPL. This is in quite excellent agreement with the measured values shown in Figure 12 (0.92 s cm^{-1} for Li400, 0.87 s cm^{-1} for Li400 perforated, and 1.17 s cm^{-1} for commercial MPL/GDL). As it has already been shown that no liquid water is present in the MPL/GDL-substrate under the standard conditions of Figure 8b (T_{cell} = 80°C, RH = 100%, p_{abs} = 170 kPa) and as our above calculation does not include the additional oxygen transport resistance which would be present under conditions where the GDL is saturated with liquid water, we can conclude from the agreement between measured and calculated R_{T,O_2} values that also at the conditions of Figure 12 (T_{cell} = 80°C, RH = 100%, p_{abs} = 300 kPa) no significant amount of liquid saturation occurs in the GDL.

Nevertheless, in the polarization curves with air and 10% O_2 at 300 kPa (Figure 12), mass transport effects obviously become significant at relevant voltages >0.6 V, leading to a very different performance of the various GDLs, in strong contrast to the 170 kPa polarization curves (Figure 8b). Due to accelerated ORR kinetics, current densities between 2.2 A cm^{-2} and 3.2 A cm^{-2} are reached at 0.6 V. Because the mass transport overpotential is a function of the current density, larger differences in the performance are detected at 300 kPa compared to 170 kPa. When simulating the stack outlet conditions with supplying 10% O_2 in N_2 to the cathode, the limiting current density is decreasing by a similar ratio compared to air as expected from the decrease in oxygen concentration. From Equation 3, one would expect a ratio between the air and 10% O_2 condition of 21/10 = 2.1 assuming a constant R_{T,O_2} independent of the limiting current density. In reality, however, we measure a smaller ratio of 1.6–1.7 (depending on GDL), which we attribute to the increasing R_{T,O_2} at elevated i_{lim} > 4 A cm^{-2} as explained in the previous discussion. The better performance for the Li400 perforated MPL shows that also at smaller oxygen partial pressure gradients, the MPL still exhibits a major role. Hence, for high pressure operation and standard temperature and RH (80°C and 100% RH), sophisticated MPLs are necessary, which feature a high diffusivity (i.e. high ε/τ) for oxygen in order to protract the beginning of the oxygen transport limited region and to reach high current densities, even though only minor amounts of liquid water are present. At the same time, robust MPLs/GDLs have to be able to effectively transport both oxygen and liquid water under conditions where significant amounts of water saturation in the GDL occur.

Conclusions

In this paper we present fuel cell data and characterization for two MPLs with different carbon blacks and a commercial MPL. We observe that the MPL pore structure has significant influence on the oxygen transport, in particular at conditions of high liquid water saturation. The results at T_{cell} = 50°C, RH = 120%, p_{abs} = 300 kPa show a 15% smaller total oxygen transport resistance and better performance for the MPL with large pores (maximum 328 nm) than for the MPL with smaller pores (maximum 67 nm), while the performance at dry conditions (T_{cell} = 80°C, RH = 70%, p_{abs} = 170 kPa) is almost identical for both materials. This is explained by a reduced capillary pressure for larger hydrophobic pores which facilitates the transport of liquid water and prevents a blockage of oxygen transport pathways, while the oxygen transport in dry GDLs is unaffected.

Furthermore we present an approach to introduce large pores and cracks into the MPL by using a thermally decomposable pore former polymer. Our measurements suggest that these perforations create preferred transport pathways for liquid water, which reduce the oxygen transport resistance compared to the conventional carbon black based MPLs at humid operating conditions. From our results we can conclude that the transport of oxygen and water proceeds via separate pores of different size, which reduces the accumulation of liquid water at the MPL/cathode interface. Also at high pressure and normal conditions (T_{cell} = 80°C, RH = 100%, p_{abs} = 300 kPa), the newly developed MPLs exhibit advantages in performance due to the better diffusivity of oxygen through their structure, even though no significant amounts of liquid water are expected.

Summarized, with the present strategy the fuel cell performance at 0.6 V and humid conditions (T_{cell} = 50°C, RH = 120%, p_{abs} = 300 kPa) is improved by variation of the carbon black and by perforation via the reduction of the total oxygen transport resistance (R_{T,O_2}). Furthermore at elevated operating

pressure (T_{cell} = 80°C, RH = 100%, p_{abs} = 300 kPa), we observe a significant impact of the MPL structural properties on the performance at a typical fuel cell operating temperature of 80°C, at which the perforated MPL exhibits a 45% higher current density than the commercial reference MPL.

Acknowledgments

This research was carried out within the framework of the joint project "Optigaa2". Financial support by the German Federal Ministry of Economic Affairs and Energy (grant number 03ET6015E), Freudenberg Performance Materials SE & Co. KG and Daimler AG is gratefully acknowledged. We are very thankful for the valuable discussions with Achim Bock (Freudenberg). The authors would also like to thank Kerstin Fischinger (ZSW Ulm) for the mercury porosimetry measurements, Katia Rodewald (Wacker-Chair of Macromolecular Chemistry, TUM) for the SEM measurements, and Wan Sen Zhen (Singapore Institute of Technology and Chair of Technical Electrochemistry, TUM) for the BET measurements. Furthermore, we are grateful for the GDL materials provided free-of-charge by Freudenberg, Germany (GDL), Denka, Japan (Li100 and Li400 acetylene black), Soken, Japan (MX-3000 PMMA powder), and 3M Dyneon, Germany (TF 5035GZ PTFE dispersion).

List of Symbols

Variable	Unit	Description
A	cm^2	area
D_{eff}	$m^2\ s^{-1}$	effective diffusion coefficient
$D_{O_2\|M}$	$m^2\ s^{-1}$	diffusion coefficient of oxygen in a gas mixture
d_{MPL}	µm	MPL thickness
$d_{particle}$	µm	particle diameter
d_{pore}	µm	pore diameter
E_{cell}	V	cell voltage
HFR	Ω cm^2	high frequency resistance
i	A cm^{-2}	current density normalized to geometric electrode area
i_{lim}	A cm^{-2}	limiting current density normalized to geometric electrode area
m	g	mass
p_{abs}	kPa	absolute pressure
p_c	kPa	capillary pressure
p_{H_2O}	kPa	partial pressure of water (at cell inlet)
$q_{vol.}$	%	volume fraction
R_{T,O_2}	s cm^{-1}	total oxygen transport resistance
R_{x,O_2}	s cm^{-1}	oxygen transport resistance of the component (x = GDL, MPL, flow field, cathode) or mechanism (x = PI (pressure independent), PD (pressure dependent))
RH	%	relative humidity
s	-	Reactant stoichiometry
T_{cell}	°C	fuel cell temperature
T_{sample}	°C	sample temperature
V	ml	volume
w	wt.%	mass fraction
$x_{O_2,dry}$	%	dry mole fraction of oxygen

Constant	Value	Unit	Description
F	96485	C mol^{-1}	Faraday constant
R	8.3145	J mol^{-1} K^{-1}	ideal gas constant

Greek	Unit	Description
γ_{H_2O}	N m^{-1}	surface tension of water
γ_{Hg}	N m^{-1}	surface tension of mercury porosity
ε	%	
θ	°	contact angle
ρ	g cm^{-3}	density
τ	-	tortuosity
ϕ_{PMMA}	vol.%	PMMA volume fraction

References

1. M. F. Mathias, J. Roth, J. Fleming, and W. Lehnert, in *Handbook of Fuel Cells*, W. Vielstich, H. A. Gasteiger, and A. Lamm, Editors, John Wiley & Sons, Ltd (2010).
2. J. P. Owejan, J. E. Owejan, W. B. Gu, T. A. Trabold, T. W. Tighe, and M. F. Mathias, *J. Electrochem. Soc.*, **157**, B1456 (2010).
3. J. M. Morgan and R. Datta, *J. Power Sources*, **251**, 269 (2014).
4. S. Park, J.-W. Lee, and B. N. Popov, *J. Power Sources*, **177**, 457 (2008).
5. S. Park, J.-W. Lee, and B. N. Popov, *J. Power Sources*, **163**, 357 (2006).
6. J. T. Gostick, M. A. Ioannidis, M. W. Fowler, and M. D. Pritzker, *Electrochem. Commun.*, **11**, 576 (2009).
7. P. Deevanhxay, T. Sasabe, S. Tsushima, and S. Hirai, *Electrochem. Commun.*, **34**, 239 (2013).
8. J. Lee, R. Yip, P. Antonacci, N. Ge, T. Kotaka, Y. Tabuchi, and A. Bazylak, *J. Electrochem. Soc.*, **162**, F669 (2015).
9. Y. Ji, G. Luo, and C.-Y. Wang, *J. Electrochem. Soc.*, **157**, B1753 (2010).
10. P. Deevanhxay, T. Sasabe, S. Tsushima, and S. Hirai, *J. Power Sources*, **230**, 38 (2013).
11. S. Prass, S. Hasanpour, P. K. Sow, A. B. Phillion, and W. Mérida, *J. Power Sources*, **319**, 82 (2016).
12. T. Sasabe, P. Deevanhxay, S. Tsushima, and S. Hirai, *Electrochem. Commun.*, **13**, 638 (2011).
13. R. Alink, J. Haussmann, H. Markotter, M. Schwager, I. Manke, and D. Gerteisen, *J. Power Sources*, **233**, 358 (2013).
14. S. S. Alrwashdeh, H. Markötter, J. Haußmann, T. Arlt, M. Klages, J. Scholta, J. Banhart, and I. Manke, *Energy*, **102**, 161 (2016).
15. J. Haußmann, H. Markötter, R. Alink, A. Bauder, K. Dittmann, I. Manke, and J. Scholta, *J. Power Sources*, **239**, 611 (2013).
16. D. Gerteisen, T. Heilmann, and C. Ziegler, *J. Power Sources*, **177**, 348 (2008).
17. Z. Lu and J. Waldecker, "Microporous layer structures and gas diffusion layer assemblies in proton exchange membrane fuel cells", *United States Pat. US 8,945,790 B2*, (issued: Feb. 3, 2015).
18. Z. Lu, J. Waldecker, M. Tam, and M. Cimenti, *ECS Transactions*, **69**, 1341 (2015).
19. H. Markötter, J. Haussmann, R. Alink, C. Totzke, T. Arlt, M. Klages, H. Riesemeier, J. Scholta, D. Gerteisen, J. Banhart, and I. Manke, *Electrochem. Commun.*, **34**, 22 (2013).
20. M. P. Manahan, M. C. Hatzell, E. C. Kumbur, and M. M. Mench, *J. Power Sources*, **196**, 5573 (2011).
21. M. P. Manahan and M. M. Mench, *J. Electrochem. Soc.*, **159**, F322 (2012).
22. C. S. Kong, D.-Y. Kim, H.-K. Lee, Y.-G. Shul, and T.-H. Lee, *J. Power Sources*, **108**, 185 (2002).
23. E. Gauthier, Q. Duan, T. Hellstern, and J. Benziger, *Fuel Cells*, **12**, 835 (2012).
24. D. R. Baker, D. A. Caulk, K. C. Neyerlin, and M. W. Murphy, *J. Electrochem. Soc.*, **156**, B991 (2009).
25. D. R. Baker, C. Wieser, K. C. Neyerlin, and M. W. Murphy, *ECS Transactions*, **3**, 989 (2006).
26. D. A. Caulk and D. R. Baker, *J. Electrochem. Soc.*, **157**, B1237 (2010).
27. H. Oh, Y. i. Lee, G. Lee, K. Min, and J. S. Yi, *J. Power Sources*, **345**, 67 (2017).
28. J. P. Owejan, T. A. Trabold, and M. M. Mench, *Int. J. Heat Mass Transfer*, **71**, 585 (2014).
29. B. Tjaden, S. J. Cooper, D. J. L. Brett, D. Kramer, and P. R. Shearing, *Current Opinion in Chemical Engineering*, **12**, 44 (2016).
30. D. A. G. Bruggeman, *Annalen der Physik*, **416**, 636 (1935).
31. J. Landesfeind, J. Hattendorff, A. Ehrl, W. A. Wall, and H. A. Gasteiger, *J. Electrochem. Soc.*, **163**, A1373 (2016).
32. G. Selvarani, A. K. Sahu, P. Sridhar, S. Pitchumani, and A. K. Shukla, *J. Appl. Electrochem.*, **38**, 357 (2008).
33. L. R. Jordan, A. K. Shukla, T. Behrsing, N. R. Avery, B. C. Muddle, and M. Forsyth, *J. Appl. Electrochem.*, **30**, 641 (2000).
34. L. R. Jordan, A. K. Shukla, T. Behrsing, N. R. Avery, B. C. Muddle, and M. Forsyth, *J. Power Sources*, **86**, 250 (2000).
35. E. Passalacqua, G. Squadrito, F. Lufrano, A. Patti, and L. Giorgi, *J. Appl. Electrochem.*, **31**, 449 (2001).
36. E. Antolini, R. R. Passos, and E. A. Ticianelli, *J. Power Sources*, **109**, 477 (2002).
37. X. L. Wang, H. M. Zhang, J. L. Zhang, H. F. Xu, Z. Q. Tian, J. Chen, H. X. Zhong, Y. M. Liang, and B. L. Yi, *Electrochim. Acta*, **51**, 4909 (2006).
38. G. Y. Gor, M. Thommes, K. A. Cychosz, and A. V. Neimark, *Carbon*, **50**, 1583 (2012).
39. A. V. Neimark, Y. Lin, P. I. Ravikovitch, and M. Thommes, *Carbon*, **47**, 1617 (2009).
40. C. Simon, F. Hasché, D. Müller, and H. A. Gasteiger, *ECS Transactions*, **69**, 1293 (2015).
41. C. Simon, F. Hasché, and H. A. Gasteiger, *J. Electrochem. Soc.*, **164**, F591 (2017).
42. H. Beyer, S. Meini, N. Tsiouvaras, M. Piana, and H. A. Gasteiger, *PCCP*, **15**, 11025 (2013).
43. K. C. Neyerlin, W. Gu, J. Jorne, A. Clark, and H. A. Gasteiger, *J. Electrochem. Soc.*, **154**, B279 (2007).
44. A. Kongkanand and M. F. Mathias, *The Journal of Physical Chemistry Letters*, **7**, 1127 (2016).
45. P. Antonacci, S. Chevalier, J. Lee, N. Ge, J. Hinebaugh, R. Yip, Y. Tabuchi, T. Kotaka, and A. Bazylak, *Electrochim. Acta*, **188**, 888 (2016).

46. O. S. Burheim, H. Su, S. Pasupathi, J. G. Pharoah, and B. G. Pollet, *Int. J. Hydrogen Energy*, **38**, 8437 (2013).
47. R. Bock, A. Shum, T. Khoza, F. Seland, N. Hussain, I. V. Zenyuk, and O. S. Burheim, *ECS Transactions*, **75**, 189 (2016).
48. Y. A. Gandomi, M. D. Edmundson, F. C. Busby, and M. M. Mench, *J. Electrochem. Soc.*, **163**, F933 (2016).
49. C. K. Mittelsteadt and H. Liu, in *Handbook of Fuel Cells*, W. Vielstich, A. Lamm, and H. A. Gasteiger, Editors, John Wiley & Sons, Ltd (2010).
50. O. S. Burheim, G. Ellila, J. D. Fairweather, A. Labouriau, S. Kjelstrup, and J. G. Pharoah, *J. Power Sources*, **221**, 356 (2013).
51. A. Forner-Cuenca, J. Biesdorf, A. Lamibrac, V. Manzi-Orezzoli, F. N. Büchi, L. Gubler, T. J. Schmidt, and P. Boillat, *J. Electrochem. Soc.*, **163**, F1038 (2016).

4.3. Interaction of Pore Size and Hydrophobicity/Hydrophilicity for Improved Oxygen and Water Transport through Microporous Layers

The article entitled "Interaction of Pore Size and Hydrophobicity/Hydrophilicity for Improved Oxygen and Water Transport through Microporous Layers" was submitted in June 2019 and accepted for publication in the peer-reviewed Journal of the Electrochemical Society in August 2019 as an open access article, distributed under the terms of the Creative Commons Attribution 4.0 License (CC BY-NC-ND). The paper was presented by Christoph Simon at the 6th European PEFC Electrolyser Forum (July 2017) in Lucerne, Switzerland (abstract number: A1105). The permanent web link to the article is http://dx.doi.org/10.1149/2.1111913jes.

While in our previous article, we investigated pore properties of hydrophobic diffusion media, the target of this investigation was to distinguish between effects from the pore size distribution and from hydrophilic/hydrophobic surface properties. In recent studies, various research groups suggested that MPLs with hydrophilic properties have superior performance over conventional hydrophobic MPLs at both dry and humid operating conditions. When studying these publications carefully, we found that in all of these studies hydrophilic and hydrophobic MPLs which had different carbon materials were compared, so that an interaction with differences in pore size distribution and porosity could not be excluded.

In our present study, we first developed a class of MPLs which allowed to adjust the pore size distribution between small pores and large pores. Based on our previously published "Li400" MPL recipe, we prepared MPLs with different ratios of carbon black and vapor grown carbon fibers. We characterized our MPLs with mercury porosimetry and SEM. While the carbon black MPLs reveal a structure with smaller pores and lower porosity, the admixture of carbon fibers shifts the pore size distribution towards larger pore sizes and larger porosities. For the hydrophobic MPLs, we use hydrophobic polytetrafluroethylene as binder. Our fuel cell tests show that the higher the carbon fiber content is, the better the materials perform at humid operating conditions. The effect can be rationalized by a reduced capillary pressure barrier for liquid water in

larger pore sizes, as was found in our previous publications.

To investigate the effect of hydrophilicity, we developed a preparation procedure for MPLs with the same carbon components as before, but with a hydrophilic perfluorosulfonic acid polymer binder instead. In the SEM images, we could not see a difference between the two considered materials with 0% vs. 80% carbon fiber content. Our fuel cell measurements show that at dry conditions, oxygen transport resistances, high frequency resistances, and overall fuel cell performances are very similar. At humid conditions however, the hydrophobic materials clearly outperform their hydrophilic equivalent. While the high frequency resistances are very similar, the oxygen transport resistances of the hydrophilic MPLs are significantly higher. As for hydrophobic MPLs, the hydrophilic MPL with a high carbon fiber content performed significantly better than the carbon black based MPL with a lower oxygen transport resistance.

We explain these observations with a flooding of the small hydrophilic pores in the presence of liquid water and the concomitant blocking of oxygen transport pathways. Furthermore, we suggest a possible explanation for the studies by other research groups that showed performance enhancements by hydrophilic MPLs. When comparing a hydrophobic carbon black based MPL with small pores (i.e., high capillary pressure barrier for liquid water) to a hydrophilic MPL with large pores as our carbon fiber containing MPL (i.e., capillary pressure close to 0), we could falsely conclude that the hydrophilic material shows a better performance.

In summary, in our study we rigorously investigated the effect of pore size distribution and hydrophilicity/hydrophobicity on the oxygen transport resistance and the fuel cell performance at various operating conditions. By replacing carbon black in the MPL with carbon fibers, we could increase the overall fuel cell performance at normal operating conditions for high-pressure applications by 48% at 0.6 V. We furthermore disproved the hypothesis that all-hydrophilic MPLs are superior over conventional hydrophobic MPLs, and presented an explanation for this misinterpretation.

Author contributions

C.S., J.E., and B.N. conducted the experimental work and analyzed the data (preparation of microporous layers, fuel cell measurements and SEM analysis). F.W. contributed the pore size analysis. C.S. wrote and H.G. revised the manuscript. All authors discussed the data, commented on the results, and reviewed the manuscript.

Interaction of Pore Size and Hydrophobicity/Hydrophilicity for Improved Oxygen and Water Transport through Microporous Layers

Christoph Simon,[1,*,z] Joseph Endres,[1] Benjamin Nefzger-Loders,[1] Florian Wilhelm,[2] and Hubert A. Gasteiger[1,]**

[1] *Chair of Technical Electrochemistry, Department of Chemistry and Catalysis Research Center, Technical University of Munich, D-85748 Garching, Germany*
[2] *Centre for Solar Energy and Hydrogen Research Baden-Wuerttemberg, Division 3, Electrochemical Energy Storage and Conversion, D-89081 Ulm, Germany*

Microporous layers consisting of different ratios of acetylene black and carbon fibers with either a hydrophobic polytetrafluoroethylene (PTFE) or a hydrophilic perfluorosulfonic acid (PFSA) ionomer binder are investigated with regards to oxygen and water transport in PEMFCs. For that, the materials are characterized by scanning electron microscopy and mercury porosimetry, revealing an increase of porosity and pore sizes for an increasing carbon fiber content. MPLs, coated onto a commercial hydrophobized non-woven gas diffusion layer substrate, are examined in H_2/air fuel cell tests under differential-flow conditions at various dry and humid operating conditions. For both hydrophobic and hydrophilic MPLs in the presence of significant amounts of liquid water in the diffusion layer substrate, the materials with larger pore sizes, i.e. higher carbon fiber contents, perform superior at 0.6 V and show the lowest oxygen transport resistance. However, at the same carbon composition, hydrophilic MPLs have a lower performance compared to the corresponding hydrophobic MPLs, which is explained by the capillary pressure barriers for different pore properties. At operating conditions relevant for automotive applications, a performance enhancement of 48% could be achieved for a purely carbon fiber based MPL compared to a commercial reference.

 [DOI: 10.1149/2.1111913jes]

Manuscript submitted June 17, 2019; revised manuscript received August 12, 2019. Published September 10, 2019.

Polymer electrolyte membrane fuel cells (PEMFC) require efficient transport pathways for reactant gases (O_2 and H_2) and product water in order to reach high current densities. The depletion of oxygen at the cathode electrode is one of the major sources of overpotentials at high current densities, which is particularly relevant at conditions of high liquid water saturation in the cell.[1–3] The gas diffusion layer (GDL) is the intermediate layer between the gas flow fields and the electrode layers, and is responsible for species transport (O_2/H_2, H_2O), heat removal, and compression distribution. It consists of a carbon fiber-based gas diffusion layer substrate (GDL-S), which is conventionally coated with a microporous layer (MPL). Both the GDL-substrate and the MPL are typically hydrophobically treated with PTFE in order to prevent the flooding of the pores.[4–7]

With its smooth surface, the MPL creates a close contact to the electrode layers, which reduces contact resistances and mitigates the accumulation of liquid water at the interface between GDL-S/MPL and the electrode layer. The MPL is ≈20–50 μm in thickness and has pore sizes on the order of 100–500 nm, much smaller than that of the substrate of ≈10–30 μm.[4,8] It thus represents a layer with a network of small pores, which moves liquid water accumulations away from the electrode toward the GDL-substrate, because small hydrophobic pores are unlikely to store liquid water. Thus, implementing an MPL reduces the overall water fraction in the porous layers, which in turn allows fast oxygen diffusion from the GDL-substrate toward the cathode even at conditions of liquid water condensation.[3,9,10]

The MPL typically consists of one or more carbon materials (carbon black, graphite, etc.) and 10–30wt% of polymer binder (e.g. PTFE) which stabilizes the layer and serves as hydrophobic agent.[4,11–13] Depending on the choice and composition of materials as well as the manufacturing procedure, different properties of the microporous layer can be adjusted, such as porosity/pore size distribution,[13–20] hydrophobicity/hydrophilicity,[21–31] and surface morphology.[6,32] These parameters influence the oxygen and water transport through the layer, and hence, also the overall fuel cell performance. Porosity and pore interconnection which can be influenced by the type of carbon, by a combination of different carbon materials, and/or by additional perforations determine the effective diffusivity of gas through the layer. Particularly at humid conditions, cracks, regular perforations, and large pores serve as effective water transport pathways and were shown to prevent flooding of the layers and interfaces.[15,33,34] Additionally, Tanuma et al. have shown for hydrophilic MPLs that the fuel cell performance is enhanced for carbon materials that result in high porosities.[19,35] Further studies have shown that the hydrophilicity in MPLs can enhance fuel cell performance due to a hypothesized storage of water in hydrophilic pores, which are thought to (i) keep electrodes and membrane hydrated under low relative humidity conditions, and to (ii) facilitate liquid water release from the electrode through the microporous layer by a wicking effect. Thus, the best-performing hydrophilic MPLs prepared by Tanuma and co-workers were based on ionomer binder and carbon fibers.[23,24,30] Another example are the various MPLs prepared by Kitahara et al., based on either (i) carbon black with TiO_2/silicon binder or with PVA binder coated on a hydrophobic sublayer MPL, or (ii) on hydrophilic carbon nanotubes with PTFE binder.[25–27,36,37] Furthermore, a study by Spernjak et al. showed improved oxygen transport and better fuel cell performance for MPLs containing hydrophilic multiwalled carbon nanotubes (MWCNT) or hydrophilic alumosilicate fibers when compared to a commercial hydrophobic MPL; the authors ascribed the superior performance of the fiber based MPLs to the creation of hydrophilic and hydrophobic domains in the MPL.[31] A different paper by Lee et al. using the same MWCNT material is showing similar results, however attributing the improvements in water transport rather to the larger pore sizes present in the MPL with MPLs the muliwalled carbon nanotube containing MPL.[38] On the other hand, Shrestha and et al. reported an increased water saturation at the electrode/MPL interface and a higher mass transport resistance of a GDL with an MPL consisting of a hydrophilic top-layer placed onto a hydrophobic sublayer.[39] However, recently Aoyama et al.[30] reported an analysis of both hydrophilic and hydrophobic MPLs with identical structural properties with respect to porosity, pore size distribution (PSD), and thickness, evaluating the differential-flow H_2/air performance of these MPLs. As will be discussed later, some of their findings are at variance with our H_2/air

*Electrochemical Society Member.
**Electrochemical Society Fellow.
[z]E-mail: christoph.simon@mail.de

performance data and are also inconsistent with our oxygen transport resistance data, which had not been provided in their study.

An important parameter to describe the behavior of liquid water within a microporous structure is the capillary pressure (p_c) determined by the Young-Laplace equation:

$$p_c = p_l - p_v = \frac{4 \cdot \gamma_{H_2O} \cdot \cos\theta}{d_{pore}} \quad [1]$$

where p_l is the liquid phase pressure, p_v is the vapor phase pressure, γ_{H_2O} is the surface tension of water, θ is the inner contact angle of water with the pore surface, and d_{pore} is the pore diameter. This pressure has to be overcome for water in order to penetrate into a hydrophobic pore ($90° < \theta < 180°$, for which $p_c < 0$ kPa) or to deplete a water filled hydrophilic pore ($0° < \theta < 90°$, for which $p_c > 0$ kPa). Both θ and d_{pore} determine the magnitude of p_c, hence, by modifying either one or both one can tune the liquid water transport properties of the material.[40,41]

To analyze the oxygen transport properties of gas diffusion layers in PEM fuel cells, the measurement of the limiting current density (i_{lim}) under differential-flow conditions is a valuable method.[15,33,42–48] Knowing the dry oxygen content in the feed gas ($x_{O_2,dry}$), the cell temperature (T_{cell}), the absolute gas pressure (p_{abs}), and the partial pressure of water vapor (p_{H_2O}), the oxygen transport resistance (R_{T,O_2}) of the cell can be calculated:

$$R_{T,O_2} = \frac{4 \cdot F \cdot x_{O_2,dry}}{i_{lim}} \cdot \frac{p_{abs} - p_{H_2O}}{R \cdot T_{cell}} \quad [2]$$

Here, R_{T,O_2} is composed of the sequential diffusion resistances of oxygen transport from the flow field channels to the active sites of the catalyst layer:

$$R_{T,O_2} = R_{FF,O_2} + R_{GDL-S,O_2} + R_{MPL,O_2} + R_{cathode,O_2} + R_{other,O_2} \quad [3]$$

where R_{FF,O_2} is the resistance within the flow field channels, $R_{GDL\text{-}S,O_2}$ is the resistance of the GDL-substrate, R_{MPL,O_2} is resistance of the MPL, $R_{cathode,O_2}$ is the resistance of the cathode catalyst layer, and R_{other,O_2} is the remaining resistance from other sources (e.g., interfacial resistances between catalyst layer and MPL[47]). The resistances can be discerned into pressure dependent (R_{PD,O_2}) and pressure independent (R_{PI,O_2}) contributions, the former being associated with molecular diffusion processes mostly in the gas diffusion layer and MPL, while the latter is ascribed to Knudsen diffusion in the small pores of the cathode catalyst layer and to diffusion to the platinum catalyst surface across a thin ionomer film so that it increases with decreasing platinum surface area.[43,49,50]

In our previous studies, we have already applied the limiting current density diagnostic to determine interfacial transport resistances originating from the formation of liquid water films as a function of diffusion medium compression as well as to examine the impact of different carbon blacks and MPL perforations on the oxygen transport resistance of microporous layers.[15,47,51] The first scope of the present study is to examine the impact of MPL porosity and pore size distribution (PSD) on the oxygen and water transport in an operating fuel cell. For this, we first prepare microporous layers with polytetrafluoroethylene (PTFE) as hydrophobic binder and different mixtures of carbon black and carbon fibers (between 0 and 100wt%), and then characterize them with scanning electron microscopy and mercury intrusion porosimetry. These MPLs are coated onto commercial GDL-substrate (Freudenberg) and tested in a differentially operated single-cell fuel cell under dry and humid conditions in order to correlate the morphological properties of MPLs with differential-flow H_2/air performance, with the associated high frequency resistances, and with oxygen transport resistances quantified by limiting current density measurements. The second scope of this study is to determine the differences in performance and oxygen transport resistance caused by replacing the hydrophobic with a hydrophilic binder, while maintaining the same MPL morphology (i.e., same carbon composition, thickness, porosity, and pore size distribution). For this, we prepare two MPLs with hydrophilic perfluorosulfonic acid (PFSA) ionomer as binder and compare their oxygen transport resistances and their H_2/air performances to those obtained with hydrophobic MPLs with the same carbon composition and MPL morphology. With this study, we show how oxygen and water transport are impacted by the MPL porosity/PSD and rigorously prove that all-hydrophilic MPLs are actually decreasing performance in the presence of liquid water.

Experimental

MPL and GDL-Substrate materials.—The acetylene black Li400 (Denka; specifications: spec. surface area = 39 m^2 g^{-1}, average particle size = 48 nm) and the vapor grown carbon fibers VGCF-H (Showa Denko; specifications: spec. surface area = 13 m^2 g^{-1}, fiber length = 10–20 μm, fiber diameter = 150 nm) are used as carbon components for the MPLs. Two different binders were used: (i) a hydrophobic PTFE agent and binder (58wt% PTFE dispersion TF 5035GZ from 3M Dyneon) with an average particle size of 200 nm; (ii) a hydrophilic PFSA agent and binder, namely a low equivalent weight PFSA ionomer in a water/alcohol dispersion with an ionomer content of 20wt% (700 EW from Asahi Kasei). As solvent for the MPL ink, either deionized water (Milli-Q, 18 MΩ cm) or 1-propanol (SigmaAldrich) is used. To tune the dispersibility and rheological properties of the PTFE containing inks, Triton X-100 (Sigma Aldrich) and methyl cellulose (SigmaAldrich) are admixed. The compositions of the inks used for the preparation of all the MPLs in this study as well as the final MPL compositions are given in Table I.

As a reference GDL-S/MPL material, a commercially available GDL-substrate with a commercial MPL (Freudenberg) is used, which consists of a ≈50 μm thick MPL composed of carbon black and a hydrophobic binder, applied onto a GDL-S (Freudenberg; hydrophobically treated, ≈154 ± 10 μm thick). The same GDL-substrate was used for the preparation of MPL coatings in the present study, so that when comparing different cathode GDL-S/MPL variants, the only difference is the MPL. The commercially available GDL-S/MPL and GDL-S examined here are the same as those which we had used in our previous study.[15]

Preparation of hydrophobic MPLs.—MPLs with PTFE as binder are prepared as described in our previous work[15] for the pure carbon black MPLs. The here called "0% VGCF MPL" is the same as the one referred to as "Li400 MPL" in Reference 15. While for the pure carbon black or pure VGCF MPLs only one carbon component is used (0% or 100% VGCF MPL), for MPLs with 50% and 80% VGCF, the respective amounts of carbon black and carbon fibers are added. Table I lists all ink compositions; it also lists the final MPL compositions after an initial drying on air at 80°C and a subsequent thermal treatment under air with a final temperature of 380°C to decompose Triton X-100 and the methyl cellulose as well as to evenly spread out the PTFE particles. Free-standing MPLs used for MPL mercury porosimetry analysis were prepared by coating the MPL inks onto a smooth glass plate instead of the GDL-substrate, followed by drying at 80°C and removal from the glass plate by a razor blade. For more details, see Reference 15.

The final thickness of the MPL coated onto the GDL-S (d_{MPL}) is determined with a dial gauge (Mitutoyo series 543; ±3 μm accuracy) by taking the thickness of the GDL-S/MPL at five positions ($d_{GDL\text{-}S\,+\,MPL}$) and subtracting the thickness of the GDL-S ($d_{GDL\text{-}S}$) that is measured at 8 positions around the coated area:

$$d_{MPL} = d_{GDL-S+MPL} - d_{GDL-S} \quad [4]$$

Based on these measurements, all MPLs considered for fuel cell testing in this study have an MPL thickness of $d_{MPL} = 30 \pm 5$ μm.

Preparation of hydrophilic MPLs.—MPLs with PFSA ionomer as hydrophilic agent and binder are prepared as follows. Carbon components and 1-propanol (see Table I) are combined in a 100 ml polypropylene cup which is fixed into a cooling holder maintained at ≈0°C (Thinky 250AD-COOL). The substances are mixed for 2 min at 2000 rpm in a planetary mixer (Thinky ARV-310) at ambient pressure. Subsequently, the PFSA dispersion is added and mixed for 10 min at

Table I. Ink composition for the preparation of MPLs and final MPL compositions.

	ink composition									MPL composition	
MPL	Li400 carbon black [g]	VGCF-H carbon fibers [g]	Triton X-100[1] [g]	methyl cellulose [g]	DI Water [g]	1-propanol [g]	PTFE dispersion[2] [ml]	PFSA dispersion[3] [ml]	solids content[4] [wt%]	VGCF content[5] [wt%]	binder content[6] [wt%]
0% VGCF hydrophobic	6.40	-	0.176	0.77	34.00	-	1.83	-	18	0	20
0% VGCF hydrophilic	6.40	-	-	-	-	29.50	-	6.63	18	0	20
50% VGCF hydrophobic	3.20	3.20	0.176	0.77	34.00	-	1.83	-	18	40	20
80% VGCF hydrophobic	1.28	5.12	0.176	0.77	34.00	-	1.83	-	18	64	20
80% VGCF hydrophilic	1.28	5.12	-	-	-	29.50	-	6.63	18	64	20
100% VGCF hydrophobic	-	6.40	0.176	0.77	34.00	-	1.83	-	18	80	20

[1]For accurate admixture, an aqueous solution with 0.2 $ml_{Triton\ X\text{-}100}/g_{solution}$ was used.
[2]3M Dyneon TF 5035GZ dispersion with 58wt% PTFE content.
[3]Low EW PFSA ionomer dispersion with 20wt% ionomer content.
[4]Content of carbon and PTFE/PFSA: $m_{carbon+PTFE/PFSA}/m_{ink}$.
[5]Prospected VGCF content in MPL, assuming only carbon and binder remain after the final heat treatment: $m_{VGCF}/m_{carbon+PTFE/PFSA}$.[15]
[6]Prospected binder (PTFE/PFSA) content in MPL assuming only carbon and binder remain after the final heat treatment: $m_{PTFE/PFSA}/m_{carbon+PTFE/PFSA}$.

500 rpm. Finally the ink is degassed under vacuum (30 kPa) at the same rotation speed for 2 min.

The coating is accomplished with 75 μm (80% VGCF) or 100 μm (0% VGCF) thick stencils and a doctor blade (analogously to the way described in Reference 15), followed by drying at 80°C for 30 min. In contrast to the PTFE containing coatings, a subsequent heat-treatment procedure at higher temperatures is not necessary, because: (i) the PFSA dispersion is free of additives, hence, no decomposition of unwanted substances is needed; and (ii) the polymer is highly dispersed in the 1-propanol rich solvent,[52] which makes a higher temperature step to enable a flow of the polymer redundant. The thicknesses are measured as for hydrophobic coatings by applying Eq. 4.

Mercury intrusion porosimetry.—Mercury intrusion porosimetry measurements of hydrophobic GDL-S/MPL and hydrophobic freestanding MPL samples ($m_{sample} \approx$ 100 mg–300 mg) are conducted with two porosimeters (Pascal 140 and Pascal 440; CE Elantech, Inc. USA). For freestanding MPLs, the MPL porosity (ε_{MPL}) is calculated from the total cumulative pore volume normalized to the MPL mass v_{pore} (in units of $mm^3_{pore}\ g^{-1}_{sample}$) and the bulk MPL volume v_{MPL} (in units of $mm^3_{pore}\ g^{-1}_{sample}$) which is the sum of the MPL mass normalized pore volume (v_{pore}), the bulk volume of the carbon materials (carbon black and VGCF assuming bulk densites of $\rho_{CB} = 1.9\ g\ cm^{-3}$ and $\rho_{VGCF} = 2.0\ g\ cm^{-3}$) and of the bulk volume of the PTFE binder (using a bulk density of $\rho_{PTFE} = 2.16\ g\ cm^{-3}$).

$$\epsilon_{MPL} = \frac{v_{pore}}{v_{MPL}} = \frac{v_{pore}}{v_{pore} + \frac{w_{CB}}{\rho_{CB}} + \frac{w_{VGCF}}{\rho_{VGCF}} + \frac{w_{PTFE}}{\rho_{PTFE}}} \quad [5]$$

where w_{CB}, w_{VGCF}, and w_{PTFE} refer to the wt% of carbon and PTFE, respectively, in the MPL. The detailed procedure is described in Reference 15.

Scanning electron microscopy.—Images of carbon black, carbon fibers, and all prepared GDL-S/MPL samples (in top- and cross-sectional view) are taken by scanning electron microscopy (SEM). This was mostly done using a FESEM 7500F field emission SEM (JEOL) at acceleration voltages between 0.5 kV and 1.0 kV in the secondary electron imaging mode. For this, the carbon materials are immobilized on a carbon tape and loose particles are blown off. Images of the Li400 carbon black powder are taken at a magnification of x50,000 and images of VGCF at a magnification of x10,000. Top-view images of all prepared MPLs coated on the GDL-substrate were recorded at magnifications of x10,000 and x25,000. Furthermore, cross-sectional images are taken for hydrophobic 0% VGCF and the 100% VGCF MPLs coated on GDL-substrates at a magnification of x250. For that, the samples are prepared by bending the GDL until the MPL breaks naturally and then fixing them in a cross-section sample holder (these images are shown in Figures 4e/4f and will be discussed later).

Finally, the MPLs coated on GDL-substrates with 0% VGCF and 100% VGCF are additionally examined in top- and cross-sectional view in a JCM-6000 benchtop SEM (JEOL) at 5 kV acceleration voltage and a magnification of x500 by the secondary electron detector. Images are shown in Figures 4a–4d. The cross-sectional samples are prepared by cutting the materials with a razor blade in order to create a clean cutting edge; subsequently the materials are fixed in a cross-section sample holder together with the top-view sample (these images, recorded as was done in Reference 15 are shown in Figures 4a–4d and will be discussed later).

Fuel cell test setup.—The fuel cell test assembly is identical to the one used in Reference 15. The most important specifications are summarized in Table II.

Fuel cell test procedures.—Fuel cell tests were conducted according to Ref. 15. Initial cell conditioning is performed by stepping the voltage under hydrogen (1390 nccm; 1 nccm ≡ 1 norm cubic centimeter per minute or 1 nml min^{-1} defined at 0°C and 1 atm, which corresponds to $7.43 \cdot 10^{-7}$ mol s^{-1}) and air (3320 nccm) at $T_{cell} = 80°C$, $p_{abs} = 150$ kPa, and 100% relative humidity (RH) in the following sequence: 0.6 V for 45 min, 0.95 V for 10 min, and 0.85 V for 5 min; this sequence is repeated ten times. Each investigated GDL-S/MPL type is measured two times in individually built cells; the error bars shown in the polarization curves, for the high frequency resistance (*HFR*) and for the oxygen transport resistances (R_{T,O_2}) represent the standard deviation from these two repeat experiments. Differential-flow H_2/air or H_2/dilute-air (10% O_2 in N_2) polarization curves are recorded in potentiostatic mode by stepping the voltage from 0.9 V to 0.3 V (or in some cases 0.05 V) in steps of 50 mV after pre-conditioning the cell at 0.75 V for 15 min, followed by measuring the open circuit voltage (OCV). Each point is held for 10 min to reach steady-state and the shown data are averaged over the last 30 s at each voltage. Impedance spectra are recorded for each data point from 100 kHz to 10 Hz with a perturbation voltage of ±10 mV, using the low noise setup of the hybrid impedance mode of the Gamry potentiostat; the *HFR* is extracted from the high-frequency intercept of the impedance data with the real axis in the associated Nyquist plots. High constant flow rates of 2000 nccm of hydrogen and 5000 nccm of either air or 10% O_2 in N_2 are applied in order to realize differential-flow conditions (stoichiometries for hydrogen and oxygen ≥10 at the highest current densities) at the operating conditions 1–3 listed in Table III.

Please consider that our here shown "dry operating conditions" at $T_{cell} = 80°C$, $p_{abs} = 170$ kPa, and $RH = 70\%$ with differential flows

Table II. Details of fuel cell test setup.

Property	Description
fuel cell setup	single cell with 5 cm^2 active area (Fuel Cell Technologies)
flow fields	5 cm^2 active area, 7 channels with 1 serpentine (Poco Graphite, see Ref. 51)
MEA	W. L. Gore & Associates, Primea Mesga A510.1/M715.18/C580.4
electrode loadings	anode: 0.1 mg_{Pt} cm^{-2}; cathode: 0.4 mg_{Pt} cm^{-2}
GDLs	anode: commercial GDL-substrate w/ MPL (Freudenberg) cathode: commercial GDL-S/MPL (Freudenberg) or in-house prepared MPLs on the same commercial GDL-S
compression/gaskets	PTFE coated glass fabrics (FIBERFLON GmbH & Co. KG) on both electrodes at thicknesses in order to realize ≈20% GDL compression (details in Ref. 47)
fuel cell test station	custom-designed Greenlight Innovation G60 fuel cell test station
test equipment	load module: 120 A Agilent N3306A; potentiostat: Gamry Reference 3000

(hydrogen and air stoichiometries of ≥10) have been developed to result in no liquid water in the fuel cell, in order to investigate the hydrophobic/hydrophilic MPLs at low membrane humidification and in order to be comparable with "dry operating conditions" in single cell tests with stoichiometrically controlled hydrogen and air flows. For example, to achieve an average *RH* of 70% (arithmetic average value between inlet and outlet *RH*) at typical stoichiometries of 1.5 for hydrogen and 1.8 for air and at a cell pressure of 170 kPa_{abs}, the inlet *RH* would have to be approximately 24% considering a co-flow configuration (calculated by a gas and water vapor mass balance between inlet and outlet, and assuming an isothermal cell with negligible pressure drops).

For the measurement of the limiting current density, anode flow rates of 2000 nccm H_2 and cathode flow rates of 5000 nccm diluted oxygen in 10 different dry mole fraction ($x_{O_2,dry}$) between 0.5% and 28% are set. At each $x_{O_2,dry}$, the current densities obtained at 0.30 V, 0.15 V, 0.10 V, and 0.05 V are recorded by holding for 2 min to reach steady-state at each voltage and then averaging the measured current for 15 s. The total oxygen transport resistance (R_{T,O_2}) is calculated according to Eq. 2 and plotted vs. the limiting current density i_{lim}.

Morphology and Performance of Hydrophobic MPLs with Carbon Fibers

Morphology of carbon materials.—For the preparation of all MPLs in this study, two different carbon materials are used: Li400 carbon black (Denka) and vapor grown carbon fibers VGCF-H (Showa Denko). Figure 1 shows SEM images of both materials at different magnifications to capture their dimensional extension. The acetylene black (Figure 1a) consists of carbon black particles, which clearly have widely varying diameters between 20 nm and 300 nm. While the manufacturer provides a mean diameter of 48 nm, Figure 1a shows that the primary particles have a wide range of particle sizes; assuming dense spherical primary carbon particles with a density of ≈1.9 g cm^{-3}, our measured BET area of ≈37 m^2 g^{-1}[15] would yield an average particle size of ≈85 nm. This means that some large particles with >100 nm in diameter must consist of several fused smaller primary particles. All primary particles agglomerate to larger secondary structures of several 100 nm in size, which have different shapes from chains to bulky spheres.

The VGCF-H carbon fibers are shown in Figure 1b. While we measure fiber lengths of mostly <10 µm, the manufacturer specifies 10–20 µm. On the other hand, the measured fiber diameters in the range of ≈70–200 nm fit well with the manufacturer specification of ≈150 nm. Although the SEM image in Figure 1b is made from the pure VGCF-H fibers, some spherical particles and particle agglomerates can be observed, which are adhered to the fibers. Contrary to the rather bulky structures of the Li400 carbon black, the VGCF-H material consist of long carbon fibers, which are on the order of magnitude of the MPL thickness of 30 ± 5 µm. This completely different morphology of the VGCF-H fibers is thus expected to significantly affect the MPL structural properties, which is why we decided to utilize these two materials. Note that furtheron, VGCF-H will be referred to as VGCF for simplicity.

Structural characterization of GDLs and MPLs.—In the following, we analyze freestanding MPLs and the respective MPLs coated on GDL-substrates by SEM imaging in order to investigate their structural properties (Figure 2 and Figure 4) as well as by mercury porosimetry to determine porosities and pore size distributions of the porous materials (Figure 3 and Figure 5). For MPLs with hydrophobic PTFE binder (for compositions see Table I), VGCF contents of 0% (pure carbon black, Figures 2a/2b), 50% (Figures 2e/2f), 80% (Figures 2g/2h), and 100% (i.e., only VGCF, Figures 2k/2l) are realized. The SEM top-view images of these MPLs (from the final GDL-S/MPL samples) are shown in Figure 2. The structures of the materials which consist of only one carbon component (0% and 100% VGCF MPLs) are determined by the carbon component itself. The pure carbon black based MPL (0% VGCF MPL, Figures 2a/2b) shows rather small pores, resulting from the carbon black secondary agglomerate structure; on the other hand, the pure VGCF based MPL (100% VGCF MPL, Figures 2k/2l) is dominated by the structure-forming carbon fibers, which create a pore

Table III. Fuel cell test conditions, with the same conditions being applied to anode and cathode. Cell pressures are always given as absolute pressures measured at the cell inlet.

N°	Name	T_{cell} [°C]	p_{abs} [kPa]	*RH* [%]	Figures
1	dry[1,2]	80	170	70	Figure 7, Figure 12
2	humid[1,2]	50	300	120	Figure 8, Figure 13
3	normal[1,2,3,4]	80	300	100	Figure 9, Figure 10
4	transition[1]	50	400	77	Figure 6, Figure 11

[1]measurement of the limiting current density.
[2]differential-flow H_2/air polarization curves in air.
[3]differential-flow polarization curves with H_2 and 10% O_2/N_2.
[4]only measured for the hydrophobic commercial MPL, the 0% VGCF MPL, and the 100% VGCF MPL.

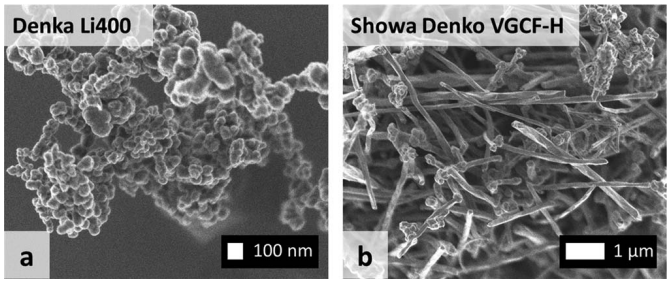

Figure 1. Scanning electron microscopy images of (a) Denka Li400 carbon black with a magnification of x50,000, and (b) Showa Denko VGCF-H carbon fibers with a magnification of x10,000.

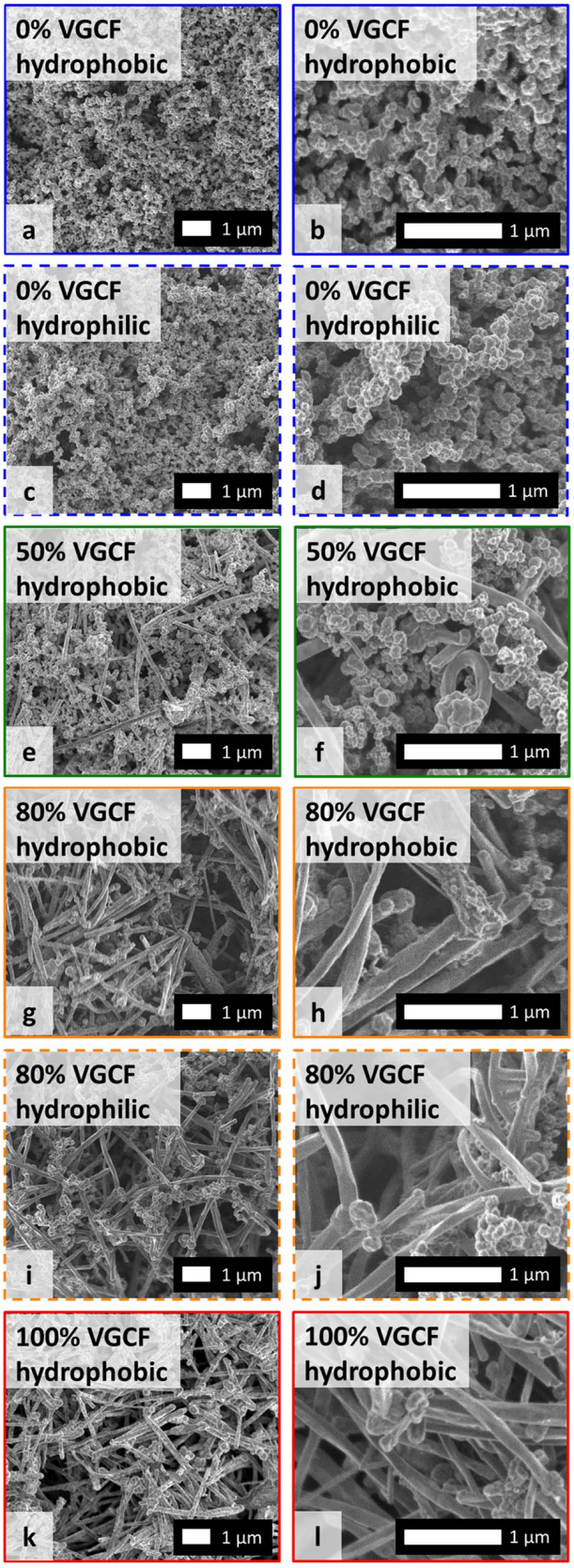

Figure 2. SEM top-view images of the MPL side of GDL-S/MPL samples for fuel cell testing showing hydrophobic and hydrophilic MPLs with: (a,b) 0% VGCF and PTFE binder, (c,d) 0% VGCF and PFSA binder, (e,f) 50% VGCF and PTFE binder, (g,h) 80% VGCF and PTFE binder, (i,j) 80% VGCF and PFSA binder, and (k,l) 100% VGCF and PTFE binder. Magnifications are x10,000 (a,c,e,g,i,k) and x25,000 (b,d,f,h,j,l,). Images of 0% VGCF MPL are taken from Ref. 15.

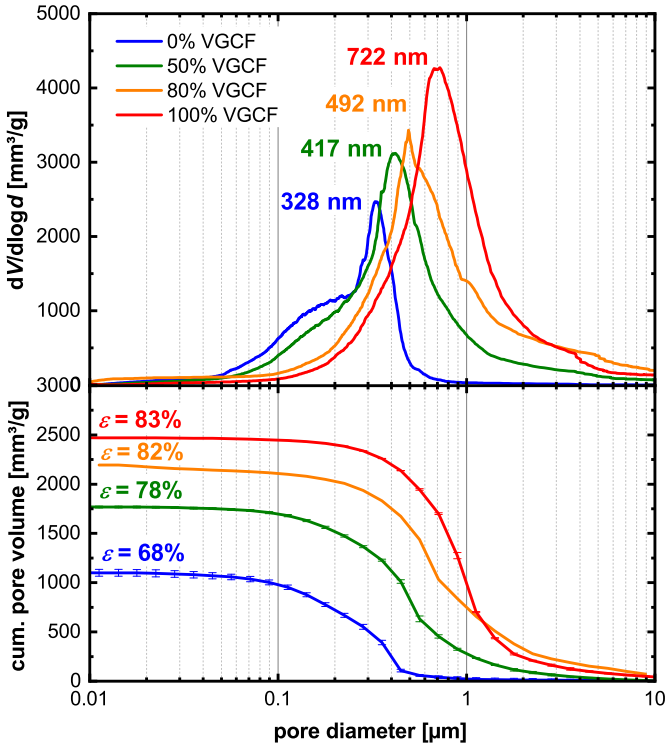

Figure 3. Mass-normalized cumulative pore volume (lower panel) and differential pore volume d*V*/dlog*d* (upper panel) as function of pore diameter for freestanding hydrophobic MPLs with 0% VGCF (blue lines), 50% VGCF (green lines), 80% VGCF (orange lines), and 100% VGCF (red lines), all using PTFE binder (for compositions see Table I). Porosities ε [%] obtained from the cumulative pore volumes (v_{pore}) using Eq. 5 and the PSD-maxima [nm] are referred in the graph. Data of 0% VGCF MPL are taken from Ref. 15.

network with clearly larger pores and an apparently higher porosity. The small particles which are visible for the 100% VGCF MPL in Figures 2k/2l are also visible in the as-received fiber material in Figure 1b, so that it must originate from the fiber rather than from the MPL production. The 50% and 80% VGCF MPLs (Figures 2e–2h) appear as expected like mixtures of the pure materials. Qualitatively, the SEM images suggest an increase of pore size and porosity with increasing VGCF content. Interestingly, while all MPLs contain 20wt% of PTFE (corresponding to ≈20vol.% PTFE), there are no PTFE particles visible any of the in-lab prepared MPLs compared to the commercial MPL (as was shown in Fig. 3b of Ref. 15). This indicates that the PTFE is finely dispersed, presumably as a thin film within the MPL, as previously shown.[15]

By mercury porosity measurements a quantification of the pore size distribution and the porosities is achievable for the MPL when using freestanding MPLs (i.e., w/o GDL-substrate). Figure 3 shows the differential mass-normalized pore volume d*V*/dlog*d* in the upper graph and the cumulative mass-normalized pore volume in the lower graph. All MPLs have pore sizes in the range from 50 nm to 10 µm, except for the 0% VGCF MPL (blue line) for which the largest pores are only ≈800 nm and which has the smallest PSD-maximum of 328 nm, as reported previously.[15] With increasing VGCF content of 50% (green line), 80% (orange line) and 100% (red line), the pore size distribution broadens and is shifting toward larger pore sizes, with PSD-maxima of 417 nm, 492 nm, and 722 nm. At the same time, the total cumulative pore volume of the MPLs (v_{pore}) is increasing with increasing VGCF content, from 1100 mm^3 g^{-1} for 0% VGCF to 2470 mm^3 g^{-1} for 100% VGCF. Using Eq. 5, this corresponds to an increase in porosity from 68% for 0% VGCF, to 78% for 50% VGCF, to 82% for 80% VGCF, and finally to 83% for 100% VGCF. Thus, the quantitative porosity results from mercury intrusion measurements on freestanding MPLs confirm the impression from the SEM images in Figure 2, which qualitatively

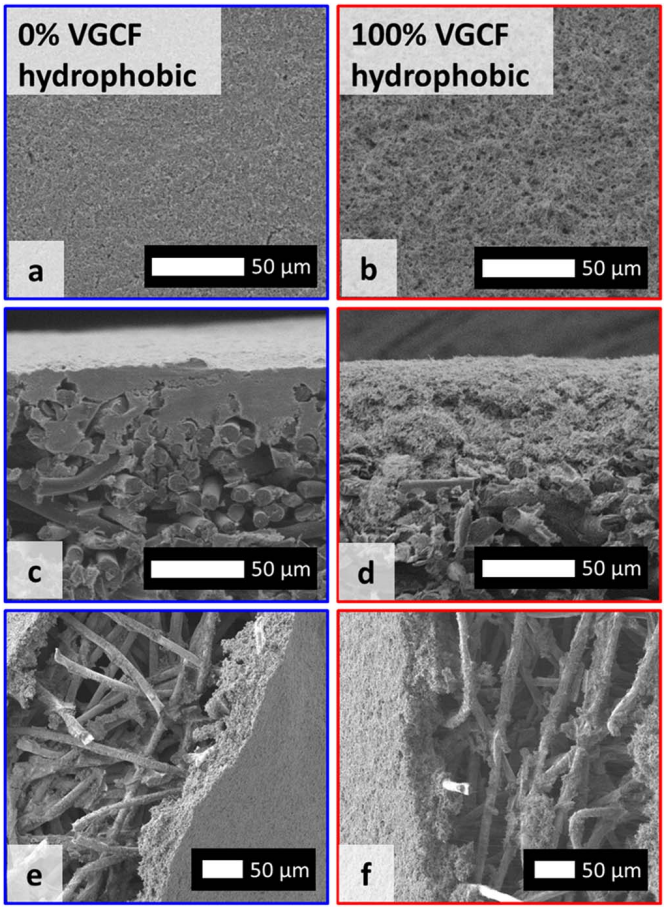

Figure 4. Scanning electron microscopy images of GDL-S/MPL samples for fuel cell testing composed of MPLs with (a,c,e) 0% VGCF and PTFE binder, and (b,d,f) 100% VGCF and PTFE binder. Images show top-views of the MPLs with magnification of x500 (a,b) as well as cross-sectional views prepared either by cutting with a magnification of x500 (c,d; MPL on top) or by bending the samples with a magnification of x250 (e,f). Images of 0% VGCF MPL are taken from Ref. 15.

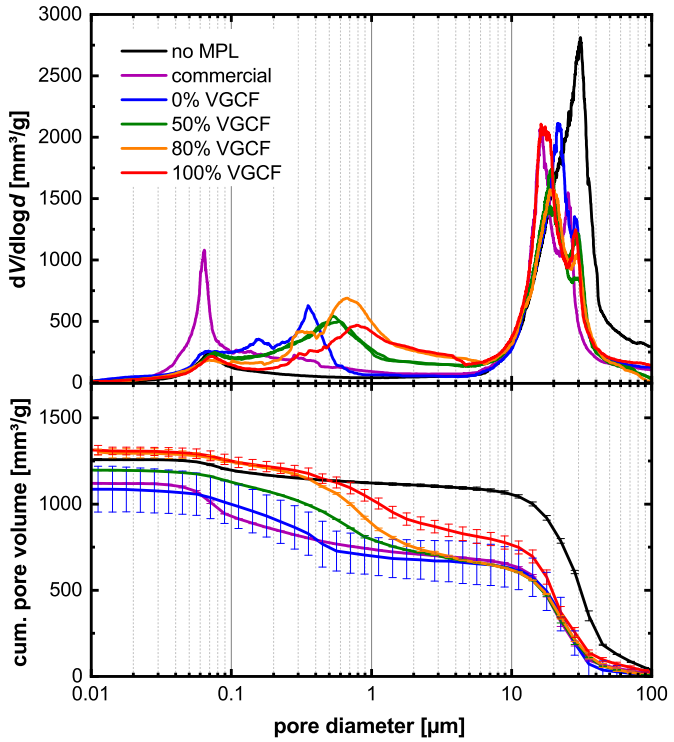

Figure 5. Mass-normalized cumulative pore volume (bottom) and differential pore volume d*V*/dlog*d* (top) as function of pore diameter measured by mercury intrusion porosimetry for the Freudenberg GDL-substrate w/o MPL (black lines) and for the hydrophobic (20wt% PTFE) GDL-S/MPL samples based on the same substrate coated with the following MPLs: commercial MPL (purple lines), MPLs with 0% VGCF (blue lines), with 50% VGCF (green lines), with 80% VGCF (orange lines), and 100% with VGCF (red lines). Data of the 0% VGCF MPL, the commercial MPL, and for GDL-substrate without MPL are taken from Ref. 15.

indicated an increase in pore size and porosity for an increasing VGCF content.

SEM images of the hydrophobic GDL-S/MPL samples used for electrochemical testing are shown in Figure 4 for 0% VGCF (a,c,e) and 100% VGCF (b,d,f), with top-views of the MPLs (a,b) and in also in cross-sectional views produced either by cutting (c,d) or by bending the samples (e,f). In the top-view of the MPL images at a magnification of x500, no macroscopic cracks are observed in neither the 0% VGCF MPL (a) nor in the 100% VGCF MPL (b). Nevertheless, even at these low magnifications, we can see in both the top-view (a,b) and the cross-sectional view (c,d) the dense structure of the pure carbon black MPL (a,c) compared to the fluffy structure of the 100% VGCF MPL (b,d). For both MPLs, distinct intrusion of the MPL into the GDL substrate is observed. Despite the length of the VGCF fibers of up to 10 µm, these imbibe snugly into the larger pore structure of the GDL-substrate with pore sizes of around 30 µm. From the MPL cross-sectional images obtained by bending the samples (Figures 4e/4f), one can get an impression about the adhesive interaction between MPL and GDL substrate: when applying mechanical bending stress, the MPL is breaking, while the rather robust GDL-substrate still remains intact. Even though the MPL is breaking, it still adheres to the GDL-substrate. At the position, which becomes free of the MPL layer, there are still particles of carbon black or VGCF left sticking to the GDL-substrate, indicating that the carbon/PTFE composite has a very strong contact to the GDL-substrate and that the MPL exhibits a high mechanical stability.

To investigate the interaction between MPL and GDL-substrate, Figure 5 is showing the results of mercury intrusion porosimetry of the different GDL-S/MPL samples, with MPLs coated onto the same GDL-S, including a commercial MPL and the GDL-substrate without MPL (details see also Ref. 15). The substrate without MPL ("no MPL", black line) is showing one large peak at ≈30 µm containing most of the pore volume. Additionally it exhibits another a small peak at ≈70 nm, which presumably originates from a carbon containing impregnation of the GDL-substrate.[15] If an MPL is coated onto the GDL-substrate, its pore size distribution is shifted toward smaller pore sizes, with a now lower PSD-maximum of ≈20 µm, likely due to the filling of large pores by the intruding MPL.[15]

As outlined before, pore sizes of the MPL are registered in the range of up to 10 µm. The purple line reveals the data from the commercial GDL-S/MPL (same data as in Ref. 15), with a second PSD-maximum at 64 nm from the MPL, which constitutes the MPL with the smallest pores in the present study. The 0% VGCF MPL shows a PSD-maximum at 353 nm (freestanding MPL: 328 nm), the 50% VGCF MPL at 586 nm (freestanding MPL: 417 nm), the 80% VGCF MPL at 671 nm (freestanding MPL: 492 nm), and the 100% VGCF MPL at 782 nm (freestanding MPL: 722 nm). The pore sizes follow the same trend as for the freestanding MPLs (see Figure 3), with an increase in pore size with increasing VGCF content. It should be noted that the PSD-maxima ascribed to the MPL when referencing the data in Figure 5 to the MPL weight are slightly smaller in case of the coated MPLs. However, one has to state that the absolute MPL volume in case of the GDL-S/MPL samples is significantly smaller than for the equivalent freestanding MPL, and also that the MPL features in the PSD partially overlap with those of the GDL-substrate at ≈ 70 µm, which is why the data in the relevant pore size range is not so clear as for the freestanding MPLs in Figure 3. Also, the total cumulative pore

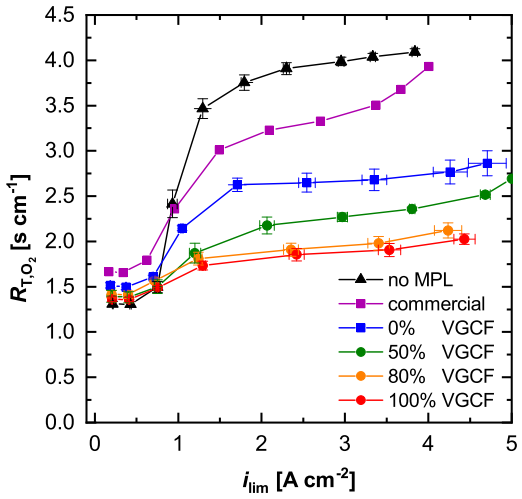

Figure 6. R_{T,O_2} as function of limiting current density under **transition conditions** for the Freudenberg GDL-substrate with no MPL (black) and with the following hydrophobic cathode MPLs coated on the same substrate: commercial MPL (purple), 0% VGCF (blue), 50% VGCF (green), 80% VGCF (orange), and 100% VGCF (red), with PTFE as binder. Operating conditions are $T_{cell} = 50°C$, $RH = 77\%$, $p_{abs} = 400$ kPa; i_{lim} was measured for various dry oxygen contents ($x_{O_2,dry}$) between 0.5% and 28%. Data of 0% VGCF MPL, commercial MPL and no MPL are taken from Reference 15. The error bars represent the standard deviation of from two independently measured cells.

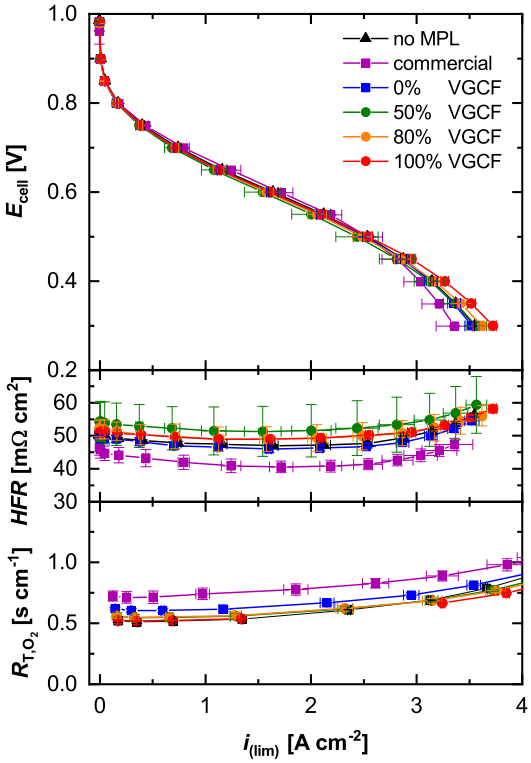

Figure 7. Differential-flow H_2/air polarization curves under **dry conditions** ($T_{cell} = 80°C$, $RH = 70\%$, $p_{abs} = 170$ kPa) showing cell voltage (E_{cell}, top) and high frequency resistance (HFR, middle) versus current density (i) as well as total oxygen transport resistance (R_{T,O_2}, bottom) versus the limiting current density (i_{lim}) for the GDL-substrate with no MPL (black) and the following hydrophobic cathode MPLs coated on the same GDL-substrate: commercial MPL (purple), 0% VGCF MPL (blue), 50% VGCF MPL (green), 80% VGCF MPL (orange), and 100% VGCF MPL (red), with PTFE as binder. The limiting current density is measured for various dry oxygen contents ($x_{O_2,dry}$) between 0.5% and 28%. The error bars represent the standard deviation of two independently measured cells. Data of the 0% VGCF MPL, the commercial MPL, and no MPL are taken from Reference 15.

volumes (Figure 5, lower graph) do not follow the trend of the free-standing MPLs in Figure 3, because in the present case the cumulative pore volume is dominated by the larger portion of the GDL-substrate.

Oxygen transport resistance and fuel cell performance.—To analyze the oxygen transport properties at dry and humid conditions, the oxygen transport resistance was determined via the limiting current density at various dry oxygen contents ($x_{O_2,dry}$) in the cathode feed gas. Figure 6 shows the total oxygen transport resistance (R_{T,O_2}) versus the limiting current density (i_{lim}) at conditions where a transition from a dry to a water saturated diffusion medium is observable ($T_{cell} = 50°C$, $RH = 77\%$, $p_{abs} = 400$ kPa). At small limiting current densities of $i_{lim} < 0.5$ A cm^{-2}, obtained with $x_{O_2,dry}$ of 0.5% and 1.0%, the GDL, the MPL, and the cathode electrode do not contain liquid water and R_{T,O_2} is constant at a low level. At elevated current densities, liquid water is condensing inside the pores of the GDL-S/MPL and the cathode electrode, causing a partial blockage of gas diffusion pathways. This leads to an increase of R_{T,O_2} until a maximum level of water saturation at >2 A cm^{-2} is reached for all MPLs.

In the dry region, the GDL without MPL ("no MPL", black symbols) has the smallest R_{T,O_2} of 1.3 s cm^{-1} due to the absence of the additional diffusion resistance imposed by the MPLs. As already shown in our previous study, the GDL with the commercial MPL (purple symbols), which is thicker (≈50 μm) and has a lower effective diffusivity,[15] shows the highest dry R_{T,O_2} of ≈ 1.7 s cm^{-1}. On the other hand, the thinner 0% VGCF MPL (blue line) has a distinctly smaller dry R_{T,O_2}; the addition of VGCF further reduces R_{T,O_2}, but the curves of 50%, 80%, and 100% VGCF (green/orange/red lines) are actually overlapping in the dry region.

In the region where the porous layers have reached their water saturation level, obtained at i_{lim} >2 A cm^{-2}, more significant differences can be observed. A GDL-substrate without MPL is known to flood immediately at the interface between GDL and cathode if liquid water is present, which leads to a severe increase of oxygen transport resistance and to high R_{T,O_2}.[3,15,47] The presence of the commercial MPL reduces R_{T,O_2} at humid conditions significantly. Applying the 0% VGCF MPL, a further reduction to a level of R_{T,O_2} ≈ 2.6 s cm^{-1} is achieved. By replacing the carbon black with a VGCF containing MPL, the oxygen transport can be decreased to a level of ≈2.3 s cm^{-1} (50% VGCF), ≈2.0 s cm^{-1} (80% VGCF), and ≈1.9 s cm^{-1} (100% VGCF). This corresponds to a reduction of R_{T,O_2} by ≈25% comparing the 0% VGCF with the 100% VGCF MPL.

These findings significantly affect the differential-flow H_2/air performance particularly at humid (Figure 8) and normal conditions (Figure 10) where liquid water is present in the diffusion medium, while the performance impact under dry conditions is minor (Figure 7). The latter is illustrated for the dry operating conditions ($T_{cell} = 80°C$, $RH = 70\%$, $p_{abs} = 170$ kPa) in Figure 7, with the cell voltage (E_{cell}; top panel) and the high frequency resistance (HFR; middle panel) plotted versus the current density (i) as well as with the oxygen transport resistance (R_{T,O_2}) plotted versus the limiting current density (i_{lim}). Here, the H_2/air polarization curves of all tested materials are indeed very similar, with a current of around 1.6 A cm^{-2} at a cell voltage of 0.6 V. The associated HFR values at the open circuit voltage (OCV) range from 40–55 mΩ cm^2, then decrease slightly with increasing current density due to a humidification of the membrane, and finally increase at current densities of >2 A cm^{-2} due to membrane dry-out as explained in Reference 15. The R_{T,O_2} values for all materials are at a very low level between 0.5 s cm^{-1} and 0.75 s cm^{-1}, increasing very little with increasing i_{lim}, which is consistent with the expectation that the under these dry conditions the porous media remain free of liquid water at all limiting current densities and that no water condensation is taking place.

The essentially identical cell voltage at 1.6 A cm^{-2} suggests that the O_2 transport induced losses must be negligible under dry conditions, which is indeed consistent with the O_2 transport induced voltage losses

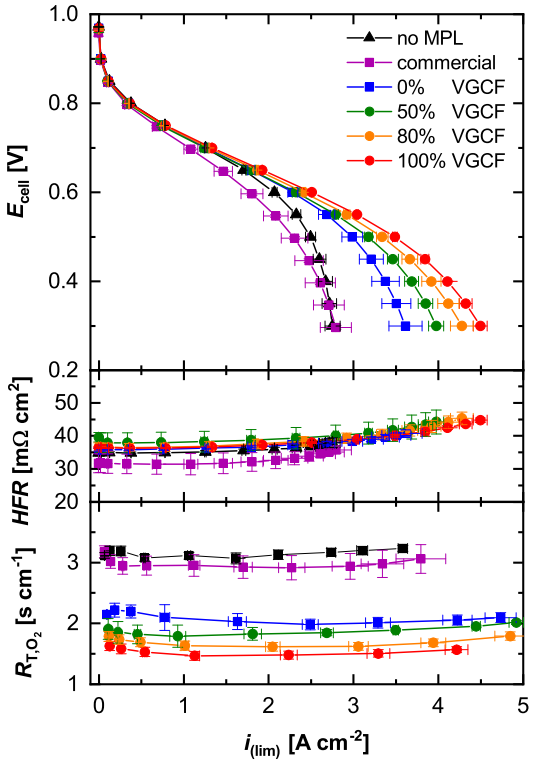

Figure 8. Differential-flow H_2/air polarization curves at **humid conditions** ($T_{cell} = 50°C$, $RH = 120\%$, $p_{abs} = 300$ kPa) showing cell voltage (E_{cell}, top) and high frequency resistance (*HFR*, middle) versus current density (i) as well as total oxygen transport resistance (R_{T,O_2}, bottom) versus the limiting current density (i_{lim}) for the GDL-substrate with no MPL (black) and the following hydrophobic cathode MPLs coated on the same GDL-substrate: commercial MPL (purple), 0% VGCF MPL (blue), 50% VGCF MPL (green), 80% VGCF MPL (orange), and 100% VGCF MPL (red), with PTFE as binder. The limiting current density is measured for various dry oxygen contents ($x_{O_2,dry}$) between 0.5% and 28%. The error bars represent the standard deviation of two independently measured cells. Data of the 0% VGCF MPL, the commercial MPL, and no MPL are taken from Reference 15.

of $\Delta U_{O2-tx} \approx 7$–11 mV calculated for $i = 1.6$ A cm^{-2} according to:[53]

$$\Delta U_{O_2-tx} = \frac{RT}{F} \cdot \left(\frac{1}{4} + \frac{\gamma}{\alpha}\right) \cdot \ln\left(\frac{p_{O_2,channel} - \frac{RT}{4F} \cdot R_{T,O_2} \cdot i}{p_{O_2,channel}}\right) \quad [6]$$

where R is 8.314 J mol^{-1} K^{-1}, F is the Faraday constant, γ is the ORR reaction order with respect to oxygen partial pressure ($\gamma = 0.75$), α is the effective transfer coefficient for the oxygen reduction reaction ($\alpha = 1$), and $p_{O_2,channel}$ is the O_2 partial pressure in the flow field channel of $p_{O_2,channel} \approx 28$ kPa (based on a cathode pressure of 170 kPa$_{abs}$, an O_2 concentration of 21%, and a water vapor pressure of ≈33 kPa at 80°C and 70% RH). Hence, at conditions where no liquid water is present in the diffusion medium, the impact of the MPL for a given GDL-substrate at relevant cell voltages is rather negligible.

This is very different for the differential-flow H_2/air performane at humid conditions ($T_{cell} = 50°C$, $RH = 120\%$, $p_{abs} = 300$ kPa; see Figure 8), at which a significant fraction of liquid water saturation in the GDL-S/MPL occurs. At 0.6 V, the hydrophobic 0% VGCF MPL based on carbon black reaches a current density of 2.3 A cm^{-2} (blue symbols/lines), which is an enhancement compared to the GDL-substrate without MPL of 2.1 A cm^{-2} (black symbols/lines). Due to the higher thickness (∼50 μm compared to 30 μm in-lab prepared MPLs) and lower effective diffusivity (smaller pore sizes, see Figure 5), both reflected by the significantly higher oxygen transport resistance (1.5–2 times higher compared to the in-lab prepared MPLs), the GDL with the commercial MPL even undercuts this performance with a current density of 1.8 A cm^{-2} (purple symbols/lines). The higher oxygen transport resistance even cannot be compenstated by the ∼10 mΩ cm^2 lower *HFR* (a more detailed analysis can be found in Reference 15). With increasing VGCF content, however, we are able to increase the current density to 2.5 A cm^{-2} for 100% VGCF (red symbols/lines). The *HFRs* at OCV vary between 32-40 Ω cm^2, with the commercial MPL showing the lowest value, at high current densities of >2 A cm^{-2} and the accompanying lower efficiencies, the *HFR* also at the humid conditions increases slightly by 25%, presumably due to membrane dry-out. The reason for the superior performance of the hydrophobic VGCF based MPLs is the oxygen transport resistance: the higher the VGCF content, the lower becomes R_{T,O_2}. In the present case the GDL-S/MPL contains large amounts of liquid water already at the lowest current densities due to the over-humidified reactant feeds (120% *RH*) which result in the condensation of water in the porous layers. The constant level of R_{T,O_2} with constant values independent from the limiting current density indicates that the water saturation within the layers does not change significantly with current density, so that the effective O_2 diffusivity remains essentially constant. By using VGCF in the MPL, R_{T,O_2} can be effectively reduced by ≈29% from ≈2.1 s cm^{-1} for 0% VGCF to ≈1.5 s cm^{-1} for 100% VGCF. The GDL-substrate without MPL and with the commercial MPL are at significantly higher levels of ≈3.0–3.1 s cm^{-1}, analogous to what was already observed in Figure 6.

To see how the materials perform at operating conditions relevant for automotive applications, we measured differential-flow polarization curves, high frequency resistances, and limiting current densities at $T_{cell} = 80°C$, $RH = 100\%$, $p_{abs} = 300$ kPa in both air (simulating the stack inlet) as well as in 10% O_2 in N_2 (simulating the oxygen concentration at the stack outlet at an oxygen stoichiometry of 1.75).[54] The results for the cathode GDL-substrates with the hydrophobic commercial MPL, the 0% VGCF MPL, and the 100% VGCF MPL are shown in Figure 9 (10% O_2 in N_2) and in Figure 10 (air, i.e., 21% O_2). The performances at 0.6 V in either 10% O_2/N_2 or air are 1.5 A cm^{-2} and 2.2 A cm^{-2} for the commercial MPL, 2.1 A cm^{-2} and 3.1 A cm^{-2} for the 0% VGCF MPL, and 2.3 A cm^{-2} and 3.3 A cm^{-2} for the 100% VGCF MPL, respectively. The corresponding high frequency resistances are all at ≈30 mΩ cm^2 and show an increase at current densities >2 A cm^{-2} for 10% O_2 and >4 A cm^{-2} for air, where the efficiency of the cell decreases and the heat release increases. This also indicates membrane dry-out as discussed before.

The oxygen transport resistances shows a similar trend as at humid conditions (see Figure 8), where the commercial MPL exhibits a higher R_{T,O_2} of 1.2 s cm^{-1} compared to the 0% and 100% VGCF MPLs with a rather similar R_{T,O_2} of ≈0.9 s cm^{-1}. As shown in Reference 15 for the same or similar GDL materials at an identical point of operation, the GDL substrate, MPL, and cathode electrode are free of liquid water, so the oxygen transport resistance, which also in the present case is essentially constant over the whole range of i_{lim}, is only determined by the structural properties of the materials. Hence, the effective diffusivity of oxygen through the dry porous layers determines R_{T,O_2}.

Morphology and Performance of Hydropbobic vs. Hydrophilic MPLs

Characterization of hydrophilic MPLs.—For preparing hydrophilic MPLs, we replace the hydrophobic PTFE binder with a hydrophilic PFSA ionomer as a binder, a polymeric acid consisting of a fluorinated backbone polymer functionalized with sulfonic acid groups.[55] This material absorbs water and effectively reduces the contact angle θ (see Eq. 1).[35,56,57] Because PFSA already starts to decompose at temperatures of ≈300°C in air[58,59] as compared to PTFE with decomposition temperatures of >400°C, it is not possible to perform a temperature treatment to >300°C, which would be necessary in order to decompose Triton X-100 and methylcellulose.[15] Hence, an alternative preparation procedure is developed with 1-propanol as a solvent, in which the carbon components are well dispersable without additional stabilizers or thickeners (see Table I). We prepare hydrophilic MPLs with 0% VGCF (Figures 2c/2d) and 80% VGCF (Figures 2i/2j) in

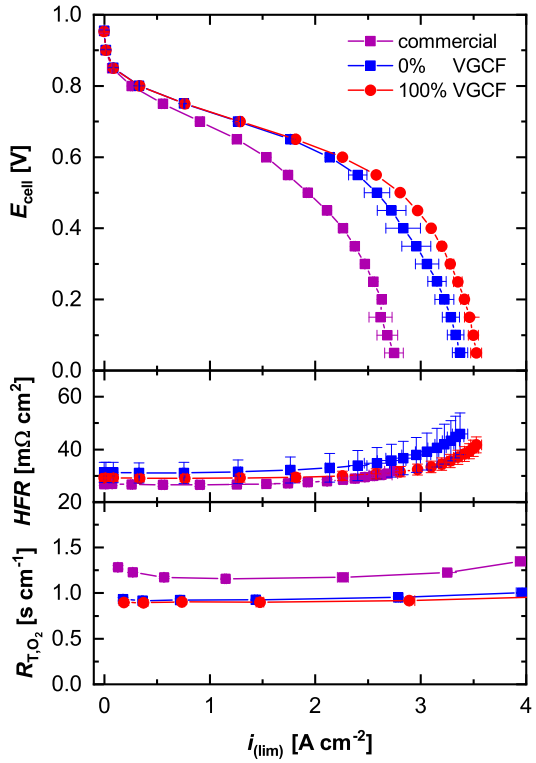

Figure 9. Differential-flow polarization curves under **normal conditions** relevant for automotive applications ($T_{cell} = 80°C$, $RH = 100\%$, $p_{abs} = 300$ kPa) with **H_2 and 10% O_2 in N_2** to mimick the stack outlet conditions, showing cell voltage (E_{cell}, top) and high frequency resistance (*HFR*, middle) versus current density (i) as well as total oxygen transport resistance (R_{T,O_2}, bottom) versus the limiting current density (i_{lim}) for the following hydrophobic cathode MPLs coated on the same Freudenberg GDL-substrate: commercial MPL (purple), 0% VGCF MPL (blue), and 100% VGCF MPL (red), with PTFE as binder. The limiting current density is measured for various dry oxygen contents ($x_{O_2,dry}$) between 0.5% and 28%. The error bars represent the standard deviation of two independently measured cells. Data of 0% VGCF MPL and commercial MPL are taken from Ref. 15.

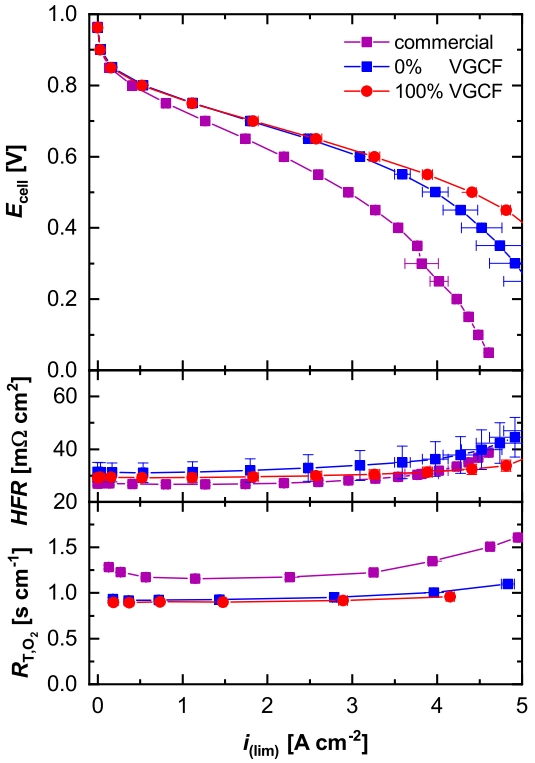

Figure 10. Differential-flow H_2/air polarization curves under **normal conditions** relevant for automotive applications ($T_{cell} = 80°C$, $RH = 100\%$, $p_{abs} = 300$ kPa) with **H_2/air** to mimick the stack inlet conditions showing cell voltage (E_{cell}, top) and high frequency resistance (*HFR*, middle) versus current density (i) as well as total oxygen transport resistance (R_{T,O_2}, bottom) versus the limiting current density (i_{lim}) for the following hydrophobic cathode MPLs coated on the same Freudenberg GDL-substrate: commercial MPL (purple), 0% VGCF MPL (blue), and 100% VGCF MPL (red), with PTFE as binder. The limiting current density is measured for various dry oxygen contents ($x_{O_2,dry}$) between 0.5% and 28%. The error bars represent the standard deviation of two independently measured cells. Data of the 0% VGCF MPL and the commercial MPL are taken from Reference 15.

order to create a significant structural contrast. These materials can be compared to the hydrophobic MPLs with the same carbon composition namely 0% VGCF (Figures 2a/2b) and 80% VGCF (Figures 2g/2h). The morphology of the hydrophilic and hydrophobic MPLs are indistinguishable in the SEM images. For 0% VGCF, the more dense structure is dominated by the carbon black, while for 80% VGCF the carbon framework is defined by the carbon fibers and only few carbon black particles are observed in the SEM images. Even though the hydrophobic and hydrophilic MPLs are prepared by different procedures and with ink compositions (see Experimental section), the morphology of the resulting MPLs are very similar, so that their main differences are expected to be due to differences in their hydrophilicity.

Oxygen transport and fuel cell performance of hydrophilic/hydrophobic MPLs.—The oxygen transport resistance R_{T,O_2} for hydrophilic MPLs is investigated at $T_{cell} = 50°C$, $RH = 77\%$, $p_{abs} = 400$ kPa, the same condition at which the hydrophobic MPLs were first evaluated (Figure 6). The data for the hydrophilic MPLs (open symbols) with 0% VGCF (blue lines/symbols) and 80% VGCF (orange lines/symbols) are plotted in Figure 11 together with the correspondent hydrophobic MPLs (full symbols) of the same carbon composition (same data as in Figure 6). At small limiting current densities of $i_{lim} < 0.5$ A cm^{-2}, obtained with $x_{O_2,dry}$ of 0.5% and 1.0%, the GDL-S/MPLs do not contain liquid water and the measured oxygen transport resistances are very similar with $\approx$1.5 s cm^{-1} for all four MPLs, with the 80% VGCF MPLs showing slightly smaller R_{T,O_2} values as was observed also in Figure 6. This is

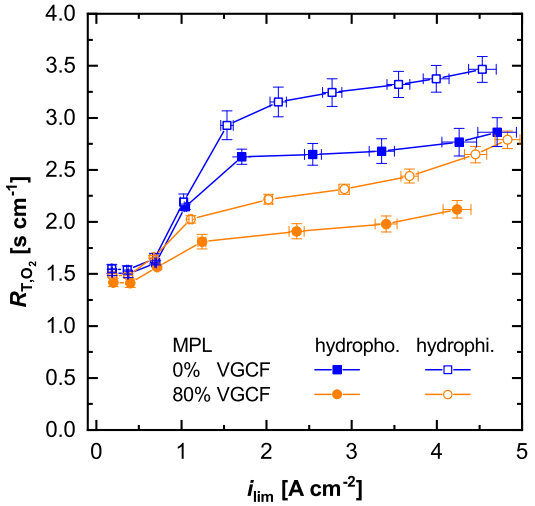

Figure 11. R_{T,O_2} as function of limiting current density under **transition conditions** for the following MPLs coated on the Freudenberg GDL-substrate: 0% VGCF with hydrophobic PTFE (blue line, full squares) or hydrophilic PFSA (blue line, empty squares) as binder, and 80% VGCF with PTFE (orange line, full squares) or PFSA (orange line, empty squares) as binder. Operating conditions are $T_{cell} = 50°C$, $RH = 77\%$, $p_{abs} = 400$ kPa; i_{lim} was measured for various dry oxygen contents ($x_{O_2,dry}$) between 0.5% and 28%. Data of the hydrophobic 0% VGCF MPL is taken from Reference 15. The error bars represent the standard deviation of from two independently measured cells.

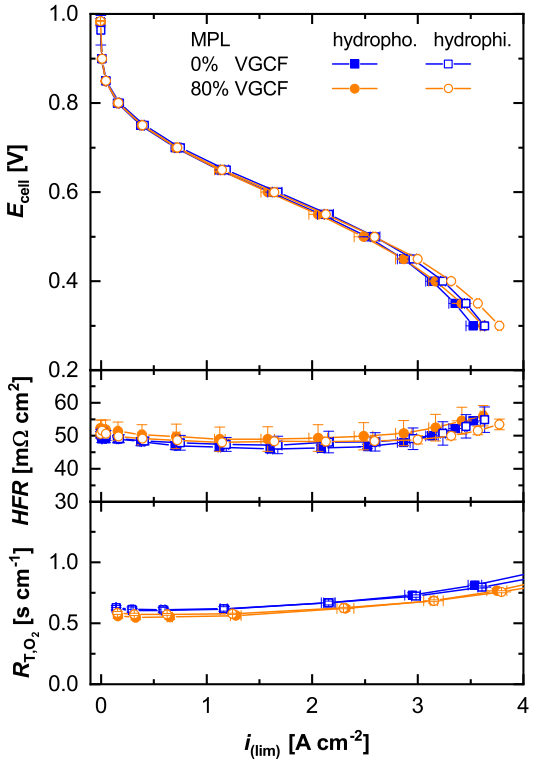

Figure 12. Differential-flow H_2/air polarization curves under **dry conditions** (T_{cell} = 80°C, RH = 70%, p_{abs} = 170 kPa) showing cell voltage (E_{cell}, top) and high frequency resistance (*HFR*, middle) versus current density (i) as well as total oxygen transport resistance (R_{T,O_2}, bottom) versus the limiting current density (i_{lim}) for the following cathode MPLs coated on the Freudenberg GDL-substrate: 0% VGCF with hydrophobic PTFE (blue line, full squares) or hydrophilic PFSA (blue line, empty squares) as binder, and 80% VGCF with PTFE (orange line, full squares) or PFSA (orange line, empty squares) as binder. The limiting current density is measured for various dry oxygen contents ($x_{O_2,dry}$) between 0.5% and 28%. The error bars represent the standard deviation of two independently measured cells. Data of the hydrophobic 0% VGCF MPL is taken from Reference 15.

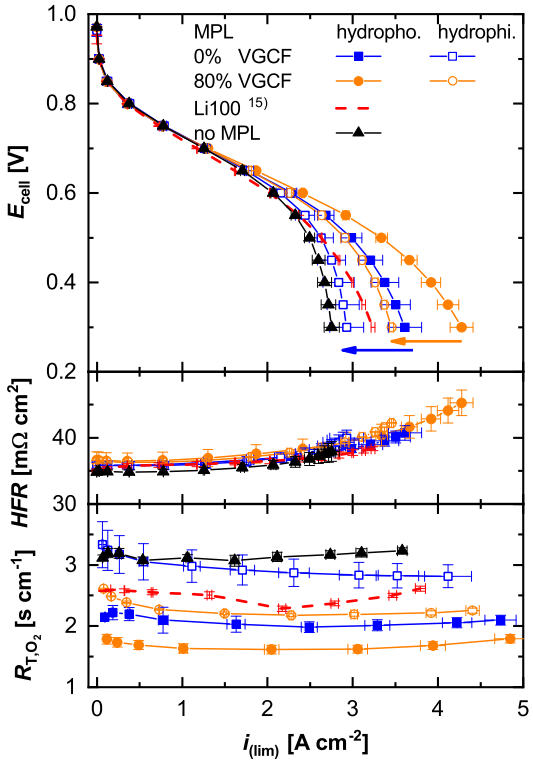

Figure 13. Differential-flow H_2/air polarization curves under **humid conditions** (T_{cell} = 50°C, RH = 120%, p_{abs} = 300 kPa) showing cell voltage (E_{cell}, top) and high frequency resistance (*HFR*, middle) versus current density (i) as well as total oxygen transport resistance (R_{T,O_2}, bottom) versus the limiting current density (i_{lim}) for the following for the Freudenberg GDL-substrate with no MPL (black) and the following cathode MPLs coated on the Freudenberg GDL-substrate: 0% VGCF with hydrophobic PTFE (blue line, full squares) or hydrophilic PFSA (blue line, empty squares) as binder, 80% VGCF with PTFE (orange line, full squares) or PFSA (orange line, empty squares) as binder, and Li100 MPL with PTFE as binder (red dotted line; data taken from Reference 15). The limiting current density is measured for various dry oxygen contents ($x_{O_2,dry}$) between 0.5% and 28%. The error bars represent the standard deviation of two independently measured cells. Data of the hydrophobic 0% VGCF MPL, no MPL and the Li100 MPL are taken from Reference 15.

an indication that the different binders and preparation procedures do not significantly affect the effective diffusivity in the dry MPL, and hence, porosity and tortuosity are expected to be independent of the binder.

At higher current densities of >0.5 A cm^{-2}, water starts to condense in the porous media and R_{T,O_2} increases significantly until it reaches a higher level at i_{lim} > 1.5 A cm^{-2}, with all hydrophilic MPLs (open symbols) exhibiting significantly higher R_{T,O_2} values compared to their hydrophobic counterparts, whereby the 80% VGCF MPLs have lower values than the 0% VGCF MPLs. Additionally, in the region with substastantial liquid water content in the porous media (i.e., at >1.5 A cm^{-2}), the hydrophobic MPLs (full symbols) reveal only a slightly positive slope of R_{T,O_2} with increasing i_{lim}, while the hydrophilic MPLs (open symbols) show a significantly higher slope, indicating a continuous increase of water content in the porous media with increasing i_{lim}.

In the following we compare differential-flow H_2/air polarization curves and the associated high frequency resistances and oxygen transport resistances at dry conditions (T_{cell} = 80°C, RH = 70%, p_{abs} = 170 kPa, Figure 12) and humid conditions (T_{cell} = 50°C, RH = 120%, p_{abs} = 300 kPa, Figure 13) in order to evaluate the binder impact in the absence and presence of liquid water. At dry conditions (Figure 12), all materials perform similarly and reach a performance of around 1.6 A cm^{-2} at 0.6 V (top graph). Also, the *HFR* values (middle graph) and the R_{T,O_2} values of the hydrophilic MPLs are essentially identical with those of their hydrophobic counterparts. This indicates that the binder type does not affect the humidification of the membrane, the HFR, the binder volume fraction (at this low relative humidity), and the binder distribution.

On the other hand, the differential-flow H_2/air performance curves at humid conditions differ significantly from each other (Figure 13, top), as one would have expected based on the high i_{lim}-region shown in Figure 11. For both hydrophobic and hydrophilic binder, the 80% VGCF MPLs (orange lines/symbols) perform better than the 0% VGCF MPLs (blue lines/symbols), whereby the hydrophilic versions of these MPLs (open symbols) in both cases yield a ≈150 mA cm^{-2} lower performance at 0.6 V. This difference is even more pronounced at lower voltages, where the clear trend is highlighted by the blue and orange arrows in the upper panel of Figure 13. At the same time, however, the *HFR* values are essentially identical for all MPLs, independent of fiber content and binder type, so that the performance difference must be related to the oxygen transport resistance. This is indeed the case, and the R_{T,O_2} values for a given carbon composition of the MPL are always significantly higher for the hydrophilic MPLs. The observation that the hydrophilic 80% VGCF MPL (open orange symbols) shows a higher oxygen transport resistance than the hydrophobic 0% VGCF MPL (blue full symbols), which is the opposite of what we observe under the slightly higher-pressure conditions in Figure 11 (with T_{cell} = 50°C, RH = 77%, p_{abs} = 400 kPa) is likely due to the fact that in Figure 13 the inlet gas stream is already fully humidified at 120% RH, which means that a stable saturation of the

GDL-S/MPL with liquid water can already be achieved at lower current densities, while for $RH = 77\%$ (Figure 11), the saturation is still changing with current density, as indicated by the continuously increasing R_{T,O_2} with increasing limiting current density in the region of high water saturation in the porous media. As a reference, we included the GDL-substrate without MPL in Figure 13, showing the lowest performance and highest oxygen transport resistance, which is consistent with Tanuma et al., who has shown a similar result at humid operating conditions.[23]

Discussion

Impact of MPL pore size on oxygen and water transport.—Even though, all tested hydrophobic MPLs, show very different properties, either in pore size distribution or in hydrophilicity, the materials perform similarly at dry conditions ($T_{cell} = 80°C$, $RH = 70\%$, $p_{abs} = 170$ kPa), while differences are only observed at humid conditions ($T_{cell} = 50°C$, $RH = 120\%$, $p_{abs} = 300$ kPa) and high pressure operation ($T_{cell} = 80°C$, $RH = 100\%$, $p_{abs} = 300$ kPa). In this section, we will discuss the results and will seek to explain why the materials show this specific behavior.

From the SEM images of the prepared GDL-S/MPL materials (Figure 2) as well as from the mercury porosimetry data of either free-standing MPLs (Figure 3) or of MPLs on the final diffusion media (Figure 5), it becomes clear that by mixing different ratios of carbon black and VGCF, we can tune the porosity (ε), the pore size distribution, and the pore shapes of the MPL. Increasing the VGCF content leads to higher porosity and larger pore sizes, which in turn effectively impacts the ratio of tortuosity over porosity (τ/ε) and hence, the effective diffusivity.[15] This means that with higher porosity, the effective diffusivity is increasing and the oxygen transport resistance is decreasing, as is observed in Figure 6 at small limiting current densities of $i_{lim} < 0.5$ A cm^{-2}. However, the impact of these small changes in R_{T,O_2} are very minor, because the MPL contributes to only a small fraction to the overall R_{T,O_2}. At dry conditions (Figure 7), R_{T,O_2} can be reduced by only ≈15% between the 0% VGCF MPL and the best performing 100% VGCF, but the observed as well as the projected differences in H_2/air performance at a relevant voltage of 0.6 V are negligible and within the error of measurement.

A significant impact of the cathode MPL composition on H_2/air performance becomes visible in the presence of distinct amounts of liquid water in the porous media, which occur at our humid operating conditions ($T_{cell} = 50°C$, $RH = 120\%$, $p_{abs} = 300$ kPa; see Figure 8) that are meant to mimick the transport conditions that occur during the warm-up process of a fuel cell stack. Here, even at 0.6 V, a clear trend of increasing current density and decreasing oxygen transport resistance with higher VGCF content and thus higher porosity and larger pore sizes becomes visible. This confirms that liquid water transport takes place more efficiently through larger pores, as has been shown previously for MPLs with large cracks or perforations.[9,15,33,34,60–64] Previous studies already discussed the enhancing effect of adding small amounts of carbon nanotubes or aluminosilicate fibers, but mainly justified it with the hydrophilic properties of the fiber surface which would facilitate faster water absorption.[28,29,31,36,65] On the other hand, our study strongly suggests that the improved performance of fiber containing MPLs is simply due to their larger porosity and their larger pore sizes, rather than the supposedly higher hydrophilicity of carbon fibers, since in all of our MPLs the relatively large PTFE binder content (20 wt%) renders the MPL very hydrophobic for MPLs both without and with carbon fibers. Nevertheless, as the possibility that hydrophilic domains are present in our MPLs cannot be excluded, we also examined the performance of carbon fiber based MPLs with hydrophobic (PTFE) and with hydrophilic binder (PFSA), since this allows to clearly determine the effect of hydrophobic vs. hydrophilic properties for morphologically identical samples (see Figure 2).

The conceptual differences in transport properties of MPLs with differently sized pores and different hydrophobic/hydrophilic properties are illustrated in Figure 14, whereby the sketched small pore represents the small pores in carbon black based MPLs (see blue line in Figure 3 as well as purple and blue lines in Figure 5) and the sketched large pore represents the additional much larger pore sizes observed in the VGCF fiber containing MPLs (see Figure 3). According to the Young-Laplace equation (Eq. 1), a large hydrophobic pore (contact angle $\theta > 90°$) has a smaller capillary pressure p_c than a small hydrophobic pore (negative sign), which means that for the latter a larger liquid pressure is necessary in order to wet the pore and transport water through it, particularly through small pores. As water is produced in the cathode catalyst layer and transported through the MPL toward the GDL-substrate, it will take the least resistive pathway through the largest pores. Small hydrophobic pores would be free of water and available for the opposing O_2 diffusion. For a wide pore size distribution between large and small pores, clearly observed for the VGCF containing MPLs with hydrophobic binder (see Figure 3), this bifunctional transport mechanism seems to effectively reduce the total oxygen transport resistance. This bifunctional transport mechanism is less effective for a narrow pore size distribution with mostly small hydrophobic pores found for the 0% VGCF MPL with hydrophobic binder (see Figure 3, particularly considering logarithmic scaling), where liquid water transport will take place through a larger pore volume fraction leading to more liquid water being retained at the MPL/cathode interface due to the higher capillary pressure. The commercial MPL with hydrophobic binder has even smaller pores and a very narrow pore size distribution with small pores (see Figure 5), which has the effect to even further increase R_{T,O_2} compared to the other hydrophobic MPLs.

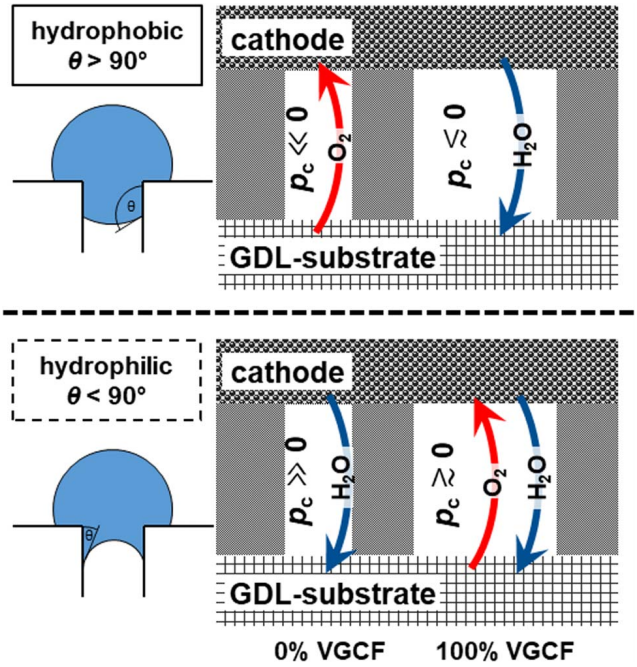

Figure 14. Illustration of capillary pressure p_c and the correspondent liquid water transport through MPL pores with different water contact angles ($\theta > 90° \equiv$ hydrophobic; $\theta < 90° \equiv$ hydrophilic) and with different pore sizes, whereby the large pores are most prevalent for VGCF based MPLs, and small pores are most prevalent in carbon black based MPLs.

At normal conditions (Figure 9 and Figure 10), no or minor amounts of liquid water are expected to be present in the porous media.[15] This means that the performance is mainly limited by the dry transport through the porous MPL structure. As already indicated at dry conditions (Figure 7), the dry transport resistance decreases with increasing VGCF content. As the pressure dependent component of the oxygen transport resistance is proportional to the absolute gas pressure,[43,44] a higher pressure increases the differences between different materials, as can be seen by comparing the R_{T,O_2} values at the low limiting current densities between Figure 6 (400 kPa_{abs}) and Figure 7 (170 kPa_{abs}). This has the effect, that the differential-flow fuel

cell performance at $T_{cell} = 80°C$, $RH = 100\%$, $p_{abs} = 300$ kPa, the current density at 0.6 V increases by ≈40% between the commercial and the 0% VGCF MPL and by ≈50% between the commercial and the 100% VGCF MPL, both for 10% O_2/N_2 (Figure 9; mimicking stack outlet conditions) and for air (Figure 10; mimicking stack inlet conditions). Hence, the hydrophobic 100% VGCF MPL with its very broad pore size distribution containing large pores and with its high porosity performs best at low humidity, as it allows a facile bifunctional transport mechanism of liquid water through the larger pores and of oxygen through the smaller pores which remain free of liquid water due to their high capillary pressure. This is illustrated in the upper panel of Figure 14.

Impact of MPL hydrophilicity and hydrophobicity.—In the previous section we provided a rationale as to why the larger pores produced by the addition of carbon fibers can improve the oxygen diffusivity in MPL with a hydrophobic binder, particularly under humid and normal operating conditions. In the following, we will focus on the binder properties and want to clarify, why in the literature all-hydrophilic MPLs are often presented as superior over conventional hydrophobic MPLs.[19–22,35,66]

At dry conditions (Figure 12) and under conditions where no liquid water is present in the porous media (Figure 11 at small i_{lim}), the total oxygen transport resistance is similar for the MPLs with hydrophilic and hydrophobic binder when comparing MPLs with the same carbon composition, i.e., with the same morphology (0% VGCF or 80% VGCF). Consequently, at dry conditions the H_2/air performance is essentially identical for hydrophilic and hydrophobic MPLs (Figure 12), as is the *HFR*. In the absence of liquid water, the transport properties of the MPL are defined by its porosity and tortuosity and, as shown in Figure 12 do not depend on the hydrophobic/hydrophilic properties of the applied binder. This observation is rather conclusive, as the content of either the PFSA or the PTFE binder was identical (20 wt%) and as their densities are similar (≈2.1 g cm^{-3} and ≈2.2 g cm^{-3}, respectively), which means that the dry volume fractions of both binders in the MPLs are essentially identical. Considering an expected 10% weight gain due to the water uptake of the PFSA ionomer at $RH = 70\%$,[56] the wet volume fraction of the PFSA binder is expected to be only ≈15% higher than that of PTFE (no volume change in contact with water), which is rather negligible considering that the estimated void volume fraction in the MPLs ranges between ≈68–83% for all the here tested MPLs.

In the presence of liquid water (Figure 11 at high i_{lim} and Figure 13) differences between the hydrophobic and the hydrophilic MPLs become visible. A hydrophilic pore has per definition a water contact angle of $< 90°$ as illustrated in Figure 14 (lower panel), which results in a positive capillary pressure and a voluntary water-filling of the pores (the concave shape of the intruding water droplet is illustrated on the left). While small hydrophilic pores (as e.g., in the 0% VGCF MPL with PFSA binder) result in high (positive) capillary pressures, larger pores exhibit capillary pressures closer to ≈0 kPa. In the latter case, a pore can be relieved from water by a small additional pressure. The voluntary filling of hydrophilic pores results in a continuous blocking of these pores for oxygen transport, which is contrary to what is expected for hydrophobic pores, for which eruptive water transport mechanisms are proposed, due to which the extent of the liquid water content in a given pore is changing periodically over time.[34,62,67,68] As these phenomena strongly depend on the pore size distribution, the transport properties of hydrophilic vs. hydrophobic pores must be compared for the same carbon composition, i.e., for the same morphology, porosity, and pore size distribution (hydrophilic/hydrophobic 0% VGCF MPL or hydrophilic/hydrophobic 80% VGCF MPL). Doing so, it becomes obvious that the oxygen transport resistances are always lower for hydrophobic compared to hydrophilic MPLs, consistent with the superior H_2/air performance at high current densities (see Figure 11 and Figure 13). As one would expect from our earlier discussion, the 80% VGCF MPLs are always performing better than the 0% VGCF MPL because of its larger pores, as their absolute capillary pressure is smaller, which facilitates water removal from/through large pores.

In summary, as the hydrophilic binder in both cases increases R_{T,O_2} and lowers the fuel cell performance at humid operating conditions, while at the same time no advantages are observed at dry operating conditions, we can conclude unequivocally that all-hydrophilic MPLs are not advantageous for fuel cell operation. Furthermore, we expect severe issues at sub-zero temperatures. Although Tabe et al. reported an improved freeze-start up when using a hydrophilic carbon fiber MPL instead of a hydrophobic carbon black as the hydrophobic MPL, which formed an ice layer at the interface to the cathode catalyst layer, we do believe that this behavior rather arises from the higher ice capacity due to the higher pore volume of the carbon fiber MPL than from the hydrophilic binder.[69] In particular due to the fact that hydrophilic pores are not easy to dry out during the shut-down process, significant issues are expected at sub-zero temperatures, at which residual water freezes and due to volume expansion may break the MPL and possibly the adjacent electrode.[70]

This still leaves the question as to why other authors found significant fuel cell performance enhancements of all-hydrophilic MPLs compared to hydrophobic MPLs.[21–30,36,37] Inspecting the MPL compositions used in these studies, it becomes apparent that the effect of different binders was compared for MPLs with a different composition of carbon materials. In References 21–24,30,35,66 for example, Aoyama et al. and Tanuma et al. compare hydrophobic carbon black based MPLs with hydrophilic carbon fiber based MPLs, which according to Figure 3 will have totally different pore size distribution, therefore varying simultaneously both pore sizes and hydrophilicity/hydrophobicity; while these authors show that the pore size distributions of their hydrophilic and hydrophobic MPL are very different (by SEM images or PSD measurements), they do not explicitly consider this effect in their analysis.[19–24,30,35,66] In their latest publication,[30] however, Aoyama et al. reported MPL compositions with either carbon black (CB) or the same carbon fibers (CF) as were used in our study, both with either hydrophobic PTFE or hydrophilic PFSA as binder. Their obtained differential-flow H_2/air performance at high current densities (taken at 70°C, 100% RH, $p_{out} = 101$ kPa_{abs} (information kindly provided by the authors); MEA properties are unspecified) is essentially identical for all their 15 μm thick MPLs, i.e., for a hydrophobic CB MPL, a hydrophilic CB MPL, and a hydrophilic CF MPL (1.43 ± 0.01 A cm^{-2} at 0.4 V and 1.81 ± 0.02 A cm^{-2} at 0.2 V). This seems to be in contrast with our results, where under wet operating conditions hydrophilic MPLs with the same carbon material perform clearly worse than hydrophobic MPLs, and where CB based MPLs with the same binder perform clearly worse than CF based MPLs. One explanation might be that their testing conditions more closely reflect our "dry" conditions (80°C, 70% *RH*, 170 kPa; see Figure 7) where differences between the carbon material do not become apparent compared to our "humid" conditions (see Figure 8). This is indicated by the fact that when conducting our fuel cell measurements at 80°C, 100% *RH,* and 170 kPa (only change is from *RH* of 70% to a fully saturated gas stream; graph not shown in this paper), we also did not see any difference between hydrophilic and hydrophobic MPLs as in Figure 7. This unexpected phenomenon has been already discussed in our previous study (compare Figures 7a and 7b in Reference 15) and was explained by the absence of liquid water in the GDL-substrate (presumably by a high temperature gradient within the GDL-substrate) even at 100% *RH*. As Aoyama et al. also uses a Freudenberg GDL-substrate (with presumably a similar thermal conductivity as ours) and the operating pressure is lower than in our study (101 kPa_{abs} vs. 170 kPa_{abs}) suggesting a higher water uptake of the gas streams, we believe that the liquid water content at their operating conditions is comparably low and that their results are mainly dominated by the dry oxygen transport.

When considering an MPL thickness of 40 μm, the H_2/air performance of the hydrophobic CF MPL is the same as for the 15 μm variants (i.e., as above), while thicker hydrophilic CF MPL was clearly superior (≈1.78 A cm^{-2} at 0.4 V and ≈2.15 A cm^{-2} at 0.2 V). In our view, it is somewhat perplexing that the 40 μm thick hydrophilic CF

MPL would perform better than the 15 μm thick CF MPL, an effect which the authors hypothesize to be due to the higher surface area for water evaporation which is provided within the thicker hydrophilic CF MPL. While the thickness of the MPLs examined in our study (30 ± 5 μm) is closer to the thicker MPLs examined by Aoyama et al.,[30] in contrast to their findings we clearly see a superior H_2/air performance and a lower oxygen transport resistance at humid conditions for all hydrophobic MPLs compared to the hydrophilic MPLs of the same carbon composition (see Figure 11 and Figure 13). The origin of this discrepancy is not clear. It may be due to the fact that MPLs do have optima in thickness (trade-off between transport properties and resistances)[8,71,72] or in the binder/carbon ratio (a higher PFSA content of 41% has shown better performance at 80°C and 100% RH),[23] and that perhaps these optima are different for hydrophobic and hydrophilic MPLs.

In summary, the data shown in the present study with MPLs of equal thickness show a different trend with regards to the effect of hydrophilic vs. hydrophobic binders in the MPL: (i) When comparing samples with the same thickness and the same carbon materials and hence, structure (see Figure 2 and Figure 4), we can conclude unequivocally that hydrophobic MPLs always perform superior compared to hydrophilic MPLs, which is consistent with established water transport mechanisms. (ii) However, considering the strong effect of pore size distribution on MPL performance, one should of course be able to find a hydrophobic MPL which performs superior over a hydrophilic MPL based on a different carbon material which yield a more advantageous pore size distribution. To illustrate this possibility, we also investigated the fuel cell performance and the oxygen transport properties of a hydrophobic MPL based on a carbon black which we had examined in a previous study (Li100 carbon black from Denka), which is shown in Figure 13 (red symbols/lines; data taken from our previous publication[15]). This hydrophobic Li100 carbon black based MPL clearly performs worse than the hydrophilic 80% VGCF MPL, but this is not due to the hydrophobic binder in the former, but due to its unfavorable pore size distribution with a PSD-maximum at ≈70 nm (see Figure 4 in Reference 15) compared to the 80% VGCF MPL of ≈490 nm (see Figure 3).

Hence, we cannot find any scientifically rigorous proof for the claimed superiority of all-hydrophilic MPLs with regards to oxygen transport and fuel cell performance. As a matter of fact, our data and analysis suggest the opposite, namely that hydrophobic MPLs are superior to hydrophilic MPLs under fuel cell operating conditions where liquid water transport is required. This, however, does not mean, that hydrophilic regions in the MPL are unfavorable per se. MPLs with both hydrophilic and hydrophobic sites are supposed to be advantageous for parallel liquid water and oxygen transport as already shown for diffusion media which are designed such that they provide regions of μm-sized domains with distinctly hydrophilic and distinctly hydrophobic properties in the MPL.[73,74] However, sophisticated preparation methods are necessary to effectively create these different domains within an MPL and their economic viability is currently unclear.

Conclusions

The present study investigates the influence of the pore size distribution of MPLs with hydrophobic PTFE or hydrophilic PFSA ionomer binder on fuel cell performance and on the oxygen transport resistance. We prepared hydrophobic MPLs with different compositions of acetylene black and vapor grown carbon fibers (VGCF; VGCF content of 0%, 50%, 80% and 100%) and found by mercury porosimetry that the porosity and the pore size distribution maximum of the MPLs increases with the VGCF content. SEM images visually confirm the more porous and more open structure of the VGCF containing MPLs compared to the acetylene black based MPL.

At fuel cell operation in the absence of liquid water ($T_{cell} = 80°C$, $p_{abs} = 170$ kPa, $RH = 70\%$), all materials perform similarly. However, explicit differences are detected at relevant automotive operating condition ($T_{cell} = 80°C$, $p_{abs} = 300$ kPa, $RH = 100\%$) with the 100% VGCF MPL with hydrophobic binder performing ≈48% better at 0.6 V better than the commercial reference MPL, which can be attributed to the larger porosity and the very wide pore size distribution with a significant fraction of large pores of the 100% VGCF MPL. In the presence of significant amounts of liquid water, a clear trend is observed that larger pore sizes enhance fuel cell performance and reduce the oxygen transport resistance. We propose that this is due to a bifunctional transport mechanism, improving the parallel transport of oxygen to the electrode in small pores and of liquid water to the GDL-substrate in large pores. We rationalize this observation with the lower capillary pressure of larger hydrophobic pores decreasing the backpressure at the MPL/cathode interface, which is necessary in order to transport water through the MPL.

By replacing PTFE with PFSA ionomer binder, we prepared hydrophilic MPLs based on 0% VGCF and 80% VGCF content with hydrophilic pores, which are structurally indistinguishable from their hydrophobic counterparts as shown by SEM images. While in the absence of liquid water no significant differences in fuel cell performance and oxygen transport are detected, at humid conditions with significant amounts of liquid water a decrease in performance and in increase of oxygen transport resistance for the hydrophilic MPLs is observed, rationalized by liquid water filling of hydrophilic pores. Despite numerous claims in the literature that hydrophilic MPLs may provide superior fuel cell performance and lower oxygen transport resistance, a scientifically rigorous comparison of hydrophobic and hydrophilic MPLs using the same carbon composition (i.e., the same pore size distribution and porosity), unequivocally proves that the investigated hydrophilic MPLs are not performing better under the considered dry operating conditions ($T_{cell} = 80°C$, $p_{abs} = 170$ kPa, $RH = 70\%$) and that the hydrophobic MPLs are always superior at the here considered humid conditions ($T_{cell} = 50°C$, $p_{abs} = 300$ kPa, $RH = 120\%$).

Acknowledgments

This research was carried out within the framework of the joint project "Optigaa2". Financial support by the German Federal Ministry of Economic Affairs and Energy (grant number 03ET6015E), Freudenberg Performance Materials SE & Co. KG and Daimler AG is gratefully acknowledged. We are very thankful for the valuable discussions with Achim Bock (Freudenberg). The authors would also like to thank Kerstin Fischinger (ZSW Ulm) for the mercury porosimetry measurements, Katia Rodewald (Wacker-Chair of Macromolecular Chemistry, TUM) for the SEM measurements and David Müller (Chair of Technical Electrochemistry, TUM) for the development of the MPL preparation procedure. Furthermore, we appreciate the free of charge support of materials from Freudenberg, Germany (GDL substrate and commercial MPL), Denka, Japan (Li400 acetylene black), and 3M Dyneon, Germany (TF 5035GZ PTFE dispersion).

List of Symbols

Variable	Unit	Description
A	cm^2	area
D_{eff}	$m^2\ s^{-1}$	effective diffusion coefficient
d_{MPL}	μm	MPL thickness
$d_{particle}$	μm	particle diameter
d_{pore}	μm	pore diameter
E_{cell}	V	cell voltage
HFR	$\Omega\ cm^2$	high frequency resistance
i	$A\ cm^{-2}$	current density normalized to geometric electrode area
i_{lim}	$A\ cm^{-2}$	limiting current density normalized to geometric electrode area
m	g	mass
p_{abs}	kPa	absolute pressure
p_{H_2O}	kPa	partial pressure of water (at cell inlet)

Variable	Unit	Description
R_{T,O_2}	s cm^{-1}	total oxygen transport resistance
R_{x,O_2}	s cm^{-1}	oxygen transport resistance of the component x (GDL, MPL, flow field, electrode
RH	%	relative humidity
T_{cell}	°C	fuel cell temperature
V	ml	volume
w	wt%	mass fraction
$x_{O_2,dry}$	%	dry mole fraction of oxygen

Constant	Value	Unit	Description
F	96485	C mol^{-1}	Faraday constant
R	8.3145	J mol^{-1} K^{-1}	ideal gas constant

Greek letter	Unit	Description
γ_{H_2O}	N m^{-1}	surface tension of water
γ_{Hg}	N m^{-1}	surface tension of mercury
ε	%	porosity
θ	°	contact angle
ρ	g cm^{-3}	density
τ	-	tortuosity

ORCID

Christoph Simon https://orcid.org/0000-0002-2381-7641
Hubert A. Gasteiger https://orcid.org/0000-0001-8199-8703

References

1. W. Gu, D. R. Baker, Y. Liu, and H. A. Gasteiger, in *Handbook of Fuel Cells*, Vol. **6**, W. Vielstich, H. A. Gasteiger, and A. Lamm, Editors, p. 631, John Wiley & Sons, Ltd (2009).
2. A. Weber, R. Darling, J. Meyers, and J. Newman, in *Handbook of Fuel Cells*, Vol. **1**, W. Vielstich, H. A. Gasteiger, and A. Lamm, Editors, p. 47, John Wiley & Sons, Ltd (2010).
3. J. P. Owejan, J. E. Owejan, W. B. Gu, T. A. Trabold, T. W. Tighe, and M. F. Mathias, *J. Electrochem. Soc.*, **157**, B1456 (2010).
4. M. F. Mathias, J. Roth, J. Fleming, and W. Lehnert, in *Handbook of Fuel Cells*, Vol. **3**, W. Vielstich, H. A. Gasteiger, and A. Lamm, Editors, p. 517, John Wiley & Sons, Ltd (2010).
5. L. Cindrella, A. M. Kannan, J. F. Lin, K. Saminathan, Y. Ho, C. W. Lin, and J. Wertz, *J. Power Sources*, **194**, 146 (2009).
6. J. M. Morgan and R. Datta, *J. Power Sources*, **251**, 269 (2014).
7. S. Park, J.-W. Lee, and B. N. Popov, *Int. J. Hydrogen Energy*, **37**, 5850 (2012).
8. P. Antonacci, S. Chevalier, J. Lee, N. Ge, J. Hinebaugh, R. Yip, Y. Tabuchi, T. Kotaka, and A. Bazylak, *Electrochim. Acta*, **188**, 888 (2016).
9. J. T. Gostick, M. A. Ioannidis, M. W. Fowler, and M. D. Pritzker, *Electrochem. Commun.*, **11**, 576 (2009).
10. Y. Tabe, Y. Aoyama, K. Kadowaki, K. Suzuki, and T. Chikahisa, *J. Power Sources*, **287**, 422 (2015).
11. F. Lufrano, E. Passalacqua, G. Squadrito, A. Patti, and L. Giorgi, *J. Appl. Electrochem.*, **29**, 445 (1999).
12. S. Park, J.-W. Lee, and B. N. Popov, *J. Power Sources*, **177**, 457 (2008).
13. E. Passalacqua, G. Squadrito, F. Lufrano, A. Patti, and L. Giorgi, *J. Appl. Electrochem.*, **31**, 449 (2001).
14. C. S. Kong, D.-Y. Kim, H.-K. Lee, Y.-G. Shul, and T.-H. Lee, *J. Power Sources*, **108**, 185 (2002).
15. C. Simon, D. Kartouzian, D. Müller, F. Wilhelm, and H. A. Gasteiger, *J. Electrochem. Soc.*, **164**, F1697 (2017).
16. L. R. Jordan, A. K. Shukla, T. Behrsing, N. R. Avery, B. C. Muddle, and M. Forsyth, *J. Appl. Electrochem.*, **30**, 641 (2000).
17. X. L. Wang, H. M. Zhang, J. L. Zhang, H. F. Xu, Z. Q. Tian, J. Chen, H. X. Zhong, Y. M. Liang, and B. L. Yi, *Electrochim. Acta*, **51**, 4909 (2006).
18. X. L. Wang, H. M. Zhang, J. L. Zhang, H. F. Xu, X. B. Zhu, J. Chen, and B. L. Yi, *J. Power Sources*, **162**, 474 (2006).
19. T. Tanuma, M. Kawamoto, and S. Kinoshita, *J. Electrochem. Soc.*, **164**, F499 (2017).
20. T. Tanuma and M. Kawamoto, *ECS Transactions*, **69**, 1323 (2015).
21. Y. Aoyama, K. Suzuki, Y. Tabe, T. Chikahisa, and T. Tanuma, *ECS Transactions*, **64**, 527 (2014).
22. Y. Aoyama, K. Suzuki, Y. Tabe, T. Chikahisa, and T. Tanuma, *ECS Transactions*, **69**, 743 (2015).
23. T. Tanuma, *J. Electrochem. Soc.*, **157**, B1809 (2010).
24. T. Tanuma and S. Kinoshita, *Energy Procedia*, **28**, 12 (2012).
25. T. Kitahara, H. Nakajima, M. Inamoto, and M. Morishita, *J. Power Sources*, **234**, 129 (2013).
26. T. Kitahara, H. Nakajima, and K. Mori, *J. Power Sources*, **199**, 29 (2012).
27. T. Kitahara, H. Nakajima, and K. Okamura, *ECS Transactions*, **69**, 1313 (2015).
28. T. Kitahara, H. Nakajima, and K. Okamura, *J. Power Sources*, **283**, 115 (2015).
29. R. Schweiss, M. Steeb, and P. M. Wilde, *Fuel Cells*, **10**, 1176 (2010).
30. Y. Aoyama, Y. Tabe, R. Nozaki, K. Suzuki, T. Chikahisa, and T. Tanuma, *J. Electrochem. Soc.*, **165**, F484 (2018).
31. D. Spernjak, R. Mukundan, R. L. Borup, L. G. Connolly, B. I. Zackin, V. De Andrade, M. Wojcik, D. Y. Parkinson, D. L. Jacobson, D. S. Hussey, K. L. More, T. Chan, A. Z. Weber, and I. V. Zenyuk, *ACS Applied Energy Materials*, **1**, 6006 (2018).
32. I. V. Zenyuk, E. C. Kumbur, and S. Litster, *J. Power Sources*, **241**, 379 (2013).
33. Z. Lu, J. Waldecker, M. Tam, and M. Cimenti, *ECS Transactions*, **69**, 1341 (2015).
34. H. Markotter, J. Haussmann, R. Alink, C. Totzke, T. Arlt, M. Klages, H. Riesemeier, J. Scholta, D. Gerteisen, J. Banhart, and I. Manke, *Electrochem. Commun.*, **34**, 22 (2013).
35. T. Tanuma and S. Kinoshita, *J. Electrochem. Soc.*, **159**, B150 (2012).
36. T. Kitahara, H. Nakajima, and K. Okamura, *ECS Transactions*, **64**, 477 (2014).
37. T. Kitahara and H. Nakajima, *Int. J. Hydrogen Energy*, **41**, 9547 (2016).
38. J. Lee, R. Banerjee, M. G. George, D. Muirhead, P. Shrestha, H. Liu, N. Ge, S. Chevalier, and A. Bazylak, *J. Electrochem. Soc.*, **164**, F1149 (2017).
39. P. Shrestha, R. Banerjee, J. Lee, N. Ge, D. Muirhead, H. Liu, A. K. C. Wong, D. Ouellette, B. Zhao, and A. Bazylak, *J. Power Sources*, **402**, 468 (2018).
40. A. Z. Weber, R. M. Darling, and J. Newman, in *J. Electrochem. Soc.*, *Vol.* **151**, p. A1715 (2004).
41. K. G. Gallagher, R. M. Darling, T. W. Patterson, and M. L. Perry, *J. Electrochem. Soc.*, **155**, B1225 (2008).
42. D. R. Baker, C. Wieser, K. C. Neyerlin, and M. W. Murphy, *ECS Transactions*, **3**, 989 (2006).
43. D. R. Baker, D. A. Caulk, K. C. Neyerlin, and M. W. Murphy, *J. Electrochem. Soc.*, **156**, B991 (2009).
44. D. A. Caulk and D. R. Baker, *J. Electrochem. Soc.*, **157**, B1237 (2010).
45. D. A. Caulk and D. R. Baker, *J. Electrochem. Soc.*, **158**, B384 (2011).
46. J. P. Owejan, T. A. Trabold, and M. M. Mench, *Int. J. Heat Mass Transfer*, **71**, 585 (2014).
47. C. Simon, F. Hasché, and H. A. Gasteiger, *J. Electrochem. Soc.*, **164**, F591 (2017).
48. H. Oh, Y. I. Lee, G. Lee, K. Min, and J. S. Yi, *J. Power Sources*, **345**, 67 (2017).
49. J. P. Owejan, J. E. Owejan, and W. B. Gu, *J. Electrochem. Soc.*, **160**, F824 (2013).
50. T. A. Greszler, D. Caulk, and P. Sinha, *J. Electrochem. Soc.*, **159**, F831 (2012).
51. C. Simon, F. Hasché, D. Müller, and H. A. Gasteiger, *ECS Transactions*, **69**, 1293 (2015).
52. A. Orfanidi, P. J. Rheinländer, N. Schulte, and H. A. Gasteiger, *J. Electrochem. Soc.*, **165**, F1254 (2018).
53. P. Zihrul, I. Hartung, S. Kirsch, G. Huebner, F. Hasché, and H. A. Gasteiger, *J. Electrochem. Soc.*, **163**, F492 (2016).
54. A. Kongkanand and M. F. Mathias, *The Journal of Physical Chemistry Letters*, **7**, 1127 (2016).
55. C. S. Gittleman, F. D. Coms, and Y.-H. Lai, in *Polymer Electrolyte Fuel Cell Degradation*, Vol., M. M. Mench, E. C. Kumbur, and T. N. Veziroglu, Editors, p. 15, Academic Press, Boston (2012).
56. C. K. Mittelsteadt and H. Liu, in *Handbook of Fuel Cells*, Vol., W. Vielstich, A. Lamm, and H. A. Gasteiger, Editors, John Wiley & Sons, Ltd (2010).
57. S. Goswami, S. Klaus, and J. Benziger, *Langmuir*, **24**, 8627 (2008).
58. S. De Almeida and Y. Kawano, *J. Therm. Anal. Calorim.*, **58**, 569 (1999).
59. L. G. Lage, P. G. Delgado, and Y. Kawano, *J. Therm. Anal. Calorim.*, **75**, 521 (2004).
60. R. Alink, J. Haussmann, H. Markotter, M. Schwager, I. Manke, and D. Gerteisen, *J. Power Sources*, **233**, 358 (2013).
61. S. S. Alrwashdeh, H. Markötter, J. Haußmann, T. Arlt, M. Klages, J. Scholta, J. Banhart, and I. Manke, *Energy*, **102**, 161 (2016).
62. P. Deevanhxay, T. Sasabe, S. Tsushima, and S. Hirai, *J. Power Sources*, **230**, 38 (2013).
63. S. Prass, S. Hasanpour, P. K. Sow, A. B. Phillion, and W. Mérida, *J. Power Sources*, **319**, 82 (2016).
64. T. Sasabe, P. Deevanhxay, S. Tsushima, and S. Hirai, *Electrochem. Commun.*, **13**, 638 (2011).
65. R. Mukundan, J. Davey, J. D. Fairweather, D. Spernjak, J. S. Spendelow, D. S. Hussey, D. Jacobson, P. Wilde, R. Schweiss, and R. L. Borup, *ECS Transactions*, **33**, 1109 (2010).
66. T. Tanuma and S. Kinoshita, *ECS Transactions*, **41**, 603 (2011).
67. S. Litster, D. Sinton, and N. Djilali, *J. Power Sources*, **154**, 95 (2006).
68. C. Hartnig, I. Manke, R. Kuhn, S. Kleinau, J. Goebbels, and J. Banhart, *J. Power Sources*, **188**, 468 (2009).
69. F. Onishi, Y. Tabe, and T. Chikahisa, *ECS Transactions*, **86**, 89 (2018).
70. S. Kim and M. M. Mench, *J. Power Sources*, **174**, 206 (2007).
71. A. Z. Weber and J. Newman, *J. Electrochem. Soc.*, **152**, A677 (2005).
72. S. Park, J.-W. Lee, and B. N. Popov, *J. Power Sources*, **163**, 357 (2006).
73. A. Forner-Cuenca, J. Biesdorf, A. Lamibrac, V. Manzi-Orezzoli, F. N. Büchi, L. Gubler, T. J. Schmidt, and P. Boillat, *J. Electrochem. Soc.*, **163**, F1038 (2016).
74. A. Forner-Cuenca, J. Biesdorf, V. Manzi-Orezzoli, L. Gubler, T. J. Schmidt, and P. Boillat, *J. Electrochem. Soc.*, **163**, F1389 (2016).

4.4. Voltage Loss Contributions of Different MPLs and GDL-Substrates

This chapter consists of results and analyses, which have been conducted by Christoph Simon, Thomas Kopfmüller, and Hubert Gasteiger. The results have been presented by Christoph Simon under the title "Impact of Microporous Layer Properties for High Current Density Operation" at the 232nd ECS Meeting in National Harbor, MD, USA, (I01: Polymer Electrolyte Fuel Cells 17 (PEFC 17), A-11 GDL and MPL (Oct. 2017)).

Target of this study was to show the impact of GDL-substrate properties on oxygen transport properties and to reveal the interaction of the MPL and the GDL-substrate. For this, fuel cell measurements were conducted, including polarization curves, limiting current measurements, and AC impedance spectroscopy at various operating conditions. Furthermore, a voltage loss analysis was conducted for one MPL type on the two different substrates to show how the substrate properties impact the contributions to particular overpotentials.

As a result, we could show how the oxygen transport resistance develops differently for the two substrate materials, how proton resistivity of the membrane depends on the GDL substrate, and how this impacts the voltage loss. A major influence is suspected to be the different thermal conductivity of the substrate. Conclusively, we state that the Freudenberg GDL-S with a rather low thermal conductivity performs better at humid conditions, as it tends towards membrane dry-out, while the Toray GDL-S performs better at dry operating conditions, as it tends towards GDL flooding.

Author contributions

C.S. and T.K. conducted the experimental work and analyzed the data (preparation of microporous layers, fuel cell measurements, SEM analysis, and voltage loss analysis). C.S., T.K. and H.G. discussed and interpreted the data. C.S. wrote this chapter for his PhD thesis.

4.4.1. Introduction

There have been several studies focusing on the impact of the GDL-substrate and the MPL on the overall performance.[26,36,43,132] However, most of them either concentrate

on the impact of the microporous layer or on the substrate individually neglecting their interaction, or they did not consider the overall impact of the materials on parameters like the proton conductivity in the membrane and the oxygen transport resistance as a function of the operating parameters. As we already investigated the properties of various MPLs in our previous studies on a Freudenberg GDL-substrate,[54,90] this chapter is focused on the interplay of MPLs and two different GDL-subtrates (Freudenberg and Toray 030T).

Caulk et al. showed that the thermal conductivity of the GDL-substrate impacts significantly the onset of liquid water formation as the thermal gradient (i.e., saturation vapor pressure gradient) across the GDL is the driving force for the vapor phase water transport from the electrode to the GDL-S.[26,127] Owejan et al. furtheron showed for a Toray 060 and an MRC105 GDL-substrate with two different MPLs that the thermal properties of the GDL-substrate have a larger impact on the water transport than the liquid water permeability of the MPL, which implies that vapor phase transport of water dominates the water transport across the MPL. However, this is in contrast to many studies (including our group), where a significant impact of the MPL properties on liquid phase transport was found.[36,54,67,90,97,103,105]

To present a more thorough analysis of the impact of the GDL on the particular overpotentials in a fuel cell as a function of the operating conditions, we conducted a voltage loss analysis according to section 2.1.2. By this method, a quantification of the voltage loss contributions was possible and we could suggest GDL properties for specific applications.

4.4.2. Experimental

Materials

As GDL-substrate, two different types of materials were used:

- **Freudenberg**: non-woven ~150 µm, 70% porosity, thermal resistivity $R_{\mathrm{th}} = 6.3\,\mathrm{m^2\,K\,W^{-1}}$ at 1.5 MPa; used in our previous studies in section 4.2 and 4.3[54,90] (see also section 2.2.2).
- **Toray 030T**: carbon paper ~110 µm, 80% porosity, thermal resistivity $R_{\mathrm{th}} = 2.66\,\mathrm{m^2\,K\,W^{-1}}$ at 1.5 MPa (see also section 2.2.2).

As cathode MPL, three different combinations were applied:

Table 4.1. Summary of polarization curve measurement conditions conducted under differential flows of H_2 and air.

Condition [-]	T_{cell} [° C]	p_{abs} [kPa]	RH [%]
humid	50	300	100
normal	80	300	100
dry	95	300	70

- **no MPL**
- **Carbon black MPL** (CB/Li400 MPL), 20% PTFE content, 30 µm thick, 68% porosity, pore size distribution maximum of 328 µm; developed in our previous studies in sections 4.2 and 4.3.[54,90]
- **Carbon fiber MPL** (CF/100% VGCF MPL), 20% PTFE content, 30 µm thick, 83% porosity, pore size distribution maximum of 722 µm; developed in our previous study in section 4.3.[90]

Fuel cell testing

Differential H_2/air polarization curves, limiting current measurements, and AC impedance measurements in air were recorded at various operating conditions, of which three representative conditions are shown in this section and listed in **Table 4.1**.

Furthermore, to calculate the voltage loss contributions, several parameters are required, which are measured for each individual cell. For the ORR overpotential, mass activities were measured by polarization curves in 100% O_2, and the mass activity at 0.9 V was determined in a Tafel plot corrected for the high frequency resistance and hydrogen crossover current. The contact resistance ($R_{contact}$) was estimated to be ~12.5 mΩ cm^2 via through-plane resistance measurements with two GDLs between two graphite plates (corresponding to Mathias et al.[17]) The membrane resistance ($R_{membrane}$) was determined from the *HFR* minus $R_{contact}$, so that in sum the voltage drop of the total ohmic resistance is considered. The effective proton conductivity of the cathode ($R_{H^+,ca}$) was calculated with the sheet resistance (R_{sheet}), measured by AC impedance measurements in H_2/N_2 (i.e. blocking electrode configuration corresponding to Liu et al.[133]) from which the catalyst utilization was estimated based on equation 2.13 and 2.14. The voltage loss analysis was conducted via equation 2.4.

4.4.3. Results

Oxygen transport resistance

Limiting current measurements are shown in **Figure 4.1** at the three different operating conditions. At $T_{\text{cell}} = 50\,^{\circ}\text{C}$ and $RH = 100\%$ (top graph), all GDLs are saturated with liquid water already at small current densities (also compare to sections 4.2 and 4.3[54,90]). The GDLs without MPL (black symbols) show the highest oxygen transport resistances, which are increasing with current density. Here, the Toray 030T

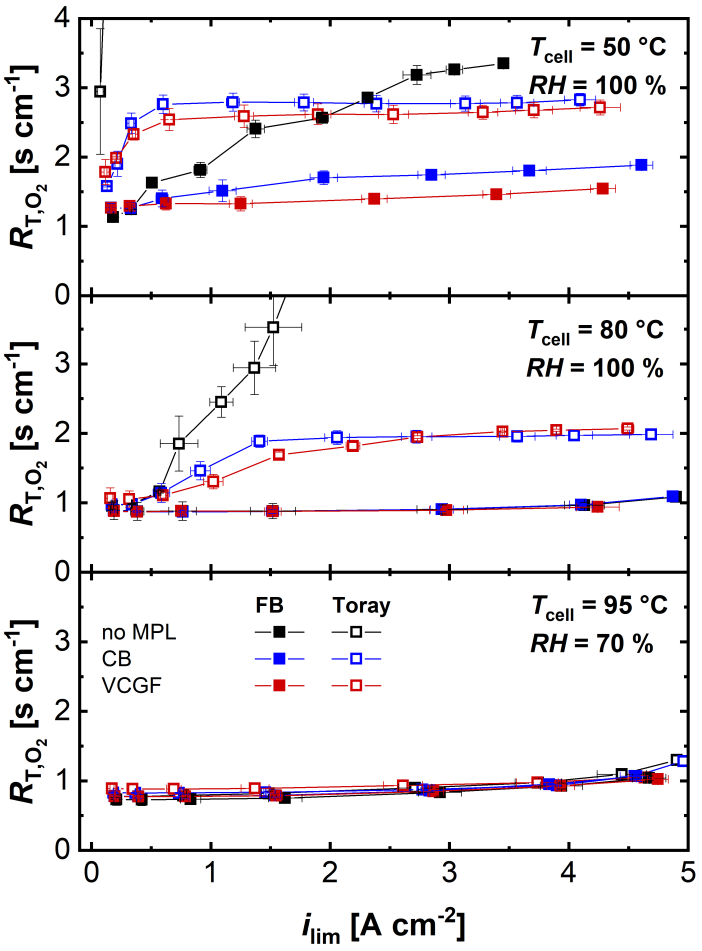

Figure 4.1. Total oxygen transport resistance ($R_{\text{T,O}_2}$) versus the limiting current density (i_{lim}) at $T_{\text{cell}} = 50\,^{\circ}\text{C}$ and $RH = 100\%$ (top graph), $T_{\text{cell}} = 80\,^{\circ}\text{C}$ and $RH = 100\%$ (center graph), and $T_{\text{cell}} = 95\,^{\circ}\text{C}$ and $RH = 70\%$ (bottom graph), with $p_{\text{abs}} = 300\,\text{kPa}$. Cathode GDLs were Freudenberg (FB) and Toray 030T substrates either without MPL or coated with a carbon black (Li400) MPL or carbon fiber (100% VGCF) MPL. The anode MPL was in all cases a carbon black (Li400) MPL. The MEA (from Gore) was a 18 µm membrane with $0.1/0.4\,\text{mg}_{\text{Pt}}\,\text{cm}^{-2}$ on anode/cathode. The error bars represent the standard deviation from two independently measured cells

GDL-substrate (black open symbols) shows significantly higher R_{T,O_2} with a maximum of $9.6\,s\,cm^{-1}$ (only one data point shown in the range of the y-axis due to the fast increase), while the Freudenberg GDL (black filled symbols) reaches $3.5\,s\,cm^{-1}$. The addition of an MPL is in both cases advantageous, with a lowest oxygen transport resistance for the VGCF based MPLs (red symbols). However, while the Freudenberg GDLs stay at a rather low level of $R_{T,O_2} < 2\,s\,cm^{-1}$, the Toray paper shows a steep increase of R_{T,O_2} at $i_{lim} < 1\,A\,cm^{-2}$ before remaining at a constant level of $2.8\,s\,cm^{-1}$ for the carbon black MPL (blue symbols) and $2.6\,s\,cm^{-1}$ for the VGCF MPL.

At $T_{cell} = 80\,°C$ and $RH = 100\%$ (center graph), the two substrate materials behave totally contrary. As already observed in reference 54 and section 4.2, the Freudenberg GDL with and without MPLs all stay at the same level of $R_{T,O_2} = 0.9\,s\,cm^{-1}$ to $1.1\,s\,cm^{-1}$. We argue that due to the low thermal conductivity, and hence, a large temperature gradient, the GDL-S, the MPL, and the cathode remain free of liquid water, which results in a constant low plateau of R_{T,O_2}. For the Toray 030T substrate without MPL, again a significant increase of R_{T,O_2} is observed caused by flooding with liquid water. Both MPLs result in the stabilization of R_{T,O_2} at a rather low level of $\sim 2.0\,s\,cm^{-1}$, which is, however, significantly higher than for the Freudenberg materials. Interestingly, for the Toray paper, both MPLs develop the same level of the wet plateau, which means that the property of the MPL does not seem to make a difference.

For dry operating conditions, i.e., $T_{cell} = 95\,°C$ and $RH = 70\%$ (bottom graph), all GDLs stay at the dry plateau of the transport resistance, which indicates that no or negligible amounts of liquid water are formed in the porous media in all six cases.

Polarization curves

While the limiting current density is solely dominated by the oxygen transport resistance, all voltage loss contributions are reflected in the polarization curves. E_{cell} (top graph) and the *HFR* (bottom graph) are shown in **Figure 4.2** for the three different operating conditions. The differences in voltage loss between the different GDL-S/MPL combinations at humid conditions ($T_{cell} = 50\,°C$ and $RH = 100\%$, $p_{abs} = 300\,kPa$; **Figure 4.2** left graph) are mainly dominated by the oxygen transport resistance. The GDL-S without MPLs clearly underperform, with the Toray 030T substrate showing significant mass transport limitations so that at 0.6 V only $0.8\,A\,cm^{-2}$ are obtained,

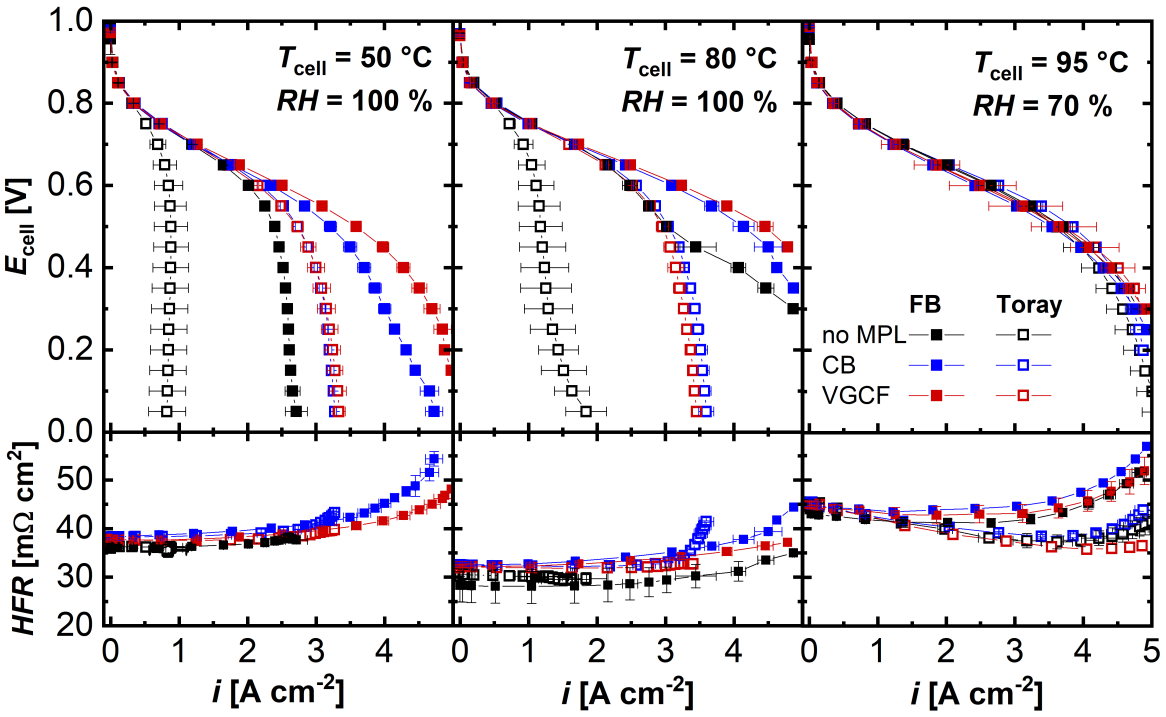

Figure 4.2. Cell voltage (E_{cell}) (top graphs) and high frequency resistance (HFR) (bottom graphs) versus the current density i at T_{cell} = 50 °C and RH = 100% (left graph), T_{cell} = 80 °C and RH = 100% (middle graph), and T_{cell} = 95 °C and RH = 70% (right graph), with p_{abs} = 300 kPa. Cathode GDLs were Freudenberg (FB) and Toray 030T substrates either without MPL or coated with a carbon black (Li400) MPL or carbon fiber (100% VGCF) MPL. The anode MPL was in all cases a carbon black (Li400) MPL. The MEA (from Gore) was a 18 µm membrane with 0.1/0.4 mg_{Pt} cm^{-2} on anode/cathode. The error bars represent the standard deviation from two independently measured cells

in contrast to 2.0 A cm^{-2} for the Freudenberg substrate (filled black symbols). The addition of an MPL enhances the performance for both substrates, with the Toray 030T substrate reaching 2.2 A cm^{-2} for both MPLs and the Freudenberg substrate even 2.3 A cm^{-2} for the carbon black MPL and 2.5 A cm^{-2} for the VGCF MPL. As the HFR for all materials is very similar (between 35 and 40 Ω cm^2 at OCV) and develops equally up to ~3 A cm^{-2}, and as the used electrodes and thus the ORR kinetics and the proton conductivity are the same, the differences between the materials can only be explained by the differences of R_{T,O_2}. The performance behaves in the same order as the oxygen transport resistances in **Figure 4.1**, with the Toray 030T substrate without MPL having the highest and the Freudenberg GDL-S with VGCF MPL exhibiting the lowest R_{T,O_2}.

The normal conditions (T_{cell} = 80 °C and RH = 100%, p_{abs} = 300 kPa) shown in

Figure 4.2 (center graph) represent a typical operating point for a high-pressure automotive fuel cell system. Also, as observed in **Figure 4.1**, the Toray 030T substrate without MPL is prone to early flooding and shows an early mass transport limitation. Adding an MPL, the performance of the Toray GDLs increases to $2.5\,\mathrm{A\,cm^{-2}}$ at 0.6 V, independent of the MPL type. Also, the Freudenberg GDL-S without MPL shows an early voltage drop, however, reaching significantly higher current densities of $2.5\,\mathrm{A\,cm^{-2}}$ at 0.6 V. It has to be noted that the here detected S-shape of the polarization curve is observed for both tested individual cells, which cannot be explained by any of the existing models and is at variance with the low and current-independent $R_{\mathrm{T,O_2}}$ determined for this material (see middle panel of **Figure 4.1**). One reason could be that during the limiting current measurement that is conducted at $< 0.3\,\mathrm{V}$ (i.e., at very high heat to electrical power ratio), the heat generation is just high enough to keep the Freudenberg GDL-S water-free, and that this is not possible at the higher cell voltage during polarization curve measurements. However, the reason for this behavior could not be resolved by our available methods. The addition of an MPL also results in a significant increase of performance, with the highest performance for the VGCF MPL on the Freudenberg GDL-S yielding $3.4\,\mathrm{A\,cm^{-2}}$ at 0.6 V.

If no water is condensed in the porous media at dry operating conditions ($T_{\mathrm{cell}} = 95\,^{\circ}\mathrm{C}$ and $RH = 70\%$, $p_{\mathrm{abs}} = 300\,\mathrm{kPa}$), the polarization curves for all six material combinations show a very similar performance, with currents ranging between $2.4\,\mathrm{A\,cm^{-2}}$ and $2.8\,\mathrm{A\,cm^{-2}}$ at 0.6 V; noteworthy is only the large error range for the two cells with Toray 030T with VGCF MPL due to a very different performance for the two repeat measurements ($2.2\,\mathrm{A\,cm^{-2}}$ vs. $2.9\,\mathrm{A\,cm^{-2}}$ at 0.6 V). At dry operating conditions, the oxygen transport resistance has a minor role, as **Figure 4.1** shows that all $R_{\mathrm{T,O_2}}$ values are on the same and very low level. One major difference between the two different GDL-substrates can be glanced from the variation of the *HFR* with current density (lower graph). While all materials show an *HFR* of ~$45\,\mathrm{m\Omega\,cm^2}$ at OCV, the *HFR* increases for the Freudenberg GDLs with increasing current density to values of up to $57\,\mathrm{m\Omega\,cm^2}$, while the *HFR* values for the Toray GDLs decrease down to $36\,\mathrm{m\Omega\,cm^2}$ with increasing current density. This trend is also indicated in the polarization curves with the Toray 030T with the VGCF MPL (red solid symbols in the right panel of **Figure 4.2**) that performs slightly better than the rest at very high current densities.

4.4.4. Discussion

From the data shown in **Figure 4.1** and **Figure 4.2**, we can conclude that an MPL is essential (aside from other requirements shown in section 2.2.3) when at some point of operation liquid water formation is occurring. This phenomenon has been attributed to the function of the MPL to prevent water accumulation at the GDL/MPL interface and is discussed in sections 4.1 and 4.2.[34,43,54,132] While at $T_{\text{cell}} = 50\,^{\circ}\text{C}$, where a lot of liquid water is formed, we could observe most significant differences between the performance and transport resistances of the MPLs on the Freudenberg GDL-S (as already shown in section 4.3 and reference 90), while the MPL type does not seem to make a difference on a Toray 030T GDL-S (see **Figures 4.1** and **4.2**). This is somehow perplexing, as due to the higher thermal conductivity, and thus lower thermal gradient as shown in section 2.2.2, a higher amount of liquid water should be present, which would require a more permeable MPL. This has been already observed by Owejan et al.,[43] testing two types of MPL on Toray 060 and MRC105, which also have different thermal conductivities. They concluded that the thermal gradient in the GDL-S is dominating the oxygen transport overpotential over the liquid phase transport in the MPL. However, contrary to their study, we found significant differences for the GDL-substrate with the lower thermal conductivity (i.e., the Freudenberg GDL-S) when varying the MPL. One reason could be, that in case of the Toray 030T substrate, the differences in pore structure, wettability etc. could cause a dominance of the substrate properties for the Toray 030T substrate, compared to the Freudenberg GDL-S, where the MPL seems to contribute significantly to the voltage drop. Unfortunately, this lack of understanding could not yet been resolved.

To understand how the GDL properties contribute to the voltage loss, a voltage loss analysis was conducted for the Freudenberg and Toray 030T GDL-substrates with the best-performing VGCF MPL at two operating conditions, which are relevant for the operation of a fuel cell system, namely at normal operating conditions at $T_{\text{cell}} = 80\,^{\circ}\text{C}$ and $RH = 100\%$, and at dry operating conditions (relevant for high-temperature systems) at $T_{\text{cell}} = 95\,^{\circ}\text{C}$ and $RH = 70\%$. The overpotentials for the ORR (η_{ORR}) and the voltage losses due to the proton resistance in the membrane ($i \cdot R_{\text{membrane}}$), the contact resistance ($i \cdot R_{\text{contact}}$), the proton resistance in the cathode ($i \cdot R^{\text{eff}}_{\text{H}^+,\text{ca}}$), and the oxygen transport overpotential ($\eta_{\text{tx},\text{O}_2}$) have been considered according to section 2.1.2.

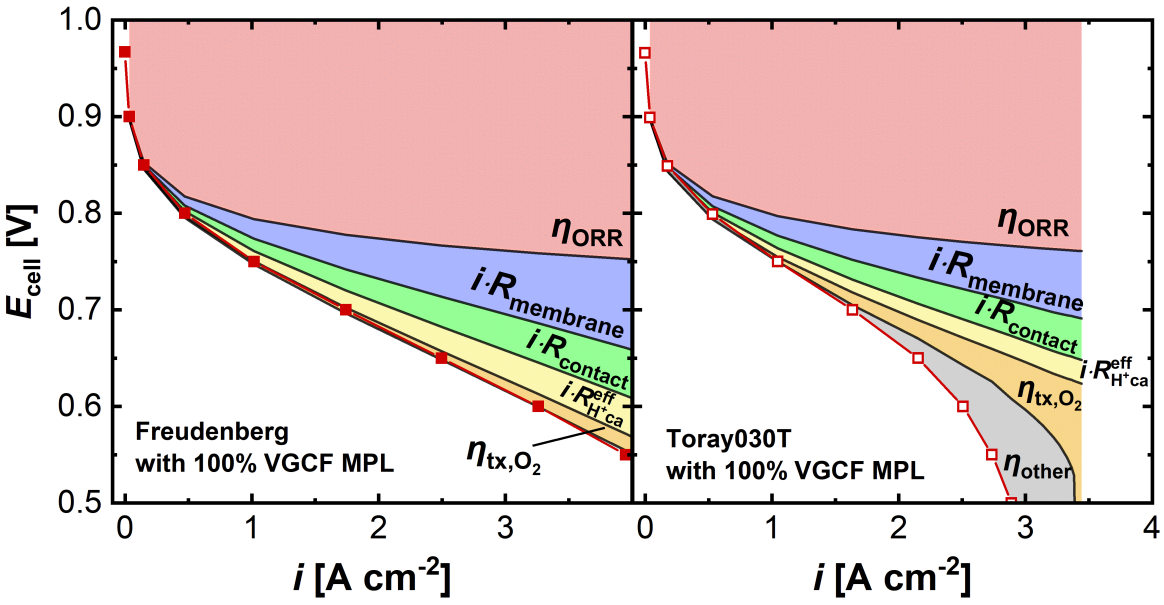

Figure 4.3. Voltage loss analysis for an MEA with Freudenberg substrate (left graph) and with Toray 030T substrate (right graph), both equipped with a carbon fiber (100% VGCF) MPL on the cathode and a carbon black (Li400) MPL on the anode. The MEA (from Gore) was a 18 µm membrane with 0.1/0.4 $mg_{Pt}\,cm^{-2}$ on anode/cathode. Operating conditions were T_{cell} = 80 °C, RH = 100%, and p_{abs} = 300 kPa.

For T_{cell} = 80 °C and RH = 100%, the results are shown in **Figure 4.3** up to 4.0 A cm^{-2}. While the voltage losses caused by the ORR, the membrane resistance, the contact resistance, and the electrode proton conductivity are very similar (0.63 V for Freudenberg vs. 0.64 V for Toray at 3.0 A cm^{-2}, see bottom line of the yellow field in **Figure 4.3**), the calculated oxygen transport overpotentials at 3.0 A cm^{-2} differ significantly with 12 mV for Freudenberg and 50 mV for Toray (see width of the orange field in **Figure 4.3**). When comparing the measured polarization curve (red line) vs. the projected performance (bottom line of the orange field), the Freudenberg GDL matches very well. However, for the Toray material, the measured polarization curve deviates for $i > 1.6$ A cm^{-2} from the projected performance and exhibits an additional unaccounted voltage loss of η_{other} = 147 mV at 3.0 A cm^{-2}. This voltage loss is not described by our model and could have several causes. The most likely reason is that η_{other} is also caused by an oxygen transport overpotential that however, cannot be measured by limiting current density measurements. As R_{T,O_2} is measured at low voltages of 0.05 V (i.e., at low fuel cell efficiencies), the saturation of liquid water could be different at the significantly higher voltage of the polarization curve, where less heat is evolved. At these higher voltages, the local electrode temperature, and hence, the

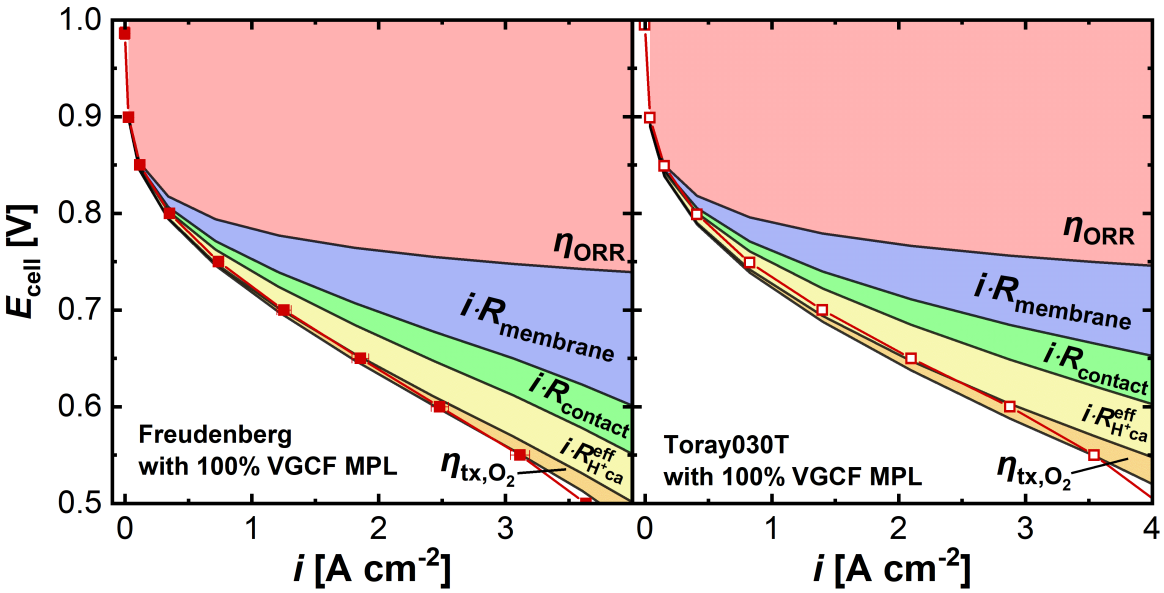

Figure 4.4. Voltage loss analysis for an MEA with Freudenberg substrate (left graph) and Toray 030T substrate (right graph), both equipped with a carbon fiber (100% VGCF) MPL on the cathode and a carbon black (Li400) MPL on the anode. The MEA (from Gore) was a 18 µm membrane with 0.1/0.4 mg_{Pt} cm^{-2} on anode/cathode. Operating conditions were $T_{cell} = 95\,°C$, $RH = 70\%$ and $p_{abs} = 300\,kPa$.

temperature gradient across the GDL is expected to be lower. Hence, the calculated η_{tx,O_2} based on R_{T,O_2} might underestimate the real oxygen transport overpotential.

At dry operating conditions, i.e., $T_{cell} = 95\,°C$ and $RH = 70\%$, where no presence of liquid water is expected in the porous media (data see **Figure 4.4**), the calculated polarization curve very well matches the measured curves for both materials. At $i = 3.0\,A\,cm^{-2}$, the calculated value for the Freudenberg substrate (lower line of the orange field) overlaps with the measured curve (red line); for Toray 030T, the measured voltage at $i = 3.0\,A\,cm^{-2}$ is only 8 mV higher than the projected performance, which is, however, within the range of error. Except for $i \cdot R_{membrane}$, the voltage loss contributions do not differ significantly from each other, which is expected as the same MEA is used, and the oxygen transport resistances are identical for the two cells. The difference in high-frequency resistances at increased current density causes also differences in the associated voltage drops. As the contact resistance is assumed to be constant, the change is purely attributed to the membrane resistance. This results at $i = 3.0\,A\,cm^{-2}$ in $i \cdot R_{membrane} = 96\,mV$ for the Freudenberg GDL and 74 mV for the Toray GDL. At higher current densities the gap increases even more. Due to the low thermal conductivity of the Freudenberg GDL, the temperature at the membrane

is increased, so that the relative humidity near the membrane is decreased, which in turn increases the membrane resistance. This causes an increased voltage drop, but even more critical, results in a faster aging of the membrane.[13]

4.4.5. Conclusions

The interaction of different GDL-substrates with the functionality of the MPL has rarely been studied in the literature, and in most studies different MPLs have only been tested on one GDL-substrate. For this reason, we have tested two of the MPLs developed in previous studies on two GDL-substrates with different thermal properties, which are a non-woven Freudenberg GDL-S and Toray 030T carbon paper.

As the thermal conductivity of the Toray 030T GDL-S is higher than that of the Freudenberg material by a factor of 2.5, the associated temperature gradient driving the vapor phase transport is higher for the Freudenberg material. This means that at fully saturated operating conditions (i.e., $T_{\text{cell}} = 50\,^{\circ}\text{C}$ or $T_{\text{cell}} = 80\,^{\circ}\text{C}$, $RH = 100\%$, and $p_{\text{abs}} = 300\,\text{kPa}$) the Toray 030T is prone to flooding, showing a mass transport limitation at low current densities, while the Freudenberg material can release liquid water efficiently and thus exhibits a small oxygen transport resistance. However, at dry operating conditions (i.e., $T_{\text{cell}} = 95\,^{\circ}\text{C}$, $RH = 70\%$, and $p_{\text{abs}} = 300\,\text{kPa}$), the Freudenberg GDL-S is prone to membrane dry-out at elevated current densities, while the Toray GDL-S maintains a lower local temperature and a concomitant higher local relative humidity at the membrane which results in a lower *HFR*. Hence, the Freudenberg GDL-S is recommended to be used at rather humid operating conditions, while the Toray 030T GDL-S performs best at rather dry operating conditions.

Concerning the effect of the MPL, for both materials an MPL is required for efficient oxygen transport for operating points where the presence of liquid water is expected. Although for the Freudenberg GDL-S, the MPL properties significantly impact the oxygen transport resistance and the overall performance, with the VGCF (carbon fiber) MPL achieving better results than a pure carbon black MPL, the MPL properties do not show a significant effect on the Toray 030T GDL-S. The reason for this behavior is not clear. One hypothesis is that the flooding of the GDL-S is superimposing the positive effect of the MPL. Further investigations would be required to resolve this phenomenon.

5. Conclusions

The motivation of the present thesis was to (1) expand the understanding of the functionality and transport mechanisms in the microporous layer in a PEMFC and (2) to improve the oxygen transport and overall performance of the fuel cell with a focus on high current density operation, which is used, e.g., in automotive applications. As basis for our investigations, we apply the so-called limiting current density method developed by Baker et al.[25] for the determination of the oxygen transport resistance and used it to examine different gas diffusion layer substrates and microporous layers with different properties.

For this purpose, we developed a new flow field design for differential flow measurements, which we used for all of our studies. Furthermore, preparation methods for microporous layers were developed to prepare different MPLs (carbon materials and binders) that exhibit different structures and different wetting characteristics.

Transport resistance at the MPL/cathode interface

By measuring the oxygen transport resistance for a commercial GDL with MPL (SGL GDL25 BC), we discovered an additional resistance at the interface between the MPL and the cathode catalyst layer, which appears when the GDL is insufficiently compressed. If the compressive strain of the GDL is 13% of its initial thickness and lower, the oxygen transport resistance increased disproportionally. We attribute this effect to the formation of a liquid water film between MPL and cathode, causing a significant diffusion barrier. The effect is compared to the similar trend for a GDL-substrate without MPL (SGL GDL25 BA), for which it is known that the GDL/cathode interface is flooding in the presence of liquid water. On the other hand, if the compressive strain is 23% and higher, the oxygen transport resistance is also increasing due to the reduction of porosity of the GDL-substrate. As a conclusion we found an optimum in in compressive strain at ~20%, which is purely oxygen transport related.

Elucidation of the impact of a hydrophilic binder

Several studies in the literature claim that all-hydrophilic MPLs, which are created by using a hydrophilic binder or a hydrophilic filler improve the PEMFC performance at both humid and dry operating conditions.[91,93–95,134] However, these studies do not rigorously compare different MPLs, i.e. hydrophilic and hydrophobic MPLs based on different carbon materials with, e.g., different pore size distributions, and the used "wet" operating conditions are not sufficiently humid to produce significant amounts of liquid water in the porous media. Hence, in section 4.3 we developed microporous layers with the same carbon composition (either pure carbon black or 80% vapor grown carbon fibers (VGCF) and 20% carbon black) with either hydrophobic PTFE (polytetrafluoroethylene) or hydrophilic PFSA (perfluorosulfonic acid) as binder.

We tested the materials under dry ($T_{\text{cell}} = 80\,^{\circ}\text{C}$, $p_{\text{abs}} = 170\,\text{kPa}$, $RH = 70\%$) and humid ($T_{\text{cell}} = 50\,^{\circ}\text{C}$, $p_{\text{abs}} = 300\,\text{kPa}$, $RH = 120\%$) operating conditions, and investigated the H_2/air performance, the high frequency resistance, and the oxygen transport resistance. While at dry operating conditions (i.e., in absence of liquid water), we found no difference between the materials, at humid conditions, the materials with hydrophobic binder always performed better than their hydrophilic counterpart; in general, the 80% VGCF MPLs performed better than the carbon black MPLs. We explained this behavior with the capillary pressure and the superposition of contact angle changes and pore size changes when changing both hydrophilicity and carbon material. We interpret the contradicting results in the literature by the fact that in most of the cases hydrophilic and hydrophobic MPLs with different carbon materials have been compared, which erroneously suggested a better performance of hydrophilic MPLs with large pore sizes over hydrophobic MPLs with small pore sizes.

GDL-substrate impact

In section 4.4, two different MPLs (pure carbon black and pure VGCF) were tested on two different GDL-substrates (Freudenberg non-woven and Toray 030T carbon paper) at dry, humid, and normal operating conditions. We identified the thermal conductivity of the GDL-substrate and its effect on the thermal gradient across the GDL to be the main driver observed dependence of the oxygen transport resistance and of the membrane conductivity on the choice of GDL-substrate. While Toray 030T GDL-S with a low thermal gradient is flooding immediately, due to the condensation of

liquid water, the poorly heat-conducting Freudenberg GDL-S produces a high thermal gradient through which product water can be removed efficiently in the vapor phase resulting in a low oxygen transport resistance. At dry operating conditions, however, the higher thermal gradient of the Freudenberg GDL-S is causing a membrane dry-out, leading to ~30% higher voltage losses for the membrane resistance compared to the Toray 030T GDL-S. Hence, we conclude that the Freudenberg GDL-S is more suitable at humid operating conditions, while the Toray 030T GDL-S is better used at dry operating fuel cell systems.

An unexpected result was that the effect of the MPL properties (i.e., the pore size distribution) is minor for the Toray 030T GDL-S, even though larger amounts of condensed water are suspected for this material. We hypothesize that the saturation of the GDL-substrate is superimposing the positive effect of the MPL concerning water and oxygen transport; however, we were not able to prove this assumption.

Improvement of the fuel cell performance by reduction of the oxygen transport resistance

We tested a large variety of materials with different carbon black materials (Denka Li100 and Li400; section 4.2 [54]), introduced perforations (section 4.2, [54]) compared hydrophilic and hydrophobic binders (section 4.3, [90]) and applied vapor grown carbon fibers to tune the pore size distribution (section 4.3. [90]) By these developments and findings, we could reduce the oxygen transport resistance of the GDL significantly. The performance results at 0.6 V at dry, normal, and humid operating conditions are shown in **Table 5.1**.

By preparation of two MPLs with different carbon blacks (Denka Li100 and Li400), we were able to modify the pore size distribution and porosity from $\varepsilon = 79\%$ and a pore size distribution maximum of 67 nm for Li100 to $\varepsilon = 68\%$ and a pore size distribution maximum of 328 nm for Li400. We found that the larger pore size significantly improves the oxygen and water transport by a reduction of the capillary pressure, which results in a reduced oxygen transport resistance and improved performance at humid conditions. Furthermore, we developed a procedure to introduce perforations by adding polymethylmethacrylate beads with a diameter of 30 µm to the MPL ink and decomposing the beads by a heat treatment step. This results in a further decrease of the oxygen transport resistance for both the Li100 and the Li400 MPLs due

Table 5.1. Overview of hydrophobic microporous layers and their current density at 0.6 V with differential flows of H_2/air for dry, normal, and humid operating conditions. The MEA (from Gore) was a 18 µm membrane with 0.1/0.4 $mg_{Pt}\,cm^{-2}$ on anode/cathode.

MPL [-]	i (dry) [1] [$A\,cm^{-2}$]	i (normal) [2] [$A\,cm^{-2}$]	i (humid) [3] [$A\,cm^{-2}$]
no MPL	1.64	2.48	2.07
commercial MPL	1.72	2.19	1.80
Li100	1.76	-	2.03
Li400 (0% VGCF)	1.60	3.09	2.28
Li100 perforated	1.35	-	2.31
Li400 perforated	1.65	3.23	2.44
50% VGCF	1.54	-	2.32
80% VGCF	1.58	-	2.42
100% VGCF	1.61	3.26	2.50

[1] $T_{cell} = 80\,°C$, $p_{abs} = 170\,kPa$, $RH = 70\%$.
[2] $T_{cell} = 80\,°C$, $p_{abs} = 300\,kPa$, $RH = 100\%$.
[3] $T_{cell} = 50\,°C$, $p_{abs} = 300\,kPa$, $RH = 120\%$.

to the creation of preferred liquid water transport pathways through the large cracks and pores, while oxygen is transported efficiently through the pore structure of the carbon black framework.

Based on these findings, we attempted to shift the pore size distribution to even higher pore sizes by replacing the Li400 carbon black with 50wt.%, 80wt.%, and 100wt.% vapor grown carbon fibers (VGCF). By this procedure, we were able to tune the porosity and pore size distribution from $\varepsilon = 68\%$ and a pore size distribution maximum of 328 nm for the pure carbon black MPL to $\varepsilon = 83\%$ and a pore size distribution maximum of 722 nm for the 100% VGCF MPL. While the fuel cell performance at dry conditions is approximately constant with values between 1.54 $A\,cm^{-2}$ and 1.61 $A\,cm^{-2}$ at 0.6 V, the performance at humid operating conditions increases by ~10% from 2.28 $A\,cm^{-2}$ for the Li400 MPL to 2.50 $A\,cm^{-2}$ for the 100% VGCF MPL. We explain this behaviour by a further reduction of the capillary pressure due to larger pore sizes, which is advantageous for the removal of liquid water from the electrode layer. Major results are summarized in **Table 5.1**.

When we benchmark our best performing MPL at a typical operating condition for high-pressure systems ($T_{cell} = 80\,°C$, $p_{abs} = 300\,kPa$, $RH = 100\%$), as they appear, e.g., in automotive applications, we find that our work improved the performance by

49% from 2.19 A cm^{-2} for the commercial MPL to 3.26 A cm^{-2} for the 100% VGCF MPL at 0.6 V. Overall, the 100% VGCF MPL gives the best performance at normal and humid operating conditions while not significantly reducing the performance at dry conditions (see **Table 5.1**).

References

[1] McKinsey & Company. Automotive revolution - perspective towards 2030 - How the convergence of disruptive technology-driven trends could transform the auto industry. Report (2016).

[2] Roland Berger GmbH. Automotive Disruption Radar. Issue 1 - Tracking disruption signals in the automotive industry (2017).

[3] European Commission. The Paris Protocol - A blueprint for tackling global climate change beyond 2020 (2015).

[4] The European Parliament and the Council of the European Union. Regulation (EU) 2019/631 of the European Parliament and of the Council of 17 April 2019 setting CO2 emission performance standards for new passenger cars and for new light commercial vehicles, and repealing Regulations (EC) No 443/2009 and (EU) No 510/2011. *Official Journal of the European Union*, (L 111/13) (2019).

[5] European Parliament. https://www.europarl.europa.eu/news/de/headlines/society/20190313STO31218/co2-emissionen-von-autos-zahlen-und-fakten-infografik, accessed on Jan. 12, 2020.

[6] U. Eberle, B. Müller, and R. von Helmolt. Fuel cell electric vehicles and hydrogen infrastructure: status 2012. *Energy & Environmental Science*, **5**(10), 8780–8798 (2012).

[7] O. Gröger, H. A. Gasteiger, and J.-P. Suchsland. Review - Electromobility: Batteries or Fuel Cells? *Journal of The Electrochemical Society*, **162**(14), A2605–A2622 (2015).

[8] H2 MOBILITY Deutschland. www.h2.live, accessed on Jan. 11, 2020.

[9] G. G. Scherer. Fuel Cell Types and Their Electrochemistry. In *Fuel Cells: Selected Entries from the Encyclopedia of Sustainability Science and Technology*, edited by K.-D. Kreuer, pp. 9–29. Springer New York (2013).

[10] T. Yoshida and K. Kojima. Toyota MIRAI Fuel Cell Vehicle and Progress Toward a Future Hydrogen Society. *The Electrochemical Society Interface*, **24**(2), 45–49 (2015).

[11] J. Wind, A. LaCroix, S. Braeuninger, P. Hedrich, C. Heller, and M. Schudy. Metal bipolar plates and coatings. In *Handbook of Fuel Cells*, volume 3, edited by W. Vielstich, A. Lamm, and H. A. Gasteiger, chapter 25, pp. 294–307. John Wiley and Sons, Ltd (2003).

[12] K. Roßberg and V. Trapp. Graphite-based bipolar plates. In *Handbook of Fuel Cells*, volume 3, edited by W. Vielstich, A. Lamm, and H. A. Gasteiger, chapter 26, pp. 308–314. John Wiley and Sons, Ltd (2003).

[13] C. S. Gittleman, F. D. Coms, and Y.-H. Lai. Chapter 2 - Membrane Durability: Physical and Chemical Degradation. In *Polymer Electrolyte Fuel Cell Degradation*, edited by M. M. Mench, E. C. Kumbur, and T. N. Veziroglu, pp. 15–88. Academic Press, Boston (2012).

[14] C. K. Mittelsteadt and H. Liu. Conductivity, permeability, and ohmic shorting of ionomeric membranes. In *Handbook of Fuel Cells*, volume 5, edited by W. Vielstich, H. A. Gasteiger, and H. Yokokawa, chapter 23, pp. 345–358. John Wiley & Sons, Ltd (2009).

[15] A. Kongkanand and M. F. Mathias. The Priority and Challenge of High-Power Performance of Low-Platinum Proton-Exchange Membrane Fuel Cells. *The Journal of Physical Chemistry Letters*, **7**(7), 1127–1137 (2016).

[16] H. A. Gasteiger, S. S. Kocha, B. Sompalli, and F. T. Wagner. Activity benchmarks and requirements for Pt, Pt-alloy, and non-Pt oxygen reduction catalysts for PEMFCs. *Applied Catalysis B: Environmental*, **56**(1-2), 9–35 (2005).

[17] M. F. Mathias, J. Roth, J. Fleming, and W. Lehnert. Diffusion media materials and characterisation. In *Handbook of Fuel Cells*, volume 3, edited by W. Vielstich, H. A. Gasteiger, and A. Lamm, chapter 46, pp. 517–537. John Wiley and Sons, Ltd (2003).

[18] J. Durst, A. Siebel, C. Simon, F. Hasché, J. Herranz, and H. A. Gasteiger. New insights into the electrochemical hydrogen oxidation and evolution reaction mechanism. *Energy & Environmental Science*, **7**(7), 2255–2260 (2014).

[19] J. Durst, C. Simon, F. Hasché, and H. A. Gasteiger. Hydrogen Oxidation and Evolution Reaction Kinetics on Carbon Supported Pt, Ir, Rh, and Pd Electrocatalysts in Acidic Media. *Journal of The Electrochemical Society*, **162**(1), F190–F203 (2015).

[20] K. C. Neyerlin, W. Gu, J. Jorne, and H. A. Gasteiger. Study of the Exchange Current Density for the Hydrogen Oxidation and Evolution Reactions. *Journal of The Electrochemical Society*, **154**(7), B631–B635 (2007).

[21] W. Sheng, H. A. Gasteiger, and Y. Shao-Horn. Hydrogen Oxidation and Evolution Reaction Kinetics on Platinum: Acid vs Alkaline Electrolytes. *Journal of The Electrochemical Society*, **157**(11), B1529–B1536 (2010).

[22] K. C. Neyerlin, W. Gu, J. Jorne, and H. A. Gasteiger. Determination of Catalyst Unique Parameters for the Oxygen Reduction Reaction in a PEMFC. *Journal of The Electrochemical Society*, **153**(10), A1955–A1963 (2006).

[23] K. C. Neyerlin, W. Gu, J. Jorne, A. Clark, and H. A. Gasteiger. Cathode Catalyst Utilization for the ORR in a PEMFC: Analytical Model and Experimental Validation. *Journal of The Electrochemical Society*, **154**(2), B279–B287 (2007).

[24] D. R. Baker, C. Wieser, K. C. Neyerlin, and M. W. Murphy. The Use of Limiting Current to Determine Transport Resistance in PEM Fuel Cells. *ECS Transactions*, **3**(1), 989–999 (2006).

[25] D. R. Baker, D. A. Caulk, K. C. Neyerlin, and M. W. Murphy. Measurement of Oxygen Transport Resistance in PEM Fuel Cells by Limiting Current Methods. *Journal of the Electrochemical Society*, **156**(9), B991–B1003 (2009).

[26] D. A. Caulk and D. R. Baker. Heat and Water Transport in Hydrophobic Diffusion Media of PEM Fuel Cells. *Journal of the Electrochemical Society*, **157**(8), B1237–B1244 (2010).

[27] V. Yarlagadda, M. K. Carpenter, T. E. Moylan, R. S. Kukreja, R. Koestner, W. Gu, L. Thompson, and A. Kongkanand. Boosting Fuel Cell Performance with Accessible Carbon Mesopores. *ACS Energy Letters*, **3**(3), 618–621 (2018).

[28] A. Orfanidi, P. Madkikar, H. A. El-Sayed, G. S. Harzer, T. Kratky, and H. A. Gasteiger. The Key to High Performance Low Pt Loaded Electrodes. *Journal of The Electrochemical Society*, **164**(4), F418–F426 (2017).

[29] T. A. Greszler, D. Caulk, and P. Sinha. The Impact of Platinum Loading on Oxygen Transport Resistance. *Journal of The Electrochemical Society*, **159**(12), F831–F840 (2012).

[30] Y. Fukuyama, T. Shiomi, T. Kotaka, and Y. Tabuchi. The Impact of Platinum Reduction on Oxygen Transport in Proton Exchange Membrane Fuel Cells. *Electrochimica Acta*, **117**, 367–378 (2014).

[31] J. P. Owejan, T. A. Trabold, and M. M. Mench. Oxygen transport resistance correlated to liquid water saturation in the gas diffusion layer of PEM fuel cells. *International Journal of Heat and Mass Transfer*, **71**, 585–592 (2014).

[32] H. Oh, Y. i. Lee, G. Lee, K. Min, and J. S. Yi. Experimental dissection of oxygen transport resistance in the components of a polymer electrolyte membrane fuel cell. *Journal of Power Sources*, **345**, 67–77 (2017).

[33] N. Nonoyama, S. Okazaki, A. Z. Weber, Y. Ikogi, and T. Yoshida. Analysis of Oxygen-Transport Diffusion Resistance in Proton-Exchange-Membrane Fuel Cells. *Journal of The Electrochemical Society*, **158**(4), B416–B423 (2011).

[34] C. Simon, F. Hasché, and H. A. Gasteiger. Influence of the Gas Diffusion Layer Compression on the Oxygen Transport in PEM Fuel Cells at High Water Saturation Levels. *Journal of The Electrochemical Society*, **164**(6), F591–F599 (2017).

[35] P. Zihrul, I. Hartung, S. Kirsch, G. Huebner, F. Hasché, and H. A. Gasteiger. Voltage Cycling Induced Losses in Electrochemically Active Surface Area and in H_2/Air-Performance of PEM Fuel Cells. *Journal of The Electrochemical Society*, **163**(6), F492–F498 (2016).

[36] J. M. Morgan and R. Datta. Understanding the gas diffusion layer in proton exchange membrane fuel cells. I. How its structural characteristics affect diffusion and performance. *Journal of Power Sources*, **251**, 269–278 (2014).

[37] L. Cindrella, A. M. Kannan, J. F. Lin, K. Saminathan, Y. Ho, C. W. Lin, and J. Wertz. Gas diffusion layer for proton exchange membrane fuel cells-A review. *Journal of Power Sources*, **194**(1), 146–160 (2009).

[38] S. Park, J.-W. Lee, and B. N. Popov. A review of gas diffusion layer in PEM fuel cells: Materials and designs. *International Journal of Hydrogen Energy*, **37**(7), 5850–5865 (2012).

[39] H. Butsch, C. Roth, D. Ritzinger, G. Hoogers, and A. Bock. Spatially Resolved Contact Pressure and Contact Resistance Measurements at the Gas Diffusion Layer: A Tool for PEM Fuel Cell Development. *Journal of the Electrochemical Society*, **159**(6), B709–B713 (2012).

[40] I. Nitta, T. Hottinen, O. Himanen, and M. Mikkola. Inhomogeneous compression of PEMFC gas diffusion layer Part I. Experimental. *Journal of Power Sources*, **171**(1), 26–36 (2007).

[41] T. Hottinen, O. Himanen, S. Karvonen, and I. Nitta. Inhomogeneous compression of PEMFC gas diffusion layer - Part II. Modeling the effect. *Journal of Power Sources*, **171**(1), 113–121 (2007).

[42] J. Kleemann, F. Finsterwalder, and W. Tillmetz. Characterisation of mechanical behaviour and coupled electrical properties of polymer electrolyte membrane fuel cell gas diffusion layers. *Journal of Power Sources*, **190**(1), 92–102 (2009).

[43] J. P. Owejan, J. E. Owejan, W. B. Gu, T. A. Trabold, T. W. Tighe, and M. F. Mathias. Water Transport Mechanisms in PEMFC Gas Diffusion Layers. *Journal of the Electrochemical Society*, **157**(10), B1456–B1464 (2010).

[44] C. Hartnig, I. Manke, R. Kuhn, S. Kleinau, J. Goebbels, and J. Banhart. High-resolution in-plane investigation of the water evolution and transport in PEM fuel cells. *Journal of Power Sources*, **188**(2), 468–474 (2009).

[45] S. Litster, D. Sinton, and N. Djilali. Ex situ visualization of liquid water transport in PEM fuel cell gas diffusion layers. *Journal of Power Sources*, **154**(1), 95–105 (2006).

[46] I. Nitta, O. Himanen, and M. Mikkola. Thermal conductivity and contact resistance of compressed gas diffusion layer of PEM fuel cell. *Fuel Cells*, **8**(2), 111–119 (2008).

[47] O. S. Burheim, G. Ellila, J. D. Fairweather, A. Labouriau, S. Kjelstrup, and J. G. Pharoah. Ageing and thermal conductivity of Porous Transport Layers used for PEM Fuel Cells. *Journal of Power Sources*, **221**(Supplement C), 356–365 (2013).

[48] O. S. Burheim, H. Su, S. Pasupathi, J. G. Pharoah, and B. G. Pollet. Thermal conductivity and temperature profiles of the micro porous layers used for the polymer electrolyte membrane fuel cell. *International Journal of Hydrogen Energy*, **38**(20), 8437–8447 (2013).

[49] G. Karimi, X. Li, and P. Teertstra. Measurement of through-plane effective thermal conductivity and contact resistance in PEM fuel cell diffusion media. *Electrochimica Acta*, **55**(5), 1619–1625 (2010).

[50] E. Sadeghi, N. Djilali, and M. Bahrami. Effective thermal conductivity and thermal contact resistance of gas diffusion layers in proton exchange membrane fuel cells. Part 1: Effect of compressive load. *Journal of Power Sources*, **196**(1), 246–254 (2011).

[51] Y. Tabe, Y. Aoyama, K. Kadowaki, K. Suzuki, and T. Chikahisa. Impact of micro-porous layer on liquid water distribution at the catalyst layer interface and cell performance in a polymer electrolyte membrane fuel cell. *Journal of Power Sources*, **287**, 422–430 (2015).

[52] I. V. Zenyuk, E. C. Kumbur, and S. Litster. Deterministic contact mechanics model applied to electrode interfaces in polymer electrolyte fuel cells and interfacial water accumulation. *Journal of Power Sources*, **241**, 379–387 (2013).

[53] A. R. Kalidindi, R. Taspinar, S. Litster, and E. C. Kumbur. A two-phase model for studying the role of microporous layer and catalyst layer interface on polymer

electrolyte fuel cell performance. *International Journal of Hydrogen Energy*, **38**(22), 9297–9309 (2013).

[54] C. Simon, D. Kartouzian, D. Müller, F. Wilhelm, and H. A. Gasteiger. Impact of Microporous Layer Pore Properties on Liquid Water Transport in PEM Fuel Cells: Carbon Black Type and Perforation. *Journal of the Electrochemical Society*, **164**(14), F1697–F1711 (2017).

[55] Y. Aoyama, K. Suzuki, Y. Tabe, T. Chikahisa, and T. Tanuma. Water Transport and PEFC Performance with Different Interface Structure between Micro-Porous Layer and Catalyst Layer. *Journal of The Electrochemical Society*, **163**(5), F359–F366 (2016).

[56] R. Bock, A. Shum, T. Khoza, F. Seland, N. Hussain, I. V. Zenyuk, and O. S. Burheim. Experimental Study of Thermal Conductivity and Compression Measurements of the GDL-MPL Interfacial Composite Region. *ECS Transactions*, **75**(14), 189–199 (2016).

[57] F. E. Hizir, S. O. Ural, E. C. Kumbur, and M. M. Mench. Characterization of interfacial morphology in polymer electrolyte fuel cells: Micro-porous layer and catalyst layer surfaces. *Journal of Power Sources*, **195**(11), 3463–3471 (2010).

[58] S. Prass, S. Hasanpour, P. K. Sow, A. B. Phillion, and W. Mérida. Microscale X-ray tomographic investigation of the interfacial morphology between the catalyst and micro porous layers in proton exchange membrane fuel cells. *Journal of Power Sources*, **319**, 82–89 (2016).

[59] T. Swamy, E. C. Kumbur, and M. M. Mench. Characterization of Interfacial Structure in PEFCs: Water Storage and Contact Resistance Model. *Journal of the Electrochemical Society*, **157**(1), B77–B85 (2010).

[60] A. Z. Weber and J. Newman. Effects of Microporous Layers in Polymer Electrolyte Fuel Cells. *Journal of The Electrochemical Society*, **152**(4), A677–A688 (2005).

[61] P. Deevanhxay, T. Sasabe, S. Tsushima, and S. Hirai. Effect of liquid water distribution in gas diffusion media with and without microporous layer on PEM fuel cell performance. *Electrochemistry Communications*, **34**, 239–241 (2013).

[62] P. Deevanhxay, T. Sasabe, S. Tsushima, and S. Hirai. Observation of dynamic liquid water transport in the microporous layer and gas diffusion layer of an operating PEM fuel cell by high-resolution soft X-ray radiography. *Journal of Power Sources*, **230**, 38–43 (2013).

[63] H. Li, Y. H. Tang, Z. W. Wang, Z. Shi, S. H. Wu, D. T. Song, J. L. Zhang, K. Fatih, J. J. Zhang, H. J. Wang, Z. S. Liu, R. Abouatallah, and A. Mazza. A review of water flooding issues in the proton exchange membrane fuel cell. *Journal of Power Sources*, **178**(1), 103–117 (2008).

[64] Z. Lu, M. M. Daino, C. Rath, and S. G. Kandlikar. Water management studies in PEM fuel cells, part III: Dynamic breakthrough and intermittent drainage characteristics from GDLs with and without MPLs. *International Journal of Hydrogen Energy*, **35**(9), 4222–4233 (2010).

[65] F. Lufrano, E. Passalacqua, G. Squadrito, A. Patti, and L. Giorgi. Improvement in the diffusion characteristics of low Pt-loaded electrodes for PEFCs. *Journal of Applied Electrochemistry*, **29**(4), 445–448 (1999).

[66] E. Passalacqua, G. Squadrito, F. Lufrano, A. Patti, and L. Giorgi. Effects of the Diffusion Layer Characteristics on the Performance of Polymer Electrolyte Fuel Cell Electrodes. *Journal of Applied Electrochemistry*, **31**(4), 449–454 (2001).

[67] S. Park, J.-W. Lee, and B. N. Popov. Effect of PTFE content in microporous layer on water management in PEM fuel cells. *Journal of Power Sources*, **177**(2), 457–463 (2008).

[68] D. Gerteisen, T. Heilmann, and C. Ziegler. Enhancing liquid water transport by laser perforation of a GDL in a PEM fuel cell. *Journal of Power Sources*, **177**(2), 348–354 (2008).

[69] D. Gerteisen and C. Sadeler. Stability and performance improvement of a polymer electrolyte membrane fuel cell stack by laser perforation of gas diffusion layers. *Journal of Power Sources*, **195**(16), 5252–5257 (2010).

[70] H. Markötter, R. Alink, J. Haussmann, K. Dittmann, T. Arlt, F. Wieder, C. Totzke, M. Klages, C. Reiter, H. Riesemeier, J. Scholta, D. Gerteisen, J. Banhart, and I. Manke. Visualization of the water distribution in perforated gas diffusion layers by means of synchrotron X-ray radiography. *International Journal of Hydrogen Energy*, **37**(9), 7757–7761 (2012).

[71] M. P. Manahan and M. M. Mench. Laser Perforated Fuel Cell Diffusion Media: Engineered Interfaces for Improved Ionic and Oxygen Transport. *Journal of The Electrochemical Society*, **159**(7), F322–F330 (2012).

[72] R. Alink, J. Haussmann, H. Markötter, M. Schwager, I. Manke, and D. Gerteisen. The influence of porous transport layer modifications on the water management in polymer electrolyte membrane fuel cells. *Journal of Power Sources*, **233**, 358–368 (2013).

[73] C. S. Kong, D.-Y. Kim, H.-K. Lee, Y.-G. Shul, and T.-H. Lee. Influence of pore-size distribution of diffusion layer on mass-transport problems of proton exchange membrane fuel cells. *Journal of Power Sources*, **108**(1), 185–191 (2002).

[74] P. M. Wilde, M. Mändle, M. Murata, and N. Berg. Structural and Physical Properties of GDL and GDL/BPP Combinations and their Influence on PEMFC Performance. *Fuel Cells*, **4**(3), 180–184 (2004).

[75] P. K. Das, X. G. Li, and Z. S. Liu. Effective transport coefficients in PEM fuel cell catalyst and gas diffusion layers: Beyond Bruggeman approximation. *Applied Energy*, **87**(9), 2785–2796 (2010).

[76] G. Lin and T. V. Nguyen. Effect of Thickness and Hydrophobic Polymer Content of the Gas Diffusion Layer on Electrode Flooding Level in a PEMFC. *Journal of The Electrochemical Society*, **152**(10), A1942–A1948 (2005).

[77] E. Gauthier, Q. Duan, T. Hellstern, and J. Benziger. Water Flow in, Through, and Around the Gas Diffusion Layer. *Fuel Cells*, **12**(5), 835–847 (2012).

[78] A. Forner-Cuenca, J. Biesdorf, A. Lamibrac, V. Manzi-Orezzoli, F. N. Büchi, L. Gubler, T. J. Schmidt, and P. Boillat. Advanced Water Management in PEFCs: Diffusion Layers with Patterned Wettability: II. Measurement of Capillary Pressure Characteristic with Neutron and Synchrotron Imaging. *Journal of The Electrochemical Society*, **163**(9), F1038–F1048 (2016).

[79] A. Forner-Cuenca, J. Biesdorf, V. Manzi-Orezzoli, L. Gubler, T. J. Schmidt, and P. Boillat. Advanced Water Management in PEFCs: Diffusion Layers with Patterned Wettability: III. Operando Characterization with Neutron Imaging. *Journal of The Electrochemical Society*, **163**(13), F1389–F1398 (2016).

[80] A. Forner-Cuenca, V. Manzi-Orezzoli, J. Biesdorf, M. E. Kazzi, D. Streich, L. Gubler, T. J. Schmidt, and P. Boillat. Advanced Water Management in PEFCs: Diffusion Layers with Patterned Wettability: I. Synthetic Routes, Wettability Tuning and Thermal Stability. *Journal of The Electrochemical Society*, **163**(8), F788–F801 (2016).

[81] H. Markötter, J. Haussmann, R. Alink, C. Totzke, T. Arlt, M. Klages, H. Riesemeier, J. Scholta, D. Gerteisen, J. Banhart, and I. Manke. Influence of cracks in the microporous layer on the water distribution in a PEM fuel cell investigated by synchrotron radiography. *Electrochemistry Communications*, **34**, 22–24 (2013).

[82] S. S. Alrwashdeh, H. Markötter, J. Haußmann, T. Arlt, M. Klages, J. Scholta, J. Banhart, and I. Manke. Investigation of water transport dynamics in polymer

electrolyte membrane fuel cells based on high porous micro porous layers. *Energy*, **102**, 161–165 (2016).

[83] Z. Lu, J. Waldecker, M. Tam, and M. Cimenti. Influence of MPL Structure Modification on Fuel Cell Oxygen Transport Resistance. *ECS Transactions*, **69**(17), 1341–1353 (2015).

[84] M. P. Manahan, M. C. Hatzell, E. C. Kumbur, and M. M. Mench. Laser perforated fuel cell diffusion media. Part I: Related changes in performance and water content. *Journal of Power Sources*, **196**(13), 5573–5582 (2011).

[85] J. Haußmann, H. Markötter, R. Alink, A. Bauder, K. Dittmann, I. Manke, and J. Scholta. Synchrotron radiography and tomography of water transport in perforated gas diffusion media. *Journal of Power Sources*, **239**, 611–622 (2013).

[86] Z. Lu and J. Waldecker. Microporous layer structures and gas diffusion layer assemblies in proton exchange membrane fuel cells (2015). US 8,945,790 B2.

[87] T. Sasabe, P. Deevanhxay, S. Tsushima, and S. Hirai. Soft X-ray visualization of the liquid water transport within the cracks of micro porous layer in PEMFC. *Electrochemistry Communications*, **13**(6), 638–641 (2011).

[88] G. Selvarani, A. K. Sahu, P. Sridhar, S. Pitchumani, and A. K. Shukla. Effect of diffusion-layer porosity on the performance of polymer electrolyte fuel cells. *Journal of Applied Electrochemistry*, **38**(3), 357–362 (2008).

[89] H. Sadeghifar, N. Djilali, and M. Bahrami. Effect of Polytetrafluoroethylene (PTFE) and micro porous layer (MPL) on thermal conductivity of fuel cell gas diffusion layers: Modeling and experiments. *Journal of Power Sources*, **248**, 632–641 (2014).

[90] C. Simon, J. Endres, B. Nefzger-Loders, F. Wilhelm, and H. A. Gasteiger. Interaction of Pore Size and Hydrophobicity/Hydrophilicity for Improved Oxygen and Water Transport through Microporous Layers. *Journal of The Electrochemical Society*, **166**(13), F1022–F1035 (2019).

[91] Y. Aoyama, Y. Tabe, R. Nozaki, K. Suzuki, T. Chikahisa, and T. Tanuma. Analysis of Water Transport inside Hydrophilic Carbon Fiber Micro-Porous Layers with High-Performance Operation in PEFC. *Journal of The Electrochemical Society*, **165**(7), F484–F491 (2018).

[92] T. Tanuma and S. Kinoshita. Impact of Gas Diffusion Layers (GDLs) on MEA Performance. *ECS Transactions*, **41**(1), 603–610 (2011).

[93] T. Tanuma. Innovative Hydrophilic Microporous Layers for Cathode Gas Diffusion Media. *Journal of the Electrochemical Society*, **157**(12), B1809–B1813 (2010).

[94] T. Tanuma, M. Kawamoto, and S. Kinoshita. Effect of Properties of Hydrophilic Microporous Layer (MPL) on PEFC Performance. *Journal of The Electrochemical Society*, **164**(6), F499–F503 (2017).

[95] T. Tanuma and S. Kinoshita. Impact of gas diffusion layers (GDLs) on MEA performance in PEFCs. *Energy Procedia*, **28**(Supplement C), 12–19 (2012).

[96] T. Tanuma and S. Kinoshita. Impact of Gas Diffusion Layers (GDLs) on Water Transport in PEFCs. *Journal of the Electrochemical Society*, **159**(2), B150–B154 (2012).

[97] T. Kitahara, T. Konomi, and H. Nakajima. Microporous layer coated gas diffusion layers for enhanced performance of polymer electrolyte fuel cells. *Journal of Power Sources*, **195**(8), 2202–2211 (2010).

[98] N. Khajeh-Hosseini-Dalasm, T. Sasabe, T. Tokumasu, and U. Pasaogullari. Effects of polytetrafluoroethylene treatment and compression on gas diffusion layer microstructure using high-resolution X-ray computed tomography. *Journal of Power Sources*, **266**, 213–221 (2014).

[99] R. Mukundan, J. Davey, J. D. Fairweather, D. Spernjak, J. S. Spendelow, D. S. Hussey, D. Jacobson, P. Wilde, R. Schweiss, and R. L. Borup. Effect of Hydrophilic Treatment of Microporous Layer on Fuel Cell Performance. *ECS Transactions*, **33**(1), 1109–1114 (2010).

[100] R. Schweiss, M. Steeb, and P. M. Wilde. Mitigation of Water Management in PEM Fuel Cell Cathodes by Hydrophilic Wicking Microporous Layers. *Fuel Cells*, **10**(6), 1176–1180 (2010).

[101] P. Shrestha, R. Banerjee, J. Lee, N. Ge, D. Muirhead, H. Liu, A. K. C. Wong, D. Ouellette, B. Zhao, and A. Bazylak. Hydrophilic microporous layer coatings for polymer electrolyte membrane fuel cells operating without anode humidification. *Journal of Power Sources*, **402**, 468–482 (2018).

[102] T. Tanuma and M. Kawamoto. Effect of Pore Volume of Hydrophilic Microporous Layer (MPL) on PEFC Performance. *ECS Transactions*, **69**(17), 1323–1329 (2015).

[103] D. Spernjak, R. Mukundan, R. L. Borup, L. G. Connolly, B. I. Zackin, V. De Andrade, M. Wojcik, D. Y. Parkinson, D. L. Jacobson, D. S. Hussey, K. L. More,

T. Chan, A. Z. Weber, and I. V. Zenyuk. Enhanced Water Management of Polymer Electrolyte Fuel Cells with Additive-Containing Microporous Layers. *ACS Applied Energy Materials*, **1**(11), 6006–6017 (2018).

[104] C.-C. Fan and M.-H. Chang. Improving proton exchange membrane fuel cell performance with carbon nanotubes as the material of cathode microporous layer. *International Journal of Energy Research*, **40**(2), 181–188 (2016).

[105] J. Lee, R. Banerjee, M. G. George, D. Muirhead, P. Shrestha, H. Liu, N. Ge, S. Chevalier, and A. Bazylak. Multiwall Carbon Nanotube-Based Microporous Layers for Polymer Electrolyte Membrane Fuel Cells. *Journal of The Electrochemical Society*, **164**(12), F1149–F1157 (2017).

[106] E. Antolini, R. R. Passos, and E. A. Ticianelli. Effects of the carbon powder characteristics in the cathode gas diffusion layer on the performance of polymer electrolyte fuel cells. *Journal of Power Sources*, **109**(2), 477–482 (2002).

[107] L. R. Jordan, A. K. Shukla, T. Behrsing, N. R. Avery, B. C. Muddle, and M. Forsyth. Diffusion layer parameters influencing optimal fuel cell performance. *Journal of Power Sources*, **86**(1), 250–254 (2000).

[108] L. Jordan, A. Shukla, T. Behrsing, N. Avery, B. Muddle, and M. Forsyth. Effect of diffusion-layer morphology on the performance of polymer electrolyte fuel cells operating at atmospheric pressure. *Journal of Applied Electrochemistry*, **30**(6), 641–646 (2000).

[109] T. Kitahara, H. Nakajima, and K. Okamura. Influence of GDL Coated with MPL Containing CNTs on PEFC Performance Under Low and High Humidity Conditions. *ECS Transactions*, **64**(3), 477–483 (2014).

[110] T. Kitahara, H. Nakajima, and K. Okamura. Gas diffusion layers coated with a microporous layer containing hydrophilic carbon nanotubes for performance enhancement of polymer electrolyte fuel cells under both low and high humidity conditions. *Journal of Power Sources*, **283**, 115–124 (2015).

[111] X. L. Wang, H. M. Zhang, J. L. Zhang, H. F. Xu, Z. Q. Tian, J. Chen, H. X. Zhong, Y. M. Liang, and B. L. Yi. Micro-porous layer with composite carbon black for PEM fuel cells. *Electrochimica Acta*, **51**(23), 4909–4915 (2006).

[112] J. Lee, R. Yip, P. Antonacci, N. Ge, T. Kotaka, Y. Tabuchi, and A. Bazylak. Synchrotron Investigation of Microporous Layer Thickness on Liquid Water Distribution in a PEM Fuel Cell. *Journal of The Electrochemical Society*, **162**(7), F669–F676 (2015).

[113] P. Antonacci, S. Chevalier, J. Lee, N. Ge, J. Hinebaugh, R. Yip, Y. Tabuchi, T. Kotaka, and A. Bazylak. Balancing mass transport resistance and membrane resistance when tailoring microporous layer thickness for polymer electrolyte membrane fuel cells operating at high current densities. *Electrochimica Acta*, **188**(Supplement C), 888–897 (2016).

[114] S. Park, J.-W. Lee, and B. N. Popov. Effect of carbon loading in microporous layer on PEM fuel cell performance. *Journal of Power Sources*, **163**(1), 357–363 (2006).

[115] T. Kitahara and H. Nakajima. Microporous layer-coated gas diffusion layer to reduce oxygen transport resistance in a polymer electrolyte fuel cell under high humidity conditions. *International Journal of Hydrogen Energy*, **41**(22), 9547–9555 (2016).

[116] T. Kitahara, H. Nakajima, M. Inamoto, and M. Morishita. Novel hydrophilic and hydrophobic double microporous layer coated gas diffusion layer to enhance performance of polymer electrolyte fuel cells under both low and high humidity. *Journal of Power Sources*, **234**, 129–138 (2013).

[117] T. Kitahara, H. Nakajima, and K. Okamura. Influence of Hydrophilic and Hydrophobic Triple MPL Coated GDL on the Oxygen Transport Resistance in a PEFC under High Humidity Conditions. *ECS Transactions*, **69**(17), 1313–1322 (2015).

[118] X. L. Wang, H. M. Zhang, J. L. Zhang, H. F. Xu, X. B. Zhu, J. Chen, and B. L. Yi. A bi-functional micro-porous layer with composite carbon black for PEM fuel cells. *Journal of Power Sources*, **162**(1), 474–479 (2006).

[119] J. Ge, A. Higier, and H. Liu. Effect of gas diffusion layer compression on PEM fuel cell performance. *Journal of Power Sources*, **159**(2), 922–927 (2006).

[120] M. B. Sassin, Y. Garsany, B. D. Gould, and K. Swider-Lyons. Impact of Compressive Stress on MEA Pore Structure and Its Consequence on PEMFC Performance. *Journal of The Electrochemical Society*, **163**(8), F808–F815 (2016).

[121] N. Zamel, X. G. Li, and J. Shen. Correlation for the Effective Gas Diffusion Coefficient in Carbon Paper Diffusion Media. *Energy & Fuels*, **23**, 6070–6078 (2009).

[122] E. L. Curtis. *Diffusion: Mass Transfer in Fluid Systems (third ed.)*. Cambridge University Press, Cambridge (2009).

[123] J. Hirschfelder, C. F. Curtiss, and R. B. Bird. *Molecular Theory of Gases and Liquids*. Wiley, New York (1966).

[124] C. Simon, F. Hasché, D. Müller, and H. A. Gasteiger. Influence of the Gas Diffusion Layer Compression on the Oxygen Mass Transport in PEM Fuel Cells. *ECS Transactions*, **69**(17), 1293–1302 (2015).

[125] G. S. Harzer, A. Orfanidi, H. El-Sayed, P. Madkikar, and H. A. Gasteiger. Tailoring Catalyst Morphology towards High Performance for Low Pt Loaded PEMFC Cathodes. *Journal of The Electrochemical Society*, **165**(10), F770–F779 (2018).

[126] G. S. Harzer, J. N. Schwämmlein, A. M. Damjanović, S. Ghosh, and H. A. Gasteiger. Cathode Loading Impact on Voltage Cycling Induced PEMFC Degradation: A Voltage Loss Analysis. *Journal of The Electrochemical Society*, **165**(6), F3118–F3131 (2018).

[127] D. A. Caulk and D. R. Baker. Modeling Two-Phase Water Transport in Hydrophobic Diffusion Media for PEM Fuel Cells. *Journal of the Electrochemical Society*, **158**(4), B384–B393 (2011).

[128] R. Bird, W. Stewart, and E. Lightfoot. *Transport Phenomena (revised second ed.)*. John Wiley & Sons, New York (2007).

[129] B. Tjaden, S. J. Cooper, D. J. L. Brett, D. Kramer, and P. R. Shearing. On the origin and application of the Bruggeman correlation for analysing transport phenomena in electrochemical systems. *Current Opinion in Chemical Engineering*, **12**, 44–51 (2016).

[130] D. Kramer, S. A. Freunberger, R. Flückiger, I. A. Schneider, A. Wokaun, F. N. Büchi, and G. G. Scherer. Electrochemical diffusimetry of fuel cell gas diffusion layers. *Journal of Electroanalytical Chemistry*, **612**(1), 63–77 (2008).

[131] J. Kim, G. Luo, and C.-Y. Wang. Modeling two-phase flow in three-dimensional complex flow-fields of proton exchange membrane fuel cells. *Journal of Power Sources*, **365**, 419–429 (2017).

[132] J. T. Gostick, M. A. Ioannidis, M. W. Fowler, and M. D. Pritzker. On the role of the microporous layer in PEMFC operation. *Electrochemistry Communications*, **11**(3), 576–579 (2009).

[133] Y. Liu, M. W. Murphy, D. R. Baker, W. Gu, C. Ji, J. Jorne, and H. A. Gasteiger. Proton conduction and oxygen reduction kinetics in PEM fuel cell cathodes: effects of ionomer-to-carbon ratio and relative humidity. *Journal of The Electrochemical Society*, **156**(8), B970–B980 (2009).

[134] T. Kitahara, H. Nakajima, and K. Mori. Hydrophilic and hydrophobic double microporous layer coated gas diffusion layer for enhancing performance of polymer electrolyte fuel cells under no-humidification at the cathode. *Journal of Power Sources*, **199**, 29–36 (2012).

List of Figures

List of Tables

Acknowledgments

This PhD thesis was prepared in the time between January 2014 and January 2020, of which I conducted my lab work between January 2014 and January 2018. Of course, I would not have successfully finished the thesis without the contributions and the support of colleagues, project partners, friends and family. From all those people, I first like to thank my PhD supervisor Hubert Gasteiger for his professional and personal support during the preparation of this thesis. In particular his advice for all scientific questions, his rigorous interest in my research topic, his commitment in late evening and weekend sessions and his patience, in particular after I left his Chair waiting for the first draft of this thesis, were essential for my dissertation. I am deeply grateful for the years I could work with him, the experiences I had, the friendship, and last but not least the fun I had during this time. I would not like to miss this time in my life.

My first contact I had with the Chair of Technical Electrochemistry was with my Master's Thesis in 2013. Frédéric Hasché and Julien Durst supervised my thesis and have taught me the fuel cell basics, of which I still profit. From the preparation of my Master's thesis on, they always had an open ear, and they motivated me to continue research as a PhD student. I would like to thank Frédéric and Julien for their guidance and their friendship.

Of course the Chair of Technical Electrochemistry would not function without the administrative support of Veronika Pichler. It would not have been possible without her to solve bureaucratic and organization issues, master travel applications, fuel cell test station and many more challenges.

Moreover my thanks goes to my great colleagues for their teamwork and their friendship. First, I would like to thank my office colleague Armin Siebel, Johannes Landesfeind, Pankaj Madkikar and Hany El-Sayed for the great room atmosphere for 4 years. Furthermore Gregor Harzer is acknowledged for his support concerning all issues in the lab and beyond and (I would like to return this honor) for being the best conference-buddy on all our business trips. Moreover I like to express my gratitute

to Michael Striednig for our common work on MPL analysis and for our cooperation with Daniel Ritzberger from the University of Vienna for a common publication. In addition, I would like to thank Michele Piana, Alin Orfanidi, Jan Schwämmlein, Hans Beyer, and Heiko Juranowitsch for any support in the lab. I thank my colleagues for great four years at the Chair, late afterwork sessions at Schwabinger 7 (including Sophie Solchenbach, Michael Metzger and Morten Wetjen), and for long-lasting friendships. A special thanks goes to Katia Rodewald, who made the best SEM images of our materials.

Without the work of diligent students, the plenty of results of this thesis would not have been possible. So I would like to thank David Müller, Dena Kartouzian, Joseph Endres, Benjamin Nefger-Loders, Wan-Zhen Sen, and Thomas Kopfmüller for their rigorous work and their engagement.

My work was carried out within the framework of the joint project "Optigaa2". Financial support by the German Federal Ministry of Economic Affairs and Energy (grant number 03ET6015E), Freudenberg Performance Materials SE & Co. KG and Daimler AG is gratefully acknowledged. In particular, I would like to thank Achim Bock from Freudenberg, who supported us in the preparation of microporous layers and injected new ideas into the project. Furthermore the support and co-authorship of Florian Wilhelm from the ZSW is acknowledged, who provided our research with the porosimetry measurements.

In addition, I experienced great help from the colleagues from General Motors fuel cell research. I would like to thank Danny Baker, who first investigated the limiting current method, for meeting with me twice and discussing my data with him. Furthermore, Mark Mathias and Mehul Vora are greatfully acknowledged for measuring the thermal conductivity of GDL substrate materials.

Last but not least, I would like to gratefully acknowledge my family. My academic studies would not have been possible without my parents Theodora and Kurt Simon, who supported my education anytime. I could always rely on them. As well, I am thankful for the support of my fiance Karin. She was always driving me to continue with my thesis and helped me to overcome scientific and personal lows. Without her emotional support, I would not have been able to finish this project.

A. Technical Drawings

A.1. Flow Field - TUM

$5\,\mathrm{cm}^2$ active area, 7 channels

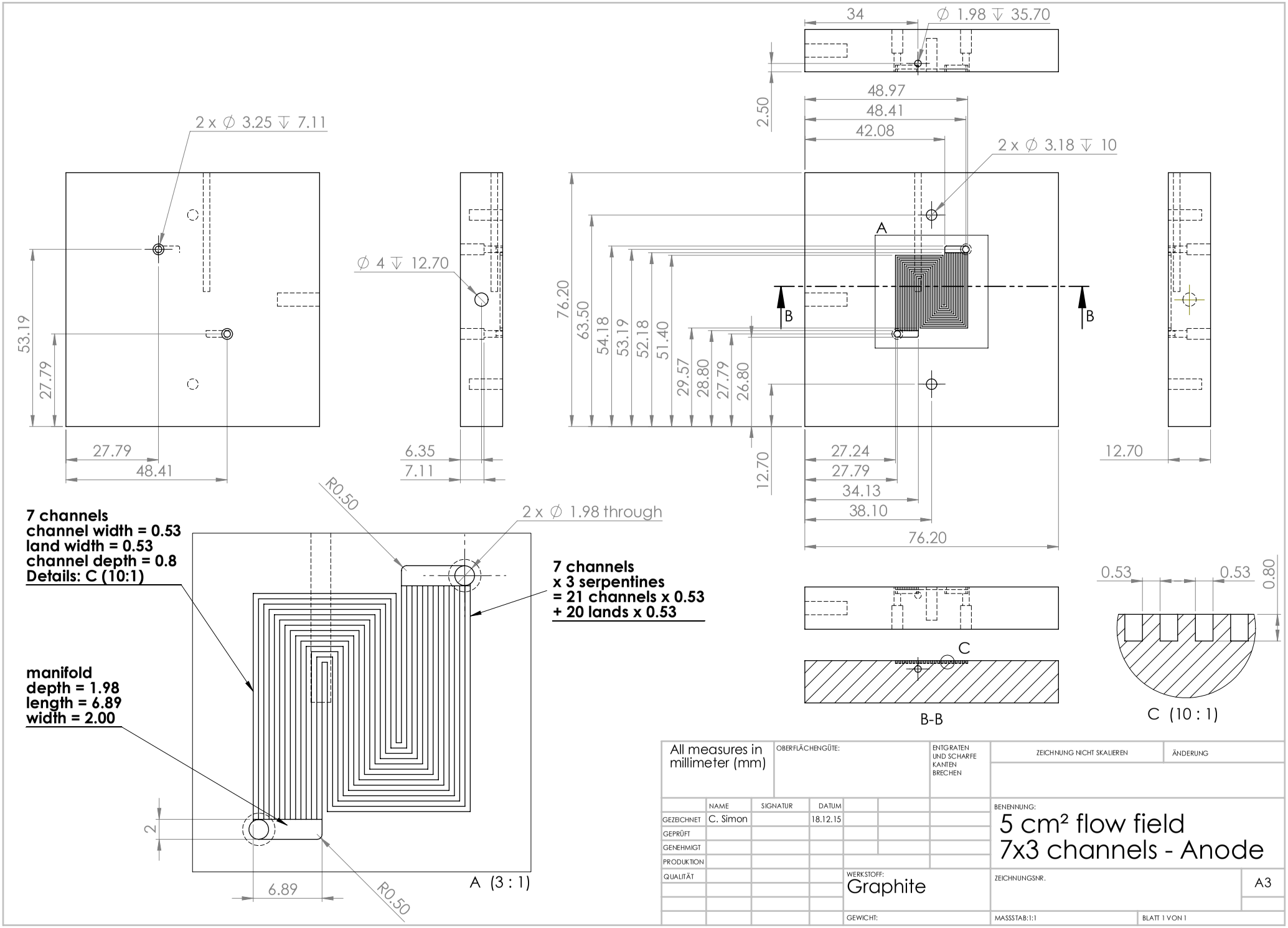

All measures in millimeter (mm)	OBERFLÄCHENGÜTE:		ENTGRATEN UND SCHARFE KANTEN BRECHEN	ZEICHNUNG NICHT SKALIEREN	ÄNDERUNG	
	NAME	SIGNATUR	DATUM	BENENNUNG: 5 cm² flow field 7x3 channels - Anode		
GEZEICHNET	C. Simon		18.12.15			
GEPRÜFT						
GENEHMIGT						
PRODUKTION						
QUALITÄT						
				WERKSTOFF: Graphite	ZEICHNUNGSNR.	A3
				GEWICHT:	MASSSTAB:1:1	BLATT 1 VON 1

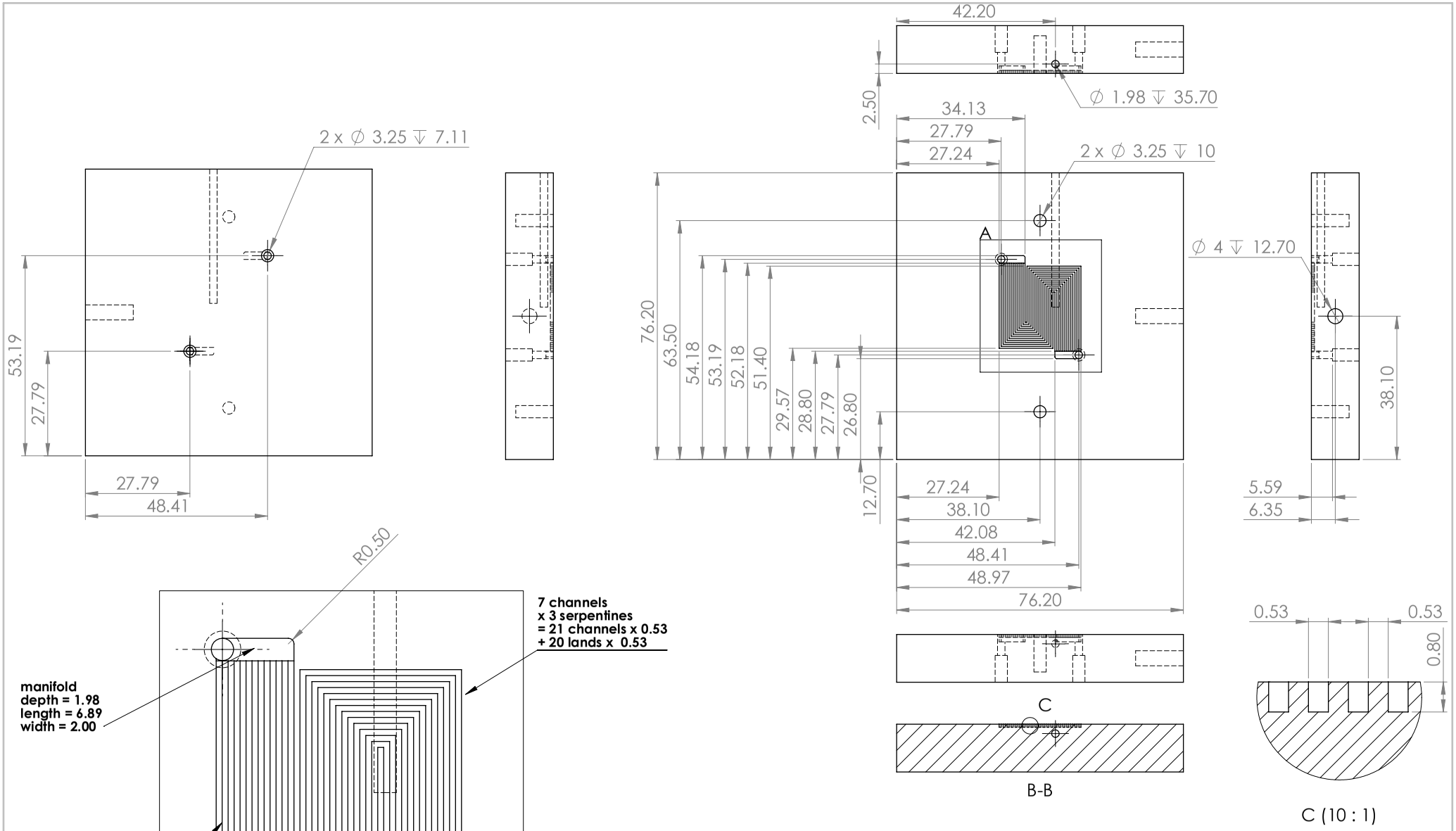

All measures in millimeter (mm)	OBERFLÄCHENGÜTE:		ENTGRATEN UND SCHARFE KANTEN BRECHEN	ZEICHNUNG NICHT SKALIEREN	ÄNDERUNG	
	NAME	SIGNATUR	DATUM	BENENNUNG:		
GEZEICHNET	C. Simon		18.12.15	5 cm² flow field 7x3 channels - Cathode		
GEPRÜFT						
GENEHMIGT						
PRODUKTION						
QUALITÄT				ZEICHNUNGSNR.	A3	
WERKSTOFF: Graphite						
GEWICHT:				MASSSTAB:1:2	BLATT 1 VON 1	

A.2. Flow Field - GM

$50\,\mathrm{cm}^2$ active area, 14 channels
(reproduced from D. R. Baker, D. A. Caulk, K. C. Neyerlin and M. W. Murphy *J. Electrochem. Soc.*, **156**, B991 (2009)[25])

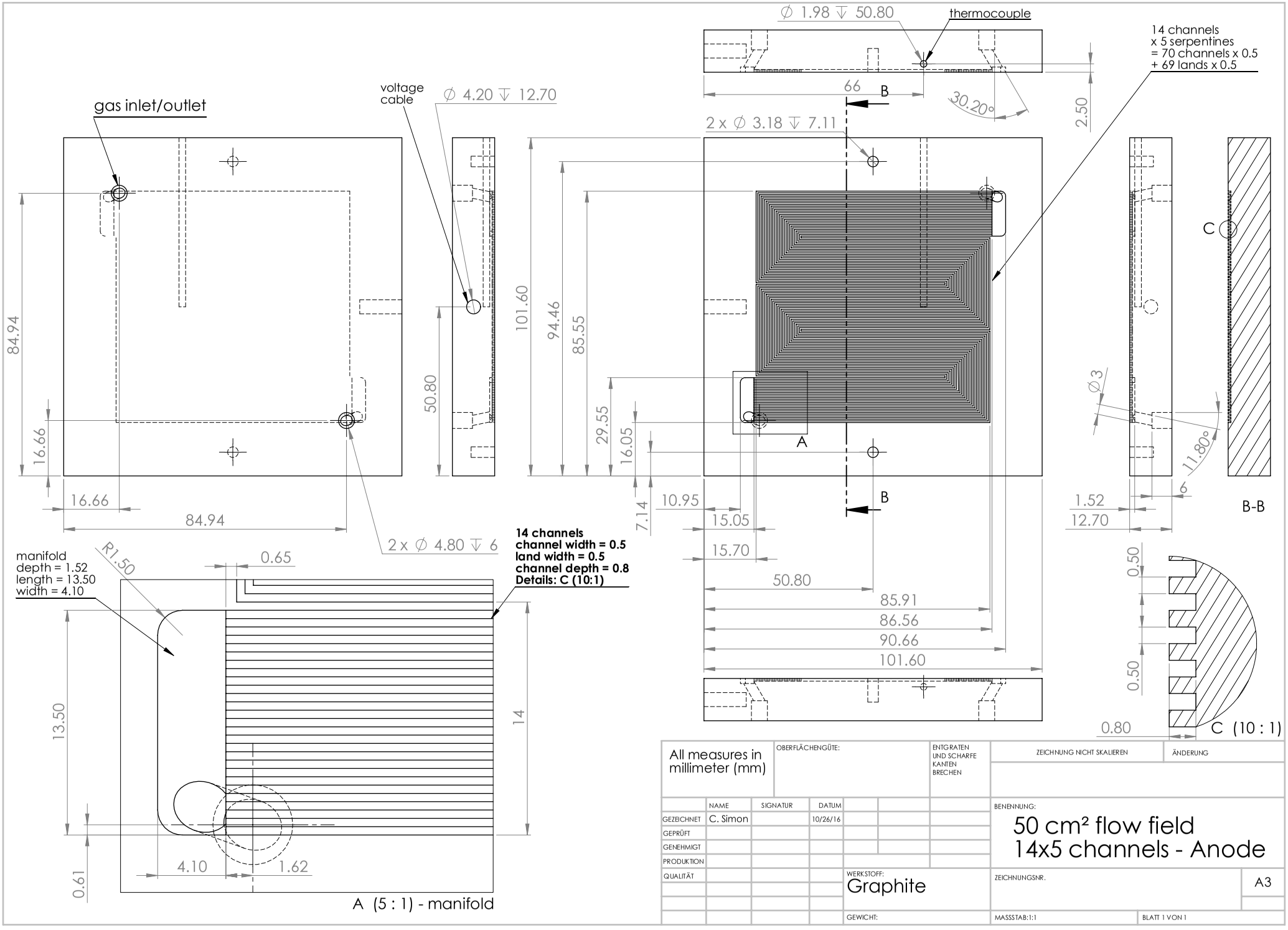

All measures in millimeter (mm)	OBERFLÄCHENGÜTE:		ENTGRATEN UND SCHARFE KANTEN BRECHEN	ZEICHNUNG NICHT SKALIEREN	ÄNDERUNG	
	NAME	SIGNATUR	DATUM	BENENNUNG:		
GEZEICHNET	C. Simon		10/26/16	50 cm² flow field 14x5 channels - Anode		
GEPRÜFT						
GENEHMIGT						
PRODUKTION						
QUALITÄT						
				WERKSTOFF: Graphite	ZEICHNUNGSNR.	A3
				GEWICHT:	MASSSTAB:1:1	BLATT 1 VON 1

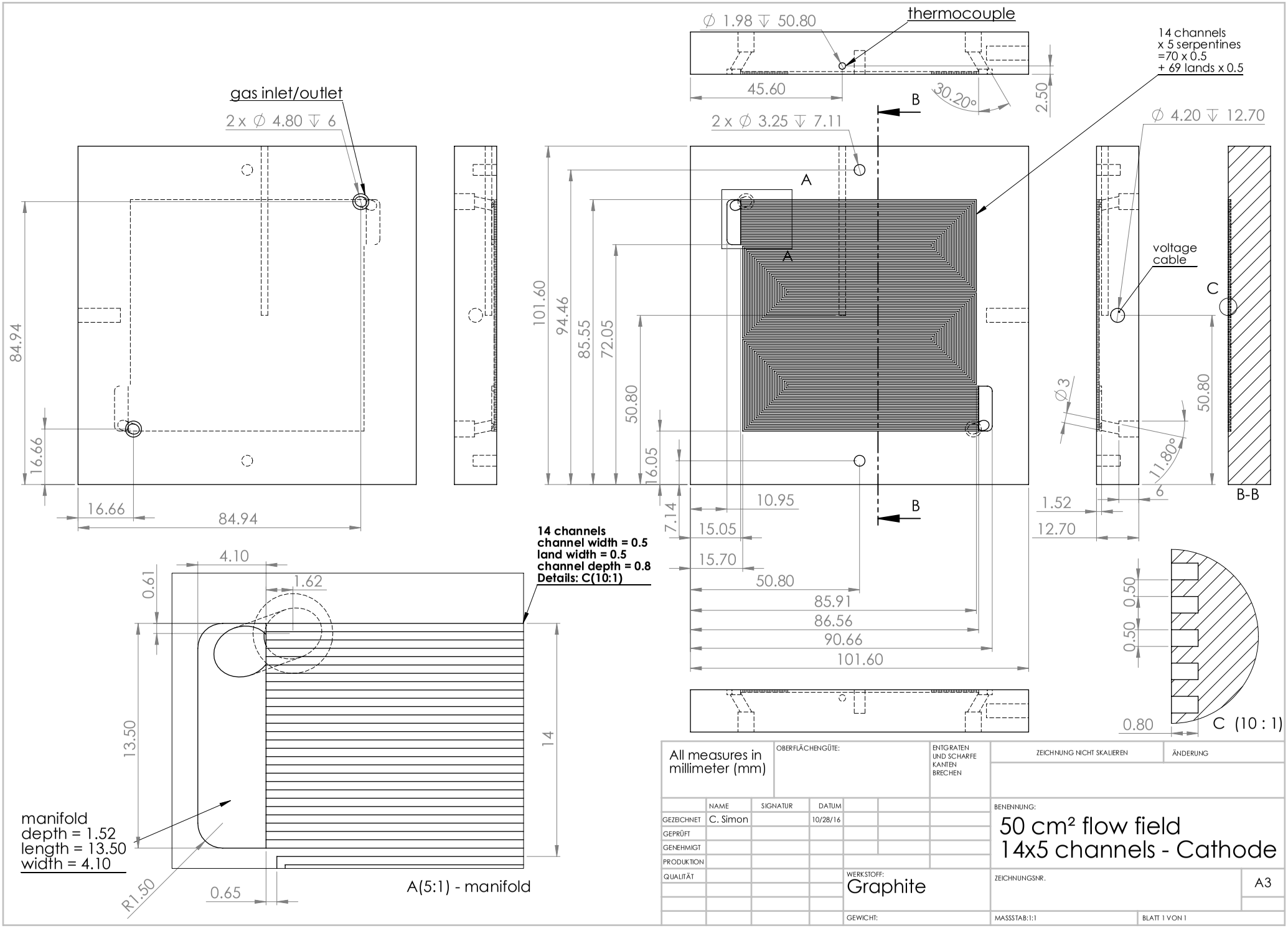

All measures in millimeter (mm)	OBERFLÄCHENGÜTE:		ENTGRATEN UND SCHARFE KANTEN BRECHEN	ZEICHNUNG NICHT SKALIEREN	ÄNDERUNG	
	NAME	SIGNATUR	DATUM	BENENNUNG:		
GEZEICHNET	C. Simon		10/28/16	50 cm² flow field 14x5 channels - Cathode		
GEPRÜFT						
GENEHMIGT						
PRODUKTION						
QUALITÄT						
				WERKSTOFF: Graphite	ZEICHNUNGSNR.	A3
				GEWICHT:	MASSSTAB:1:1	BLATT 1 VON 1